

**COMBUSTION CHARACTERISTICS AND IN-  
CYLINDER PROCESS OF CAI COMBUSTION WITH  
ALCOHOL FUELS**

A thesis submitted for the degree of Doctor of Philosophy

By

**Manida Tongroon**

School of Engineering and Design  
Brunel University  
United Kingdom

May 2010

Brunel University  
School of Engineering and Design  
United Kingdom

Manida Tongroon

**Investigation Combustion Characteristics and In-Cylinder Process of CAI  
Combustion with Alcohol Fuels**

May 2010

**Abstract**

Controlled auto-ignition (CAI) combustion in the gasoline engine has been extensively studied in the last several years due to its potential for simultaneous improvement in fuel consumption and exhaust emissions. At the same time, there has been increasing interest in the use of alternative fuels in order to reduce reliance on conventional fossil fuels. Therefore, this study has been carried out to investigate the effect of alcohol fuels on the combustion characteristics and in-cylinder processes of CAI combustion in a single cylinder gasoline engine.

In order to study the effect of alcohol fuels, combustion characteristics were investigated by heat releases analysis in the first part. The combustion process was studied through flame structure and excited molecule by chemiluminescence imaging. Furthermore, in-cylinder gas composition was analysis by GC-MS to identify the auto-ignition reactions involved in the CAI combustion. In addition, the influence of spark-assisted ignition and injection timings were also studied.

Alcohol fuels, in particular methanol, resulted in advanced auto-ignition and faster combustion than that of gasoline. In addition, their use could lead to substantially lower HC, NO<sub>x</sub> and CO exhaust emissions. Spark-assisted ignition assisted gasoline combustion by advancing ignition timing and initiating flame kernel at the centre of combustion chamber but it had marginal effect on alcohol fuels. Auto-ignition always took place at the perimeter of the chamber and occurred earlier with alcohol fuels. Fuel reforming reactions during the NVO period were observed and they had significant effect on alcohol combustion.

## **Acknowledgements**

I would like to express, first and foremost, my greatest respect, admiration and gratitude to Professor Hua Zhao for his interest, guidance and support throughout the course of my PhD by accepting me as his PhD student in the Centre for Advanced Powertrain and Fuels (CAPF). I owe him for all the knowledge and experience acquired during the past 4 years.

I am extremely grateful to thank Royal Thai Government for the financial support that made possible my study and stay in UK.

I would like to express my gratitude to the continual assistance from various technicians, Chief technician John Langdon, Technicians Clive Barrett, Ken Anstiss, and Andy Sellway for their advice and technical support. I also would like to thank Paul and Les in the stores, giving sincere advice, technical and substantial support and above all friendship.

I would like to thank my good friends and colleagues, Dr. Kiranjeev Gill, Dr. Navin Kalian, Dr. Changho Yang, Dr. Ben Leach, Dr. Mario Martins, Dr. Lyn McWilliam, Dr. Yan Zhang, Reza Herfatmanesh and Cho-Yu Lee for their continuous help, support and friendship to keep me motivated and give me a wonderful life experience.

Finally, I would like to thank my family for listening, giving me the strength, motivation and support to overcome the difficult moments and to make the most of this experience.

## Nomenclature

### General Abbreviations

AFR	Air/Fuel Ratio
AR	Activated Radical
ATAC	Active Thermo-Atmospheric Combustion
ATDC	After Top Dead Centre
AVT	Active Valve Train
BDC	Bottom Dead Centre
BTDC	Before Top Dead Centre
CA	Crank Angle
CAI	Controlled Auto-Ignition
CI	Compression Ignition
CIHI	Compression Ignited Homogeneous Charge
CNG	Compressed Natural Gas
CO	Carbon monoxide
COV	Coefficient of Variation
CO <sub>2</sub>	Carbon dioxide
DAQ	Data Acquisition System
DI	Direct Injection
DME	Dimethyl Ether
EGR	Exhaust Gas Re-Circulation
EVC	Exhaust Valve Close
FID	Flam Ionization Detector
FWHM	Full Width at Half Maximum
GC	Gas Chromatography
HC	Hydrocarbon
HCCI	Homogeneous Charge Compression Ignition
HPLC	High Performance Liquid Chromatography
HRR	Heat Release Rate
IC	Internal Combustion
ID	Internal Diameter

IMEP	Indicated Mean Effective Pressure
IR	Infrared
ISFC	Indicated Specific Fuel Consumption
IVC	Inlet Valve Close
IVO	Inlet Valve Open
LHV	Lower Heating Value
LVN	Lowest Normalised Value
LPG	Liquefied Petroleum Gas
MFB	Mass Fraction Burned
MON	Motored Octane Number
MPI	Manifold Port Injector
MS	Mass Spectrometer
NDIR	Nondispersive Infrared
NO	Nitric Oxide
NO <sub>x</sub>	Nitrogen Oxides
NO <sub>2</sub>	Nitrogen Dioxide
NTC	Negative Temperature Coefficient
NVO	Negative Valve Overlap
PC	Personal Computer
pC	Pico Coulomb
PFI	Port Fuel Injection
PLIEF	Planar Laser Induced Exciplex Fluorescence
ppm	Parts per Million
PRF	Primary Reference Fuel
P <sub>max</sub>	Maximum of Pressure
RCM	Rapid Compression Machine
rpm	Revolutions per Minute
RON	Research Octane Number
RT	Retention Time
SI	Spark Ignition
SOI	Start of Injection
SULEV	Super Low Emissions Vehicle
TDC	Top Dead Centre
THC	Total Hydrocarbon

TLEV	Transitional Low Emissions Vehicle
TS	Toyota-Soken
uHC	Unburned Hydrocarbon
UV	Ultraviolet
VTC	Variable Timing Camshaft

### **Greek Symbols**

$c_p$	Specific Heat at Constant Pressure
$\gamma$	Ratio of Specific heat
$\theta$	Crank Angle
$\lambda$	Relative air/fuel ratio
$h$	Plank's constant
$\nu$	Photon's frequency
$n$	Mole number

<b>Contents</b>	<b>Page</b>
<b>1. Introduction</b>	
1.1 Introduction	1
1.2 Objectives	3
1.3 Outline of Thesis	3
<b>2. Literature Reviews</b>	
2.1 Introduction	6
2.2 Controlled Auto-Ignition Combustion	6
2.2.1 CAI/HCCI Technology and Strategy	8
2.2.2 Spark-Assisted Ignition	9
2.2.3 Fuel Injection	10
2.3 Alternative Fuels	11
2.3.1 Methanol	12
2.3.2 Ethanol	14
2.4 Chemiluminescence Image	15
2.4.1 Total Chemiluminescence	16
2.4.2 OH Chemiluminescence	18
2.4.3 Formaldehyde Chemiluminescence	19
2.4.4 CH, C <sub>2</sub> , CHO Chemiluminescence	20
2.5 In-Cylinder Gas Sampling	20
2.6 Chemical Kinetic Reaction Mechanism	22
2.6.1 Isooctane and n-Heptane	23
2.6.2 Gasoline Fuels	24
2.6.3 Ethanol	26
2.6.4 Methanol	27
2.7 Ignition Process	28
2.7.1 Single-Stage Ignition	28
2.7.2 Two-Stage Ignition	29
2.8 Summary	31
<b>3. Experimental Test Facility</b>	
3.1 Introduction	33
3.2 Engine Testing Equipment and Facility	33

3.2.1	Research Engine	33
3.2.1.1	Crankshaft Position System	35
3.2.1.2	Air-Assisted Fuel Injection System	35
3.2.2	Pressure Transducer and In-Cylinder Pressure Acquisition System	37
3.2.3	Fuels	38
3.3	Exhaust Measurement	39
3.3.1	Unburned Hydrocarbon	39
3.3.2	Oxides of Nitrogen	40
3.3.3	CO, CO <sub>2</sub> and O <sub>2</sub>	41
3.4	Experiment setup for Chemiluminescence Imaging	42
3.4.1	Optical access to the engine	42
3.4.2	Image Acquisition System	42
3.4.2	Optical Bandpass Filter	43
3.5	In-Cylinder Sampling and Gas Composition Analysis	44
3.5.1	Fast Response In-Cylinder Gas Sampling Valve	44
3.5.2	Gas Chromatography	47
3.5.3	Mass Spectrometer	48
3.6	Summary	50
<b>4.</b>	<b>Thermodynamic Engine Test Results and Analysis</b>	
4.1	Introduction	51
4.2	Test Methodology	51
4.2.1	Selection of Injection Timing	51
4.2.2	Spark-and Non-Spark-Assisted Combustion	53
4.2.3	Fuels	53
4.2.4	Experimental Procedure	53
4.3	Results and Discussion for Fuel Injection Timing at 80 BTDC	54
4.3.1	In-Cylinder pressure data	54
4.3.2	Heat Release Analysis	66
4.3.3	Engine-Out Exhaust Emission	73
4.3.4	Effects of Injection Timing	77
4.4	Summary	81

<b>5. In-Cylinder Combustion Studies through Chemiluminescence Imaging</b>	
5.1 Introduction	83
5.2 Test Methodology	83
5.2.1 Operating Conditions	83
5.2.2 Experiment Procedure	85
5.3 Results and Discussion	86
5.3.1 Total Chemiluminescence Images	87
5.3.1.1 Spark-Assisted Ignition	87
5.3.1.2 Non-Spark-Assisted Ignition	99
5.3.2 CHO Chemiluminescence Images	110
5.3.2.1 Spark-Assisted Ignition	110
5.3.2.2 Non-Spark-Assisted Ignition	120
5.3.3 OH Chemiluminescence Images	129
5.3.3.1 Spark-Assisted Ignition	129
5.3.3.2 Non-Spark-Assisted Ignition	140
5.4 Summary	148
<b>6. In-Cylinder and Exhaust Gas Species Analysis</b>	
6.1 Introduction	150
6.2 Test methodology	150
6.2.1 Test Conditions	150
6.2.2 Experimental Procedure	151
6.3 Results and Discussion	153
6.3.1 GC-MS Spectrum of the Standard Gas	153
6.3.2 Engine-Out Exhaust Gas Speciation	155
6.3.3 In-Cylinder Gas Speciation	164
6.3.3.1 Alkanes	166
6.3.3.2 Olefins	171
6.3.3.3 Aldehydes	178
6.3.3.4 Ketones	183
6.3.3.5 Carbon dioxide	184
6.3.3.6 Gas Species in Gasoline	185
6.4 Summary	186

<b>7. Conclusions and Future Work</b>	
7.1 Summary	188
7.2 Conclusions	189
7.2.1 Effect of Alcohol Fuels on CAI Combustion Performance	189
7.2.2 Effect of Injection Timing	189
7.2.3 Effect of Spark-Assisted Ignition	190
7.2.4 Flame Structure and Auto-Ignition Sites	190
7.2.4.1 Flame Structure through Total Chemiluminescence Image	190
7.2.4.2 CHO and OH Chemiluminescence Image	191
7.2.5 Time-Resolved Detailed Species Composition	191
7.2.5.1 60 PRF and Gasoline	191
7.2.5.2 Ethanol	192
7.2.5.3 Methanol	192
7.3 Recommendation for Future Work	193
<b>Reference</b>	195
<b>Appendix A- Injection Timing at 40 degree ATDC</b>	205
<b>Appendix B- Injection Timing at 80 degree ATDC</b>	218
<b>Appendix C- Injection Timing at 200 degree ATDC</b>	231

# Chapter 1 Introduction

## 1.1 Introduction

Over the last decade, there is an increasing concern over global warming caused by man-made CO<sub>2</sub> emissions. This is in addition to the emission legislation to control harmful exhaust emissions from automobiles. Since crude oil is a limited resource with increasing high demand, its price has progressively increased every year and has experienced a sharp rise in the last few years. Along with the depletion of petroleum, air pollution has been highlighted as a problem. Its impacts result in both local and global environmental effect. On a local level, the vehicle generated pollutants are the causes of some health problems. For instance, NO<sub>x</sub>, which forms photochemical smog, can cause respiratory problems, CO leads to unconsciousness and respiratory failure, particulate matter causes lung problems etc. At the same time, the global environment has been significantly altered by global warming resulting from greenhouse gas emission of CO<sub>2</sub>.

As one of the major sources of air pollution comes from the transportation sector, continual tightening of emission legislations has been enforced in Europe, United States and Japan. Also, other countries have adopted those legislations to restrict pollutant emissions from automobiles. For the last three decades, the reduction of the major emissions from internal combustion engine including NO<sub>x</sub>, CO and volatile organic compounds has been dramatically reduced by means of exhaust gas after-treatment such as the catalytic converter, as well as improved engine technologies.

However, in order to overcome the trade-off between fuel economy (CO<sub>2</sub> emission) and pollutant emissions, many researchers have attempted to develop and modify the new concept engine combustion technology named as controlled auto-ignition combustion (CAI) or homogeneous charge compression ignition (HCCI) over the last decade. The fundamental principle of CAI is to combine the characteristics of homogeneous charge mixture of SI engines together with spontaneous multiple auto-ignition of CI engines. As a result, CAI has been achieved with fuel economy and efficiency comparable to diesel engines but with ultra - low NO<sub>x</sub> emissions. However,

developments to the process have continued intensively in order to address the major drawbacks of CAI - the limited operating range and relatively high HC emission.

To attain CAI combustion, sufficiently high temperature for self-ignition of charge mixture is a key factor. Therefore, many approaches, including heating of the intake charge, increasing the compression ratio and utilizing hot residual gas or EGR have been employed. In particular, the hot residual gas trapping method by means of negative valve overlap has been widely adopted by many researchers. In addition, many investigations have applied spark-assisted ignition as a method of extending the operating regime. Moreover, in-cylinder fuel injection strategies were adopted to control combustion phasing. Therefore, in the current study, controlled auto-ignition combustion via hot trapped residual gas by means of negative valve overlap was adopted with/without the application of spark-assisted ignition. An air-assisted injector was used to study the effect of injection.

In addition to the above methods, fuels of lower auto-ignition temperature, for example n-heptanes, DME, or blended fuels, have been employed to attain CAI combustion. Sustainable renewable fuel such as methanol and ethanol, besides aiding the implementation of CAI combustion, is an alternative way to help reduce energy depletion or even substitute crude oil based fuels. Cleaner combustion and so reduced exhaust emissions is another benefit of these oxygenated fuels. Thus, it is advantageous to combine the advantage of CAI combustion with oxygenated fuels.

In the current study, systematic investigations have been carried out on CAI combustion using alcohol fuels and their blends with gasoline. The experimental studies have been performed in three parts. Thermodynamic engine tests were firstly investigated. In this part, the influence of alcohol fuels on spark-assisted CAI at different injection timings was studied. In-cylinder pressure was recorded and analysed to understand their combustion characteristics. Also, exhaust emissions were measured at the same time.

Optical techniques are powerful tools to investigate in-cylinder combustion phenomena for both conventional and CAI combustion engines. With varying levels of complexity of both equipment and technique, they have been applied extensively

by many researchers in SI and CI engines. Chemiluminescence imaging is one of these techniques and it can be used as an effective means to investigate auto-ignition process and the subsequent high temperature combustion. Moreover, due to the specific chemiluminescence wavelength from each molecule, it can be used to identify the presence of certain species and therefore the occurrence of the reactions concerned. Therefore, to better understand auto-ignition and combustion characteristics, optical diagnostics based on natural chemiluminescence have been applied to investigate flame structure and auto-ignition process of CAI combustion in the second part of this study.

CAI combustion is strongly dependent on chemical kinetic reactions leading to auto-ignition. In order to understand such reactions, the time history of detailed specific gas composition should be indentified. This can be realized by in-cylinder gas sampling and GC-MS analysis. Therefore, in the third part of the current study, in-cylinder gas speciations were performed by means of a fast gas sampling valve and gas chromatography-mass spectrometer (GC-MS).

## **1.2 Objectives**

The objectives of this research are to:

- i) Investigate heat release characteristics and emissions of alcohol/blended fuels with varying injection timings and with/without the effects of spark-assisted ignition in a CAI combustion engine.
- ii) Study in-cylinder combustion processes and flame structures of CAI combustion by means of high speed chemiluminescence imaging.
- iii) Investigate the auto-ignition chemistry of alcohol fuels through gas sampling and GC-MS speciation analysis.

## **1.3 Outline of Thesis**

Following this introduction, Chapter 2 is a review of the relevant literature relating to this study and is split into five parts. Firstly, the history and the current state of the art

of CAI combustion research are outlined in order to understand fundamentals of CAI combustion and the area for further research. Secondly, the application and characteristics of alcohol fuels in IC engines are discussed. The success of the optical technique in the study of CAI combustion is demonstrated in the third part, in particular the suitability of the chemiluminescence imaging technique. In the fourth section, a number of papers relating to the measurement of detailed species composition is reviewed. Finally, the published chemical kinetic reactions of hydrocarbon and alcohol fuel are reviewed.

Chapter 3 presents the experiment facility and setup. The general test facility is described in the first section. The single cylinder Ricardo engine used throughout the experiment is described in detail. The specifications and properties of all fuels used in the current study along with their combustion characteristic are listed. Optical systems for chemiluminescence studies are included in the second section. Finally, instrument and set up for in-cylinder gas analysis are detailed.

Chapter 4 details the thermodynamic experiments and results. The test procedure and conditions are given in the first section. This is followed by the in-cylinder pressure and the heat release results for both gasoline and alcohol fuel blends. In addition, exhaust emissions are presented and compared for different fuel blends.

Chapter 5 presents the chemiluminescence imaging results grouped in three sections. The first section presents the total chemiluminescence images. The second section discusses CHO images. OH chemiluminescence results are then presented and discussed.

Chapter 6 begins with the experimental detail and test condition of in-cylinder gas sampling as well as the format of presenting GC-MS results. Detailed engine-out gas speciation is given to complement the standard exhaust emission measurement. The results of in-cylinder gas composition are then presented in groups of alkane, alkenes, olefin, aldehyde, ketones and CO<sub>2</sub> respectively.

Chapter 7 provides the summary and main conclusion of this study. Recommendations and suggestions are also given for the further research in CAI combustion when using alcohol fuels.

Appendix A, B and C contain the results of the thermodynamic engine tests when injection timing is 40, 80 and 210 ATDC respectively.

## **Chapter 2 Literature Reviews**

### **2.1 Introduction**

Controlled auto-ignition (CAI) combustion gasoline engines have been widely researched due to their potential efficiency comparable to a typical diesel engine. Furthermore, their NO<sub>x</sub> emissions are lower than a conventional spark ignition engine. However, due to the limited operating range and high HC emission, researchers have researched methods in order to overcome these drawbacks. Different methods to achieve CAI are in this literature review along with the different varieties of fuels used in the previous studies.

In view of the wide range of investigation, the reviewed papers will be focused on CAI combustion engines with alcohol as fuels due to this being the main aim of the current study. Different approaches to CAI will be discussed with emphasis on the trapped hot residual gas method with injection strategy during the re-compression stroke. The advantage and disadvantage of alcohol fuels for CAI operation are reviewed. The application of optical techniques and the in-cylinder gas sampling valve are examined. Finally auto-ignition reactions of hydrocarbon and oxygenated fuels are considered.

### **2.2 Controlled Auto-Ignition Combustion**

Controlled auto-ignition combustion or Homogenous charge compression ignition was firstly developed in a two-stroke cycle, spark-ignition engine named as Active Thermo-Atmospheric Combustion (ATAC) by Onishi et al. [1] or Toyota-Soken (TS) combustion by Noguchi et al [2]. The spontaneous combustion reactions take place simultaneously at many points in the premixed charge. The characteristic of the combustion process is shown in Figure 2.1 when compared with the conventional spark ignition combustion.

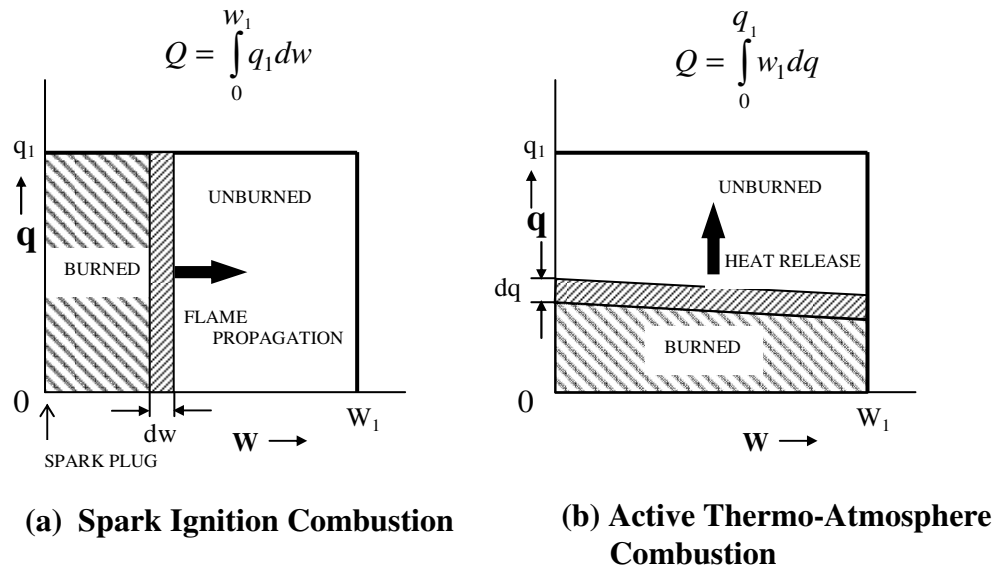


**Figure 2.1 Characteristics of Spark Ignition Combustion and ATAC [1]**

In the absence of spark discharge, cycle-to-cycle variation in flame propagation was reduced. A stable combustion was attainable through a lean and diluted mixture and load was controlled via charge ratio, resulting in fuel economy improvement and a corresponding reduction in the pumping work from un-throttled operation. In order to control the high energy release rate, the charge mixture was diluted with the residual gas to achieve acceptable noise level. As a result,  $\text{NO}_x$  emissions were dramatically reduced due to lower burned gas temperature [3] to a level similar to a conventional SI engine with after treatment.

During the engine operation, some of the gas mixtures are pushed into the crevices during the compression stroke and they flow out again into the combustion chamber resulting in high level of unburned hydrocarbon in the exhaust. Due to the lower burned gas temperature of CAI combustion, post-oxidation, including CO to  $\text{CO}_2$  reaction, is less active. As a result, high HC and sometimes high CO emissions are present in the CAI combustion exhaust. With very high level of dilution, misfire can occur in the low load region whereas unacceptable rapid heat release is experienced at the high load range. Consequently, an operating region is imposed on the CAI combustion. In addition, no direct means can be used to initiate the auto-ignition. Therefore it is difficult to control combustion phasing at any transient engine operation [3, 4].

### 2.2.1 CAI/HCCI Technology and Strategy

In order to achieve auto-ignition, sufficiently high temperature of charge mixture is required. Many approaches have been employed and investigated by researchers. Najt and Foster [5] used an air heater to increase intake temperature to acquire CIHI (Compression ignited homogeneous charge) as they referred to it, in a four-stroke single cylinder engine. They examined the influence of operating parameters including compression ratio, equivalence ratio, engine speed, recirculated exhaust gas, delivery ratio and fuel type, over ignition timing and heat release. Thring [6] also heated the intake charge by a heater to achieve HCCI combustion in a four-stroke engine. The HCCI operation regions were defined by the equivalence ratio, EGR, intake temperature and engine speed.

Higher compression ratio and lean-burn mixture to attain CAI combustion were employed in a 4-stroke engine over a wider operational range [7, 8]. Hiraya et al [9] noted that stable HCCI combustion was achieved at the low intake air temperature when increasing compression ratio. This resulted in higher maximum IMEP. However, combustion efficiency decreased and unburned hydrocarbons increased with increased compression ratio.

Hot residual gas or EGR has been employed by many researchers. Hot exhaust gas can re-enter into in-cylinder by means of the re-breathing method or trapping the burnt gas in the cylinder. Ishibashi and Asai [10] introduced a variable exhaust port for altering sufficient charge scavenging in a two-stroke engine in order to achieve Activated Radical combustion (AR), their name for CAI combustion. For the four-stroke engine, trapping a large amount of residuals was successfully implemented by a mechanical variable camshaft timing (VTC) [11-13], a fully variable electro-hydraulic actuated active valve train system (AVT) [14] and an electro-mechanical camless engine [15]. The retention of a large amount of residual gas was normally accomplished by the negative valve overlap approach. Exhaust valves are closed before TDC using a short duration camshaft. In the mean time, intake valve timings are retarded after TDC in order to minimise the backflow from the cylinder to the

intake port. Typical configuration of valve timings to achieve CAI combustion [13] is presented in Figure 2.2 together with that of a typical SI engine.

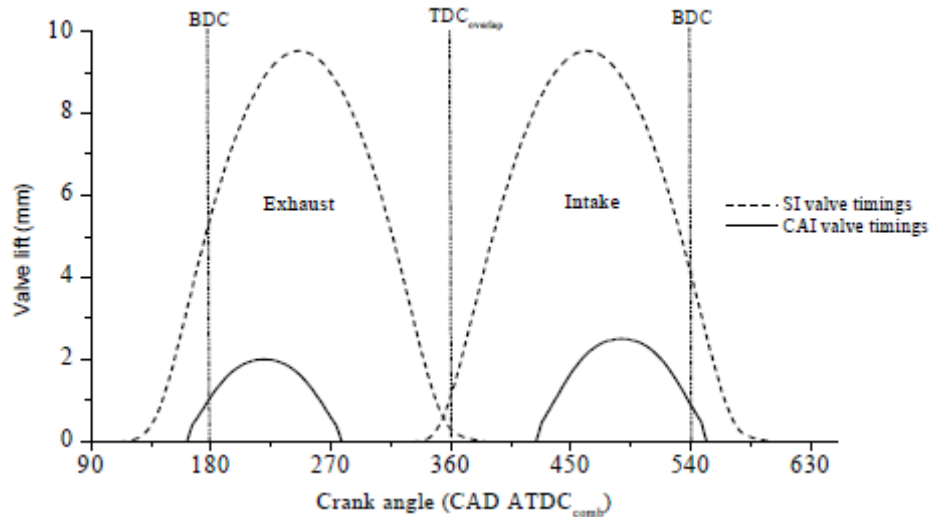


**Figure 2.2 CAI and SI Valve Timing Diagram**

### 2.2.2 Spark-Assisted Ignition

With the residual gas trapping method, it relies on the production of burned gas from the SI combustion in the previous cycle. After the engine can attain stable CAI combustion with sufficient recycling gas, the spark discharge can be turned off. However, some researchers have employed spark discharge as a means to control combustion phasing of CAI combustion.

To address the misfire at low load, Kalian et al [16] used spark-assistance in a 4-cylinder 4-stroke CAI engine. With the presence of spark, the start of combustion was advanced and resulted in higher heat release rate. ISFC was reduced while Net IMEP increased. However, with higher burnt gas temperature,  $\text{NO}_x$  increased, accordingly. Standing et al [17] studied the effects of spark discharge in the same multi-cylinder engine with varying injection and valve timings. They found that when the engine operated within the CAI operational range, the effect of spark discharge was hardly observed. Hyvönen et al [18] noted that the effectiveness of spark was decreased with

increasing air/fuel ratio. The fluctuation associated with typical SI combustion was also observed in the presence of spark-assisted ignition.

### **2.2.3 Fuel Injection**

When the CAI combustion engine was first developed, auto-ignition was initiated from a premixed charge in the port-fuel injection (PFI) engine which lent itself to the name of Homogeneous Charge Compression Ignition. In order to extend the operating regime, in-cylinder fuel injection strategies to control combustion phasing have been introduced and investigated.

Leach et al [19] studied effects of injection timing at EVC, IVO and BDC of the intake/compression stroke in a CAI engine using an air-assisted injector. They found that injection timings affected CAI combustion through mixture ignitability, mixture quality and charge cooling effect. The injection timing at EVC yielded the highest engine output, extended operating range, and produced excellent combustion stability. Li et al [20, 21] further investigated the influence of injection timing by means of optical techniques. The planar laser induced exciplex fluorescence (PLIEF) measurement showed homogeneous charge at the early injection while stratified charge was formed for late injection. More knocking tendency and higher NO<sub>x</sub> emissions were noticed when fuel injection was commenced early.

The advantages of direct injection during the negative valve overlap period and its effect on mixture ignitability have been reported by a number of papers [22-26]. As fuel was injected directly into the high temperature residual gas, it was postulated that the composition of the mixture changed due to the fuel reformation process. Depending on the oxygen available in the trapped mixture during the re-compression stroke, fuel pyrolysis or/and oxidation reactions can occur. Fuel pyrolysis is the fragmentation of the larger fuel molecule into smaller molecules such as alkenes relating to endothermic reactions. When oxidized by available oxygen, the gas mixture can produce heat due to exothermic reactions. Subsequently, advanced combustion can take place compared with injection at the intake and compression stroke. As a result, the operating regime can be extended to the leaner limit and lower

load operations. Figure 2.3 presents the fuel reforming process images from the study of Urushihara et al [22].

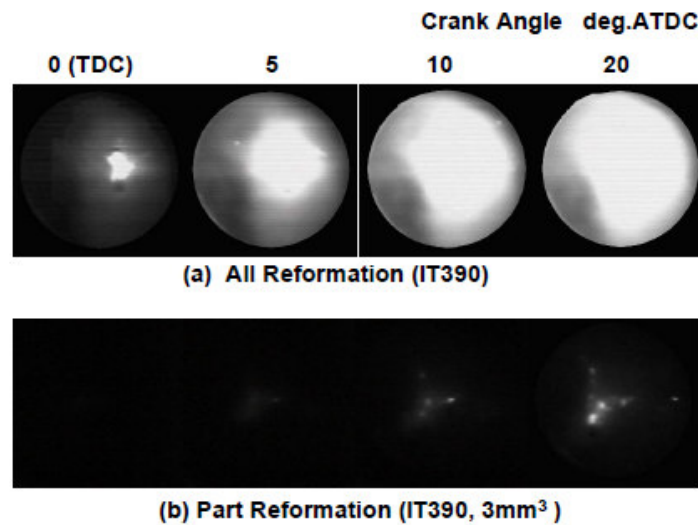


**Figure 2.3 High-Speed Photographs during Negative Valve Overlap Period [22].**

## 2.3 Alternative Fuels

Alternative fuels such as LPG, CNG, alcohols have been employed in different types of IC engines. The usage of alternative fuels in the CAI combustion engine can be either in the form of neat fuels, blending with base fuels (gasoline or diesel) or even as an additive. Table 2.1 presents a list of alternative fuels and ignition properties.

The uses of alcohol fuels, in particular ethanol, have been expanded considerably in the SI engine due to its economic viability. Ethanol can be manufactured from fermentation of many agricultural products (a renewable resource) such as sugar cane and corn while methanol can be produced from crude oil, coal, natural gas, bio-mass and organic waste. As a result, sustainable renewable fuel is an alternative way to help reduce energy depletion or even substitute crude oil based fuels [27]. Moreover, acting like environmentally friendly fuels, alcohol combustion can reduce engine out exhaust emission. Thus, it is advantageous to combine the advantage of CAI combustion with oxygenated fuels.

<b>Fuel</b>	<b>MON</b>	<b>RON</b>	<b>Cetane</b>	<b>LHV (MJ/kg)</b>
Hydrogen		>130		120
Methane	120	>127		49.9
Propane	97	112		46.3
n-Butane	89	94		45.8
Gasoline	82-89	90-100	13-17	42-44
Diesel			40-60	~42.5
F-T Diesel			74-81	~42.5
LPG	93-96	94-110	<3	~46
Methanol	92	106	<5	19.9
Ethanol	89	107	<5	26.8

**Table 2.1 Fuel Properties for Neat Alternative Fuels [3]**

### **2.3.1 Methanol**

Iida [28] conducted an experimental study of CAI combustion with neat methanol in a two-stroke ATAC engine and found that methanol provided a larger range of CAI combustion than gasoline toward the low load region. Ignition timing was advanced and combustion took place with greater maximum heat release rate. Inoue et al [29] used methanol in a two-stroke engine with varying levels of hot residual gas. They found that the combustion mode was changed from SI combustion to auto-ignition when the amount of residual gas was increased. Oakely et al [30] confirmed the results of Iida and showed that methanol and ethanol could be operated in CAI combustion mode over a wider range of relative air/fuel ratios and EGR concentrations than gasoline in a single cylinder four-stroke engine with elevated intake charge temperature. In addition, alcohol fuels produced higher engine thermal efficiency and lower NO<sub>x</sub> emissions. Figure 2.4 presents the extended operating range in terms of indicated thermal efficiency of methanol over the gasoline engine.

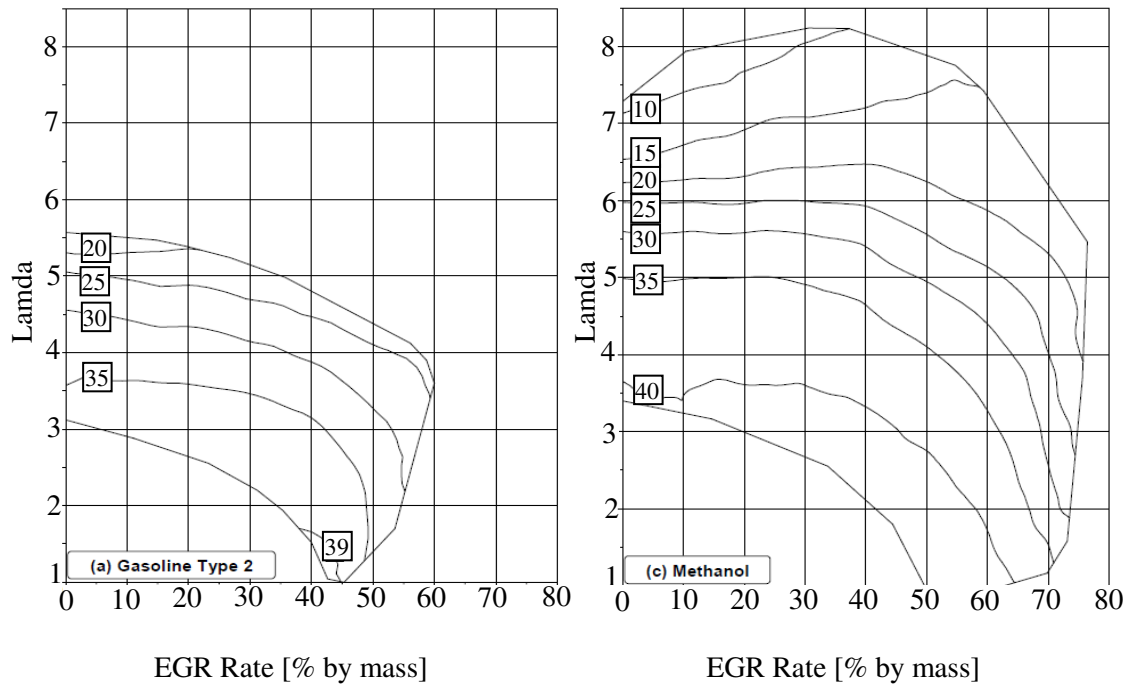


**Figure 2.4 Operating Range of Gasoline and Methanol [30]**

In addition, CAI combustion of methanol has been used in CI engines using premixed charge by Tsuchiya and Seko [31] and by Seko et al [32]. They noted that auto-ignition of methanol started at gas temperature between 900 and 1000 K. Methanol reduced dramatically  $\text{NO}_x$  emission while maintained brake specific fuel consumption similar to a diesel engine in the middle load range. Under the low load condition, the thermal efficiency of methanol was almost the same as that of diesel. Combustion duration was short resulting in a high peak of heat release rate. However, at high load region, brake thermal efficiency decreased and CO and THC emissions increased. Seko and Kuroda [33] further explored the direct injection of heated methanol into the cylinder in order to promote the flash boiling during the fuel injection process. As a result, the spray penetration was shortened due to the flash boiling state of methanol, so that a stratified fuel vapor was formed without liquid impingement. Therefore improvement of the high load region was accomplished with the lower  $\text{NO}_x$  emissions than that of ordinary premixed charge compression ignition by delayed auto-ignition because of direct injection.

Maurya and Agarwal [34] investigated the effects of methanol over cycle-to-cycle variation in a HCCI CI engine. In order to reduce stratified charge effect, premixed charge was prepared by a port injection system. The results showed that methanol

lead to more repeatable crank angle of  $P_{\max}$  but the COV of maximum rate of pressure rise was higher than gasoline at the same intake air temperature.

### **2.3.2 Ethanol**

Christensn et al [35], Maurya and Agarwal [36] showed that CAI/HCCI combustion was possible with neat ethanol when a relative high compression ratio and increased intake air temperature were used. CAI combustion of ethanol exhibited higher indicated efficiency than gasoline and very little  $\text{NO}_x$ . The effect of ethanol compared with isooctane at high compression ratio was experimented further by Gnanam et al [37] in an indirect injection diesel base engine. They found that the combustion of ethanol commenced earlier than that of isooctane at the same heated intake temperature.

Zhang et al [38] noted that the CAI combustion of pure ethanol could be achieved with a high amount of hot trapped residual gas. The operating range could be significantly extended over gasoline fuels toward higher speed with leaner charge mixtures in a 4-stroke PFI SI engine as shown in Figure 2.5. Xie et al [39] continued the previous work [38] in order to compare alcohol combustion including ethanol and methanol and its blend over gasoline combustion. The results showed that ethanol fuels tended to autoignite earlier resulting in higher peak pressure than that of gasoline. Due to lower peak combustion temperature, very little  $\text{NO}_x$  emission was emitted with pure alcohol fuels. Li et al [40] applied methanol and ethanol in a similar CAI engine [38, 39] but using an air-assisted direct injection. The benefits of lower exhaust emissions of HC, CO and  $\text{NO}_x$  from neat ethanol against gasoline were observed.

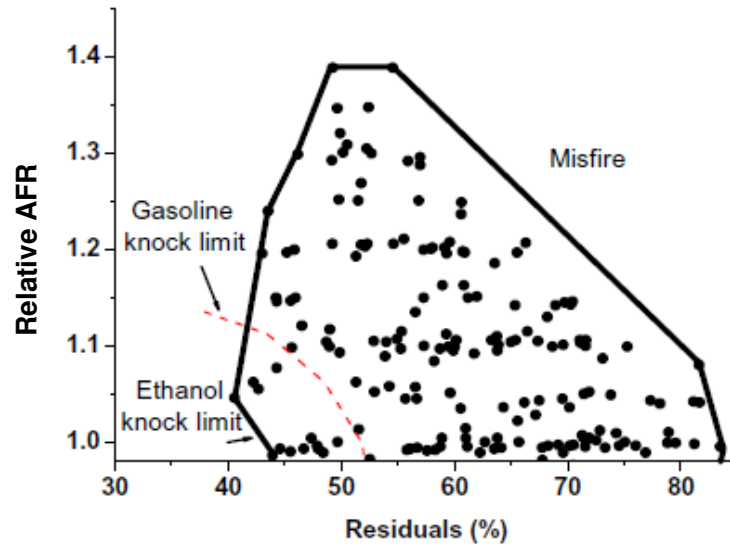


**Figure 2.5 Extended Operating Region of Ethanol with Trapped Residual [38]**

The effect of ethanol when blended with heptane was clarified by Hashimoto [41, 42]. CAI/HCCI combustion was simulated through a rapid compression machine (RCM) in which variable percentage of ethanol was compared with ordinary primary reference fuel (PRF). Ethanol exhibited the inhibition of hot ignition of HCCI combustion by strongly retarding cool flame timing and lowering the pressure rise from Heptane. He claimed that the reaction which consumes the hydroxy radical by the ethanol molecule ( $CH_3CH_2OH + OH^\bullet \rightarrow CH_3CHO + H_2O$ ) to produce 1-hydroxy-1-ethyl radical is the major cause. This result corresponded with the study of Kamio et al [43] in a four-stroke HCCI-SI hybrid engine and Xingcai et al [44] in a diesel-like engine. However, ethanol addition was found to expand the operating regime to higher IMEP and also led to higher indicated thermal efficiency.

## 2.4 Chemiluminescence Image

Optical diagnostics are non-intrusive measurement techniques widely used in the research and development of IC engines. With the advanced capabilities of modern equipment, both high spatial and temporal resolutions can be obtained. Many optical techniques are laser-based methods. However, detection of the natural emission luminosity offers a simpler approach to in-cylinder combustion visualization. Imaging

of chemiluminescence sites emitted from exothermic chemical reactions is one of the most widely used combustion visualization techniques [45]. When hydrocarbon fuel reacts with oxygen, many reactions are accompanied by the production of excited chemical species. These molecules at an excited state decay to an equilibrium energy level, during which photons are emitted giving the chemiluminescence emission. With a high speed image acquisition system, therefore, temporally and spatially resolved images of short-lived intermediate species are obtained. In addition, each molecule emits chemiluminescence in a specific wavelength band. Thus, chemiluminescence imaging coupled with a selected bandpass filter can be used to identify the presence of a particular species. Table 2.2 shows the specific spectra of significant species that are present in the combustion process in the IC engine.

CH(nm)	OH(nm)	CH <sub>2</sub> O(nm)	CO <sub>2</sub> (μm)	C <sub>2</sub> (nm)	CHO(nm)
314		368	2.69-2.77	470-474	320,330
387-389	302-309	384	4.25-4.3	516	330,340
431		395		558-563	355,360
		412-457			380,385

**Table 2.2 Strong Emission Peaks of Major Species in IC Engine [60]**

### 2.4.1 Total Chemiluminescence

Chemical reactions of hydrocarbon fuel and oxygen produce many chemical species during the combustion process. Without any bandpass filter, chemiluminescence imaging captures total natural emission of light, comprising of the excited intermediates of OH, CH<sub>2</sub>O, HCO, CH, C<sub>2</sub> etc , or products of CO<sub>2</sub>, CO or even stronger intensity of soot luminosity. These chemiluminences consist of both visible and invisible ranges of spectrum (UV and IR range). The main objective of total chemiluminescence is to see the macro structure of combustion, not the individual species. For the SI and CI engine, total chemiluminescence imaging has been applied widely in the engine combustion studies [45, 46].

For CAI combustion, total chemiluminescence imaging was applied for the first time in the two-stroke engine by Iida [28]. He noted that the self-ignition of methanol occurred over the entire chamber with active thermo-atmosphere combustion (ATAC). Through spectroscopic analysis, Augusta et al [47] found that CHO, CH<sub>2</sub>O, CH and OH were the major spectra during the combustion process. It was found that different engine parameters including intake temperature, fuel delivery methods, fuel rates and intake charge thermal history did not affect the chemiluminescence spectra other than the intensity. The chemiluminescence intensity was found to have a strong correlation with the rate of heat release. Persson et al [48] calculated flame expansion speed of spark-assisted CAI combustion and spreading speed of pure CAI combustion from total emission images. To investigate the early flame development, the images were recorded with the heat release rate curves. Initial slow heat release rate were defined to indicate the portion of SI initiated flame propagation. The total emissions showed that ignition was initiated at the centre of the combustion chamber by spark assistance whereas the perimeter was the auto-ignition sites for pure CAI combustion as shown in Figure 2.6 which is similar to the results of Yang et al [49]. Aleiferis et al [50] confirmed the previous results in which auto-ignition happened around the perimeter of the chamber but they did not observe the spark ignited flame kernel, probably due to the insensitivity of the camera and weak luminosity of diluted flame.

Hultqvist et al [51] studied the macro structure of the flame from their chemiluminescence images. The cycle-to-cycle variation of image intensity was observed at early combustion. The image indicated the strong relationship between the intensity and heat release rate as Augusta et al [47] found. Also, the boundary layer was discovered at the cylinder head and piston top by the later timing of total light emission. In another study, Dec et al [52] investigated the thermal stratification effect on HCCI combustion using high speed chemiluminescence imaging. The results indicated that thermal stratification due to the heat transfer process during compression caused the auto-ignition to occur in the centre and proceeded into cooler regions.

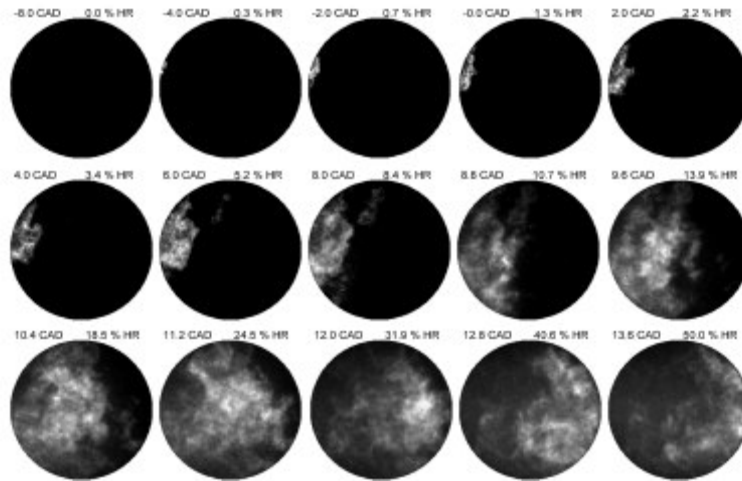


Figure 2.6 Total Chemiluminescence from Pure HCCI Combustion [48]

## 2.4.2 OH Chemiluminescence

The OH radical is an important intermediate product during hydrocarbon combustion. As detailed in many publications, it is formed during the high temperature combustion of chain-branching reactions. The chemiluminescence of OH is produced from the electronically excited hydroxyl radical ( $OH^*$ ). Its absolute concentration is defined by the elementary reaction model [53]. One of its characteristic wavelengths is near 307 nm, out of the visible range as Figure 2.7 presents. Therefore, a special UV-lens and specific bandpass filter are required as well as an UV sensitive camera.

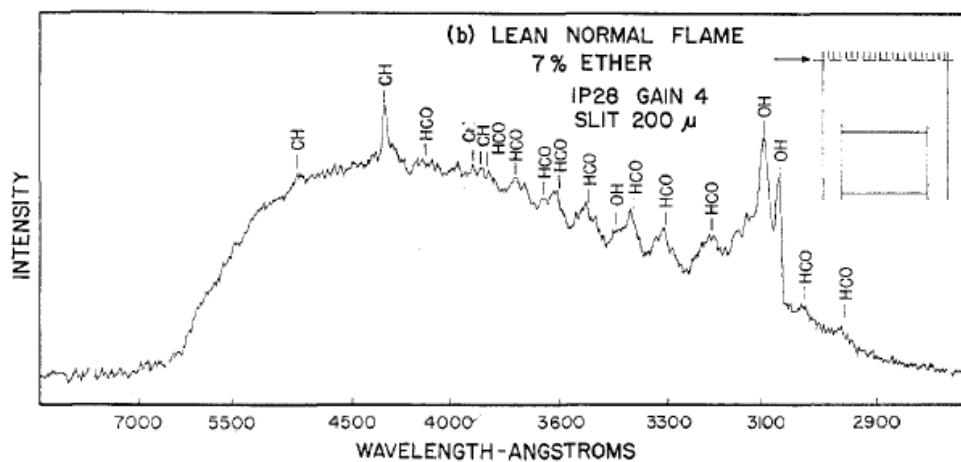


Figure 2.7 Species Spectrum from Spectrometer [59]

Due to its relative low intensity and prompt occurrence, recording the OH radical has been challenging. Most of OH imaging in the literature has been recorded by means of laser diagnostics. Collin et al [54] measured simultaneous OH and Formaldehyde in HCCI engines with PRF which is the mixture of isooctane with octane number 100 and n-heptane with octane number 0 as fuels. They noted that the OH radical was present during the main heat release process after formaldehyde concentration decreased. OH formation took place at the location in which the formaldehyde disappeared. Hultqvist et al [51] conducted the experiment through chemiluminescence imaging and found that the OH radical was formed during the main heat release and after CH formation. The OH radical was distributed throughout the combustion chamber and had a thick boundary layer on top of the piston and the cylinder head. In two-stroke engines, the OH radical measurement was firstly conducted with TS by Noguchi et al [2]. The OH radical was the last detectable radical in time in TS combustion while it appeared at the same time with other radical such as CH, C<sub>2</sub>, H and HO<sub>2</sub> in the conventional SI combustion. Iida [28] noted that OH radicals were observed before heat release began when employing methanol as fuel and its intensity was lower than that of gasoline in the ATAC engine.

### **2.4.3 Formaldehyde Chemiluminescence**

Formaldehyde is formed through low temperature oxidation and then is consumed in hot flame combustion. Therefore, the presence of formaldehyde has been used as the marker for cool flame combustion in two-stage ignition fuels. On the other hand, the decreased concentration of it has been used to define the hot flame ignition.

Detection of formaldehyde has been accomplished by means of the laser induced fluorescence techniques [54-56]. The studies of Graf et al [55] found that formaldehyde was the indicator to determine the boundary of hot- and cool flame combustion. Collin et al [54] confirmed the study of Graf et al [55] that formaldehyde was presented in the images during low temperature combustion until the early part of heat release and then was consumed when the main heat release began. In addition, Zhao et al [56] observed that formaldehyde formation was mainly dependent on the charge temperature more than the fuel concentration in a stratified charge/thermal.

However, its subsequent burning occurred at the areas in which sufficient high fuel concentration and charge temperature were satisfied.

#### **2.4.4 CH, C<sub>2</sub>, CHO Chemiluminescence**

Levedahl and Broida [57] investigated emission spectra in an auto-ignition single cylinder engine when using heptane as the fuel. They found that CH, C<sub>2</sub> and CHO were present in the hot flame region after excited formaldehyde had decreased. However, Gaydon et al [58] showed that in the early studies of flames the CHO band was also present in the excited formaldehyde spectrum in the blue-glow region and CHO strength decreased in weaker blue-glow region. Hence, hot flame reaction (yellow flame) was preferential for CHO formation. Agnew [59] studied CH, C<sub>2</sub> and CHO emissions during the two-stage diethyl ether combustion. For the second-stage flame, the transition from the formaldehyde spectrum to the pre dominantly CHO spectrum was observed when the rich mixture was altered to lean combustion.

For TS combustion (Toyota-Soken) combustion, their name of self-ignited combustion, Noguchi et al [2] detected CHO, HO<sub>2</sub> and O as well as CH and C<sub>2</sub>. The first detected radicals were CHO, HO<sub>2</sub> and O, which initiated before self-ignition and were claimed as ignition kernels for TS combustion. Subsequently, CH and C<sub>2</sub> species were formed at nearly the same time and prior to the formation of the OH radical.

### **2.5 In-Cylinder Gas Sampling**

In order to better understand the chemical and physical phenomena in the internal combustion engine, the in-cylinder gas sampling technique has been developed. Its applications have been used in both SI and CI engines from 1927 and are briefly summarized in a previous paper [60]. In this section, only experiments relating to knocking phenomena and CAI combustion are discussed as both are a result of auto-ignition.

Egerton et al [61] extracted the combustion product from the end gas region in the cylinder to investigate its relation to knock in the SI engine. They showed that the formation of aldehyde reached the maximum concentration at the moment when the flame reached the sampling valve whereas peroxides were formed and reached the maximum before the flame reached the valve. The amount of peroxides significantly affected the knock tendency. The addition of aldehyde to fuel was also studied. The results showed that aldehydes did not affect the concentration of peroxide nor the tendency of knock.

Downs et al [62] studied the critical chemical factors controlling the occurrence of knock by analysis of in-cylinder gas composition of the end gas in a SI engine. They found that knock depended on the attainment of a critical rate of formation of products present under both knock and non-knocking conditions. The results showed that peroxide was formed in a two-stage process and the formation of formaldehyde increased monotonically to its peak during the second of the two-stage of peroxide formation. The formation of peroxide is associated with cool flame formation which took place during low temperature combustion and caused the knock occurrence. The maximum concentration of peroxide gave the maximum knock.

Houliang et al [63] studied chemistry of auto-ignition of neat n-heptane, isooctane and the effect of each other when using 87 PRF fuel in a motored engine. The in-cylinder species molecules were used to relate to the chemical kinetics mechanism proposed from the other papers. They found that n-heptane showed the two-stage ignition whereas isooctane exhibited only single-stage ignition at inlet temperature of 376 K. During the first-stage ignition, approximately 52% n-heptane reacted and CO is the dominant product resulting in an increased temperature. The reactions of n-heptane and isooctane in 87 PRF fuel proceeded separately as neat n-heptane and neat isooctane without interference of each other.

Thereafter, Houliang et al [64] employed the same technique to analyse in-cylinder gas when using neat ethanol, methanol and its blend with PRF as fuels. The significant intermediates for methanol oxidation were formaldehyde, CO and CO<sub>2</sub> while acetaldehyde, CO and CO<sub>2</sub> were the major molecule in ethanol oxidation. Alcohol blend played the active role to inhibit auto-ignition by consuming the active

radical pool which was generated by PRF. Ethanol showed greater effect over methanol.

For CAI/HCCI combustion, Tsurushima et al [65] conducted in-cylinder gas sampling experiments in neat n-pentane, n-hexane and n-heptane as well as dual-component fuel of n-hexane/ethylene combustion. For all fuels, the same intermediated molecules of conjugated olefin, smaller olefin, aldehyde were detected in low temperature oxidation as the same time with fuel decomposition and decreased concentration of oxygen. The detection of CO and CO<sub>2</sub> was observed firstly after the cool flame heat release. These intermediate molecules followed the reaction pathways which were proposed by Current et al [69, 70] as detailed in the next section. Different fuels exhibit different cool flame and hot flame heat release timings. The fuels having a long straight chain have preference to being oxidized at lower temperature. As a result, cool flame and hot flame heat release are advanced. For the dual-component fuel, ignitability of low octane number fuel dominates the oxidation starting time. Varying the composition of the high and low octane number fuel can control the rate of low temperature oxidation.

The effect of methanol additive in dimethyl ether (DME) over auto-ignition reactions was studied by Tezaki et al [66]. With crank angle resolved in-cylinder pulse-valve sampling and exhaust gas analysis, formaldehyde, formic acid (HCOOH), carbon monoxide and hydrogen peroxide (H<sub>2</sub>O<sub>2</sub>) as combustion intermediates were detected at the onset of the cool flame heat release. Thereafter, these intermediate were consumed by the hot ignition. The addition of methanol decreased the cool ignition, resulting in retarded hot ignition.

## **2.6 Chemical Kinetic Reaction Mechanism**

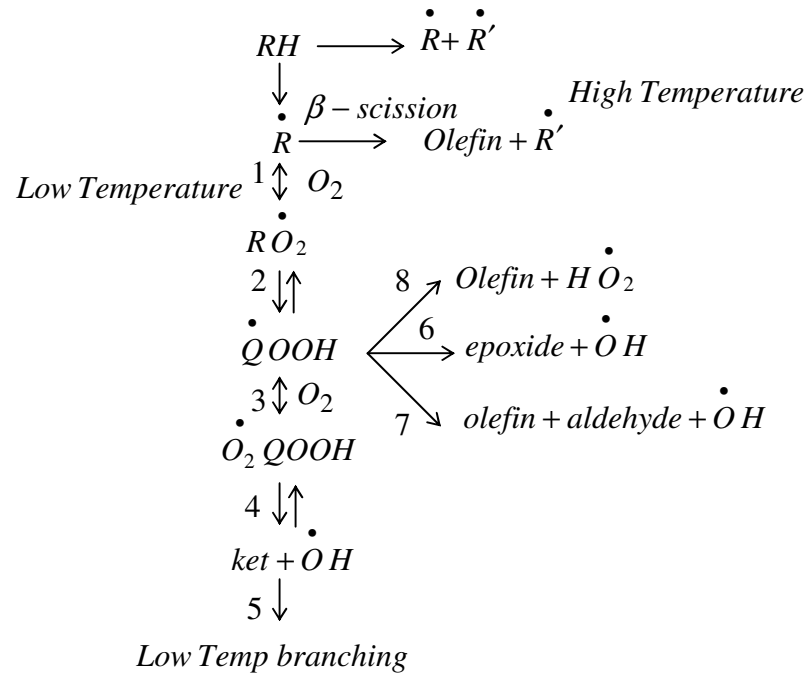
Chemical kinetic reactions of the CAI engine are the same as the reactions leading to knocking phenomena in the SI engine. Therefore, the development of chemical CAI combustion has been derived from the study of the end gas reactions prior to knock. Many chemical reaction models were developed and then verified by the experiment over a range of temperature and pressure in the shock tube, stirred reactor, rapid

combustion machine or even motored and fired engine. The chemical reactions exhibit considerably different routes depending on the temperature and pressure history. In terms of temperature, kinetic models can change drastically among three temperature regimes [67, 68]. As will be detailed below, alkylperoxy radical plays an important role in low temperature regimes (~450-800 K). After the temperature increases the alkylperoxy radicals become unstable. Subsequently, the dominant kinetic path changes markedly resulting in negative temperature coefficient (NTC) in the intermediated temperature region (~800-850 K), when reaction rates are reduced with temperature. Finally, the production of H atom dominates reaction pathways in the high temperature region (~1100-1200 K).

### 2.6.1 Isooctane and n-Heptane

Isooctane and n-heptane are the most researched paraffinic fuels because their structure is simple and they have the reference octane number of 100 and 0, respectively. Current et al [69, 70] developed comprehensive chemical kinetic mechanisms of isooctane and n-heptane and found that there are two temperature regions which separate the class of reactions as shown in Figure 2.8. At high temperature applications, nine essential elementary reactions are involved, including fuel decomposition, H-atom abstraction, Alkyl radical decomposition and oxygen addition to alkyl radical etc. The sensitivity method was employed to show the significance of fuel decomposition to two alkyl radicals and alkyl radicals decomposition to olefin and smaller alkyl radical. For low temperature application, sixteen reactions play the major role for fuel oxidation. Following the initial H atom abstraction, the main reaction which links to low temperature mechanism is an addition of the oxygen molecule with alkyl radical to produce alkylperoxy species  $\dot{R}O_2$ . Regarding the low temperature heat release pathways, isomerisation of alkylperoxy radicals to  $\dot{Q}OOH$  also takes place. Afterward, four reactions are available for  $\dot{Q}OOH$ . Three reactions are concern with the olefin, epoxide and one radical formation as shown in reaction 6, 7, and 8 in Figure 2.8 and they are related to the negative temperature coefficient phenomena. Another reaction produces ketohydroperoxide in case of n-heptane and carbonyhydroperoxide in case of iso-

octane through additional oxygen with  $\dot{Q}OOH$  and further its isomerisation. Finally, ketohydroperoxide or carbonyhydroperoxide decomposition forms two  $\dot{OH}$  radicals to initiate significant chain branching to high temperature auto-ignition.



Where dot symbols  $\dot{\phantom{x}}$  means radicals.  
dash symbols  $\dot{\phantom{x}}$  means different molecule.

**Figure 2.8 Kinetic Scheme of the Primary Oxidation [69]**

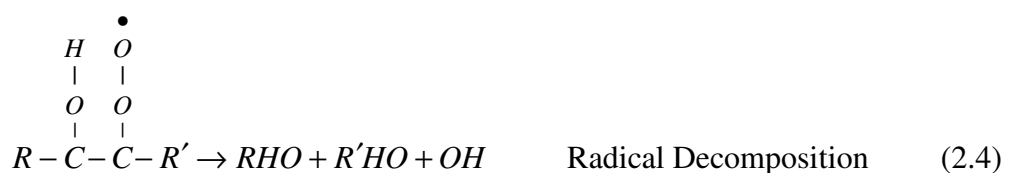
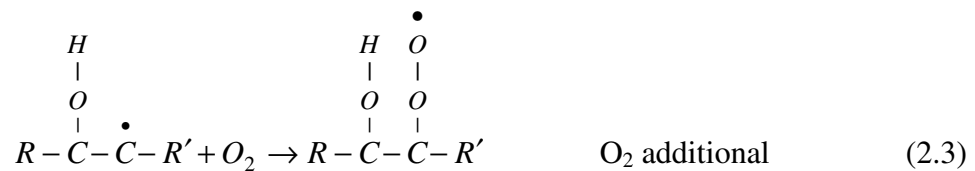
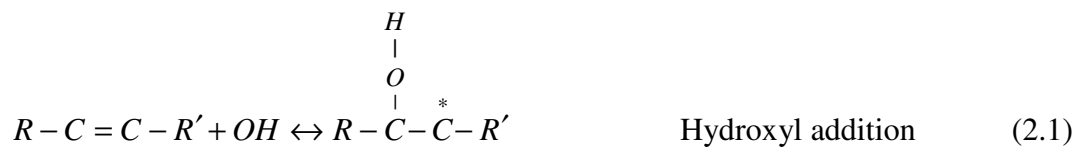
Tsurushima [71] simplified the detailed kinetic model of Current et al to a skeletal model for HCCI combustion when using blended isooctane and n-heptane (PRF) fuels. Only 33 species and 38 reactions have been induced for predicting CAI combustion.

## 2.6.2 Gasoline Fuels

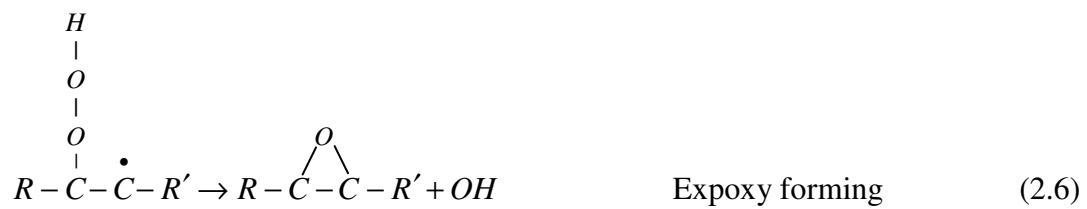
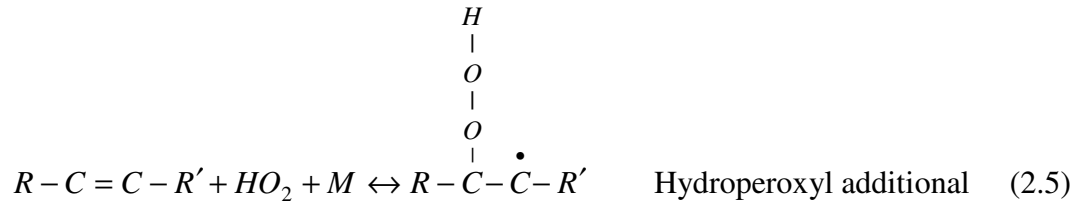
Because of its complicated structures and vast varieties of molecules in gasoline, it is not possible to produce their chemical kinetic mechanism. Instead, each type of hydrocarbons has been considered for gasoline combustion. Of simple structure and

important components in gasoline, isooctane, and n-heptane, were widely examined as the presenter of paraffin hydrocarbon as discussed.

In addition to paraffin, regular unleaded gasoline typically consists of a significant fraction of olefins. Thus, the auto-ignition of olefins has been studied to better understand gasoline combustion. Leppard [72] studied auto-ignition chemistries of olefins in a motored engine by using 1-, 2- butane, isobutene, 2-methyl-2-butene and 1-hexene as fuels. The auto-ignition of olefins did not show the negative temperature coefficient behavior like paraffinic fuels did. Instead of hydrogen abstraction from fuel, radical addition to the olefin double bond dominates olefin auto-ignition chemistry. Following hydroxyl addition, oxygen molecule adds to the adjacent radical site forming a short-lived radical which subsequently decomposes to form two carbonyls and one hydroxyl radical. Propionaldehyde, formaldehyde, acetaldehyde, acetone, valeraldehyde formation are the results of this major pathway which is dependent on the parent fuels. This major pathway is shown in equation 2.1 – 2.4 below. The symbol of star means highly energetic radicals.



Parallel to the above mechanism, epoxy intermediates are formed through additional hydroperoxyl radical in the parent fuel generating hydroperoxyalkyl radical. Subsequently, this radical cyclizes to form epoxy molecule as shown in Equation 2.5 - 2.6.

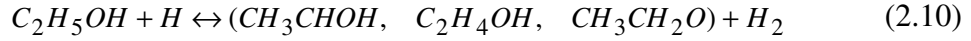
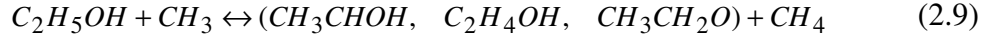
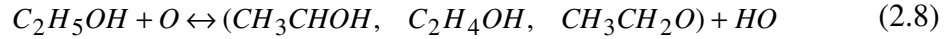
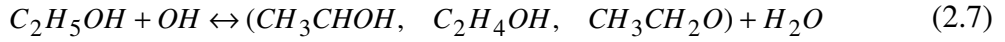


From the above reaction pathways, olefinic type fuel combustion mechanisms are shown to depend on the two mechanisms in which parent fuels are attacked at the double bond while the significant initial reaction in paraffinic fuels is hydrogen atom abstraction.

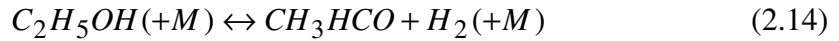
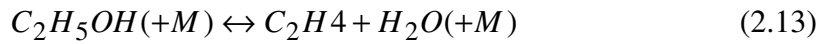
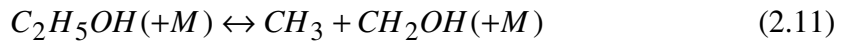
### 2.6.3 Ethanol

The increasing use of ethanol has promoted the investigation of their chemical kinetics. Marinov [73] created detailed chemical kinetic model for ethanol oxidation and compared the results with ethanol oxidations in the shock tube, jet-stirred reactor, flow reactor or rapid compression machine where the ignition delay, flame speed, intermediate and product concentration were measured. In contrast to hydrocarbon fuels, ethanol oxidation takes place in the high temperature region. As shown below, two essential mechanisms, H-atom abstraction and ethanol decomposition dominate chain branching productions during the overall chemical reactions.

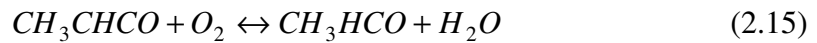
H-atom abstractions are presented in Equation 2.7-2.10. The products depend on the site of the H atom abstraction. In parentheses, the first order means the primary size H-atom abstraction and so on secondary and hydroxyl group respectively.



Ethanol decompositions are presented in Equation 2.11 -2.14.



H-atom abstraction by the OH radical at hydroxyl group dominates over 26 % of ethanol consumption. In addition, the significant intermediate such as acetaldehyde is formed through H-atom abstraction by the OH radical at the primary site (CH<sub>3</sub>CHOH) and then with additional oxygen molecule as shown in Equation 2.15.



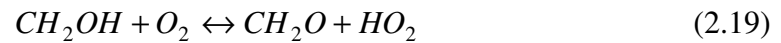
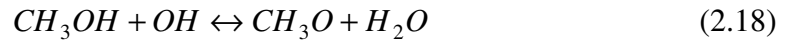
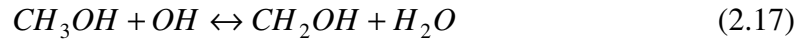
#### 2.6.4 Methanol

A comprehensive mechanism for methanol oxidation was proposed by Held and Dryer [74]. There are four available decomposition reactions for methanol. The decomposition reaction producing methyl radical dominates 75-90 % of the total decomposition rate as shown in Equation 2.16.



However, the predominant fuel consumption in the methanol mechanism is based on H-atom abstraction by the OH radical in which the abstraction can occur at either the methyl or hydroxyl group resulting in different products. Equation 2.17 presents the

reaction at methyl sites whereas Equation 2.18 shows the results for the hydroxyl group. Subsequently, formaldehyde is formed significantly through the products from the H-atom abstraction reaction as Equation 2.19- 2.20 expresses.

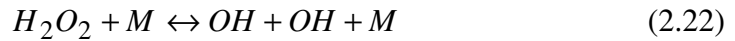


## 2.7 Ignition Process

Chemical kinetic mechanism plays the major role in auto-ignition for CAI engines. It includes many stage of reactions classified as initiation, propagation, branching and termination reaction which generates, maintains, increases and reduces radical species from reactants respectively [75]. A chain branching reaction in which the number of radical species such as H, O, OH, CH<sub>3</sub> and HO<sub>2</sub> are increased from reactants is the crucial reaction controlling the ignition process. When most of reactions act like chain branching process to generate exponential radical species growth, fuel molecules will be consumed simultaneously with those radicals. As a result, the phenomena of ignition will take place and temperature will increase. Therefore, the conditions favouring the chain branching reactions will result in a reduction in the ignition delay time. By contrast, the ignition timing is retarded when slower chain branching reactions happen.

### 2.7.1 Single - Stage Ignition

Single-stage ignition is the normal ignition which occurs at high temperature. Eminent chain branchings, which govern an onset of ignition, are illustrated in equation 2.21 and 2.22 [75] in which equation 2.21 is the most important reaction in the high temperature regime and controls such combustion as flame propagation whilst equation 2.22 is dominant in CAI combustion.



Because it requires high activation energy to abstract H-atom from alkyl radicals, the reaction in equation 2.21 can proceed at only high temperature while the OH radical from decomposition of hydrogen peroxide ( $H_2O_2$ ) are generated at moderate temperature around 900-1000 K.

Because of lean mixture and dilution from exhaust gas recirculation, CAI engines operate with low to moderate temperature. Thus, the ignition process is mainly controlled by the hydrogen peroxide decomposition as shown in equation 2.22. During the compression process and the mixing of fresh mixture with hot burned gas, hydrogen peroxide formed through low temperature chemical kinetic reactions. When in-cylinder temperature reaches 900 K or above, ignition commences since high concentration of  $H_2O_2$  radical rapidly decomposes to hydroxide radicals which consume rapidly the fuel molecules.

The ignition characteristics with different fuel component were studied by Carl et al [76] using CHEMKIN software prediction. The results show single-stage ignition happening in ethanol and toluene fuels and agree well with the results of Bollentin and Wilk [77] in a closed static reactor and Lee et al [78] in a rapid compression machine.

### 2.7.2 Two-Stage Ignition

Two-stage ignition consists of a first-stage known as a cool flame ignition and subsequently a second-stage ignition which is the same as a single-stage ignition described in section 2.7.1. Different from a single-stage ignition, the first-stage ignition in a two-stage ignition process occurs at a low temperature regime which is related to the chemical kinetics of paraffinic fuels in section 2.6.1. The dominant pathways, which produce the first-stage ignition, create either ketohydroperoxide or carbonyhydroperoxide. As shown in Figure 2.8,  $O_2^{\bullet} QOOH$  isomerisation and

ketohydroperoxide decomposition build up three radical species. These radical species consume some parent fuel and release heat initiating the first-stage ignition. The results of heat release increases the temperature by around 10 K and advances the second-stage ignition due to accelerate attainable temperature timing. In general, the first-stage ignition happens during the compression stroke in which in-cylinder charge temperature starts to rise. At the first-stage ignition, hydrogen peroxide is created and accumulates at a slow rate. When the first-stage heat release proceeds with the compression of the piston, temperature gradually increases until the reverse pathways of alkylperoxy production are predominated. The first-stage heat release is terminated and slower chemical reactions take place in the range of the NTC region. Due to the continuing rising piston, charge temperature increases to reach the second-stage ignition temperature. Subsequently, the hot ignition begins as the same mechanism as in the single-stage ignition. Hence, the second-stage temperature is the same temperature of the single-stage ignition. Figure 2.9 shows the pressure and temperature profile of two-stage ignition when using different PRF as fuels [80]. From the Figure, the relative long ignition delays happen in a rapid combustion machine but the ignition delays take place around 1 msec for the current engine test.

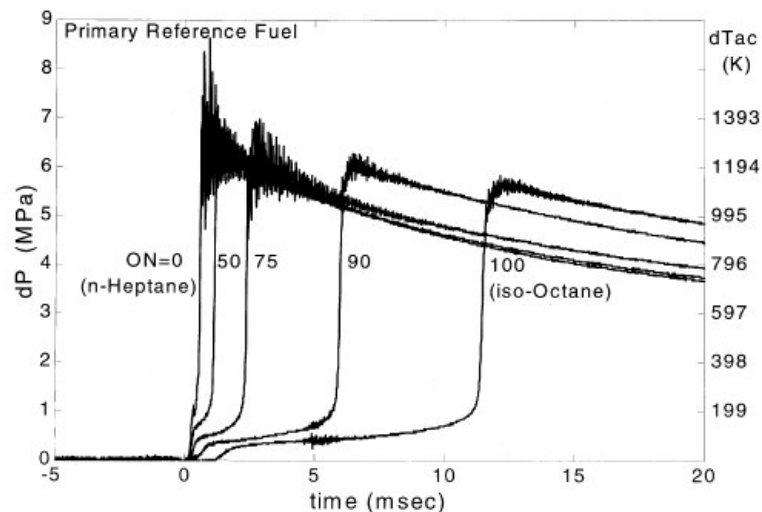


**Figure 2.9 Characteristic of Two-Stage Ignition [80]**

First-stage ignition is strongly dependent upon fuel structures [79-80]. Indeed, internal isomerization in alkylperoxy  $\dot{R}O_2$  and peroxy radical ( $\dot{O}_2 QOOH$ ) readily initiates

in fuels which contain the straight chain structure  $-CH_2-CH_2-CH_2-$  in which ring-like transition state is possible. Therefore, n-heptane shows two-stage, but toluene exhibits single-stage ignition. Figure 2.10 illustrates the isomerization reaction of  $\dot{R}O_2$  in n-heptane. The first-stage ignition plays the significant role in ignition delay time. Fuels, exhibiting more first-stage heat release, are elevated to attainable temperature, so hydrogen peroxide decomposition starts early, resulting advance ignition delay time. On the other hand, fuels which interfere internal H-atom abstraction have retarded ignition timing. Similarly, additives which promote or inhibit ignition, show their function only in the first-stage ignition, while the second-stage remain the same.

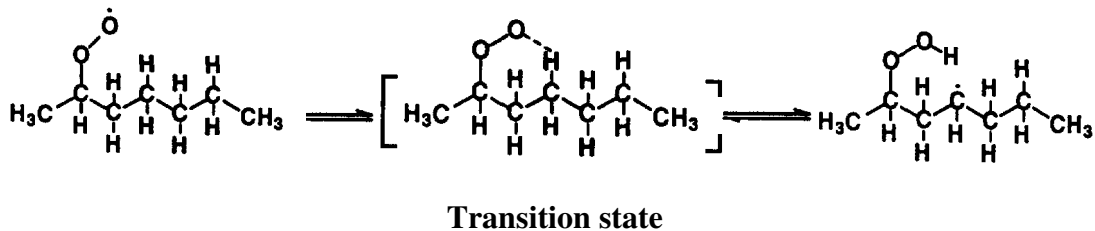


**Figure 2.10 Schematic Diagram of an RO<sub>2</sub> Isomerization reaction in n-Heptane with a 6-membered Transition State [69]**

## 2.8 Summary

In this Chapter, the previous literature which relates to the current study is described. To understand the background and principle of CAI/HCCI combustion, the history of this combustion was firstly introduced and also the drawback and the advantage were identified to emphasize the importance of any further study. Many approaches to attain CAI combustion were explained. Knowledge of using hot trapped residual gas by means of the negative valve overlap method was explored. The success of using spark-assisted ignition and injection strategy to extend the operating range was detailed. Application of alcohol fuels in CAI combustion showed their advantage in extending lean burn region and faster combustion process as well as reducing exhaust emission of HC and NO<sub>x</sub>. However, further experimental study is required due to limited literature of in-cylinder combustion process. The applications of

chemiluminescence imaging of formaldehyde, OH, CHO to internal combustion engines were reviewed to demonstrate their merit in auto-ignition studies. For in-cylinder gas sampling technique, most of the literature showed the data for the reactions leading to knock in SI engine. Very little information was acquired directly from CAI combustion engines. This technique is useful to relate the chemical reactions of different fuels in the current study. Finally, the chemical kinetic mechanisms were explained to better understand the results obtained in the current study.

## **Chapter 3 Experimental Test Facility**

### **3.1 Introduction**

In the current study, systematic investigation of CAI combustion using alcohol fuels was carried out through three different experiments. A single cylinder engine facility and equipment were used to conduct the engine tests, together with a high speed imaging system and in-cylinder sampling equipment. The single cylinder engine and its operation are described. This is followed with descriptions of the instrumentation for thermodynamic, chemiluminescence imaging and in-cylinder gas sampling testing respectively.

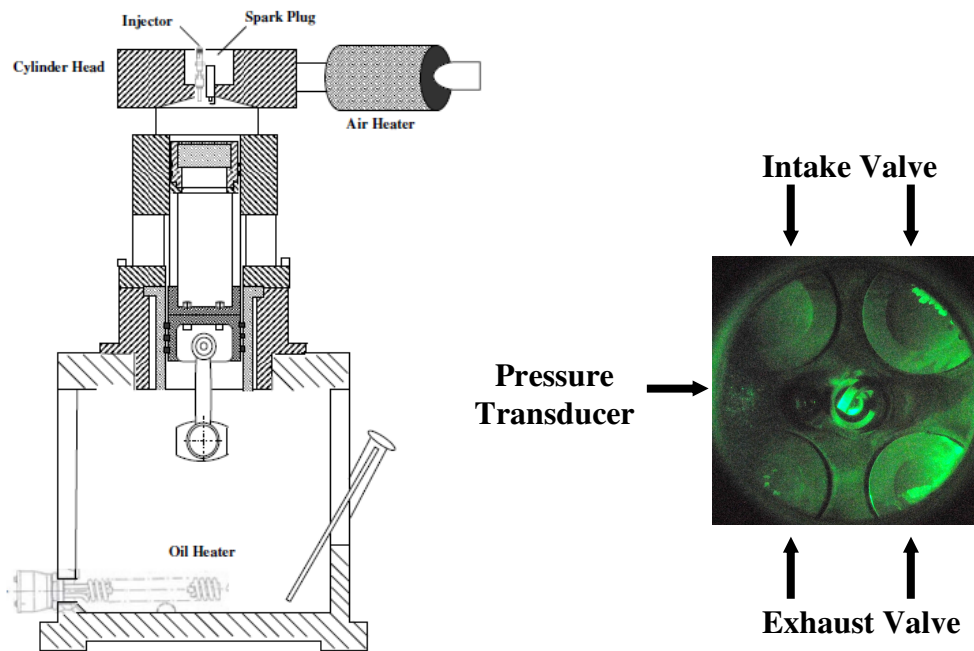
### **3.2 Engine Testing Equipment and Facility**

#### **3.2.1 Research Engine**

A Ricardo Hydra single cylinder research engine was used throughout the study. An optically accessible transparent piston window was installed for chemiluminescence imaging whereas a metal piston was fitted for thermodynamic engine and in-cylinder gas sampling tests. To achieve CAI combustion, charge mixture temperature was increased through residual gas trapping by the negative valve overlap method in conjunction with a 3 kW air heater installed in the intake pipe for heating intake air to 175 °C to ensure stable CAI combustion taken place. The engine configurations are presented in Figure 3.1a and detailed specifications are shown in Table 3.1. The CAI cam timings were not symmetrically fixed about TDC because from the previous study [81], he found that retarded inlet valve opening timings lead to the widest load range at every injection timing. An air-assisted injector with individual adjustable air and fuel quantities and timing was fitted in the center of the cylinder head provided by Orbital Engine Corporation Ltd. The engine has four valves operated with overhead camshafts and a pent roof combustion chamber. A pressure transducer was installed in the cylinder head at the left hand side as shown in Figure 3.1b.

As illustrated in the middle of Figure 3.1b, spark was controlled by an ignition system. The clock and reference signals were provided by crankshaft and camshaft

sensors. Throughout the experiments, spark timing was kept constant at 30 degree CA BTDC.



**3.1a Ricardo Hydra Engine**

**3.1b Geometry of Cylinder Head**

**Figure 3.1 A Ricardo Hydra Single Cylinder Research Engine**

Bore(Extended Piston)	80 mm.
Stroke	89 mm.
Compression Ratio	9:1
Swept Volume	450 cc.
Intake Valve Opening	90 ATDC
Exhaust Valve Closing	80 BTDC
Engine speed	1600 rpm

**Table 3.1 Engine Specification**

The engine was mounted on a Cusson's single cylinder engine test bed comprising of a 30 kW DC motor with associated water and oil conditioning systems. The engine

speed was maintained at 1600 rpm throughout the experiments and was adjusted by a dynamometer control system. The DC dynamometer was used to drive the engine during motored conditions and absorb load during fired operations. Engine torque was measured by a load cell unit.

Before testing, engine coolant and oil were warmed up to 100 °C and 50 °C respectively. The oil temperature was set lower than that of the commercial engine due to the limited of test equipment. Oil and coolant temperature were controlled by an engine test-bed control unit. The oil temperature was heated by a pair of electrical heaters which were immersed in the sump oil and controlled by a mains water heat exchanger with a closed loop control system. The coolant system featured a 3 kW immersion water heater which heats the coolant temperature. Temperature control was achieved using an electric pump driving water through a mains water heat exchanger and closed loop control system.

### **3.2.1.1 Crankshaft Position System**

In order to control the fuel injection timing, spark timing, camera exposure, cylinder pressure data acquisition and in-cylinder sampling valve, a reference signal from each engine revolution was generated by a trigger box and a clock signal. The clock signal of a resolution of 1 CA from a shaft encoder and the signal from a hall-effect cam sensor were the input to the trigger box. To provide a pulse synchronized with the encoder reference, the hall-effect sensor was attached on the exhaust camshaft pulley which was driven at half engine speed.

### **3.2.1.2 Air -Assisted Fuel Injection System**

Fuel was injected directly into the cylinder by an air-assisted injector supplied by Orbital Engine Corporation Ltd. The injector unit comprises of a conventional manifold port injector (MPI) operated with 8 bar gauge pressure to meter fuel into a chamber filled with pressurised air at 6.5 bar. Then the fuel and air mixture can be injected at 6.5 bar into the chamber. Better fuel atomization can be achieved due to compressed air injected at the same time, resulting in vaporization of liquid fuels. The

injection timing and duration of the MPI injector and the main injector can be controlled individually. The configuration of injector and injection sequence is shown in Figure 3.2.

The air-assisted injector has firstly been developed for Orbital Combustion Process in automotive 2-stroke application [82, 83]. It applies very low pressure to inject fuel into the cylinder. Therefore, the injection timings are limited due to high in-cylinder pressure during the piston moving up to TDC. The air-assisted injector utilizes air to share through the fuel rather than high pressure alone and results in good atomization with small particle size [83, 84]. However, fuel atomization should probably decrease in the production engine when compared to high pressure current state-of-the-art gasoline direct injection systems due to decreasing the differential pressure across the nozzle.

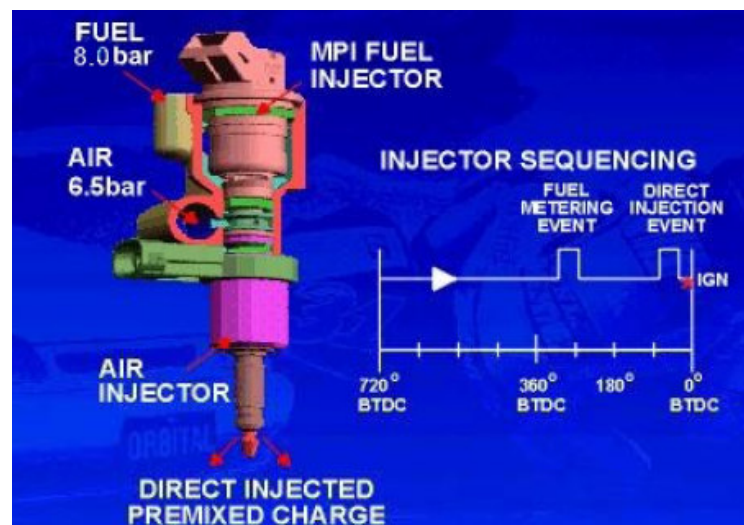


**Figure 3.2 Orbital Air-Assisted Injector with Typical Injection Sequence**

Two separate units were used to supply fuel and air for the injector. A compressed nitrogen tank was employed to pressurize fuel stored in a sealed cylinder to the MPI injector. A compressed air cylinder with a regulator was used to set and control the air supply pressure for the main injector. The output from the trigger unit was sent to a 2-channel delay unit and a 2-channel timer unit to control injection timing and duration respectively. Figure 3.3 presents the schematic of fuel injection system.

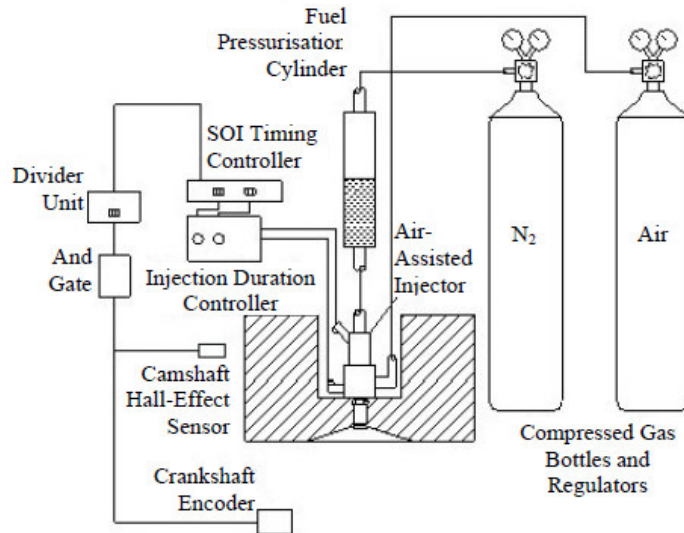


**Figure 3.3 Schematic of the Air-Assisted Injection Fuel System**

### **3.2.2 Pressure Transducer and In-Cylinder Pressure Acquisition System**

A Kistler type 6055B80 piezo-electric pressure transducer, connected to a charge amplifier Kistler type model 568, was used to measure the in-cylinder pressure. The measurement range is 0-250 bar with a sensitivity of 19 pC/bar. This pressure transducer is fitted in the cylinder head between the intake and exhaust valve as shown on the left hand side in Figure 3.1b. The charge output from the pressure transducer is converted to a proportional amplified voltage by the charge amplifier. This voltage, categorized as analog signal, was digitized in an analog-to-digital (A/D) converter which is included in a computer-based Data Acquisition System (DAQ).

The PC-based DAQ system consists of hardware to interface the computer and signal as well as a driver and application software to analysis and present the results. A National Instrument<sup>TM</sup> board type NI USB-6251 received the voltage signal from the transducer system and the clock and reference signal from the shaft encoder. LabView<sup>TM</sup> software was programmed to display the real time data on the monitor as well as to record and analyse the results.

### 3.2.3 Fuels

Nine fuels including gasoline, E20, E50, E85, E100, M20, M50, M85 and M100 were employed for the thermodynamic engine and chemiluminescence imaging experiments, where E stands for ethanol and M stands for methanol and the numeric value refers to the percentage by volume mixed with gasoline. Four pure fuels, gasoline, isooctane, ethanol and methanol were used for in-cylinder gas sampling studies. In addition, a mixture of 40/60 heptane/isooctane was also included for gas analysis. Unleaded Petrol was a RON 95 grade gasoline whereas other fuels were purchased from Sigma-Aldrich. Methanol, heptane and isooctane were HPLC grade while ethanol was a denatured grade. The main properties of the fuels are shown in Table 3.2.

	Gasoline ( $C_nH_{1.87n}$ )	Ethanol ( $C_2H_5OH$ )	Methanol ( $CH_3OH$ )	Isooctane ( $C_8H_{18}$ )	Heptane ( $C_7H_{16}$ )
Stoichiometric A/F ratio	14.6	9.00	6.47	15.13	15.18
Density( $kg/m^3$ )	720-780	789	791	692	684
RON/MON	95/85	107/89	106/92	100/100	0/0
Heat of vaporization (kJ/kg)	305	840	1103	308	318
Lower heating value (MJ/kg)	44	26.9	20	44.3	44.5
Auto-ignition Temperature( $^{\circ}C$ )	260-460	362	385	396	223
Stoic Flame Temperature ( $^{\circ}C$ )	2030	1920	1870	2001[85]	2000 [85]
Vapour Pressure @38 $^{\circ}C$ (kPa)	48-108	16.0	31.9	11.86[86]	11.15[86]
Flash Point ( $^{\circ}C$ )	-43 to -39	13	11	-12	-4
Stoich. Flame speed (m/s)	0.34	0.41	0.43	0.32[101]	0.33[101]

**Table 3.2 Fuel Properties**

Throughout each experiment, the relative air/fuel ratio of the charge mixture was kept to a stoichiometric value ( $\lambda = 1$ ) measured by a UEGO wide fast response heated lambda sensor. The sensor was connected to an AFR analyser MEXA-110 $\lambda$  for monitoring. Quantity of air for the air-assisted injector was kept constant at 10.8 mg/cycle. Due to the different stoichiometric air/fuel ratio, the quantity of fuel injected was adjusted with 7.03 mg/cycle gasoline, 8.20mg/cycle ethanol, and 9.44mg/cycle methanol, by varying the injection pulse width as shown in Table 3.3. The energy associated with each fuel is also included in the table to take into account of their Calorific values.

<b>Fuel</b>	<b>Injection Duration (ms)</b>	<b>Mass (mg)</b>	<b>Energy (J)</b>
Gasoline	3.2	7.03	309.26
E20	3.3	7.21	291.06
M20	3.3	7.21	280.14
E50	3.4	7.39	259.38
M50	3.5	7.57	237.97
E85	3.5	7.57	227.34
M85	3.9	8.42	205.82
Ethanol	3.8	8.20	220.49
Methanol	4.5	9.44	188.82

**Table 3.3 Injection Duration for each Fuel**

### **3.3 Exhaust Measurement**

#### **3.3.1 Unburned Hydrocarbon**

A flame ionization detector (FID) analyser, Rotork model AAL 520 was applied to measure exhaust UHC emissions. In the analyser, the hydrocarbon in a small,

continuous flow of sampled exhaust gas is burned in a hydrogen flame, forming ions shown as electric signal in an amount relating to the concentration of hydrocarbon in the sample. The FID is essentially a carbon counting detector responding to the total number of carbon atoms.

To prevent the retention of heavier hydrocarbon condensation within the system, the sampling system has to transfer the exhaust to the detector which is heated to a temperature of 200° C. The sample gas flows through the analyser with 5 ml/min of nominal flows. Hydrogen/Helium is the fuel used in the instrument. The FID detector was calibrated with sample gases containing known amounts of hydrocarbon. Propane (C<sub>3</sub>H<sub>8</sub>) was used for the span gas whereas zero gas was zero grade air. Therefore, the concentration of unburned hydrocarbon was presented as volume fraction in parts per million (ppm) of C<sub>3</sub>.

### 3.3.2 Oxides of Nitrogen

An AAL Model 443 Chemiluminescent analyser was used to measure the oxides of nitrogen in the exhaust gas. Either as the total level of nitrogen dioxide (NO<sub>2</sub>) or nitric oxide (NO). The instrument contains a heated sample module which is suitable for direct sampling of emissions containing no more than 15% water.

Generated within the instrument, ozone is mixed with the exhaust gas in a reaction chamber in front of the photomultiplier tube. The NO therefore reacts with the ozone forming electronically excited nitrogen dioxide molecules. These excited state molecules decay to the ground state either by emitting a photon of frequency  $\nu$  with varying wavelength between 300 and 600 nm or by energy transfer to another species, M by collision. The total reactions are expressed in the Equation 5.1-5.3.



Where  $h$  = Plank's constant

$h\nu$  = Energy of light.

The above reactions can approximate the intensity of the emitted light which is directly proportional to nitric oxide concentration. The photomultiplier tube within the detector assembly is the essential monitor. In order to determine the total  $\text{NO}_x$  concentration, the  $\text{NO}_2$  can be converted to  $\text{NO}$  prior to the reaction chamber by using a catalytic converter for decomposition.

### 3.3.3 $\text{CO}$ , $\text{CO}_2$ and $\text{O}_2$

A Horiba MEXA-554J series portable analyser was used to measure  $\text{CO}$  in the range 0-10%,  $\text{CO}_2$  in the range 0-20 % and  $\text{O}_2$  in the range 0-25% by volume. The exhaust gas was extracted from the middle of the exhaust pipe, and flowed at the rate of 2-3 L/min through a silicon rubber line. A water trap and a combined concentrate and particulate removal filter were used to filter exhaust gas before entering the analyser. An integral vacuum pump extracted the cooled exhaust gas for analysis.

$\text{CO}$  and  $\text{CO}_2$  concentration was measured by the non-dispersive infrared (NDIR) technology. The term non-dispersive refers to the fact that a broad band infrared source passes all of the infrared light through a sample cell containing the exhaust gas whereas dispersive IR detector use a grating or prism to pre-select the desired wavelength of light and pass only this through the gas sample. Absorption of the light is detected by a solid-state infrared detector. Narrow band-pass filters are employed to isolate the absorption band of  $\text{HC}$ ,  $\text{CO}$ , and  $\text{CO}_2$ . In addition, a reference beam is employed to provide the differential signal. NDIR detectors are calibrated with sample gases of known concentration. The concentration of calibration gas used was  $\text{CO}$  of 3.48 %, and  $\text{CO}_2$  of 14.04 %.

The unit applies a galvanic cell to measure  $\text{O}_2$  concentration. When potassium hydroxide in the cell comes in contact with oxygen, a chemical reaction occurs. This generates an electric current in which the voltage is proportional to the concentration

of oxygen. The signal is calibrated with a known concentration of oxygen. In the current study, 20.9 % was used.

### 3.4 Experiment setup for Chemiluminescence Imaging

#### 3.4.1 Optical access to the engine

The same engine as detailed in section 3.2.1 was used for chemiluminescence imaging by employing a transparent piston window. With the optical piston, images were obtained of the combustion chamber through a 55 mm piston quartz window by means of a 45° mirror. This was installed lower down in a Bowditch extension as shown in Figure 3.4.

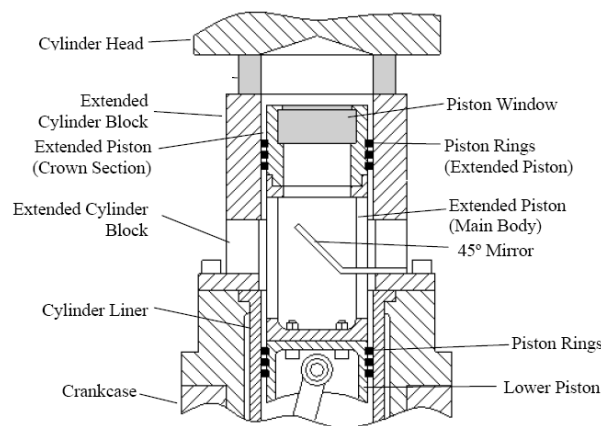


**Figure 3.4 Optical Engine Set up**

One metal compression ring and two compression type piston rings made of a PTFE material applied with lubrication grease were used instead of lubrication oil. Therefore, the engine should be disassembled regularly to assess the piston rings condition.

#### 3.4.2 Image Acquisition System

A NAC Memrecam fx 6000 high speed video camera coupled with a DRS Hadland Model ILS3-11 intensifier was the major system used to record the high speed

chemiluminescence images. With 49  $\mu$ sec exposure time, the intensifier was set at 60 % gain for total and CHO chemiluminescence, whereas 90% gain for a relative low intensity of OH images. Total and OH chemiluminescence was recorded through a UV-Nikkor 105 mm f/4.5 lens. While a Nikon Micro-Nikkor 60 mm f/2.8D lens was used for CHO. The camera recorded images at a speed of 10,000 frame/sec with a resolution of 512 x 248 pixels. Therefore, time-resolved images of less than one degree crank angle per image at an engine speed of 1600 rpm were acquired.

The camera was triggered at the same time as the data acquisition system to simultaneously record images and in-cylinder pressure data. With high temporal resolution, only 15 cycles of CAI combustion were recorded using 4 GB on-board memory. The recorded video was transferred and saved in the PC with format \*.mcf via Memrecam FX Link software. Afterward, to enhance the image quality by means of MATLAB-based software, the format \*.mcf was converted to the \*.avi format.

### 3.4.2 Optical Bandpass Filter

Sourced from Andover Corporation, a 350 nm-wavelength bandpass filter was placed in front of the intensifier to image CHO chemiluminescence. A 310 nm-wavelength filter was employed to detect OH chemiluminescence. The specification and characteristics of the filters are shown in Table 3.4 and Figure 3.5.

Species	Center wavelength (nm)	FWHM (nm)	Peak Transmission (%)	Diameter
CHO	350.0+3/-0	10.0+2/-2	25	50
OH	310.0 +3/-0	10.0 +2/-2	15	50

**Table 3.4 Bandpass Filter Specification.**

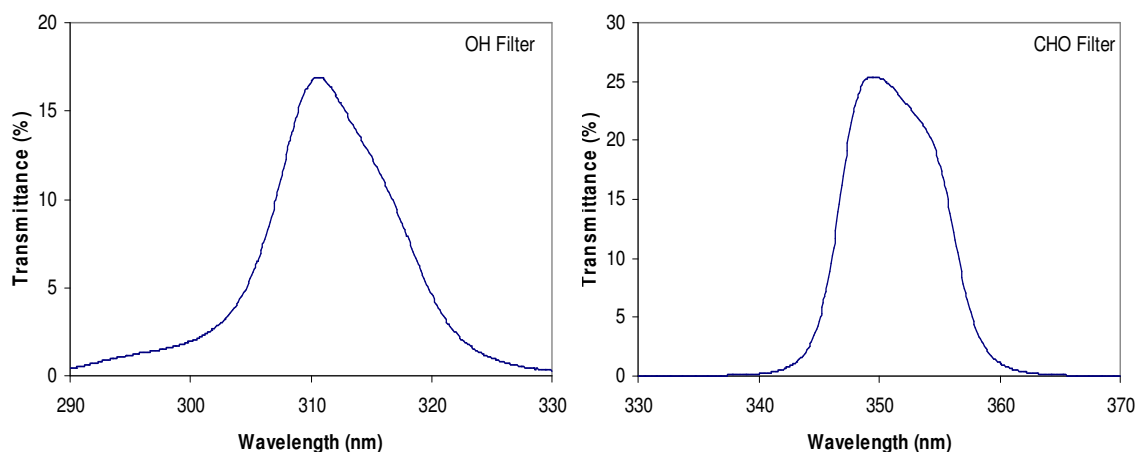


**Figure 3.5 Bandpass Characteristic of OH and CHO Filter**

### **3.5 In-Cylinder Sampling and Gas Composition Analysis**

#### **3.5.1 Fast Response In-Cylinder Gas Sampling Valve**

A gas sampling valve used in the current study was designed and manufactured at Brunel University for the previous project [87-89]. Made from high-strength steel, a poppet valve, which opens in the outward direction, was designed to shut firmly on a copper seat due to the force from the compressed return spring as well as the high pressure gas. To have great flexibility, an electromagnetic actuator could be applied directly to force the valve for opening and closing. However, its response would be slow to sample gas in a very short period of time (< ms). Therefore, the percussion principle in which the valve needle or poppet stem is not joined to the armature of the electromagnet was used as shown in Figure 3.6. The small gap between the stem of the poppet and armature is the traveling distance for the plunger to accelerate and impact the end of the stem after the electromagnetic is switched on. The valve opens for a short period and then the compression valve stem spring and gas pressure forces the poppet to shut promptly.

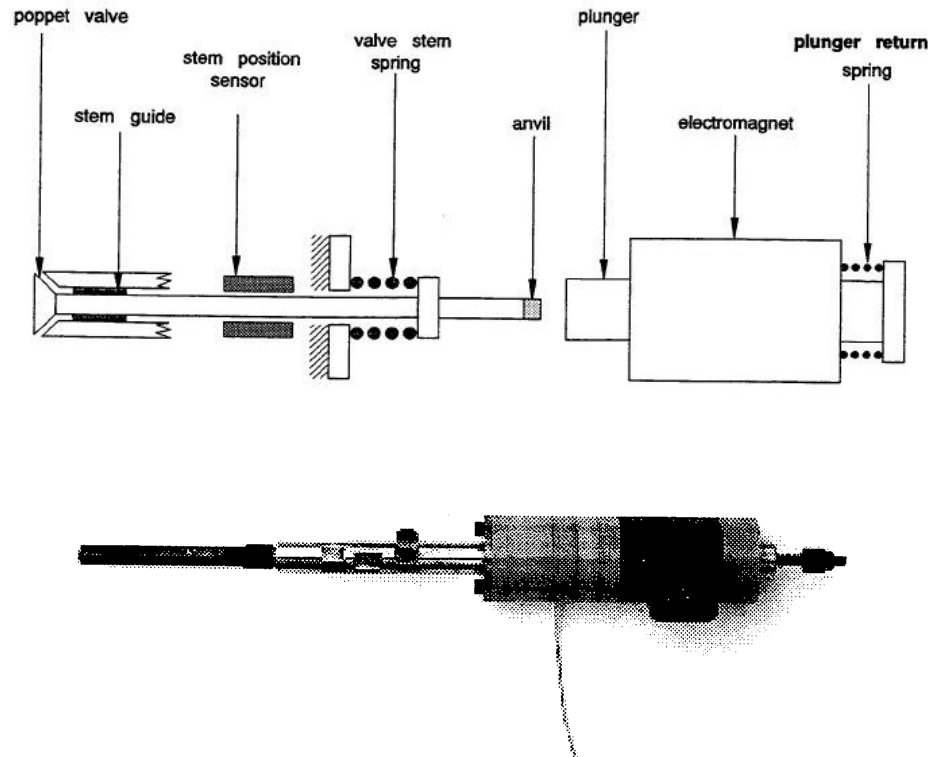


**Figure 3.6 Electromagnetic Gas Sampling valve**

The electromagnetic sampling valve was controlled by a sample valve drive unit which was supplied the 24 Volt dc, 7 amp by means of a power unit. The sample time and sampling duration was controlled through a sample valve pulse delay unit (range 5 -130 ms) which received the reference signal from the shaft encoder. On the side of the actuator, a small co-axial connector was connected to measure the actual sample timing and duration by detecting the movement of the stem. This signal was monitored and recorded with an oscilloscope. The sampling valve system diagram is shown in Figure 3.7.

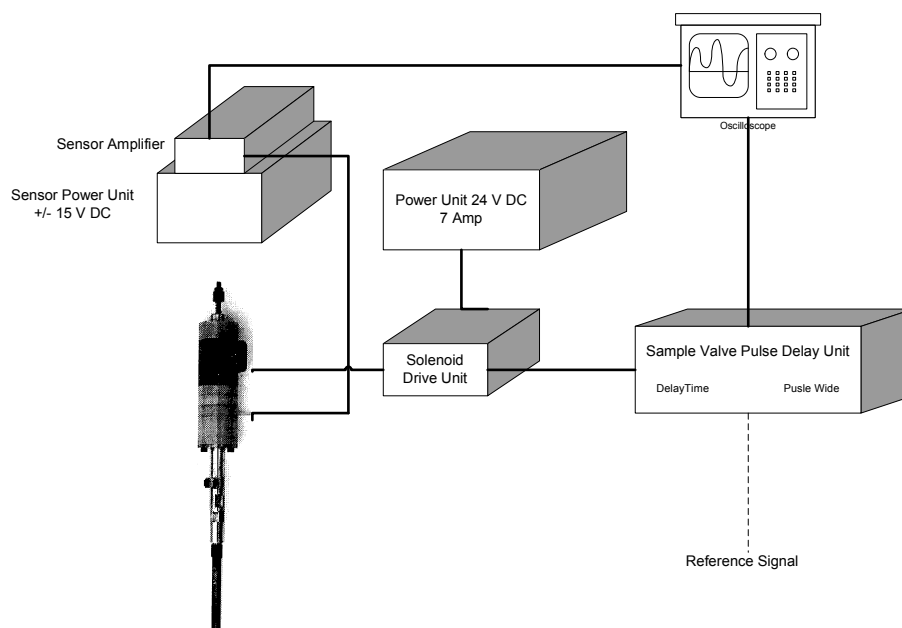


**Figure 3.7 Sampling Valve Diagram**

Since the current engine had to use the spark discharge to start running and also the air-assisted injector to inject the fuel, there was no space for the sampling valve in the cylinder head. With a diameter of 6 mm, the poppet valve was installed horizontally in side of a sandwich plate between the cylinder head and block. This restricted the valve opening time to before 54 BTDC to avoid collision with the piston. To keep a constant sampling flow rate, the sampling period was varied between 0.8-2.8 msec depending on the in-cylinder pressure. The relative small volume of the sample per cycle was necessary to minimise interference with the combustion processes through a very low valve lift of less than 0.4 mm.

According the previous work [87], after in-cylinder gas passed through the valve, it was cooled by the contact with the internal surfaces of the valve and left the valve at a temperature around 40 to 50°C. Therefore, reactions should be frozen immediately leaving charge composition of the sample gases unchanged.

The gas was sampled by a SKC Tedlar 0.5 liter sampling bag via a 3 cm long silicon rubber tube. It took about 1 minute to fill the bag. A Hamilton gas-tight syringe was then used to transfer 9 ml sample gas to GC-MS.

### 3.5.2 Gas Chromatography

Gas chromatography and mass spectrometer (GC-MS) was used to analyse the in-cylinder gas composition. A Hewlett Packard 5890 gas chromatography was connected to a TRIO-1000 mass spectrometer as shown in Figure 3.8. After the sample was introduced into the GC via the inlet port Valco valve, it was carried by a moving phase inert gas (carrier gas) passing across the stationary phase known as a column. The column was installed in the oven which can be programmed for appropriate temperature setups. On the wall of the column, a microscopic layer of specific liquid or polymer is coated for interacting with the gaseous sample. Due to different volatility which is dependent on molecular weight and reactivity rate, each species in the sample was separated at a different time referred as the retention time. Comparing with standard gases with known retention times, the gas species could be identified.

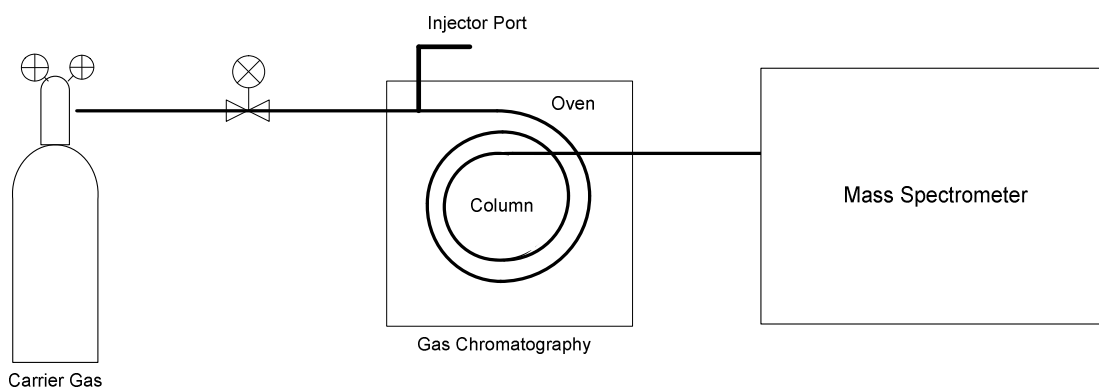


**Figure 3.8 GC-MS Configurations**

Helium gas was selected as the carrier gas in the current study. A capillary tube, Chrompack Poraplot Q type porous polymer with 0.32 mm ID, 10  $\mu\text{m}$  film thickness, and 30 meters length suitable for alcohols, C1-C6 hydrocarbons, ketones, solvents, etc was used for the column. To improve the resolution of retention time, the oven temperature was programmed as follow:

Initial Temperature: 50°C for 2 minutes

50°C - 220°C with the rate 10° C/min

Final Temperature: 220°C for 10 minutes

After finishing the analysis of the gas sample, GC was purged by repeatedly running without the injection of sample to ensure that no residue gas was trapped in the column.

### 3.5.3 Mass Spectrometer

Instead of using a FID or thermal conductivity detector, a TRIO-1000 mass spectrometer was used to measure the concentration of each species. As shown in Figure 3.9, after leaving the GC column, molecules were loaded into an ion source vacuum. Electrons at 70 V were used to ionize the molecule. According to their mass-to-charge ratio ( $m/z$ ), molecule ions and fragment ions were accelerated and separated by a magnetic field formed in a quadrupole mass analyser. The separated ions were detected by the detector in the final part of the MS resulting in a mass spectrum. The mass spectrum is presented in the format of intensity of ions versus their  $m/z$  ratio. The example of methane spectrum is shown in the top graph of Figure 3.10.

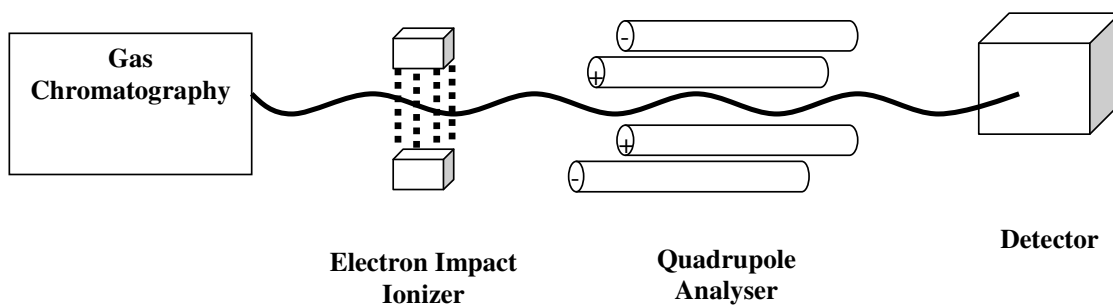


**Figure 3.9 Mass Spectrometer Configurations**

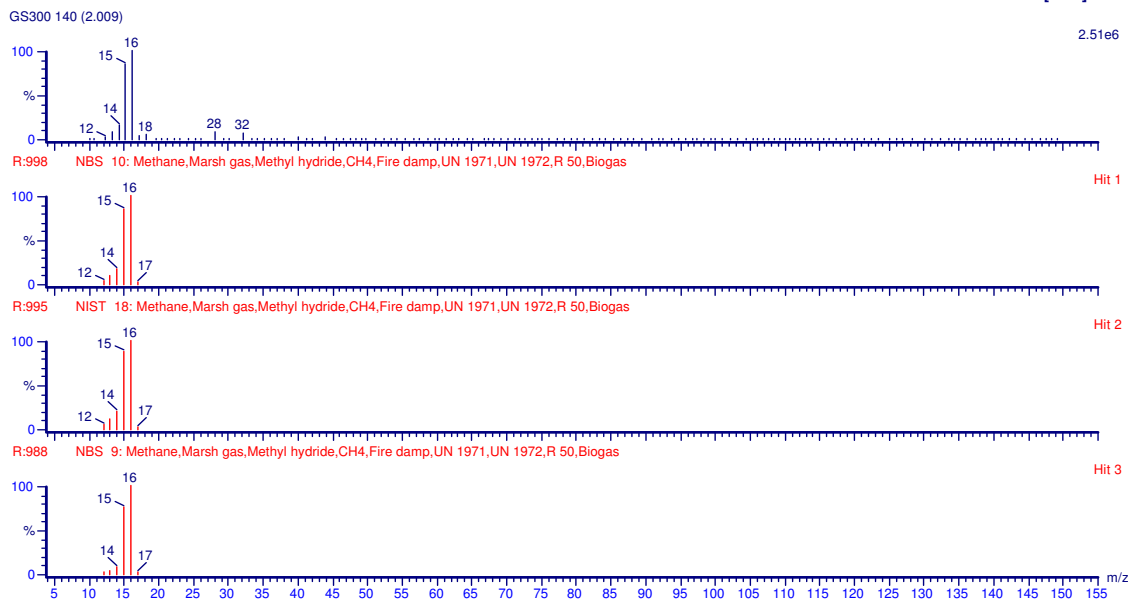


**Figure 3.10 Mass Spectrum of Methane and Results of Library Search**

MassLab program was used to control the data acquisition and record the results of GC-MS. Additionally, the program stores the mass spectra of many compounds in its library. Using library search function to compare the sample mass spectrum against a library of mass spectra, an unknown compound could be identified. The second to the last graph in Figure 3.10 are the results of the library search.

The details of standard gases used to measure the retention time and the concentration are presented in Table 3.5.

<b>Component</b>	<b>Nominal Concentration</b>	<b>Certified Concentration</b>
Benzene	0.0500	0.0502 +/- 0.0011
Hexane n-	0.0500	0.0504 +/- 0.0011
Hexene 1-	0.0500	0.0460 +/- 0.0014
Pentane n-	0.0500	0.0498 +/- 0.0010
Pentene 1-	0.0500	0.0503 +/- 0.0011
Cyclopropane	0.0500	0.0484 +/- 0.0010
Propylene	0.0500	0.0495 +/- 0.0010
Methane	0.0500	0.0506 +/- 0.0011
Ethylene	0.0500	0.0522 +/- 0.0011
Ethane	0.0500	0.0503 +/- 0.0011
Propane	0.0500	0.0503 +/- 0.0011
Butane n-	0.0500	0.0500 +/- 0.0011
Butene 1-	0.0500	0.0500 +/- 0.0010
Butadiene 1,3-	0.0500	0.0502 +/- 0.0011
Nitrogen	Balance	Balance

**Table 3.5 Standard Gas Specification**

### **3.6 Summary**

In this chapter, the single cylinder engine setup, in-cylinder pressure and exhaust emission measurements are described. The high speed imaging setup for the single cylinder engine is presented. Detailed description of the in-cylinder sampling and its subsequent analysis are given. The application of these techniques will be presented in the following chapters.

## **Chapter 4 Thermodynamic Engine Test Results and Analysis**

### **4.1 Introduction**

Engine testing is the basic experimental method used to study the thermodynamic performance of an engine. Derived from in-cylinder pressure data, combustion characteristics such as heat release rate, mass fraction burned, and combustion duration are calculated by means of laws of thermodynamics while some combustion features such as maximum pressure, coefficient of cyclic variation are obtained directly from the in-cylinder pressures.

The aim of the current study is to compare the effects of different fuels, and their effect on the combustion and emission. The experiments were carried out for various fuels and different injection timings, from which the heat release, emission results were obtained. Some engine operating conditions were then selected for the in-cylinder visualization and species measurements so that better understanding of underlying processes can be obtained.

### **4.2 Test Methodology**

#### **4.2.1 Selection of Injection Timing**

As detailed in Chapter 3, since the current engine achieved CAI combustion by utilizing hot trapped residual gas, injecting fuel during the negative valve overlap period was used to introduce fuel reforming reaction for more stable CAI combustion. However, the injection timing was constrained by the low injection pressure of the air-assisted injector. Since the exhaust valves were closed early, and intake valve opening was retarded, a second pressure rise, referred to as the re-compression peak, occurred at TDC exhaust. This re-compression phase increased the in-cylinder pressure, resulting in the in-cylinder pressure above 7 bar at 30 CA at either side of TDC and a peak value around 9-15 bar at TDC. As a consequence, injection was not possible during that period. With injection duration in the range of 30-45 degree CA, the injection must commence at least 75 degree BTDC. To avoid incomplete fuel

injection and to enhance the fuel atomization ability of the air-assisted system, the start of injection was fixed at 80 degree BTDC of the exhaust stroke.

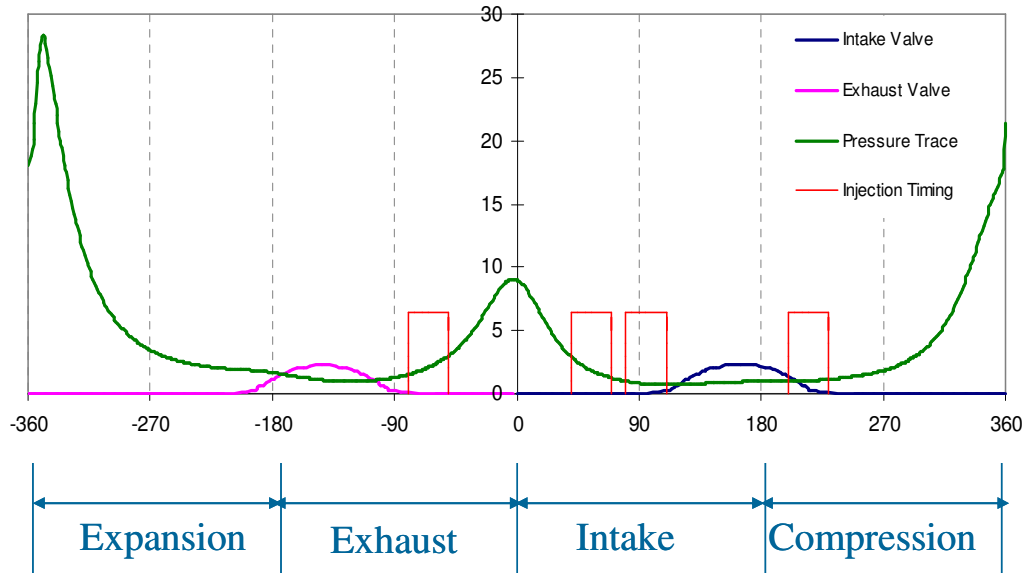


**Figure 4.1 Intake, Exhaust Valves and Injection Timing against In-Cylinder Pressure of Gasoline Conditions**

Figure 4.1 also shows two injection timings during the intake stroke in order to examine the effect of a homogeneous charge mixture. One injection was triggered at 40 degree ATDC of the intake stroke, 10 degree CA after the re-compression pressure was lower than the injection pressure. Another injection commenced at 80 degree ATDC nearly the same time as that of the intake valve opening. With this timing, the mixing of fuel, hot residual gas and air took place at the same time with sufficient mixing time.

The last selected injection timing was during the compression stroke in order to examine the effect of a stratified charge mixture. However, due to the constraints of low injection pressure and increased in-cylinder pressure during the compression stroke, the injection timing was set at 200 degree ATDC of the intake stroke as shown in Figure 4.1

## **4.2.2 Spark- and Non-Spark-assisted Combustion**

Fundamentally, CAI combustion is initiated by spontaneous self-ignition of the charge mixture. To control the auto-ignition timing, many methods have been employed such as varying injection timing or controlling the amount of hot residual gas. In addition, many researchers [16-18] have adopted spark discharge in CAI combustion to initiate combustion at specific ignition timings. In addition to controlling ignition timing, spark discharge has been applied as a method of extending the operating regime by controlling combustion phasing or even facilitating the transition between SI and CAI combustion. Thus, the effects of spark discharge were also examined in the current study.

## **4.2.3 Fuels**

Nine fuels including gasoline, E20, E50, E85, E100, M20, M50, M85 and M100 were investigated. Gasoline was used as a baseline reference to allow comparison with the alcohol fuels. In order to investigate the effect of alcohol concentration tests were carried out for a range of gasoline blends. In production SI engines, up to 20 percent of ethanol is added to gasoline without engine modification. Up to 85 % blended alcohols were included in this experiment as such fuels have been used in flexible fuel vehicles in some countries, for example, Brazil and the USA. For the last two fuels, engine tests were performed using pure alcohols in order to study the characteristics of CAI combustion of oxygenated fuels.

## **4.2.4 Experimental Procedure**

Since the implementation of CAI combustion in the current engine is based on the hot residual gas trapped from the previous cycle, it was not possible to run the engine in pure CAI mode without spark ignition combustion from cold start. Hence, for all conditions, the engine should first be run with spark-ignited combustion until sufficient and steady amount of residual gas was available to initiate CAI.

Before starting each testing, the lab equipment was turned on and the exhaust gas analysers as well as AFR analyser warmed up and calibrated. In order to simulate steady state warmed up operating conditions, engine coolant and oil were set to 100°C and 50°C respectively. For the first running of each day after re-assembly of the engine, a motoring test at the speed of 1600 rpm was conducted and in-cylinder pressure recorded to make sure that the engine performed at the same conditions. The engine was then motored at a speed of 1200 rpm with the air heater switched on. Once the intake air temperature reached 175°C, the fuel system was switched on and the spark discharge was initiated. The engine speed was then increased to 1600 rpm. The fuel injection duration was adjusted to achieve stoichiometric combustion by monitoring the AFR analyser.

With spark-assisted combustion, gasoline was the first fuel to be investigated. Stable engine operation was checked by the real-time observation of in-cylinder pressures over 100 consecutive cycles. Exhaust emission including CO, HC, NO<sub>x</sub>, O<sub>2</sub> and exhaust temperature were recorded after the engine had stabilised. At the end of each test, spark discharge was first turned off followed by the fuel injection system. CAI without spark-assisted ignition was then tested with gasoline fuel. The same procedure was followed until spark-assisted combustion was stable, the spark system was then switched off and the in-cylinder pressures recorded when stable CAI combustion was obtained.

The procedure was repeated for the other fuels, E20, M20, E50, M50, E85, M85, E100 and M100 respectively. For each fuel, the air/fuel ratio was kept to  $\lambda = 1$  by altering the injection duration. After one injection timing was completed for all 9 fuels with and without spark-assisted ignition, the engine was disassembled and the piston rings were lubricated with grease after they had been checked. The engine was then rebuilt in preparation for the next set of injection timings.

### **4.3 Results and Discussion for Fuel Injection Timing at 80 BTDC**

#### **4.3.1 In-cylinder pressure data**

## In-Cylinder Pressure

The in-cylinder pressures were recorded for 100 consecutive cycles at 1° CA resolution and then averaged for the subsequent heat release analysis. The in-cylinder pressure and heat release characteristics at injection timing of 80 BTDC are presented in this section. Injection timing of 40, 80 and 200 ATDC are shown in Appendix A, B and C.

For the implementation of CAI combustion through negative valve overlap, the most important factor affecting the combustion is the trapped residual gas. The trapped residual (%) is defined as the ratio of the charge mass trapped in the cylinder at EVC timing over the sum of the total charge.

$$\text{Trapped residual (\%)} = \frac{m_r}{m_{fc} + m_r} \times 100 \quad (4.1)$$

Where  $m_r$  = trapped residual amount

$m_{fc}$  = mass of fresh charge (air + fuel)

The trapped residual amount was calculated by the ideal gas law as shown in the equation 4.2.

$$m_r = \frac{PVM}{\tilde{R}T} \quad (4.2)$$

Where P = In-cylinder pressure at EVC

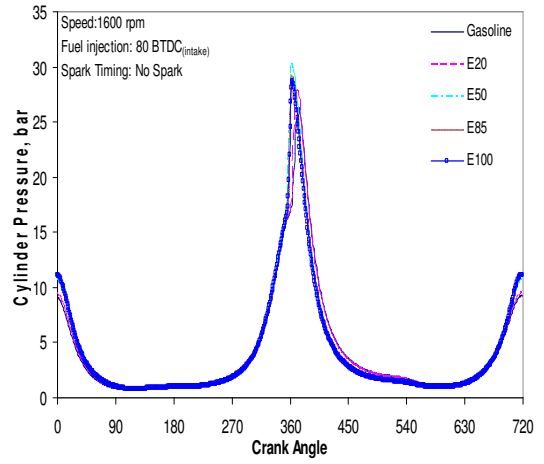
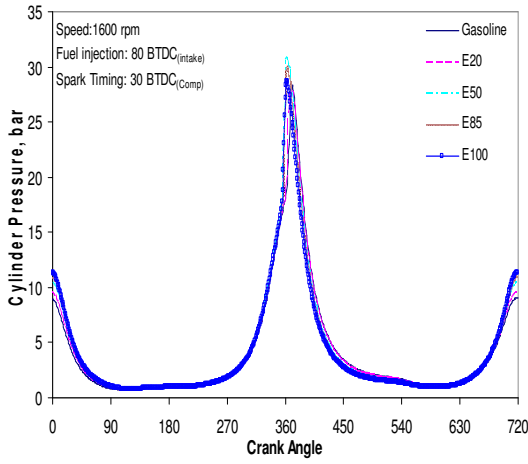
T = Burnt gas temperature at EVC

M = Molecular weight of the residual gas

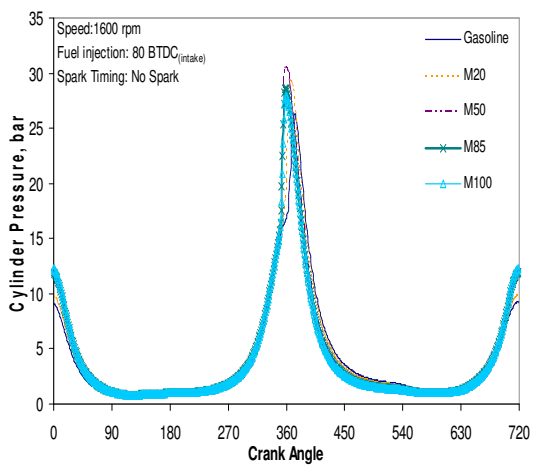
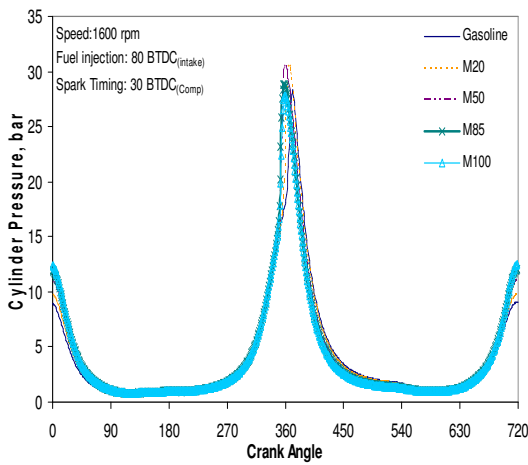
$\tilde{R}$  = Universal gas constant 8.3143 J/mol.K

The burnt gas temperature was assumed to be equal to the temperature measured by a thermocouple located in the exhaust port.

As shown in Figure 4.2, there is a re-compression peak during the negative valve overlap as well as the main peak during combustion.



**Gasoline and Ethanol blended Fuels**

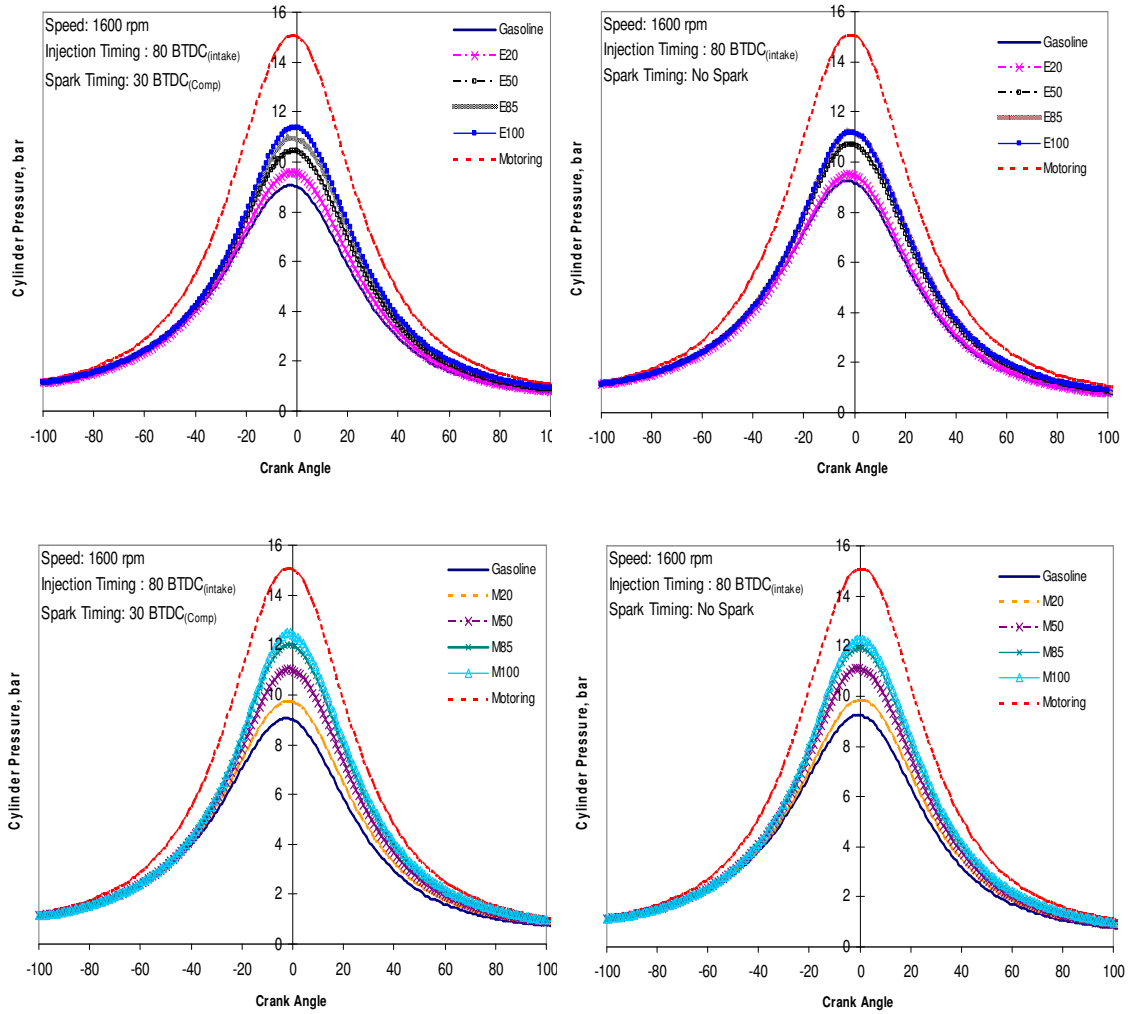


**Gasoline and Methanol Blended Fuels**

(a) Spark-assisted ignition

(b) Non-spark-assisted ignition

**Figure 4.2 In-Cylinder Pressure Traces with SOI at 80 BTDC**



(a) Spark-assisted ignition

(b) Non-spark-assisted ignition

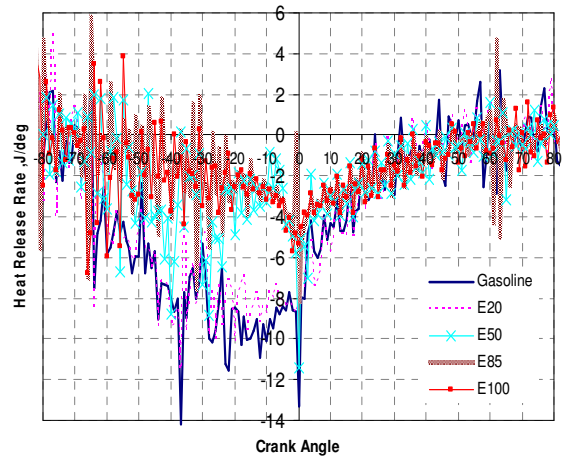
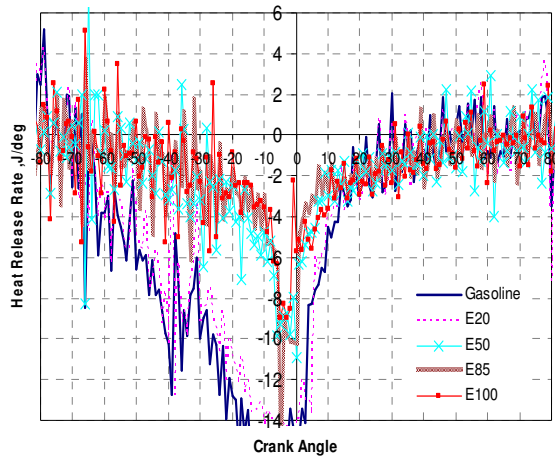
**Figure 4.3 In-Cylinder Pressures during the Negative Valve Overlap Period**

Figure 4.3 shows the detailed pressure traces during the NVO period. It is noticed that re-compression pressures are lower than the motoring pressure. There are two main reasons responsible for this. Firstly, this is due to the higher total heat capacity of the residual gas in which  $\text{CO}_2$  and  $\text{H}_2\text{O}$  are the major compounds. Generally, in the absence of combustion, the re-compression period behaves close to an adiabatic isentropic process in which the specific heat ratio, the  $\gamma$  value, plays a major role. For motoring, only fresh air which has a higher gamma value than residual gas is compressed and subsequently has a higher compressed gas temperature resulting in a higher pressure. Secondly, in terms of the charge cooling effect, liquid fuels which

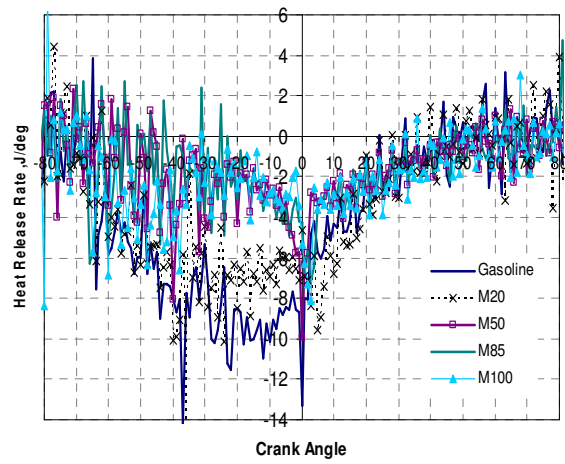
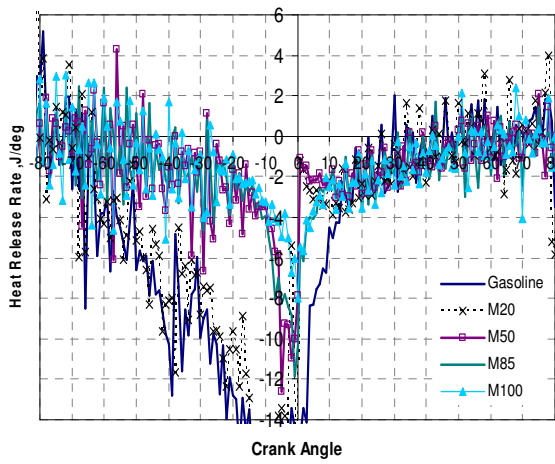
were injected directly into the cylinder at EVC absorb heat for evaporation. As a result, the charge temperatures and then in-cylinder pressures were reduced.

For fired engine tests, in-cylinder pressures during the NVO period increase with increasing percentage of alcohol. Methanol had a far greater effect than ethanol. For the current injection timing, hot trapped residual gases mixed with fresh fuel were compressed to TDC. Therefore, there are two feasible factors which promote this higher in-cylinder pressure of re-compression. The first effect is fuel and the other is hot residual gas. To keep a stoichiometric equivalence ratio ( $\lambda = 1$ ), a greater quantity of oxygenated fuels are required for combustion than with gasoline. However, the heat release rate results in Figure 4.4 seem to be contrary to the expectation that methanol should produce the largest charge cooling effect and hence the highest negative heat release rate. Instead the gasoline fuel seemed leading to more heat loss from the mixture. Such results, however, could indicate more heat release reactions may have taken place with alcohol fuels due to fuel reforming reactions. As a consequence, higher cylinder pressures at the re-compression stroke were produced with alcohol blended fuels.

In addition, it was found that more residual was trapped when using alcohol fuels. Due to the earlier ignition and more advanced combustion of alcohol fuels, in-cylinder pressure was lower during the expansion and exhaust stroke. Therefore, exhaust blow-down scavenging was reduced hence higher trapped residual mass. The greater amount of trapped gas increased the heat capacity and hence lower compression temperature and pressure. However, as it will be demonstrated that the molar effect of trapped residual gas is not as significant as the fuel effects by comparing the results with those of other injection timings.



**Gasoline and Ethanol Blended Fuels**

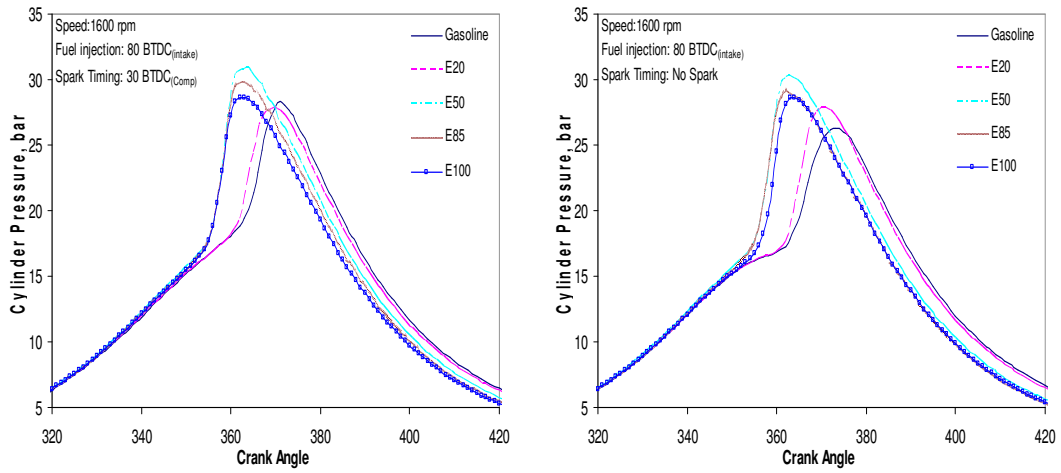


**Gasoline and Methanol Blended Fuels**

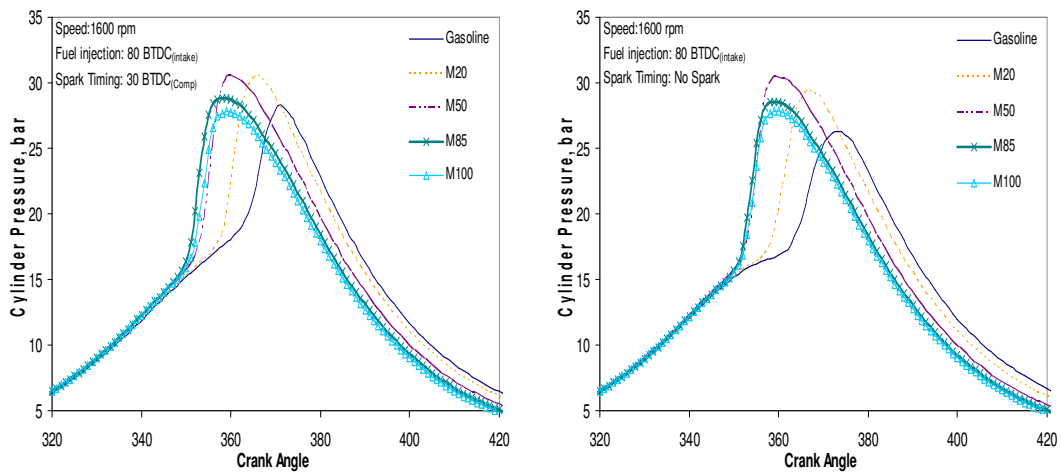
a) Spark-assisted ignition

(b) Non-spark-assisted ignition

**Figure 4.4 Heat Release Rate during the NVO Period**



### Gasoline and Ethanol Blended Fuels



### Gasoline and Methanol blended Fuels

a) Spark-assisted ignition

(b) Non-spark-assisted ignition

**Figure 4.5 In-Cylinder Pressures during the Main Combustion Process**

The effect of alcohol fuels on the main combustion process is shown in Figure 4.5. It is noted that the presence of alcohol advanced the combustion irrespective of the spark. Methanol blended fuels in the range of 0-50 percent yield the highest cylinder pressures and most advanced combustion while pure gasoline is characterized with the lowest cylinder pressure and slowest burning combustion. The methanol results are consistent with those reported in previous studies [39, 40]. However, Li et al. [40] found that ethanol fuel resulted in retarded and slower combustion than gasoline. This is likely caused by the different injection timing used. When fuel injection took place in the compression stroke in [40], the fuel stratification was more pronounced and the greater charge cooling effect of ethanol would lower the charge temperature resulting

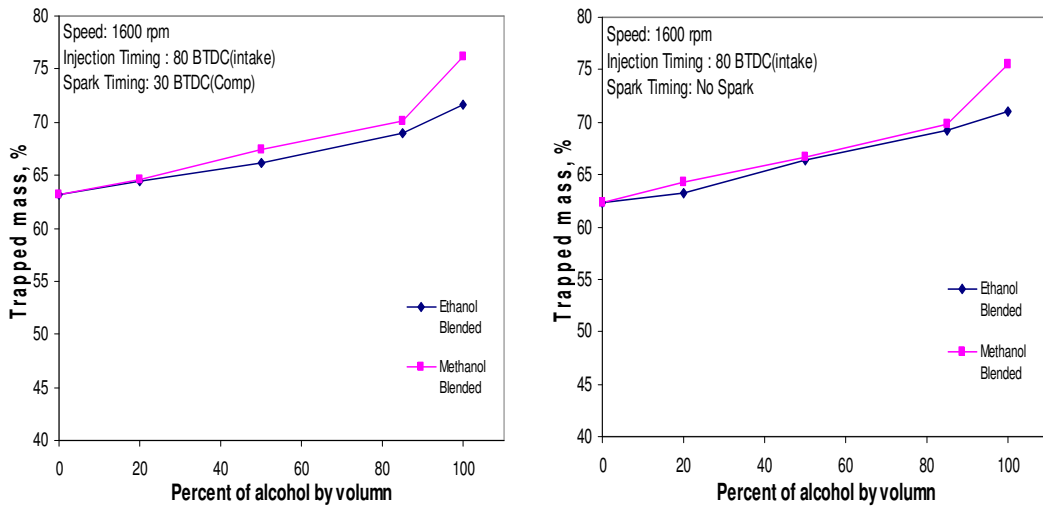
delayed auto-ignition. In the current study, at the late injection timing of 200 ATDC neat alcohols could not achieve stable combustion as shown in Appendix C.

Beyond 50 percent of alcohol, in-cylinder pressures of blended fuels gradually dropped and the combustion phase remained almost constant or slightly retarded. Methanol blended fuels had lower in-cylinder pressure due to lower energy input but still more advanced combustion than those of ethanol blended fuels.

In the presence of spark-assisted ignition, charge ignition was initiated by spark discharge at a specific crank angle, so combustion should commence at the same time for all fuels. Due to the higher flame speed of methanol, followed by the flame speed of ethanol, the flame propagation process plays a major role for the rapid and advanced combustion of oxygenated fuels whereas the slower flame speed of gasoline is responsible for the most retarded combustion. On the other hand, without spark-assisted ignition, combustion was dominated by spontaneous auto-ignition. Charge mixture temperature is the most important parameter affecting self ignition. For the current CAI engine, charge mixture temperatures were increased by means of air intake heating in conjunction with trapped hot residual gases. At constant intake air temperature, only the trapped hot residual gases affected directly the charge mixture temperature. As shown in Figure 4.6, more hot residual gas was retained in the cylinder when the percentage of alcohol increased, particularly in the case of methanol. Subsequently, the charge heating effect from those large amounts of hot residual gases promoted higher charge temperature even though oxygenated fuels require more heat of vaporization. Therefore, with the higher charge temperature, methanol can readily achieve auto-ignition. This resulted in the most advanced combustion.

Beyond 50 percent of alcohol, in-cylinder pressure decreased with increasing percentage of alcohol. There are two main reasons responsible for this decreased pressure. Firstly, high amounts of trapped residual gases were shown in Figure 4.6. The fresh charge mixture was diluted with more trapped residual gas in the case of methanol and ethanol blended fuels. Therefore, with the dilution effect, slow combustion took place and resulted in lower in-cylinder pressure. More importantly, different input energy is mostly accountable for this decreased in-cylinder pressure.

Although more alcohol fuel was injected into the cylinder, the input energy per cycle of blended fuel became lower at higher alcohol concentration due to the lower heating value of alcohol fuels. As shown in Figure 4.7, the input energies of alcohol blended fuels were less than two thirds that of gasoline when 85% of alcohol was substituted in gasoline.



(a) Spark-assisted ignition

(b) Non-spark-assisted ignition

Figure 4.6 Trapped Mass Residual for any Fuels

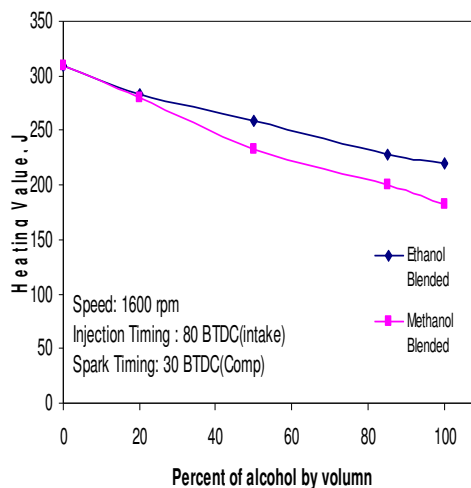
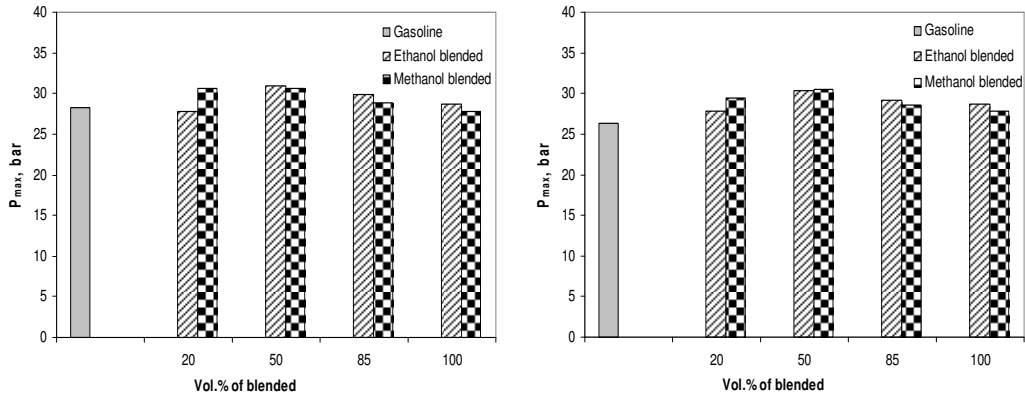


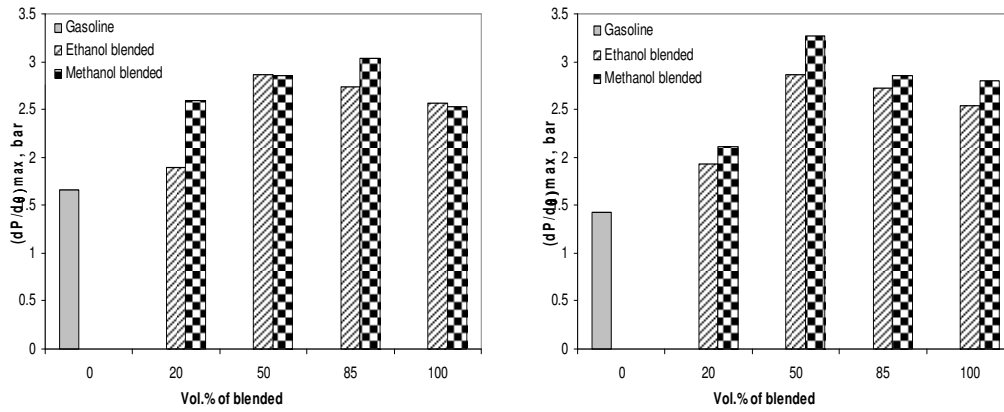
Figure 4.7 Input Energy per Cycle for any Fuels



(a) Spark-assisted ignition

(b) Non-spark-assisted ignition

Figure 4.8 Maximum Pressure for all Fuels

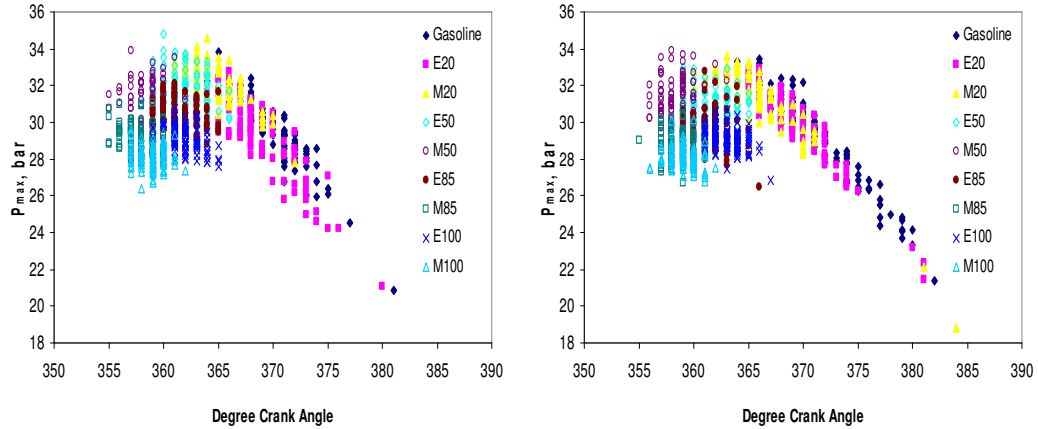


(a) Spark-assisted ignition

(b) Non-spark-assisted ignition

Figure 4.9 Maximum of  $\frac{dP}{d\theta}$  for all Fuels

As a result of advanced combustion phasing,  $P_{max}$ , and  $\left(\frac{dP}{d\theta}\right)_{max}$  increased initially with increasing alcohol concentration up to 50 % as shown in Figure 4.8 and 4.9. But the reduction in the input energy with more than 50 % alcohol caused the  $P_{max}$ , and  $\left(\frac{dP}{d\theta}\right)_{max}$  to decrease beyond.

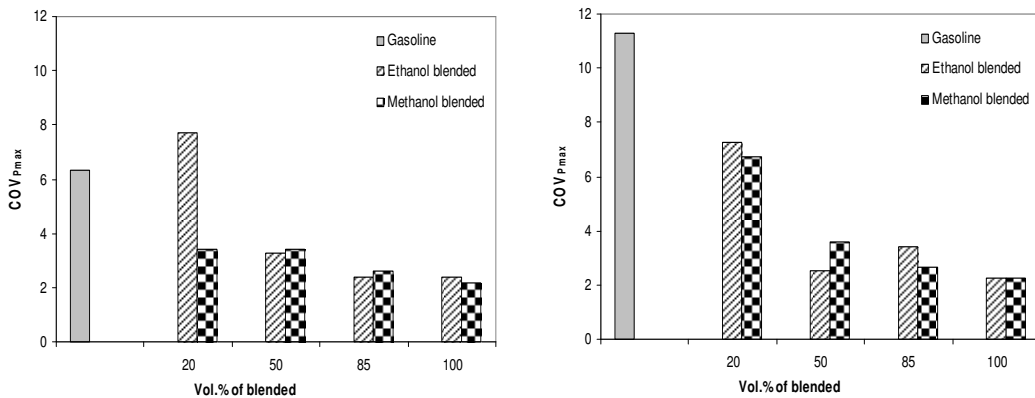


(a) Spark-assisted ignition

(b) Non-spark-assisted ignition

Figure 4.10  $P_{max}$  and  $\theta_{P_{max}}$

Figure 4.10 presents the peak pressure and the crank angle at which it occurs. The higher peak pressures from the combustion of E50 and M50 are located around TDC whereas the lower peak pressures from gasoline are located further from TDC in the expansion stroke. Due to the smaller volume change near the top dead centre, the early combustion of alcohol blended fuels yielded higher peak pressures while the retarded combustion with high dilution of gasoline occurred after TDC resulting in lower peak pressure. Moreover, Figure 4.10 shows that gasoline combusted with higher fluctuations in the peak pressures than that of the oxygenated blended fuels as shown by the COV of  $P_{max}$  in Figure 4.11. Also, the crank angle at which the peak pressures of gasoline occurred are scattered by more than 10 degree but those of alcohol blended fuels vary by only around 7 degree CA, except for 20 percent of alcohol.



(a) Spark-assisted ignition

(b) Non-spark-assisted ignition

Figure 4.11 Coefficient of Variation in Peak Pressure.

## Indicated Mean Effective Pressure

As shown by Figure 4.12, when the percentage of blended alcohol was increased the indicated mean effective pressured (IMEP) decreased. In addition to the lower input energy associated with alcohol fuels, the more advanced combustion contributed to the decreased IMEP.

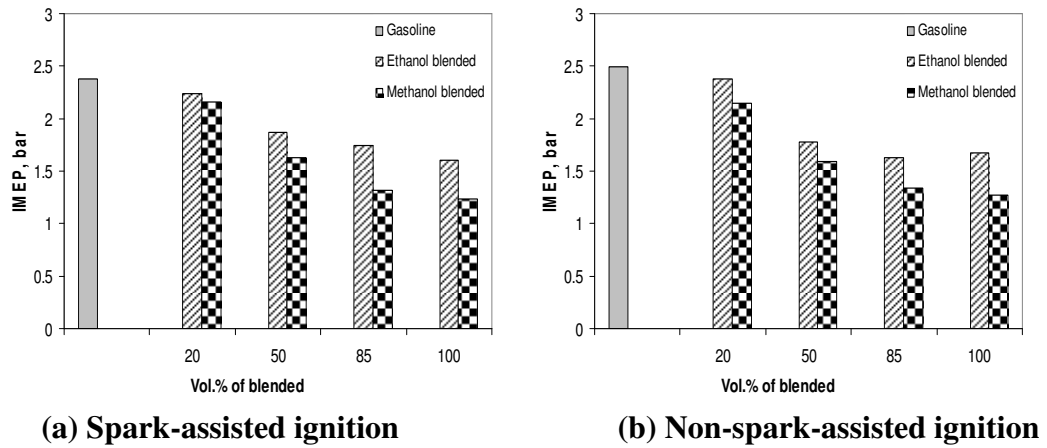


Figure 4.12 Indicated Mean Effective Pressure for all Fuels

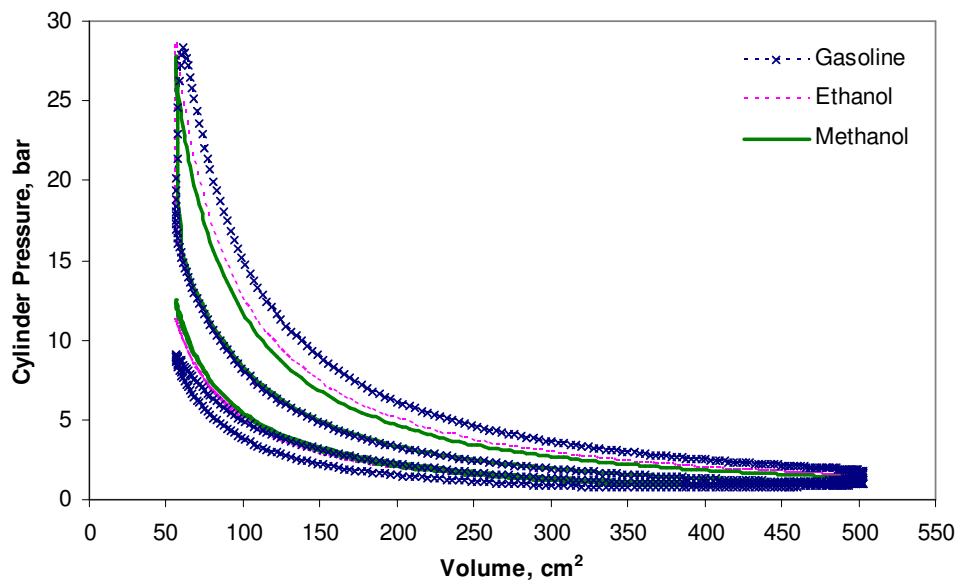
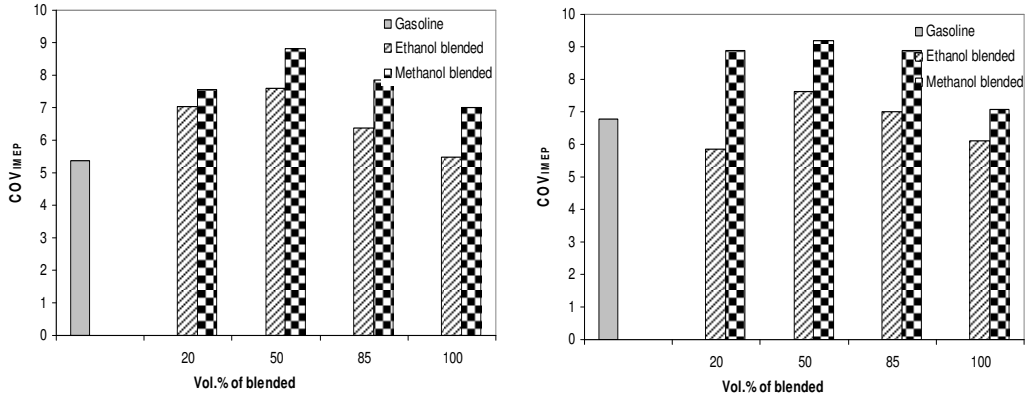


Figure 4.13 In-Cylinder Pressures against Volume



(a) Spark-assisted ignition

(b) Non-spark-assisted ignition

**Figure 4.14 Coefficient of Variation of Indicated Mean Effective Pressure**

In contrast to COV in peak pressure, cycle-to-cycle variation of indicated mean effective pressure increased with the percentage of alcohol blended fuels as Figure 4.14 presents. This corresponds well with the results of Xie et al [39]. Due to the high amount of residual gas trapped to dilute the charge mixture and the high amount of blended alcohol injected in the cylinder to keep the mixture stoichiometric, the mixing of fresh mixture and residual gas within the cylinder substantially would vary in each cycle. This cyclic variation in mixing could be a significant cause of the high COV of IMEP for alcohol blended fuels.

From table 4.2- 4.4 of 80 BTDC injection timing, Lowest Normalised Value (LNV) of IMEP are higher than 80 % for all fuels except in gasoline without spark-assisted ignition. This means that complete combustions took place for all fuels but poor combustion occurred at least one cycle in pure CAI gasoline combustion.

### 4.3.2 Heat Release Analysis

In-cylinder pressure data was used to calculate combustion characteristics including heat release rate, mass fraction burned, flame development period and combustion duration. For the current study, the first law was applied for the heat release rate calculation as shown in equation 4.3 [90].

$$\frac{dQ}{d\theta} = \frac{\gamma}{\gamma-1} p \frac{dV}{d\theta} + \frac{1}{\gamma-1} V \frac{dp}{d\theta} \quad (4.3)$$

Where  $\gamma$  is the ratio of specific heats for both unburned and burned gas which varies with temperature. In the current study, the values were estimated by the slope of the log P-log V diagram, where V is the displacement volume of the cylinder at any crank angle and was calculated from the geometry of the engine and p is the in-cylinder pressure.

In-cylinder charge temperature is the most important factor affecting CAI combustion and calculated as follows. Starting from IVC, the average in-cylinder charge temperature at IVC is calculated using an equation of enthalpy balance [91].

$$T_{IVC} = \frac{c_{p,air}m_{air}T_{air} + c_{p,charge}m_{charge}T_{charge}}{c_{p,air}m_{air} + c_{p,charge}m_{charge}} \quad (4.4)$$

Where  $T_{IVC}$  = Temperature at IVC, K

$T_{air}$  = Temperature of air (175 °C), K

$T_{charge}$  = Temperature of charge, K

$c_{p,air}$  = Specific heat of air,  $J.mol^{-1}.K^{-1}$

$c_{p,charge}$  = Specific heat of charge,  $J.mol^{-1}.K^{-1}$

$m_{air}$  = Mass of air, kg

$m_{charge}$  = Mass of charge, kg

In Equation (4.4), charge means fresh fuel and trapped residual gas during the NVO period. In-cylinder temperatures after IVC until the start of combustion are then calculated by polytropic compression as shown by Equation 4. 5.

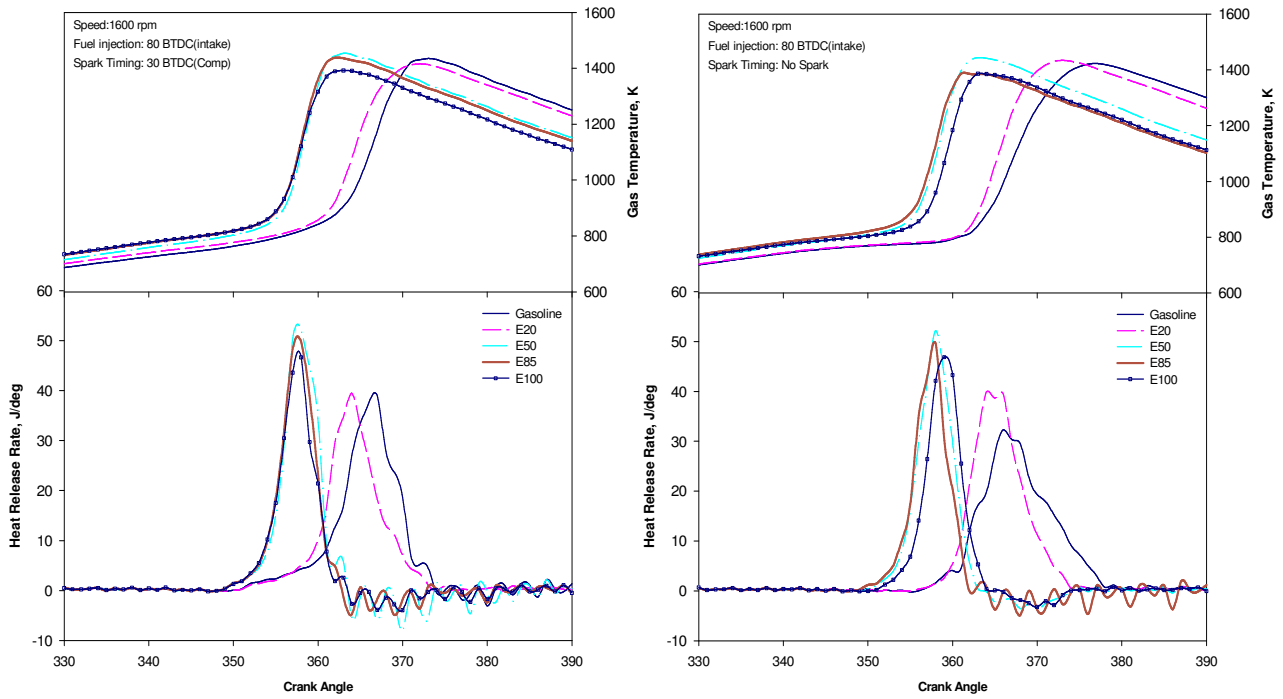
$$T_2 = T_1 \left( \frac{V_1}{V_2} \right)^{(n-1)}, \quad T_2 = T_{IVC} \left( \frac{V_{IVC}}{V_2} \right)^{(n-1)} \quad (4.5)$$

After the start of combustion, the average in-cylinder gas temperature was assumed to follow the equation of state of an ideal gas shown by Equation 4.6.

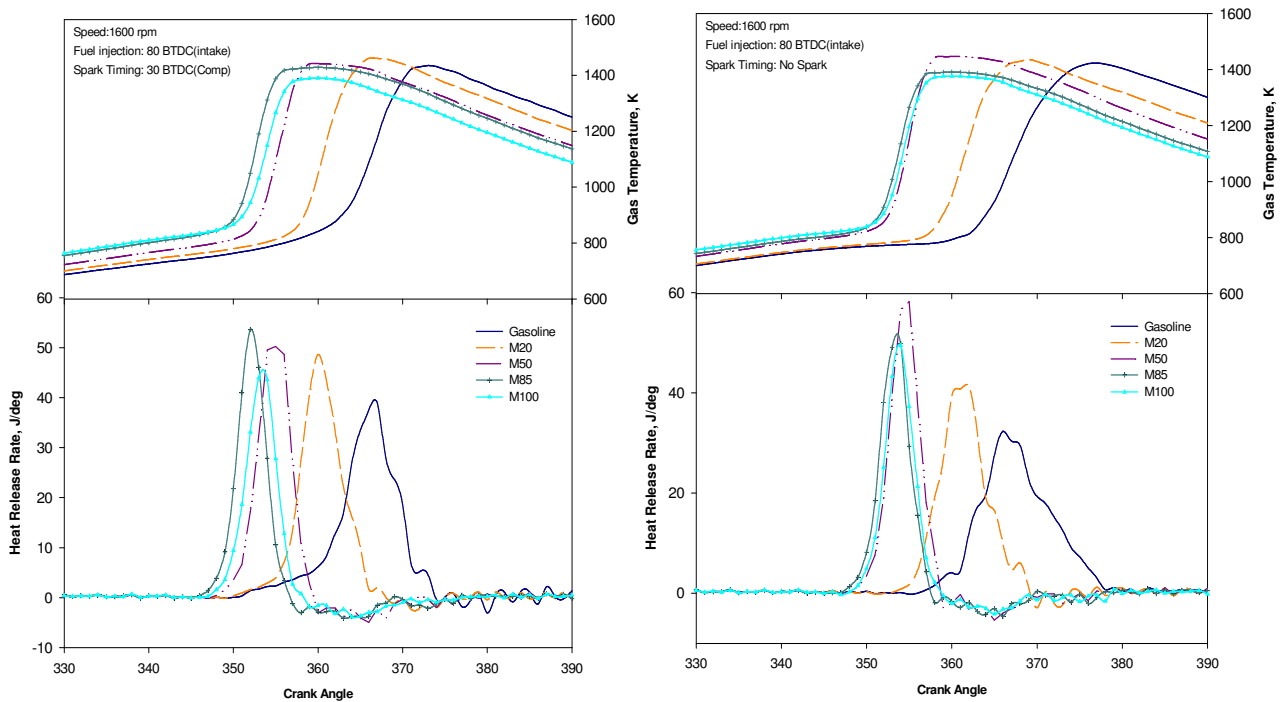
$$PV = n\tilde{R}T \quad (4.6)$$

Where  $n$  = Number of moles

## Heat Release Rate



## Gasoline and Ethanol Blended Fuels



## Gasoline and Methanol Blended Fuels

(a) Spark-assisted ignition

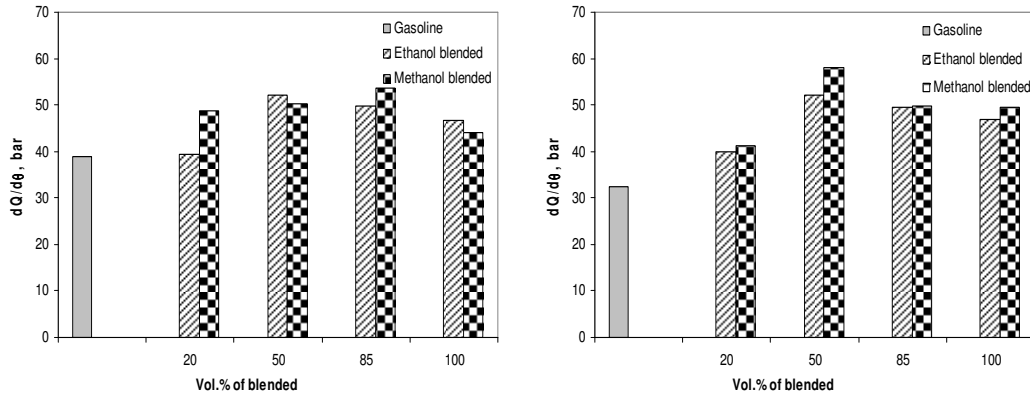
(b) Non-spark-assisted ignition

Figure 4.15 Heat Release Rate Curves and Average In-Cylinder Gas Temperature

As shown in Figure 4.15, in the absence of spark gasoline fuel exhibited a first stage slow heat release followed by a more rapid heat release as reported previously [76] whilst methanol and ethanol had only single-stage ignition [77, 78]. Auto-ignition of alcohol fuels commenced earlier, in particular for methanol. Due to their higher RON/MON number, alcohol fuels are expected to exhibit higher resistance to auto-ignition than that of gasoline. However, the results from the current and previous study [28, 39] show that alcohol fuels are more ignitable under high residual/high temperature condition. Therefore RON/MON are sometimes not a good indication of auto-ignition resistance under high residual conditions and high charge temperature in CAI combustion as the previous study noted [30, 92].

As discussed in the previous section [Figure 4.4], one possible reason is the production of intermediate species associated with fuel reforming reactions during the NVO period. However, the most direct evidence of fuel reforming reactions is shown by the elevated charge temperatures of alcohol fuels in Figure 4.15. The higher the charge temperature the earlier the auto-ignition. Therefore, it can be concluded that injection of alcohol fuels into hot residual gas produced more heat release reactions and higher residual temperature and hence advanced auto-ignition.

In the presence of spark, there was a significant delay between the spark timing at 30 CA BTDC and the first noticeable heat release. The M85, M100 and M50 had the shortest ignition delay, followed by E100, E85 and E50 which had identical delays, then M20 and E20 with gasoline fuel having the longest ignition delay. Comparison of spark-assisted heat release in Figure 4.15a and pure CAI combustion in Figure 4.15b shows that the presence of spark had a marginal effect in advancing the combustion process of alcohol fuels but a significant effect with gasoline.



(a) Spark-assisted ignition

(b) Non-spark-assisted ignition

**Figure 4.16 Maximum of  $\frac{dQ}{d\theta}$  for all of Fuels**

As shown in Figure 4.16, the heat release rate of alcohol fuels increased more rapidly than that of gasoline and the maximum value reached was increased when the percentage of alcohol was increased up to fifty percent.

Interestingly, negative heat release rates appeared during the late stages of combustion for methanol and ethanol blended fuels. The heat loss was included in the one zone thermodynamic model used for this study. Thus, the negative rate appears to be a heat loss effect from heat transfer to the chamber wall. This is supported by Tsurushima's study [93], where because of the early ignition of alcohol blended fuels there is a longer time for heat transfer, and therefore more heat loss.

### Mass Fraction Burned and Combustion Period

The mass fraction burned is defined as the ratio of mass burned at any given crank angle over the sum of total mass burned. It can be estimated from the heat release rate by assuming that the heat release is proportional to mass burned as given by Equation 4.7.

$$\text{Mass Fraction Burned} = \frac{\sum_{i=\theta_s}^{\theta} \left( \frac{dQ}{d\theta} \right)_i}{\sum_{i=\theta_s}^{EC} \left( \frac{dQ}{d\theta} \right)_i} \quad (4.7)$$

$\theta_s$  = crank angle of start of combustion

EC = crank angle of end of combustion

$\theta$  = crank angle

From the mass fraction burned, flame development period and combustion duration are defined as the crank angle of 10% and 90 % mass fraction burned respectively.

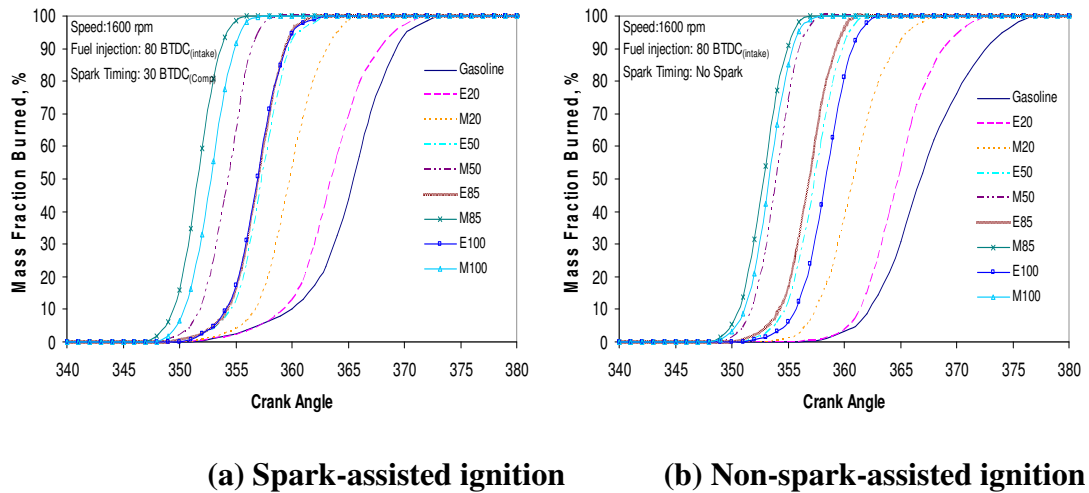
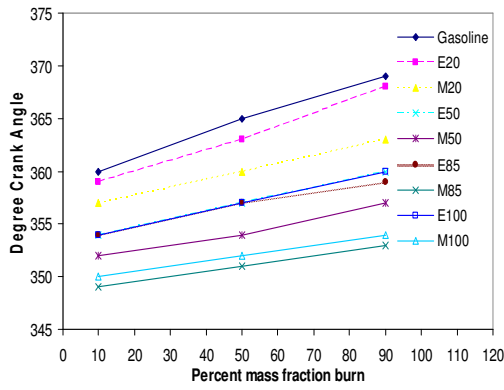
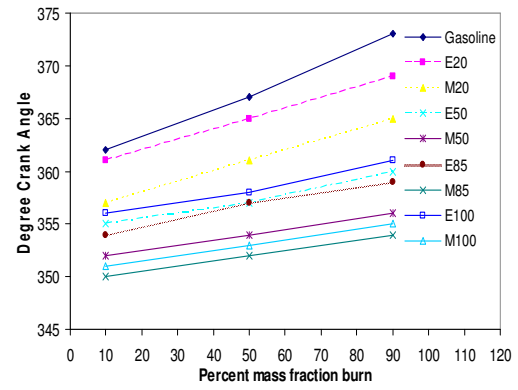


**Figure 4.17 Mass Fraction Burned**

The mass fraction curves in Figure 4.17 demonstrate the salient features of alcohol fuels heat release characteristics compared with the gasoline combustion; (i) auto-ignition occurred earlier with increased alcohol content due to heat release reaction in the NVO as quantified by Figure 4.18; (ii) the spark had much less effect on alcohol fuel than gasoline Figure 4.18 ; (iii) the alcohol fuels were characterised by much faster initial combustion than gasoline as shown quantitatively by Figure 4.19.

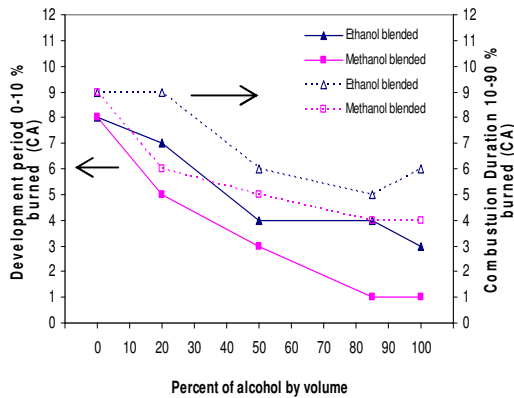


(a) Spark-assisted ignition

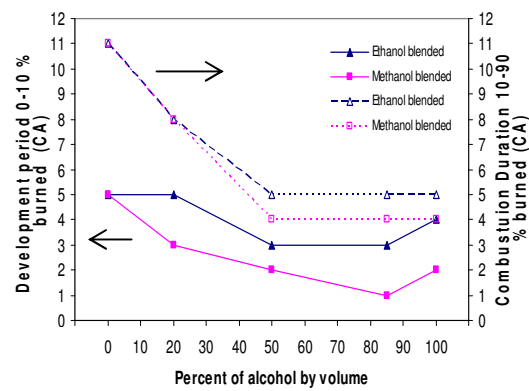


(b) Non-spark-assisted ignition

Figure 4.18 Crank Angle at Any Percentage of Mass Fraction Burned



(a) Spark-assisted ignition



(b) Non-spark-assisted ignition

Figure 4.19 Flame Development Period and Combustion Duration

Figure 4.19 shows that gasoline and 20% alcohol blended fuels exhibited longer flame development periods in the presence of spark discharge. However, the presence of spark did not affect the flame development period of alcohol blended fuel of 50% or more alcohol. Flame propagation played a major role in the spark-assisted combustion in the case of gasoline. Thus, with a diluted charge mixture and slow flame speed, the flame development period of gasoline required a long duration to reach 10% mass burned. Without spark-assisted combustion, multiple sites of the gasoline charge mixture achieved auto-ignition simultaneously with a short duration of initial heat release. In contrast to gasoline, auto-ignition combustion of alcohol blends dominated the heat release process irrespective of spark.

### 4.3.3 Engine-Out Exhaust Emission

#### Carbon Monoxide

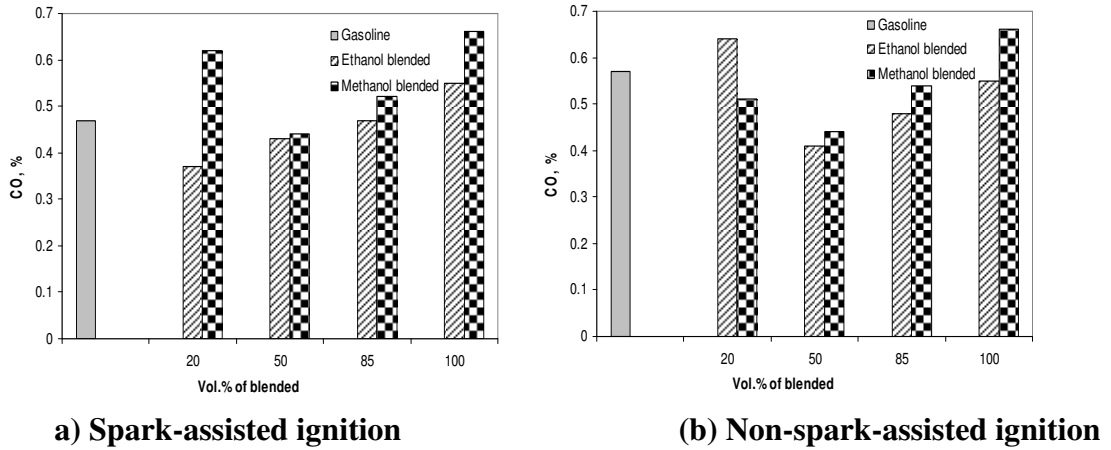
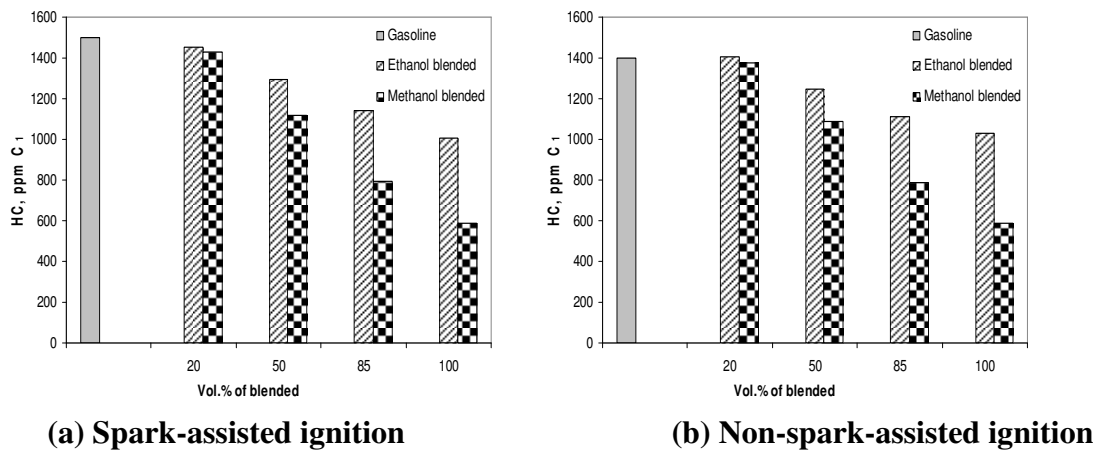


Figure 4.20 Carbon Monoxide Emissions of All Fuels

Air/fuel ratios primarily control carbon monoxide levels from internal combustion engines. From stoichiometric to lean mixtures, combustion produces low carbon monoxide because the fuel is oxidized with sufficient oxygen. In all test conditions, the air/fuel equivalence ratios measured at the exhaust port were fixed at stoichiometric, so the levels of CO observed were less than 0.7 %. In combination with the oxygenated molecule, alcohol blended fuels produced a lower amount of carbon monoxide than gasoline, except for pure alcohol in which CO was oxidized to CO<sub>2</sub> at a slower rate due to lower temperature during the exhaust stroke as Figure 4.24 shows. This lower exhaust temperature was the cause for higher CO concentration of methanol over ethanol fuels.

## Hydrocarbon



**Figure 4.21 Hydrocarbon Emissions of All fuels**

Currently, hydrocarbon emission is a major unsolved drawback for CAI combustion. Figure 4.21 shows that these emissions were nearly the same for spark and no spark-assisted ignition conditions and decreased when the percentage of alcohol increased, especially in the case of methanol. In general, 50-65 % of THC emissions is unburned hydrocarbon [94], typically species C<sub>5</sub> and above. In particular, the ratio of higher molecular weight (C<sub>6</sub>-C<sub>12</sub>) to THC of hydrocarbon emission in CAI combustion is higher than that of SI engine [95]. Those heavier hydrocarbons which have low volatility are absorbed and desorbed from oil film, crevices and deposits during the compression and expansion stroke consequently. The major portions of gasoline comprise of those heavier hydrocarbon while ethanol and methanol is a single-component fuel which has oxygen in their molecule. Because an oxygen atom is bond to carbon atom, HC analysers using a FID is less sensitive to those carbon atom [96].

Although alcohol fuel can reduce HC emissions, it promotes carbonyls compound in exhaust which are difficult to measure with typical exhaust gas analyser [96]. These carbonyls are oxygenates, odorants and irritants, so should be considered when using alcohol fuels.

## Oxides of Nitrogen

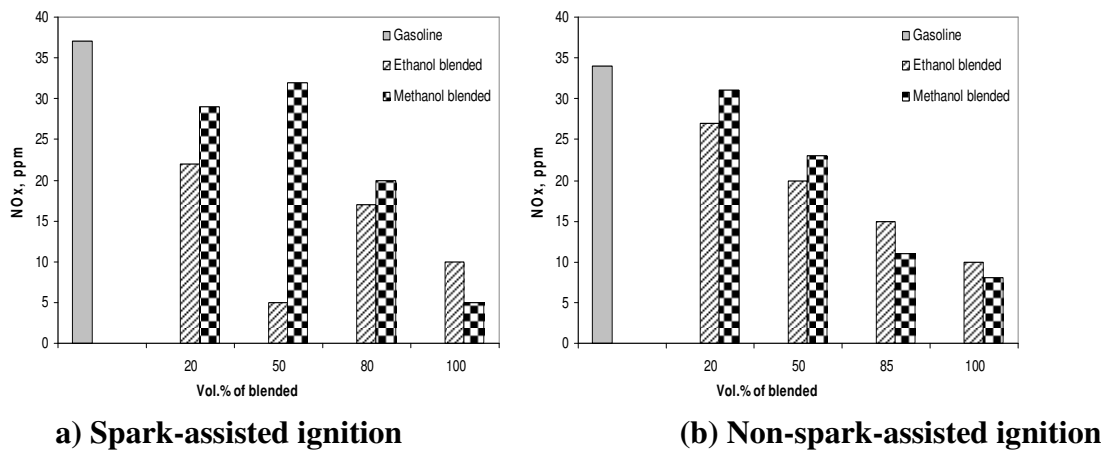


**Figure 4.22 Oxide of Nitrogen Emission of All fuels**

CAI combustion is known for its ultra-low NO<sub>x</sub> emissions as shown in Figure 4.22. Additionally, a lower amount of nitric oxide was emitted when the percentage of alcohol increased, particularly ethanol. A major source of nitric oxide is from oxidation of nitrogen from the atmosphere. Because of the oxygen in the molecule of alcohol fuels, these fuels employ less air to combust at stoichiometric when compared with gasoline. As the result, less nitrogen was introduced into the cylinder for oxidizing in the combustion process.

Fundamentally, the chemical kinetic mechanism of NO<sub>x</sub> formation intimately depends upon gas temperature during the combustion and early part of the expansion stroke. As shown in Figure 4.15, gas temperatures were lower during combustion and the exhaust stroke of ethanol and methanol fuels because of their lower flame temperature. Combined with this effect, extremely low NO<sub>x</sub> concentration was detected with alcohol fuels.

## Oxygen

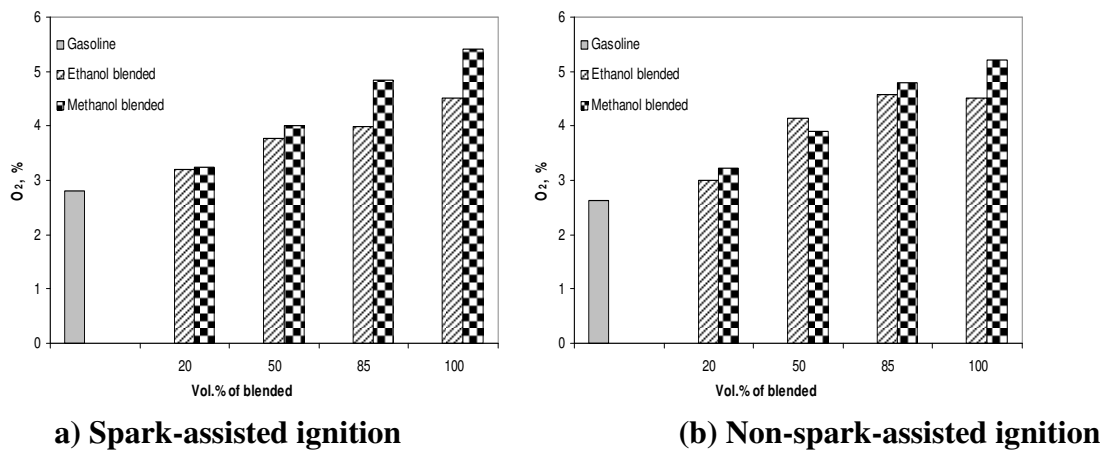


**Figure 4.23 Oxygen of all fuels**

Oxygen is one of the atoms that alcohol molecules consist of. So it is reasonable that as the volume of alcohol increased in the blended fuel, the oxygen concentration increased in the exhaust gas. This higher amount of oxygen for alcohol blended fuel confirms that sufficient  $O_2$  for alcohol combustion results in less hydrocarbon and carbon monoxide emissions.

## Exhaust Gas Temperature

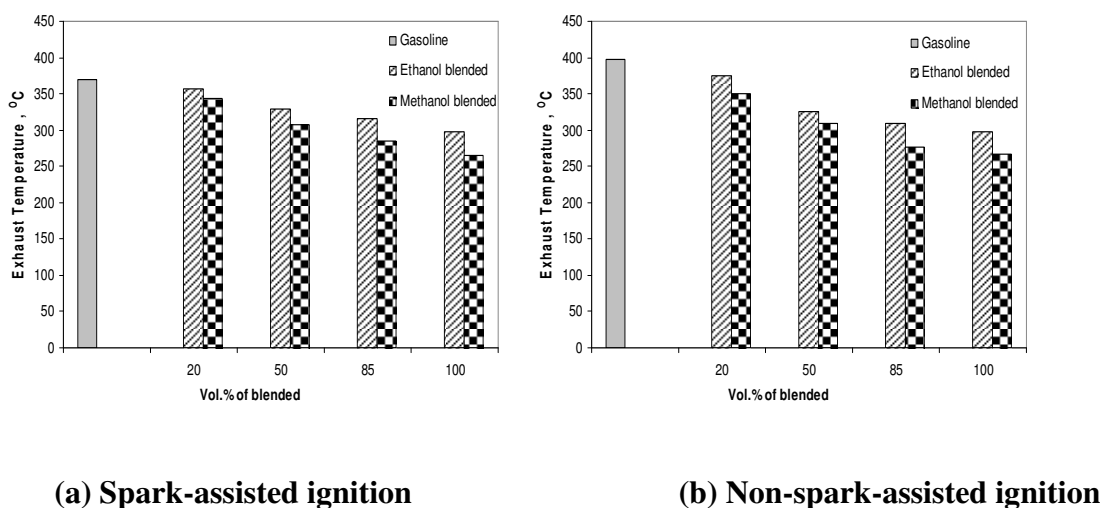


**Figure 4.24 Exhaust Gas Temperatures of All Fuels**

Figure 4.24 shows exhaust gas temperature which was measured at the exhaust port. Increasing volume of alcohol reduced exhaust gas temperature in particular for methanol fuel. There are two reasons responsible for this. Firstly, this is due to heat

transfer to the chamber wall. Since the combustion of alcohol blended fuels occurs early before TDC, there is much more time for heat transfer from the gas to the chamber wall resulting in reduced exhaust gas temperature. Secondly, the maximum burnt gas temperatures of alcohol blended fuels, shown in Figure 4.15, are lower than that of gasoline.

#### 4.3.4 Effects of Injection Timing

Limited by misfire and unstable combustion, some experiments could not be completed at the other injection timings tested. Table 4.1 summaries the accomplished tests conducted at all four injection timings at the same engine operating conditions.

**Table 4.1 Completion experiments of Parametric Test Conditions**

Fuel	80 BTDC		40 ATDC		80 ATDC		200 ATD	
	Spark	NO	Spark	NO	Spark	NO	Spark	NO
<b>Gasoline</b>	√	√	√	√	√	√	√	⊗
<b>E20</b>	√	√	√	√	√	√	√	⊗
<b>M20</b>	√	√	√	√	√	√	√	⊗
<b>E50</b>	√	√	√	√	√	√	√	⊗
<b>M50</b>	√	√	√	√	√	√	√	⊗
<b>E85</b>	√	√	√	√	√	√	√	⊗
<b>M85</b>	√	√	√	⊗	⊗	⊗	⊗	⊗
<b>Ethanol</b>	√	√	√	⊗	√	⊗	⊗	⊗
<b>Methanol</b>	√	√	⊗	⊗	⊗	⊗	⊗	⊗

TDC means TDC of exhaust/intake stroke.

Spark means spark-assisted ignition.

NO means pure CAI combustion.

√ means complete experiment.

⊗ means incomplete experiment.

After injection timing was retarded to 40 degree ATDC during the intake stroke, pure CAI combustion could not be achieved by neat alcohol whereas ethanol combustion could take place with the aid of spark discharge. When injection timing was further delayed to 80 degree ATDC, M85 could not achieve complete combustion even with the assistance of spark discharge. Finally, with the injection timing of 200 degree ATDC, pure CAI combustion could not be achieved for any of the fuels. The difficulty of alcohol fuels to achieve pure CAI was due to their higher heat of vaporization. In particular, methanol required more heat for liquid fuel evaporation. Therefore, the temperature was reduced below the attainable CAI temperature. In addition, the fuel reforming process was absent with injection during the intake and compression stroke. For the injection timing of 200 degree ATDC, the charge cooling effect was most significant after the intake valve closure.

The results obtained such as Pmax, crank angles at 10%, 50% and 90%MFB etc are presented in Table 4.2-4.4. The other results are shown in Appendix A, B and C for injection timing of 40, 80 and 200 degree ATDC respectively.

As Table 4.2 shows, the combustion characteristics of gasoline were very similar among the first three injection timings. Injection during the compression stroke resulted in later (10% MFB), slower (50%MFB), longer (10-90% MFB), less stable ( $COV_{IMEP}$ ) combustion and LNV of IMEP is lower than 80%. Poor combustion occurred on at least one cycle. As a result, higher CO and HC emissions were measured. The presence of spark in all cases brought forward the combustion event and enabled combustion with late injection.

In the case of E50/M50, the spark enabled combustion to take place with the late injection at 200 ATDC but did not affect other cases. Injection during the NVO period brought forward the combustion but produced the same combustion duration and similar emissions output to those at 40° and 80° CA ATDC injection timing. However, the advanced combustion led to lower IMEP, higher  $COV_{IMEP}$ .

**Table 4.2 Effect of Injection Timing on CAI Combustion with Gasoline**

	Spark-assisted ignition				No spark-assisted ignition			
	80 BTDC	40 ATD C	80 ATD C	200 ATD C	80 BTDC	40 ATD C	80 ATD C	200 ATD C
P <sub>max</sub> (bar)	28.30	29.35	27.56	20.92	26.27	25.10	25.05	
θ <sub>P<sub>max</sub></sub> (CA)	371	369	371	374	373	375	374	
$(\frac{dP}{d\theta})_{\max}$ (bar/CA)	1.66	2.48	1.57	0.48	1.42	1.53	1.45	
COV <sub>P<sub>max</sub></sub> (%)	6.34	3.42	6.13	15.94	11.30	8.83	7.48	
IMEP (bar)	2.37	2.25	2.21	1.91	2.50	2.40	2.26	
COV <sub>IMEP</sub> (%)	5.37	4.54	4.71	9.61	6.76	4.18	5.77	
LN <sub>V</sub> of IMEP (%)	86.56	89.66	87.30	40.30	78.59	89.50	86.00	
$(\frac{dQ}{d\theta})_{\max}$ (J/CA)	38.90	52.10	35.93	18.68	32.32	38.12	34.81	
10%MFB(°CA)	360	361	359	361	362	366	364	
50%MFB(°CA)	365	364	365	369	367	370	368	
90%MFB(°CA)	369	367	369	377	373	374	373	
10-50%MFB	5	3	6	8	5	4	4	
50-90%MFB	4	3	4	8	6	4	5	
10-90%MFB	9	6	10	16	11	8	9	
CO (%)	0.47	0.89	1.75	2.12	0.57	0.9	0.33	
HC (ppm)	1501	2294	2204	2642	1401	1969	1706	
NO <sub>x</sub> (ppm)	37	18	33	13	34	50	42	

**Table 4.3 Effect of Injection Timing on CAI Combustion with E50**

	Spark-assisted ignition				No spark-assisted ignition			
	80 BTDC	40 ATDC	80 ATDC	200 ATDC	80 BTDC	40 ATDC	80 ATDC	200 ATDC
P <sub>max</sub> (bar)	30.90	29.70	28.35	22.35	30.30	27.66	25.79	
$\theta_{P_{max}}$ (CA)	364	369	370	373	363	372	373	
$(\frac{dP}{d\theta})_{max}$ (bar/CA)	2.86	2.46	1.92	0.81	2.86	2.15	1.48	
COV <sub>P<sub>max</sub></sub> (%)	3.30	4.60	4.32	12.17	2.52	6.18	6.67	
IMEP (bar)	1.87	2.22	2.30	1.83	1.78	2.36	2.31	
COV <sub>IMEP</sub> (%)	7.58	4.54	4.63	8.01	7.63	4.42	4.21	
LN <sub>V</sub> of IMEP (%)	80.81	86.23	89.22	62.11	81.00	86.57	84.47	
$(\frac{dQ}{d\theta})_{max}$ (J/CA)	52.24	50.15	41.22	20.25	52.18	46.18	34.76	
10%MFB(°CA)	354	360	361	361	355	363	364	
50%MFB(°CA)	357	363	365	367	357	366	368	
90%MFB(°CA)	360	367	368	373	360	370	372	
10-50%MFB	3	3	4	6	2	3	4	
50-90%MFB	3	4	3	6	3	4	4	
10-90%MFB	6	7	7	12	5	7	8	
CO (%)	0.43	0.36	0.22	1.28	0.41	0.56	0.18	
HC (ppm)	1295	1868	1723	2162	1246	1700	1648	
NO <sub>x</sub> (ppm)	5	24	25	-	20	26	23	

**Table 4.4 Effect of Injection Timing on CAI Combustion with M50**

	Spark-assisted ignition				No spark-assisted ignition			
	80 BTDC	40 ATDC	80 ATDC	200 ATDC	80 BTDC	40 ATDC	80 ATDC	200 ATDC
P <sub>max</sub> (bar)	30.55	31.19	28.92	22.06	30.52	28.64	28.42	
θ <sub>P<sub>max</sub></sub> (CA)	360	367	369	371	359	371	370	
( $\frac{dP}{d\theta}$ ) <sub>max</sub> (bar/CA)	2.85	3.05	2.06	0.71	3.27	2.16	2.40	
COV <sub>P<sub>max</sub></sub> (%)	3.39	3.56	4.45	16.78	3.60	5.64	4.33	
IMEP (bar)	1.63	2.26	2.20	1.83	1.60	2.38	2.24	
COV <sub>IMEP</sub> (%)	8.80	4.35	4.32	11.29	9.18	5.12	4.58	
LNV of IMEP (%)	83.63	88.76	89.17	20.24	81.78	86.39	89.56	
( $\frac{dQ}{d\theta}$ ) <sub>max</sub> (J/CA)	50.28	60.36	42.75	16.73	58.15	45.63	50.38	
10%MFB(°CA)	352	360	360	360	352	362	361	
50%MFB(°CA)	354	362	363	366	354	365	364	
90%MFB(°CA)	357	365	367	375	356	369	368	
10-50%MFB	2	2	3	6	2	3	3	
50-90%MFB	3	3	4	9	2	4	4	
10-90%MFB	5	5	7	15	4	7	7	
CO (%)	0.44	0.23	0.20	1.25	0.44	0.22	0.16	
HC (ppm)	1120	1645	1514	1870	1086	1434	1382	
NO <sub>x</sub> (ppm)	32	30	24	-	23	44	24	

#### 4.4 Summary

Thermodynamic engine tests were carried out in the current study to investigate the effect of alcohol blended fuels on CAI combustion and emissions. It was shown that both methanol and ethanol could achieve CAI combustion. In particular, methanol was found to be able to auto-ignite earlier than gasoline and burn faster at a higher heat release rate. However, the effect of advancing and accelerating the combustion

decreased rapidly after the percentage of alcohol blended fuels exceeded 50 % due to lower energy supplied by higher percentage alcohol. In addition, alcohol blended fuels were found to produce less HC, NO<sub>x</sub> and CO than gasoline.

Due to the lower burned gas temperature, larger amount of trapped gases for alcohol blended fuels were retained in the cylinder during the NVO period. Although the auto-ignition temperature and heat of vaporization of alcohol are higher than those of gasoline, the charge heating effect from larger quantities of residual lead to increase charge temperature. The most significant finding is the presence of heat release reactions during the NVO period which was the main cause for the advanced combustion phasing of alcohol fuels. As a consequence, alcohol blended fuels were able to achieve auto-ignition earlier than gasoline when fuel was injected during the NVO period. As alcohol content increased beyond 50% the combustion became retarded and slower because of the greater dilution effect of more trapped residuals.

The effects of spark discharge and injection timing were also investigated. With gasoline combustion, spark ignition assisted in advancing combustion whereas injection timing had a larger effect on combustion phasing with alcohol fuels. The thermal/chemical effect from injecting fuel into hot trapped residual gas to accelerate combustion was noticed. In the mean time, charge cooling effect associated with injection timing during the intake stroke was observed as to retard the combustion. However, the late injection during the compression stroke had the largest charge cooling effect and hence no CAI combustion could be achieved for all fuels with the late injection. Fuel reforming process from injecting fuel at the re-compression stroke was more produced than that of gasoline. Therefore, in order to better understand the fuel reforming process and to complete the test with neat alcohol, the next two chapters will focus on the experiment where the injection timing was fixed to take place during the negative valve overlap period.

## **Chapter 5 In-Cylinder Combustion Studies through Chemiluminescence Imaging**

### **5.1 Introduction**

Imaging techniques are powerful tools to capture combustion phenomena occurring in internal combustion engines. Many approaches have been employed to obtain adequate images, including laser illumination and doped fuels. In comparison, imaging of chemiluminescence emission from chemical reactions provides a simple and effective means to observe auto-ignition and combustion processes under realistic operating conditions. Moreover, due to the specific wavelengths of the chemiluminescence from each molecule, it can be used to identify the species present and therefore the occurrence of the reactions concerned.

After acquiring preliminary results from thermodynamic engine tests, chemiluminescence imaging was applied to some selected conditions. These included one injection timing, with and without spark-assisted ignition for all nine blended fuels. Total chemiluminescence imaging was taken first to investigate the overall combustion phenomena. Subsequently, with appropriate band pass filters, chemiluminescence images of CHO and OH radicals were captured in order to identify the auto-ignition sites and high temperature combustion region. In addition, the images were used to specify the conditions for in-cylinder gas sampling experiments in the next section.

### **5.2 Test Methodology**

#### **5.2.1 Operating Conditions**

##### **Injection Timing**

From the results of the engine tests in Chapter 4, an injection timing of 80 degree BTDC was selected for chemiluminescence imaging. The results in Chapter 4 showed that all injection timings resulted in the same trend of combustion characteristics: oxygenated fuels up to 50 % blended alcohol were characterised with advanced and

accelerated combustion. However, only injection timing during the NVO period resulted in stable combustion with all nine fuels. Whereas pure methanol and ethanol as well as M85 could not achieve stable and complete combustion for the other injection timings of 40, 80 and 200 degree ATDC. The selected injection timing of 80 degree BTDC allowed the experimental tests to focus on the effect of fuels when they were injected directly into the hot residual gases.

### **Spark- and Non-Spark-Assisted Combustion**

As observed from the heat release rate and mass fraction burned in the previous chapter, spark discharge advanced the ignition of gasoline while having a lesser effect on alcohol blended fuels. In order to understand better the difference, chemiluminescence imaging was carried out on with/without spark-assisted combustion for all of nine fuels.

### **Chemiluminescence Imaging of Specific Species**

For this study, three sets of chemiluminescence images were acquired. All visible and UV wavelengths of emitted light, referred to as total chemiluminescence, were first captured through a special UV lens in which spectral transmittance is as high as 70 %, ranging from 220 nm to 900 nm and an image intensifier which has spectral response of 180-850 nm. These images comprised the emissions of excited intermediary chemical species such as OH, CH<sub>2</sub>O, CHO, CH and C<sub>2</sub> and products of CO<sub>2</sub>, CO and the stronger intensity of soot luminosity. With a vast variety of molecules present, flame structure could be identified from such images.

CAI combustion is strongly based on chemical kinetic reactions. Therefore, the chemiluminescence of specific molecules was captured in order to elucidate those reactions. The OH radical was selected to be studied because it is an important molecule for high temperature combustion. In addition, the chemiluminescence of the CHO radical was captured. The CHO radical was produced after exited formaldehyde (CH<sub>2</sub>O) formation, which is a major intermediate species formed in the auto-ignition process.

## 5.2.2 Experimental Procedure

After finishing the engine tests in Chapter 4, the metal piston was replaced by a piston with a transparent window. The high speed camera mounted together with an image intensifier was set to focus on the combustion chamber when the piston was adjusted to 30 degree BTDC. Due to the depth of field of the lens, when a cross marked on a paper was imaged from 40 to 0 degree BTDC, there was no distortion present. Hence, the quality of images acquired was the same throughout the combustion period.

The procedures for preparation and warm up are the same as with normal fired engine tests. Total chemiluminescence of gasoline combustion was the first imaged. In order to protect the intensifier, its gain value was gradually increased until the image quality was acceptable. To allow for quantitative comparisons, this gain value, 60 %, was used for all the fuels. Again, the steps to start the engine were followed as thermodynamic tests. After combustion was stable, the camera was triggered at the same time as the data acquisition system to simultaneously record images and in-cylinder pressure data. After finishing imaging, the engine was stopped running. The image file was then transferred from the camera to the PC. Subsequently, the next fuel to be tested was poured into the tank and the procedure repeated for all fuels until all tests were completed. However, before the start of testing of each new fuel, acetone was used to clean the piston window through the removed side window blanks.

Once total chemiluminescence imaging was completed, the engine was disassembled and prepared for the next set of chemiluminescence imaging. A lens of 60 mm focal length and f2.8 aperture, coupled with a 350 nm-wavelength bandpass filter, was substituted for the UV-lens for imaging CHO emissions. The gain intensity of 60 % was also used for this set of tests. Similarly, the procedure was repeated for the final set of tests, OH chemiluminescence imaging. Once more, the UV-lens was used, this time with a 310 nm filter for recording images outside the visible range. For the relatively low intensity of OH images, the gain value was increased to 90 %. This gain value was limited by the intensity of emission from gasoline combustion.

### 5.3 Results and Discussion

At an image resolution of 512 x 248 pixels, the camera recorded images at a speed of 10,000 frame/sec. Therefore, time-resolved images of less than one degree crank angle per image at an engine speed of 1600 rpm were acquired. Fifteen consecutive cycles were recorded for each test condition. From these cycles, one representative image for each point of interest was subjectively selected and the image enhanced by means of a MATLAB-based image processing routine. The selected images are based on the first visible light taking place at the crank angle in which most of cycle occurred. An average intensity and light area was calculated at each crank angle and presented together with the heat release rate and mass fraction burned plots. The average intensities were calculated for the pixels of combustion intensity above the background. Percentage of light area represents the ratio of the pixel which shows combustion and total pixels of combustion chamber as expressed in Equation 5.1.

$$\text{Light Area (\%)} = \frac{\text{Pixel of Combustion}}{\text{Total Pixel of Chamber}} \times 100 \quad (5.1)$$

In addition, probability images from the raw data of all 15 cycles were produced. Each pixel of probability image intensity was calculated by the number of cycles which intensity exceeded the threshold value as shown in Equation 5.2.

$$\text{Pixel of Probability Image Intensity} = \frac{N}{15} \times 100 \quad (5.2)$$

Where N = the number of cycles in which the pixel intensity exceeds the combustion threshold value.

Then, value in each pixel was converted to black and white probability image. Where pixels are black, chemiluminescence emission occurred repeatedly in this area and vice versa for white pixels. The probability images are displayed under the selected representative images for each same crank angle. For all Figures below, the crank angles were referred to after top dead centre in the intake stroke.

### 5.3.1 Total Chemiluminescence Images

#### 5.3.1.1 Spark-Assisted Ignition

##### Gasoline

Figure 5.1 shows the total chemiluminescence images and combustion characteristics of gasoline with spark-assisted ignition. The images at the top left hand side show the combustion emissions during the negative valve overlap period. Chemiluminescence is clearly shown in these images. During this re-compression process the charge temperature increased, further exacerbated by the hot residual gas present. Consequently, high temperature fuel reforming reactions took place after the injection of fuel and air mixture from the air-assisted injector as shown by previous modelling study of Cao et al [97]. However, such reactions did not produce sufficient heat to be detected from the in-cylinder pressure and subsequent heat release analysis as shown previously in Figure 4.4.

With spark initiation at 330 degree CA, the first visible image is seen around the centre of the combustion chamber at about 340 degree CA. With propagation from the centre, the flame occupies the whole combustion chamber by 360 degree CA. During this period, the heat release rate and mass fraction burned curves exhibit insignificant values but the area and intensity of the combustion images increase steadily. At the same time of flame travelling, auto-ignition is shown to take place on some local area which attained self-ignition temperature enhanced by expanding flame front and rising piston. Auto-ignition area near the wall can be seen on the top left hand side in the fourth image in Figure 5.1 at 355 CA. Flame propagation lasts for 20 crank angles, before it is overtaken by the sudden heat release from independent auto-ignition sites at 360 CA as shown by the 100% image intensity in Figure 5.1. During this period, the intensity of the image increases until reaching the maximum at 365 degree CA while the heat release rate starts to increase suddenly and reaches its maximum value at the same crank angle. Another significant feature visible is brighter spots in the images occurring from 355 degree CA. They were likely the lubricant being burned. The flame originated from the spark discharge agrees well with Persson et al [48] but is opposite to the results of Aleiferis et al [50] in which the reacting structures were

appeared near to the wall as pure CAI combustion. This could be caused by the low luminescence of lean-burn combustion near the spark plug in [50], which was not detected by the camera due to its low sensitivity.

Except for the crank angle for the maximum value, the timing of image intensity does not correspond with the heat release rate curve, such as the start of combustion and combustion duration. In addition, the timing of the mass fraction burned curve is delayed from the percentage of light area. The delay between the visible flame and detectable heat release rate has been observed for normal spark ignition combustion. However, the time delay seen in the current study is much greater and it is caused by the slower heat release reactions in the presence of large residual gases. There are two possible reasons for the discrepancy between HRR and chemiluminescence image: (i) The leakage from the piston ring in the optical engine is higher than production engine which can reduce the pressure rise and hence heat release registered by pressure measurement;(ii) It is known that chemiluminescence is a more sensitive technique to detect the combustion reactions which may not generate sufficient heat release.

The probability images illustrated in the bottom row show that most of the first visible signal commences at the centre of chamber, due to the spark discharge. Flame propagation plays the major role in combustion during the earlier period. Beyond 350 degree CA, however, some independent sites attain local spontaneous auto-ignition and the heat release rate experiences a sudden rise. At TDC, the combustion is dominated by the multiple auto-ignition heat release as shown by both the images and the heat release rate curve.

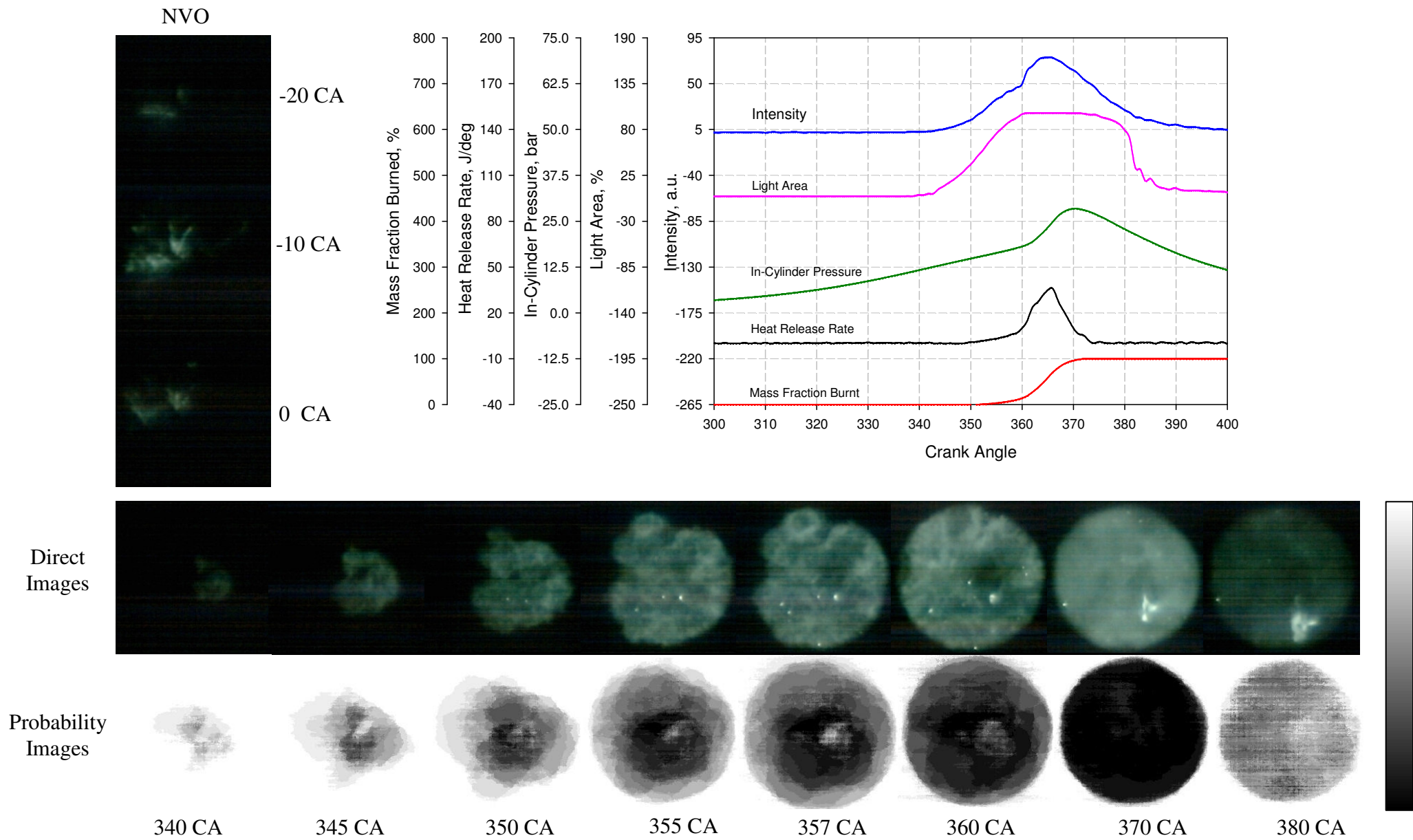


**Figure 5.1 Total Chemiluminescence Image of Gasoline with Spark-Assisted Ignition**

## Ethanol

The total chemiluminescence images of ethanol with spark discharge are shown in Figure 5.2. In contrast to gasoline, there is no chemiluminescence emission captured during the re-compression. However, the heat release curves and pressure curves in Figure 4.4 suggest that some heat release reactions have taken place but such reactions generated little chemiluminescence.

Due to the spark-assisted ignition, the first visible flame occurs at the centre of the combustion chamber and at nearly the same time as with gasoline at 340 degree CA. At 344 degree CA, another independent combustion site has appeared. Combustion rapidly spreads over the whole combustion chamber lasting only 6-10 degree crank angles, whereas gasoline combustion takes 20 degree CA. The corresponding image illustrates this with self-ignition of the mixture occurring at the bottom right hand side at 344 degree CA. Later, combustion luminosity still remains visible over the entire chamber for 15 degree CA. The images correspond well with higher and earlier heat release rate shown in the heat release curve. There are two reasons responsible for this faster burning combustion. Firstly, the higher flame speed properties of ethanol. More importantly, multiple regions attain self-ignition earlier and more readily than gasoline as a result of higher compression temperatures as explained from the previous section.

Like gasoline combustion, there is a long delay between the first appearance of chemiluminescence emission and the start of heat release. However, the time lag of ethanol combustion is shorter. The role of flame propagation for ethanol combustion is over taken at an earlier crank angle by spontaneous auto-ignition. Hence, simultaneous self ignition at multiple sites reduces the time delay between the rise of in-cylinder pressure and chemiluminescence signal.

Represented by the dark areas, the probability images show the influence of spark-assisted ignition which initiates combustion at the centre of chamber. Like gasoline combustion, flame propagation dominates the process during the early period. Shortly afterwards, auto-ignition consumes the remaining charge mixture resulting in the entire chamber contents combusting. Moreover, for most of the cycles, combustion

terminates around 370 degree CA which is sooner than that of gasoline. However, ethanol displays more cycle to cycle variation of auto-ignition timing than gasoline, illustrated by the brighter pixel area of the probability images.

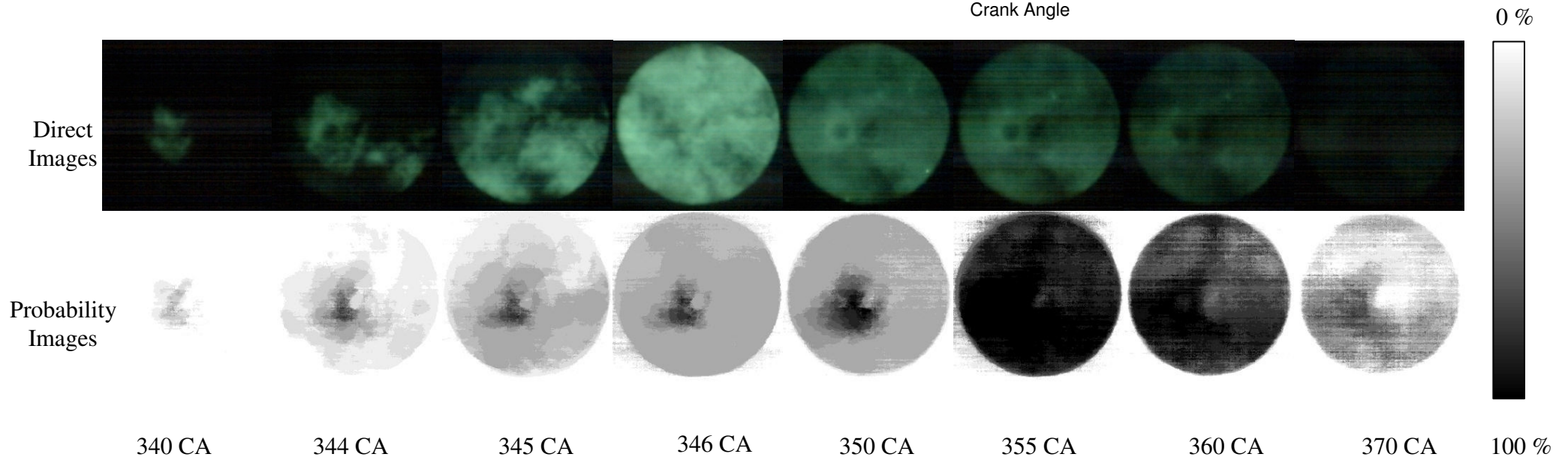
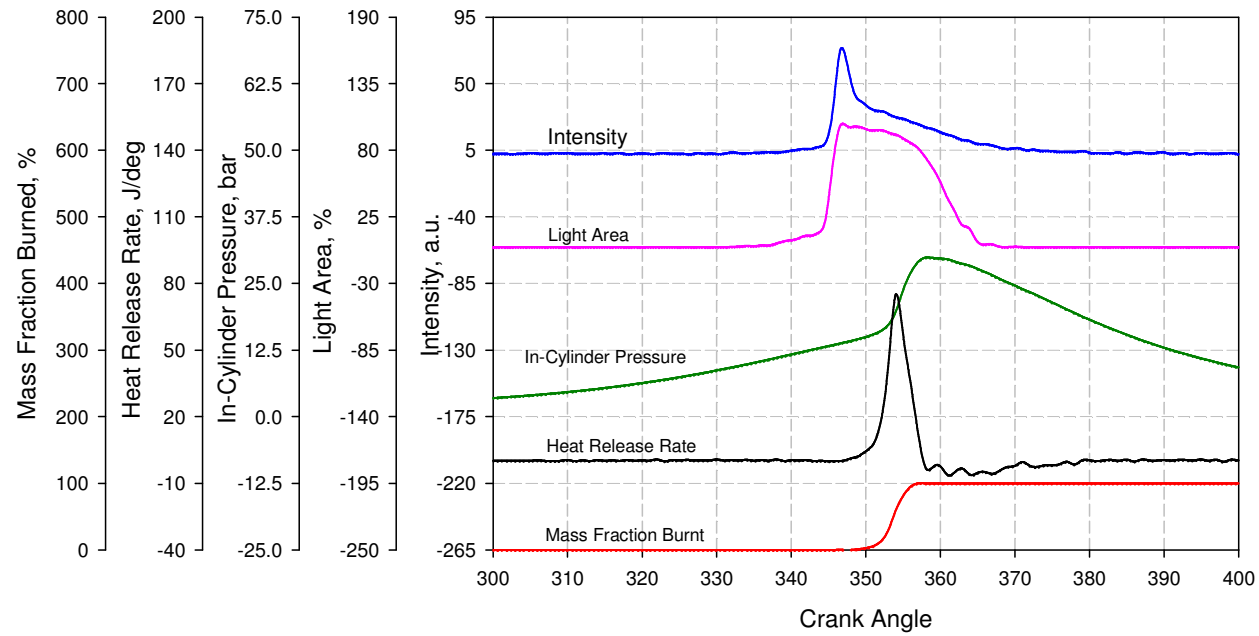


**Figure 5.2 Total Chemiluminescence Image of Ethanol with Spark-Assisted Ignition**

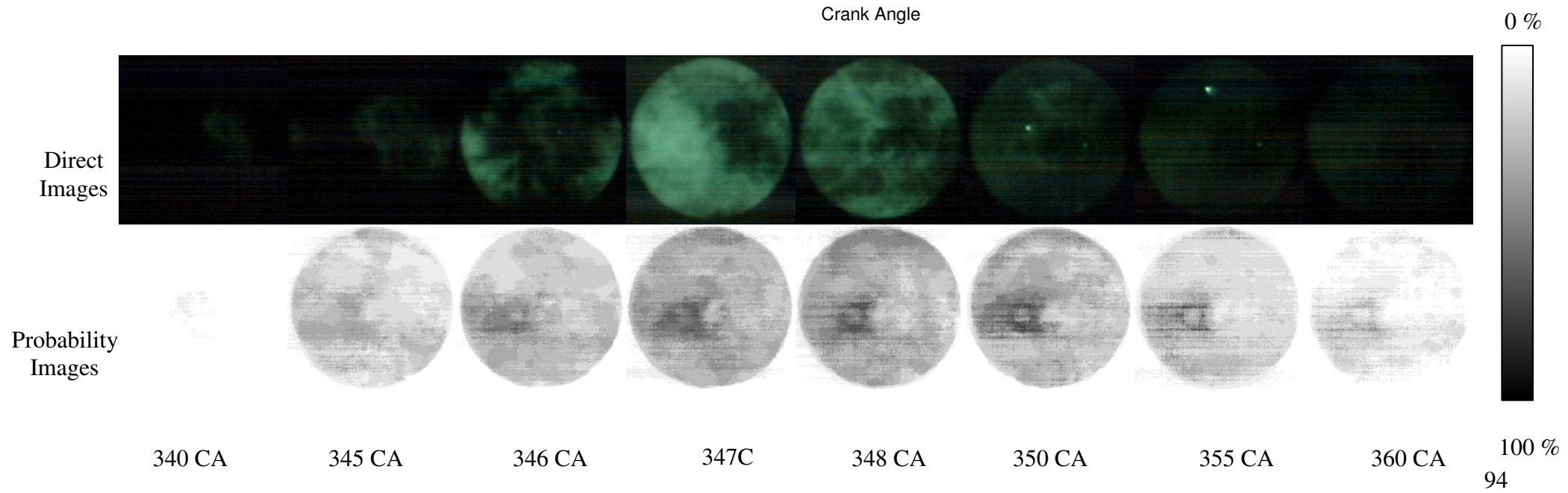
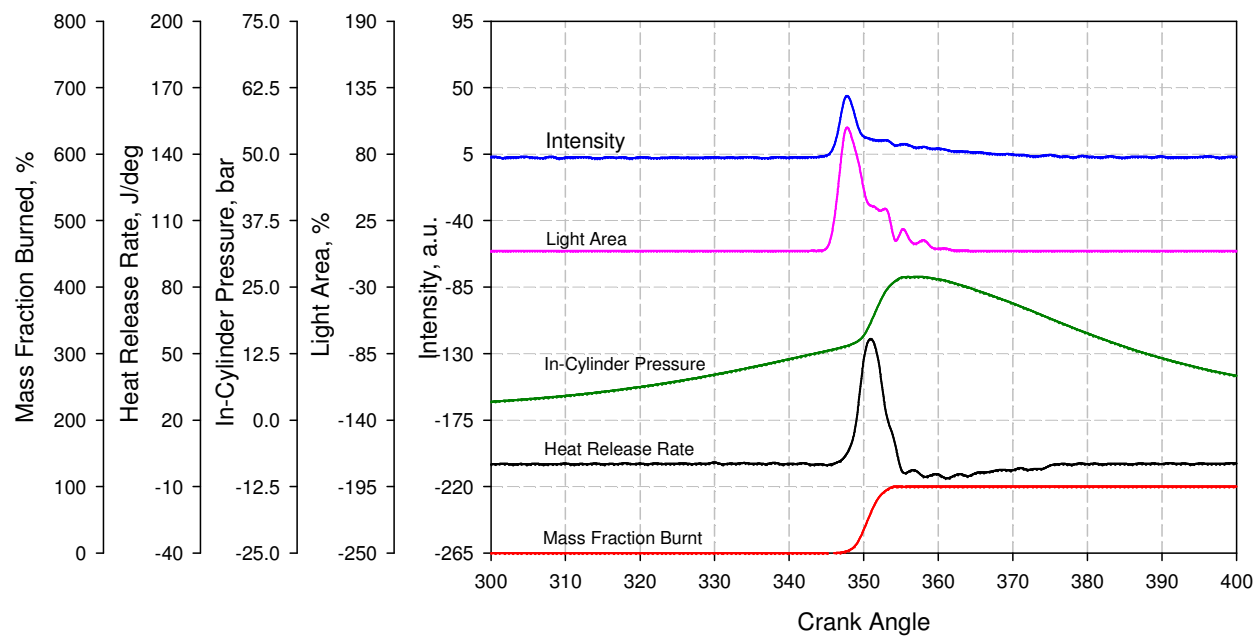
## Methanol

Figure 5.3 presents the total chemiluminescence images of methanol with spark-assisted ignition. Similar to ethanol, which has only single-stage ignition, no chemiluminescence is visible during the re-compression stroke even though the in-cylinder charge has the highest temperature of all three fuels during the compression stroke as shown in Figure 4.13.

Although at a relatively weaker intensity, methanol combustion originates near the centre of the combustion chamber at the same CA as gasoline and ethanol, of 340 degree CA. Subsequently, the flame rapidly spreads out from the centre to the outermost area, populating the whole chamber within 6-7 degree CA and prevailing for less than 10 degree CA. Meanwhile, many independent sites around the perimeter of the combustion chamber attain spontaneous auto-ignition shortly after the start of flame propagation as shown by image at 346 degree CA. Because of its highest laminar flame speed and in particular earlier simultaneous auto-ignition, methanol results in the shortest combustion duration of only 15-20 degree CA accompanied by the rapid increase in the light area shown in Figure 5.3.

Like the gasoline and ethanol fuels, the intensity and percentage of light area appear earlier than the heat release rate measured from the in-cylinder pressure. However, the time delay is of a very short period. As already discussed, spontaneous self ignition dominates shortly after spark-assisted ignition begins, reducing the time lag between light emission and heat release process. Of significant note, the maximum image intensity of methanol is much lower than both gasoline and ethanol fuels.

The dark area of probability image shows the influence of the spark discharge in initiating combustion at the center of the chamber. However, the effect of this spark assistance is overcome by auto-ignition at an early crank angle. Hence auto-ignition plays a more significant role than flame propagation in the combustion process when using methanol as a fuel. Also, the probability images verify the rapid combustion of methanol which, for most of the imaged cycles, terminates combustion before 360 degree CA. Auto-ignition sites exhibit significant distribution as shown by the probability images.



**Figure 5.3 Total Chemiluminescence Image of Methanol with Spark-Assisted Ignition**

### **Blended Fuels (E20, E50, E85, M20, M50 and M85)**

Figures 5.4 – 5.9 present total chemiluminescence images and combustion characteristic plots of blended fuels from 20 to 85 percent of alcohol by volume. With 20 – 50 % blended fuels, fuel reforming process produced detectable light emissions during the NVO period, because of the gasoline components. On the other hand, no sign of chemiluminescence emission is present when alcohol concentration is 85 %.

In the presence of spark discharge, the first visible image was captured at nearly 340 degree crank angle for all blended fuels. The percentage of blended alcohol does not show significant effect on ignition timing. However, oxygenated fuels strongly influence combustion speed where the flame propagates from the core to the periphery faster and spends a shorter time occupying the whole chamber as the volume of alcohol increases. This agrees well with the rapid heat release rate and short flame development period as discussed in Chapter 4. The higher flame speed properties of alcohol in conjunction with the readily occurring auto-ignition are responsible.

The probability images for all blended fuels show that the initial combustion started at the centre of the combustion chamber. There is no ignited charge around the periphery of the combustion chamber at the start of combustion. Comparing frame by frame for each fuel, gasoline probability image exhibits significantly more black pixel areas whilst brighter pixel areas increases with the percentage of blended alcohol. Alcohol fuels introduce more cyclic variation of combustion consistent with COV of IMEP as discussed in Chapter 4. At the end of combustion, less black pixels in the image supports the influence of alcohol in terms of advancing and speeding up the combustion process. For instance, oxidization reactions are visible more cycles at 380 degree CA whereas there are less cycles with combustion at 370 CA for ethanol and the least number of cycles for methanol at 360 CA.

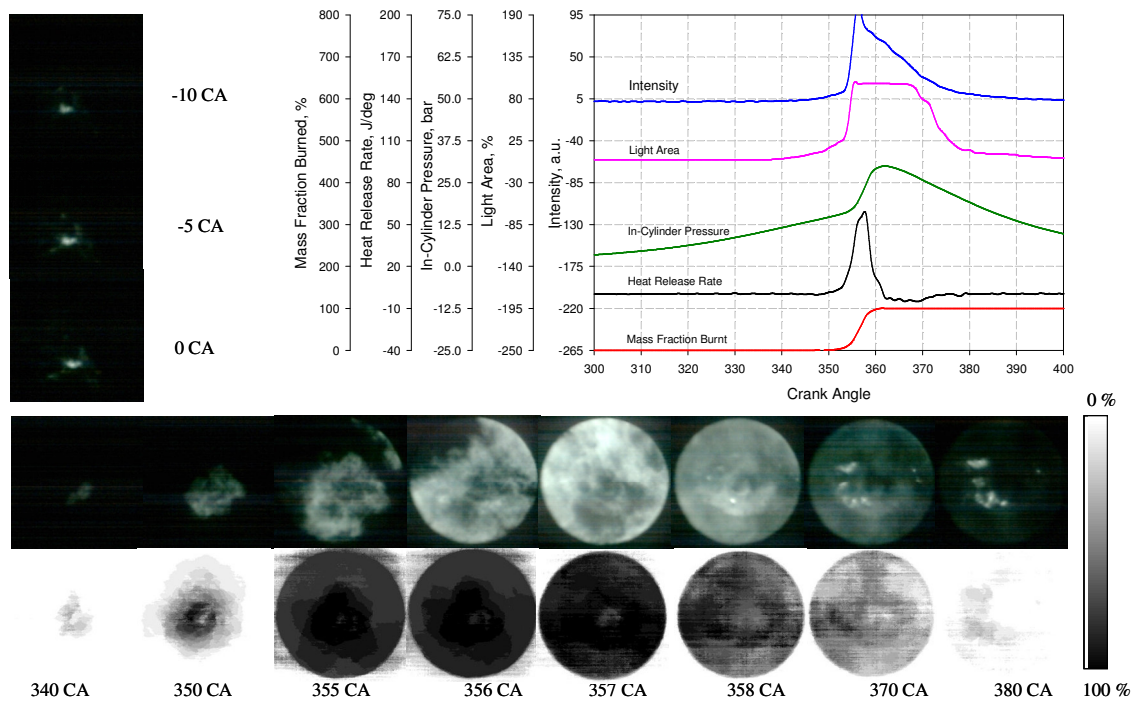


**Figure 5.4 Total Chemiluminescence Image of E20 with Spark-Assisted Ignition**

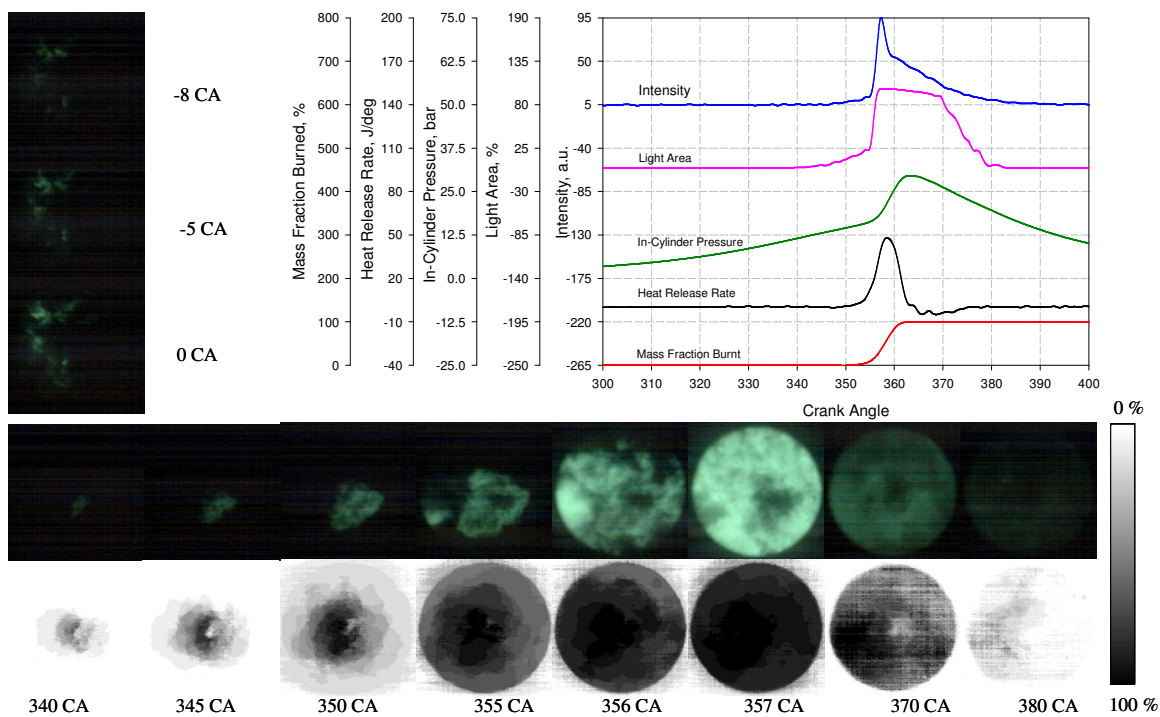


**Figure 5.5 Total Chemiluminescence Image of M20 with Spark-Assisted Ignition**

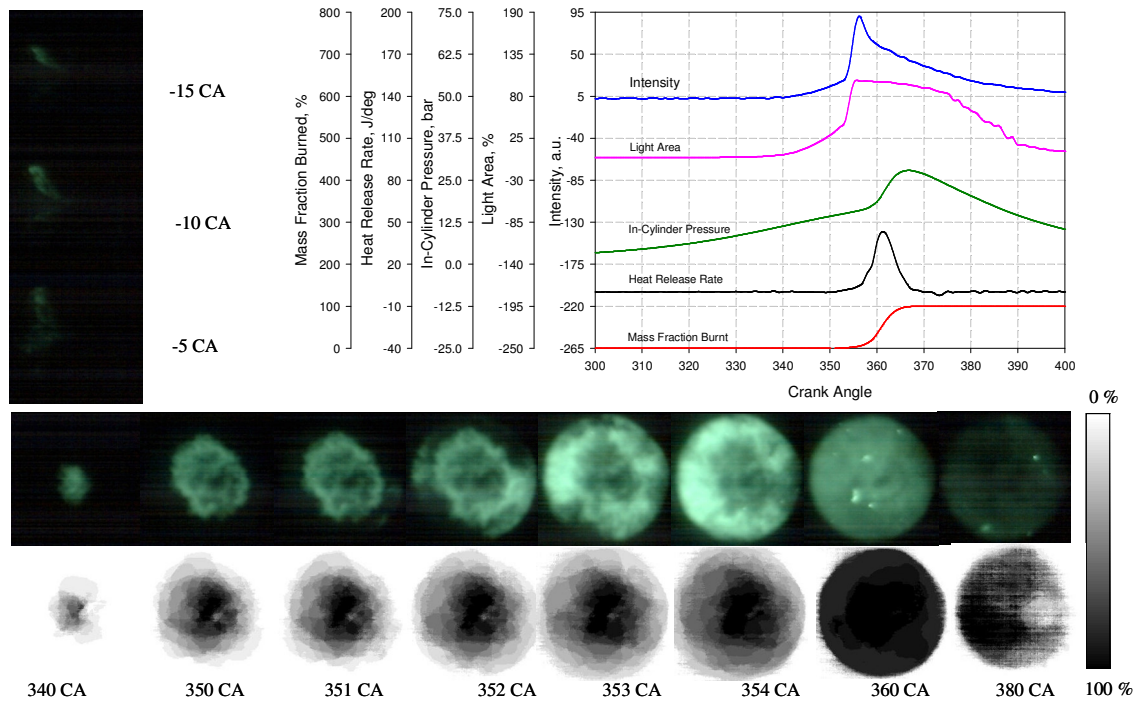


**Figure 5.6 Total Chemiluminescence Image of E50 with Spark-Assisted Ignition**

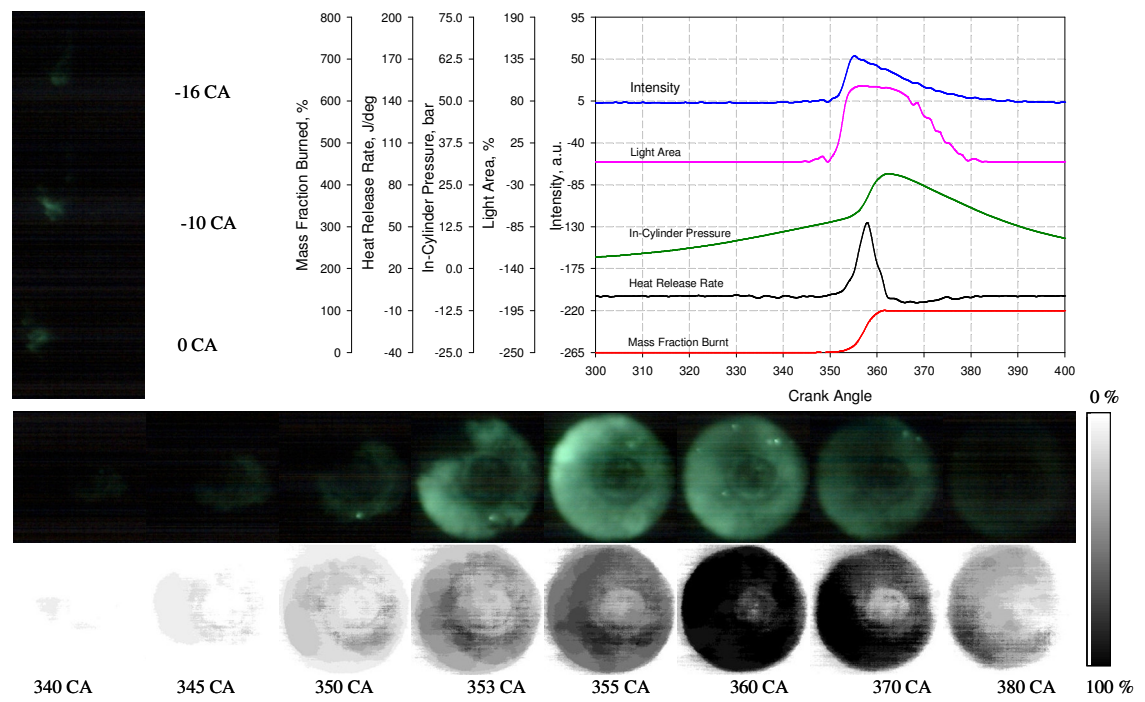


**Figure 5.7 Total Chemiluminescence Image of M50 with Spark-Assisted Ignition**

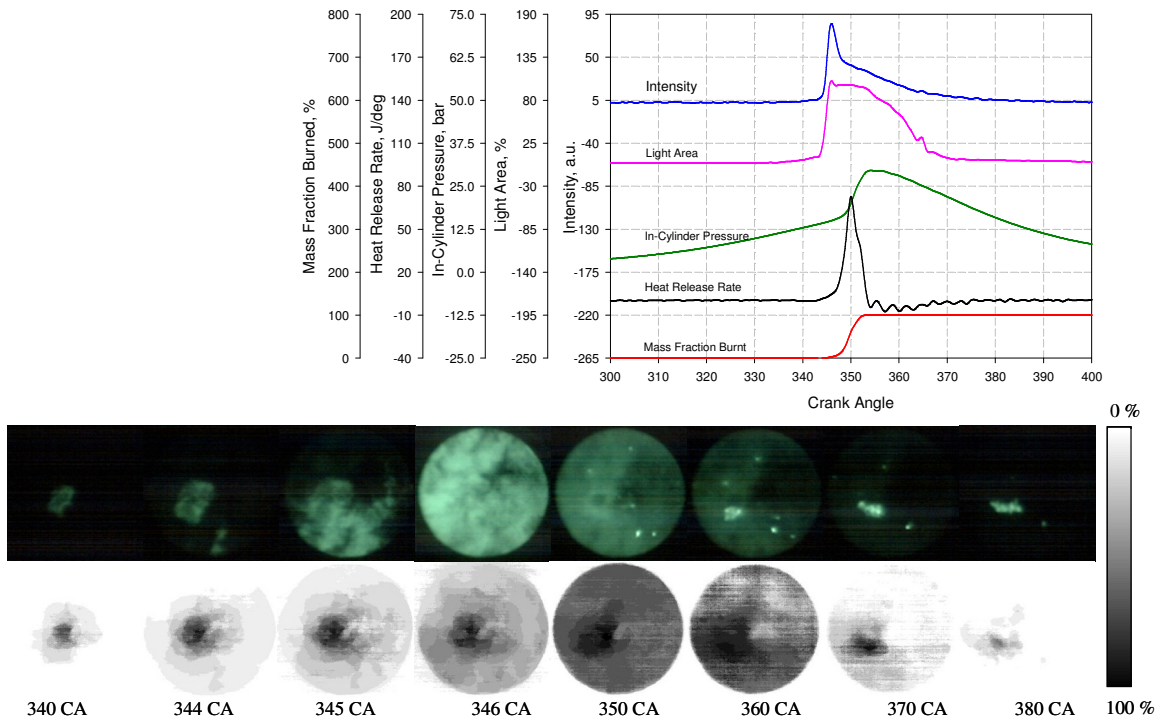


**Figure 5.8 Total Chemiluminescence Image of E85 with Spark-Assisted Ignition**

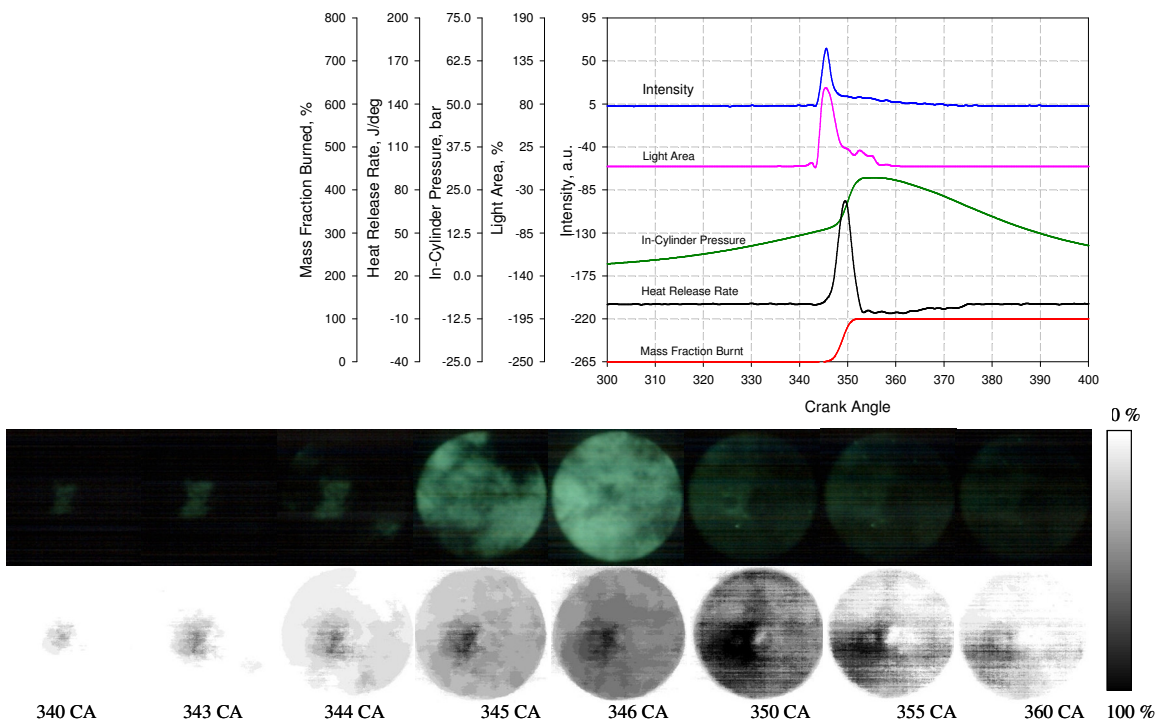


**Figure 5.9 Total Chemiluminescence Image of M85 with Spark-Assisted Ignition**

### 5.3.1.2 Non-Spark-Assisted Ignition

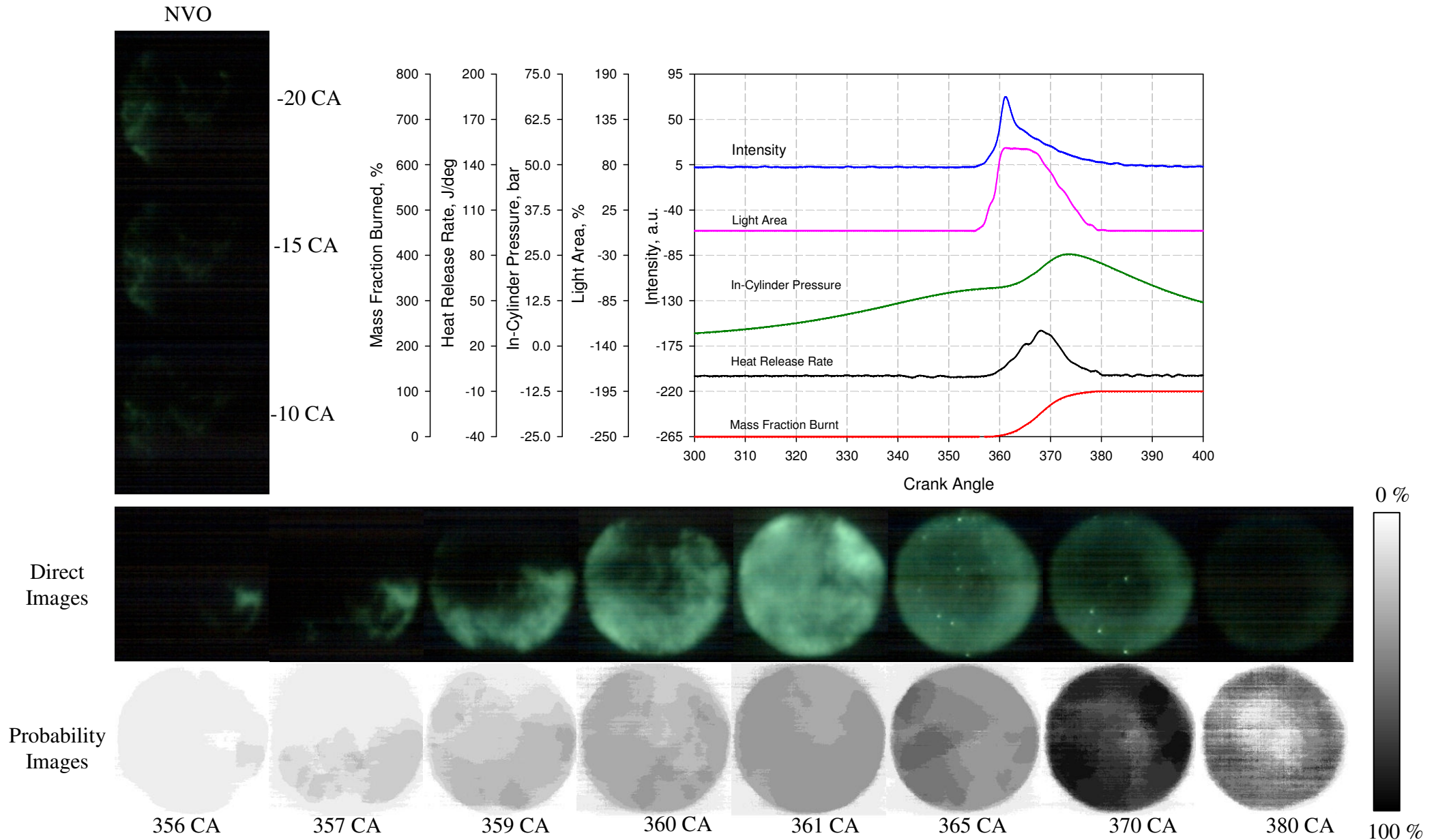
#### Gasoline

Figure 5.10 shows total chemiluminescence images and characteristics of gasoline combustion without spark-assisted ignition. Similar to spark-assisted combustion, during the re-compression stroke the images show luminous features of fuel reforming reactions of branched hydrocarbon molecules in gasoline.

Because of the absence of a spark discharge to ignite the charge mixture, auto-ignition temperature is attained solely by compression and heating from the hot residual gas. Thus, the first visible image is shown around 356 degree CA, notably later than combustion with spark-assisted ignition. Interestingly, the combustion is initiated near the perimeter of the combustion chamber rather than near the centre, as with spark-assisted ignition. Auto-ignition is achieved at multiple sites simultaneously near the cylinder wall and not throughout the entire combustion chamber. Afterwards, as a consequence of first ignited combustion sites, the temperature of other areas is increased sufficiently to achieve self-ignition. It is not possible for flame propagation to be responsible for this combustion because only 5 degree crank angles are required for combustion to engulf the whole chamber whereas flame propagation-based spark-assisted combustion took almost 20 degree crank angle to have progressed to a similar extent. The light emission is then present in the whole chamber for the next 15 degree crank angle, terminating around 380 degree CA, the same crank angle as for combustion with spark-assisted ignition. These results are similar to the results of Persson et al [48] in which the flame was initiated around the outer rim of image area. However, the slower speed of flame occupied the entire chamber presented in the previous paper [48]. The reforming reaction as shown in the re-compression stroke possibly enhanced the CAI combustion in the current study.

The probability images exhibit dark areas around the periphery of the chamber at the beginning of combustion. This indicates that the most susceptible positions for auto-ignition are located around the perimeter of combustion chamber; this corresponds with the findings of Persson et al [48] and Aleiferis et al [50] in which the CAI/HCCI was achieved with the aiding of internal exhaust gas recirculation. It was postulated

that the mixing with trapped hot gas created the spatial hot sources distributed in the combustion chamber. In the current study, those hottest gases were possibly affected by the dynamic flow to distribute around the perimeter of chamber. However, there is no clear evidence of this occurring in this study. In-cylinder temperature measurements will be required to elucidate the cause and will be carried out by a PLIF technique in the future. However, another plausible explanation for the first auto-ignition sites near the cooler cylinder wall is the so-called negative temperature coefficient phenomenon which is characterized by slower reactions with increasing temperature at intermediate temperatures. Due to the lack of spark discharge to assist ignition at any specific crank angle, the commencing of auto-ignition varies significantly.



**Figure 5.10 Total Chemiluminescence Image of Gasoline without Spark-Assisted Ignition**

## **Ethanol**

The total chemiluminescence images of ethanol without spark-assisted ignition are shown in Figure 5.11. On account of the single-stage ignition property of ethanol, there is no indication of any low temperature oxidation occurring at the high charge temperature reached during the re-compression stroke.

Without initiation from the spark discharge, combustion commenced later at a crank angle of around 351 degree CA. Ethanol combustion takes place earlier than gasoline but proceeds with the same process. The combustion initiation sites are located near the perimeter of the chamber as that of gasoline. In addition, the images show that ethanol achieves simultaneously auto-ignition covering nearly the whole combustion area. Subsequently, the combustion persists for 15 degree crank angle and then terminates at 370 degree CA, almost the same time as spark-assisted ignition combustion. Without the spark discharge, simultaneous auto-ignition of multiple regions over the entire chamber plays the dominate role in consuming the charge mixture within a shorter period of time. Combustion of ethanol occurs faster and starts earlier than that of gasoline. The higher gas temperatures at the beginning of the compression stroke with ethanol have an effect on the early combustion timing while simultaneous auto-ignition of many independent sites are responsible for the faster combustion.

The intensity and percentage of light area curves show the same result but have a slight time lag with heat release rate and mass fraction burned curves, when compared with spark-assisted combustion. The probability images show cycle to cycle variation of the crank angle at which auto-ignition occurs. The images also show that auto-ignition occasionally starts before 351 degree CA. Auto-ignition distributes preferentially around the perimeter of the combustion chamber.

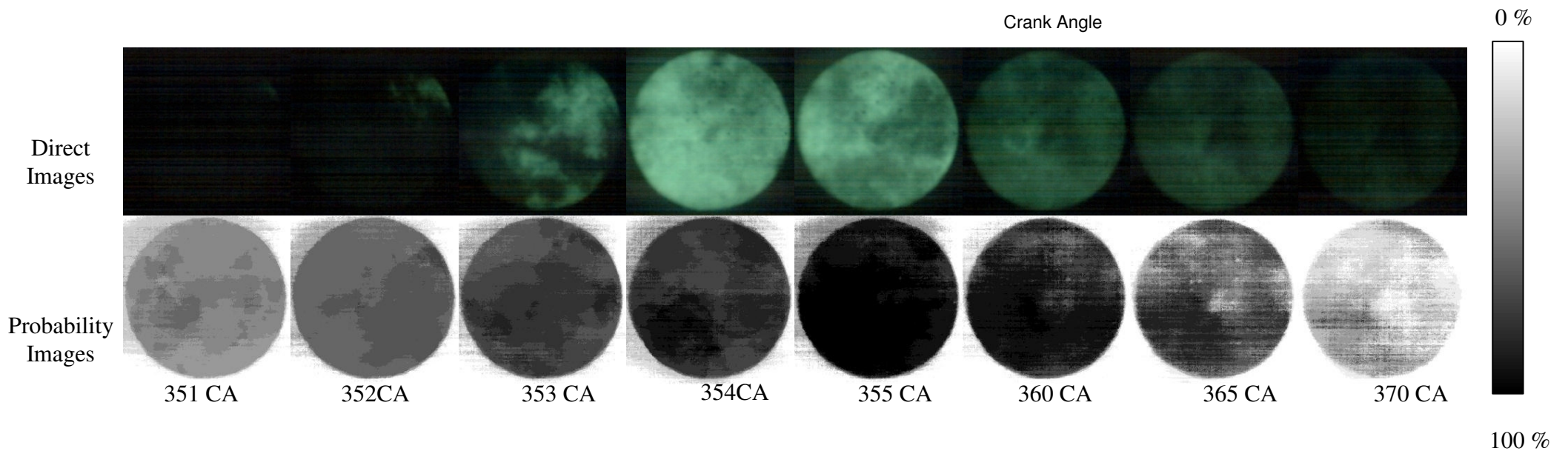
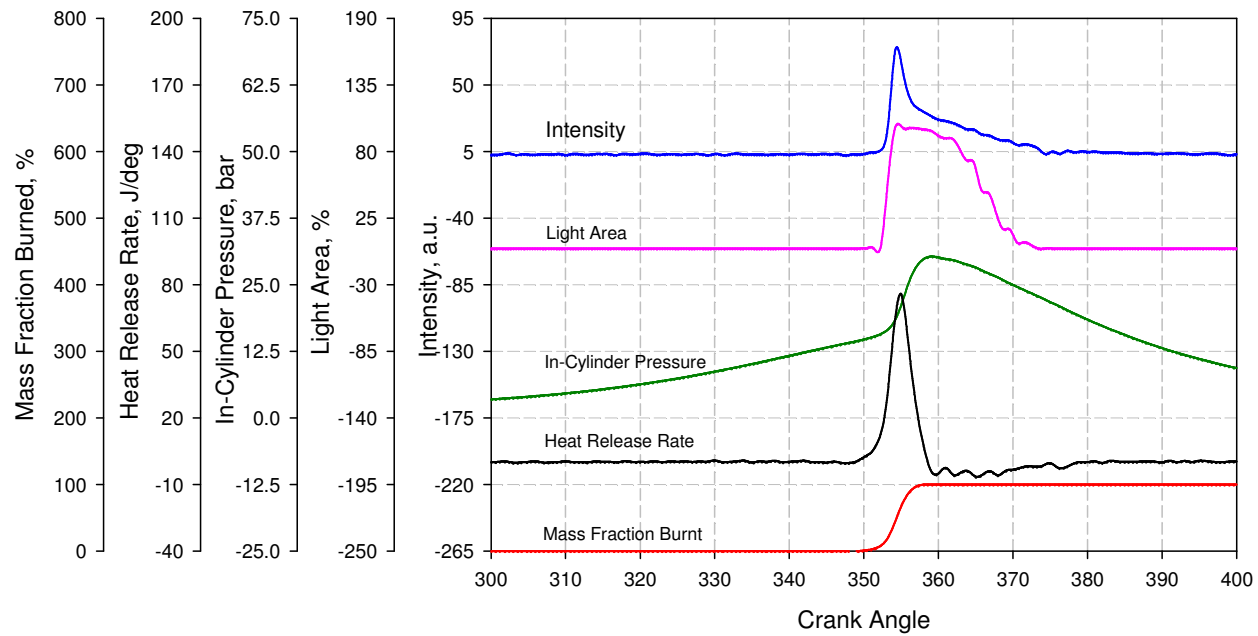


Figure 5.11 Total Chemiluminescence Image of Ethanol without Spark-Assisted Ignition

## **Methanol**

Figure 5.12 illustrates the total chemiluminescence images of methanol without spark assistance. There is no chemiluminescence detected during the re-compression stroke.

Interestingly, total chemiluminescence of methanol is similar between with/without spark-assisted ignition. Figure 5.12 shows that the auto-ignition was achieved at 341 degree CA, nearly the same time as that from spark discharge at 340 degree CA, as shown in Figure 5.3. Of significant difference compared to spark-assisted combustion, the auto-ignition sites appear around the perimeter of the chamber. The crank angle in which charge temperature attain auto-ignition is almost the same with spark igniting combustion. Therefore, it is possible that some cycles of spark-assisted combustion was initiated by auto-ignition while some cycles were dominated by spark ignition. Moreover, the image intensity and percent of light area plots look similar to those of spark-assisted combustion and have a time lag with heat release rate and mass fraction burned.

The probability images show the likely areas of auto-ignition are located on the periphery of the combustion chamber biased towards the exhaust valves, the same side to that of gasoline, where the charge is exposed to higher surface temperature. For most cycles, the bulk charge is consumed in less than 10 degree CA and combustion terminates before 355 degree CA. Compared with the previous fuels, CAI combustion with methanol as the fuel is characterised the fastest and earliest initiating process.

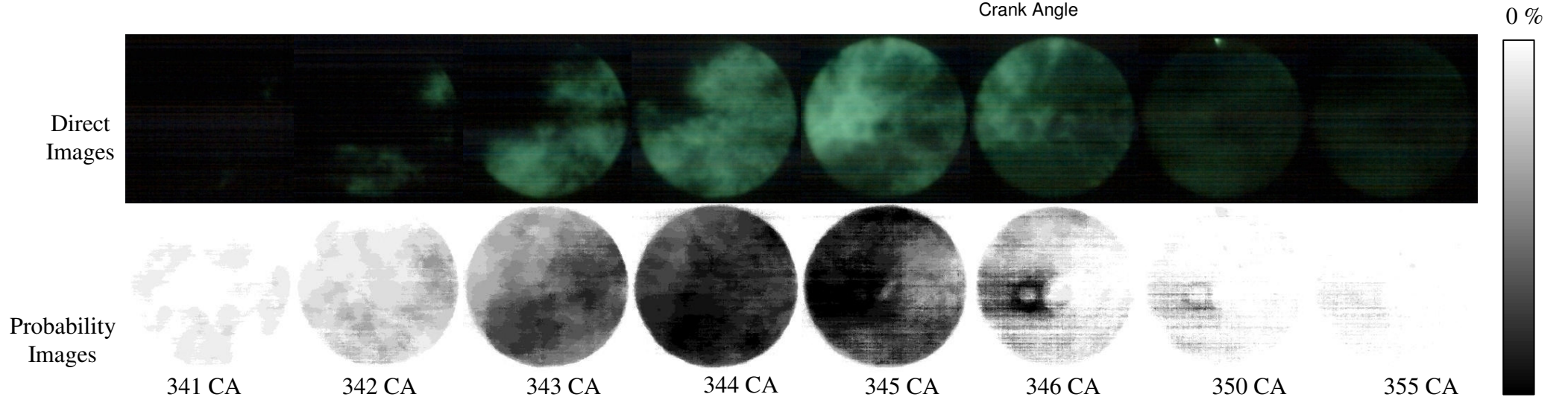
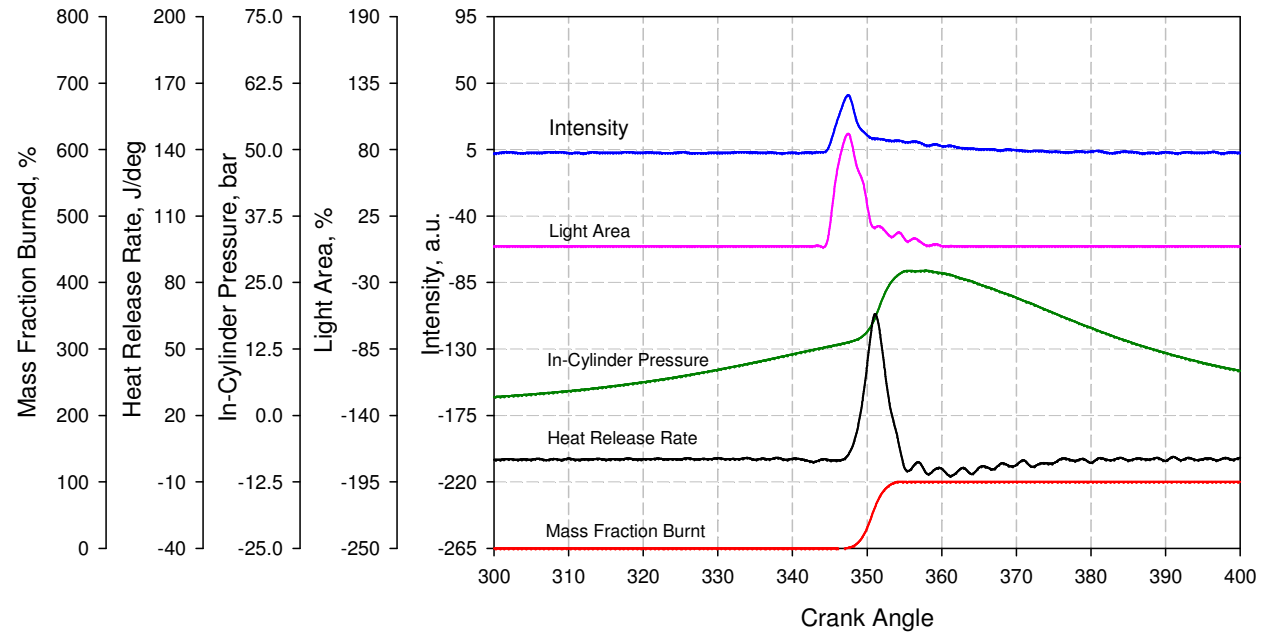


**Figure 5.12 Total Chemiluminescence Image of Methanol without Spark-Assisted Ignition**

105 %

### **Blended Fuels (E20, E50, E85, M20, M50 and M85)**

Figures 5.13 – 5.18 present the total chemiluminescence images of blended fuels from 20 to 85 percent of alcohol without spark-assisted ignition. As with the same combustion with spark discharge, during the negative valve overlap period the chemiluminescence emission of gasoline reforming reactions is detected for blended fuel of 20 to 50 % alcohol. At higher alcohol concentration, no light emission is shown.

Without spark-assisted ignition, the combustion processes for all of the blended alcohols follow with the same features of gasoline, ethanol and methanol as discuss above. However, ignition timing and combustion duration effects are more pronounced with increasing percentage of alcohol. Up to 50 %, the presence of alcohol advances the onset of auto-ignition with increasing percentage of alcohol, in particular for the methanol blend. Subsequently, for 50 and 85 % of blended alcohol ignition occurs at nearly the same time with pure alcohol. The original sites for self-ignition are observed at the perimeter and then simultaneous combustion occurs at multiple sites. Noticeably, the duration that combustion engulfed the whole chamber for and the time taken to consume the whole charge (combustion termination) are reduced with increasing amounts of alcohol.

Probability images confirm that the perimeter areas of the combustion chamber are the preferred locations for auto-ignition to occur and also combustion terminates earlier when higher percentage of alcohol are blended in the fuel.

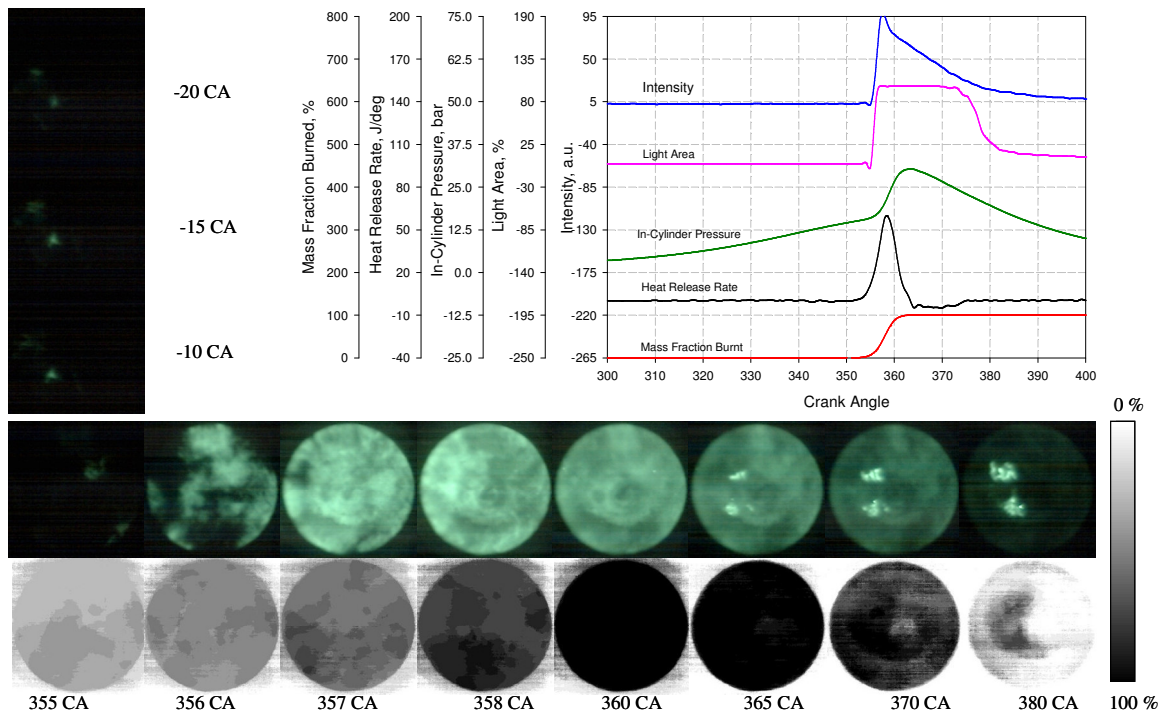


**Figure 5.13 Total Chemiluminescence Image of E20 without Spark-Assisted Ignition**

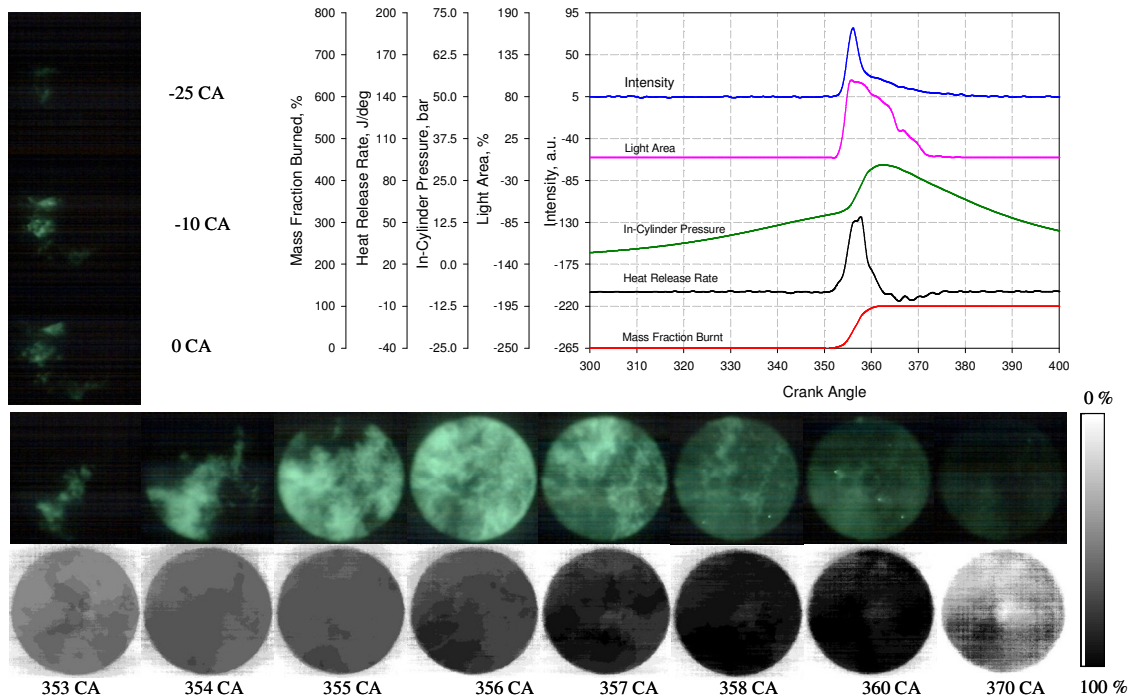


**Figure 5.14 Total Chemiluminescence Image of M20 without Spark-Assisted Ignition**

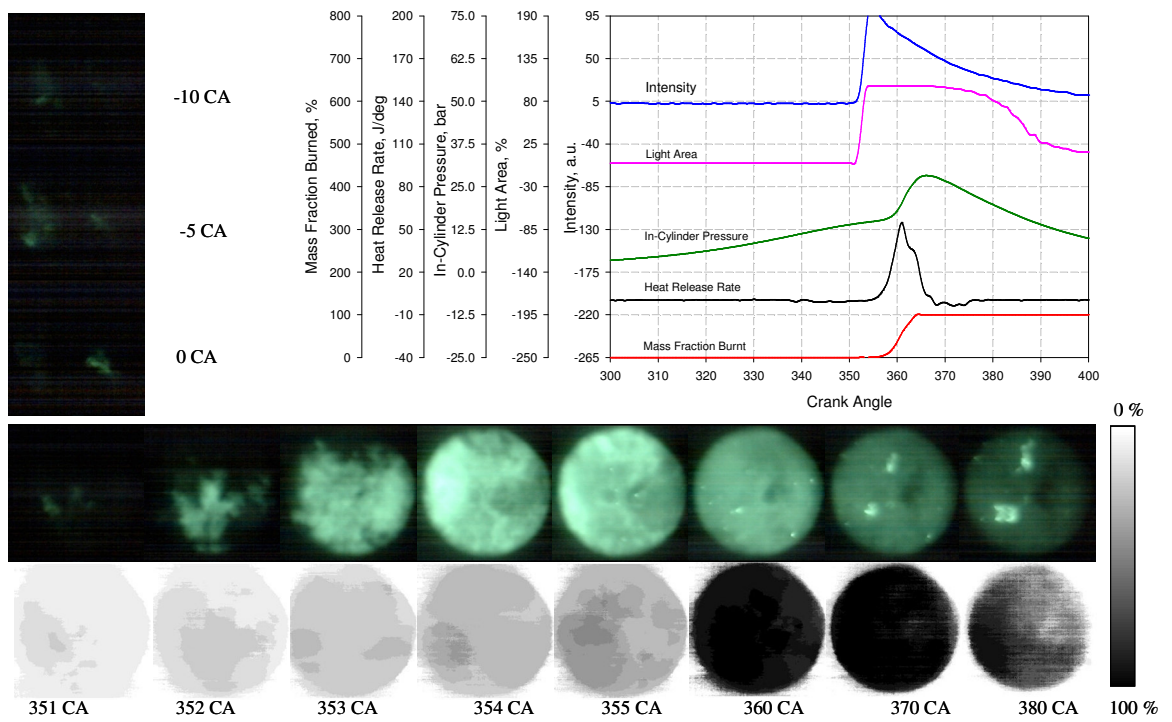


**Figure 5.15 Total Chemiluminescence Image of E50 without Spark-Assisted Ignition**

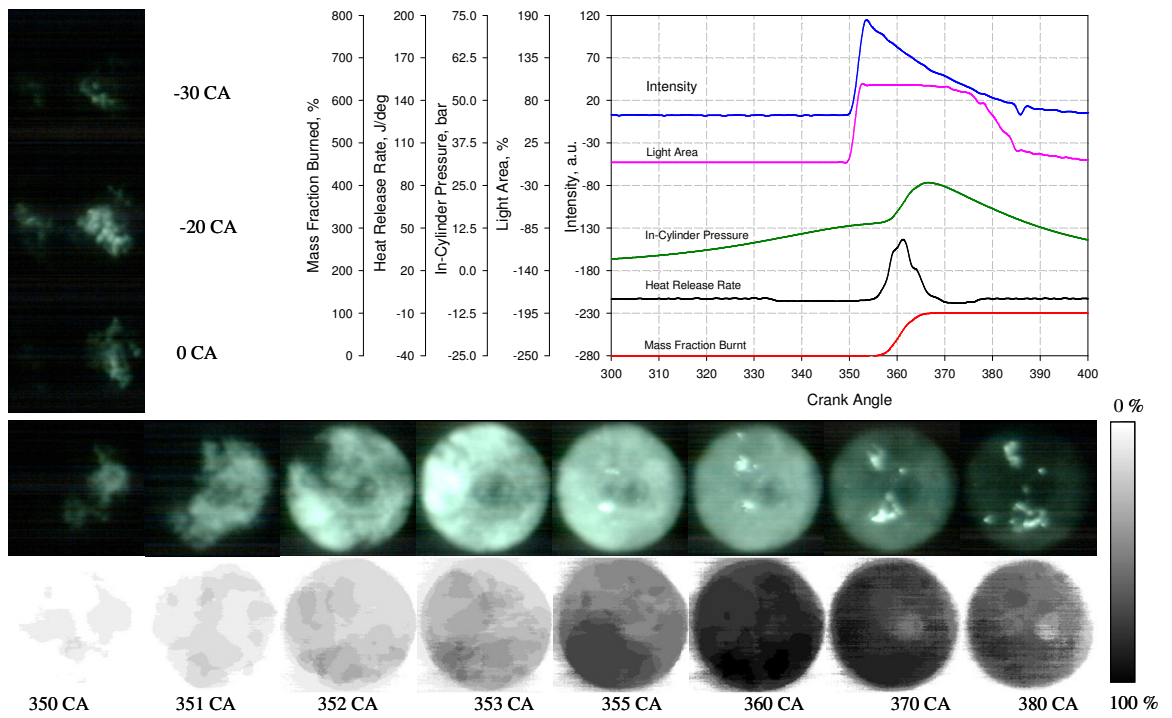


**Figure 5.16 Total Chemiluminescence Image of M50 without Spark-Assisted Ignition**

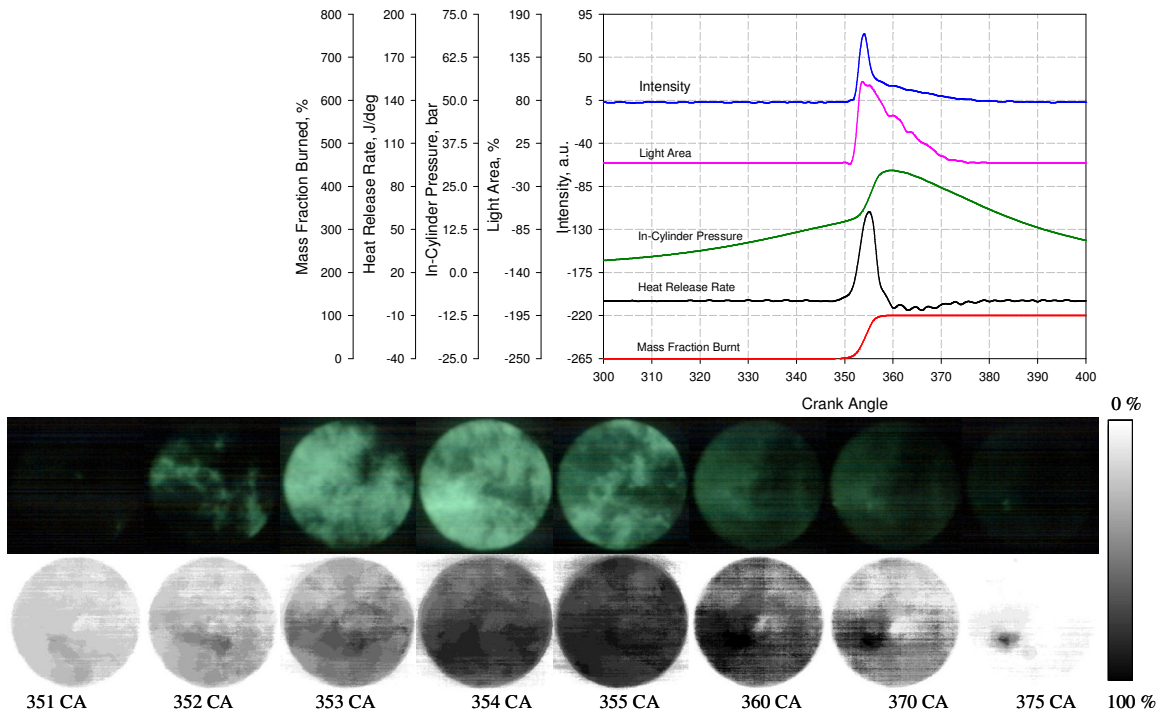


**Figure 5.17 Total Chemiluminescence Image of E85 without Spark-Assisted Ignition**

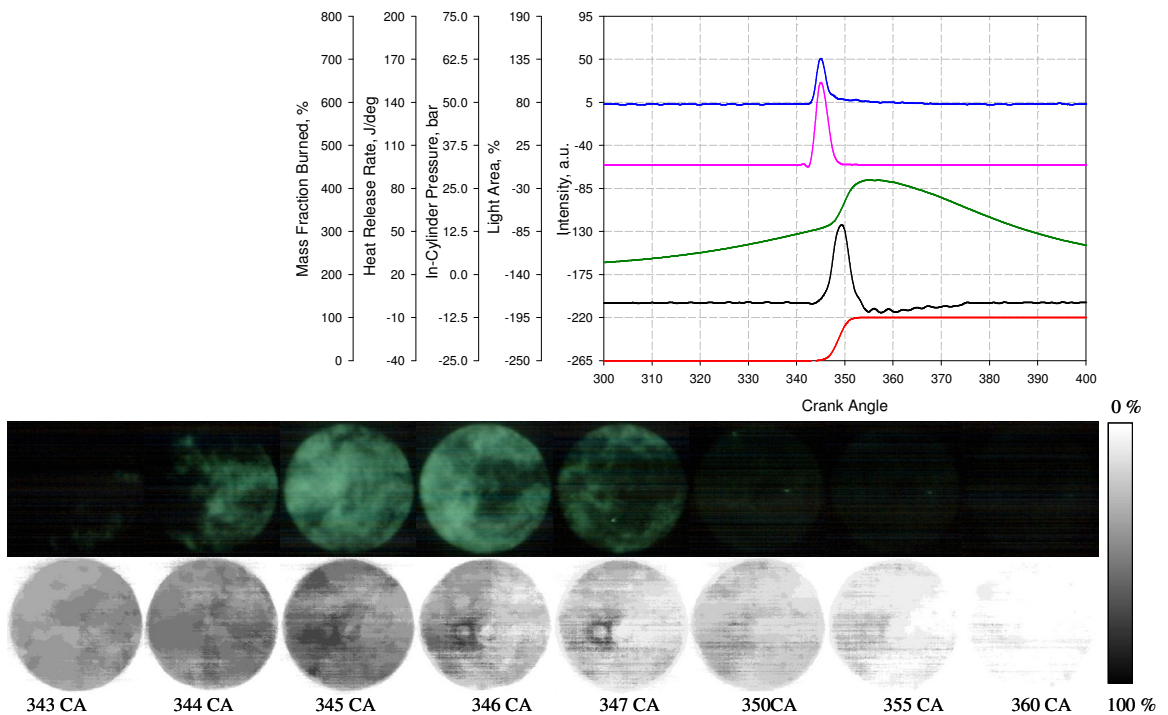


**Figure 5.18 Total Chemiluminescence Image of M85 without Spark-Assisted Ignition**

## 5.3.2 CHO Chemiluminescence Images

### 5.3.2.1 Spark-Assisted Ignition

#### Gasoline

For spark-assisted ignition, Figure 5.19 presents the CHO chemiluminescence images of gasoline combustion. There is no CHO image signal captured during the negative valve overlap. This conflicts with the total chemiluminescence image results. CHO formation takes place after excited formaldehyde prior to hot flame combustion and its concentration is more prominent in lean mixtures. The failure of detecting CHO emission means that the reforming reaction of gasoline did not lead to sufficient CHO production due to lack of oxygen during the re-compression stroke. In order to protect the intensifier from harmfully strong intensity during the main combustion, the gain of the intensifier was set at 60% for this study. Therefore, a future study should increase this gain value in order to complete the investigation. In the next chapter, in-cylinder gas sampling will be detailed to clarify the fuel reforming reaction.

During the main combustion event, the first visible CHO chemiluminescence was recorded later than the total emission image, with a very weak signal. In addition, unlike previous images, CHO is formed away from the centre. As reported in the literature, CHO is an intermediate radical formed after the low temperature reactions but before the onset of high temperature combustion. Therefore their spatial distribution represents the start of high temperature combustion as a result of the low temperature auto-ignition reactions. As a result, there is no CHO in the centre where spark ignition combustion dominates. The onset of the average intensity images and the light area of CHO chemiluminescence agree well with the heat release rate and mass fraction burned. The range of the average intensity and light area correspond with the duration of the total heat release rate.

Of the significant features, there are much brighter areas of CHO chemiluminescence around the perimeter of the chamber at later crank angles. This appears to be a boundary layer as explained by Hultqvist [51]. The spatial distribution of CHO in

which greater concentrations appeared around the perimeter of the chamber confirmed the susceptible locations for auto-ignition as being the outmost areas of the cylinder.

The bottom row shows the probability images of CHO. These show the spatial distribution of CHO covering the combustion chamber from the center to the perimeter at the right hand side. Although the first visible frame of CHO appears later than the total chemiluminescence, the CHO distribution then goes on to cover the entire chamber earlier. Formation of CHO for most cycles is terminated before total chemiluminescence ceases. In addition, the dark areas of the probability images confirm the presence of a boundary layer.

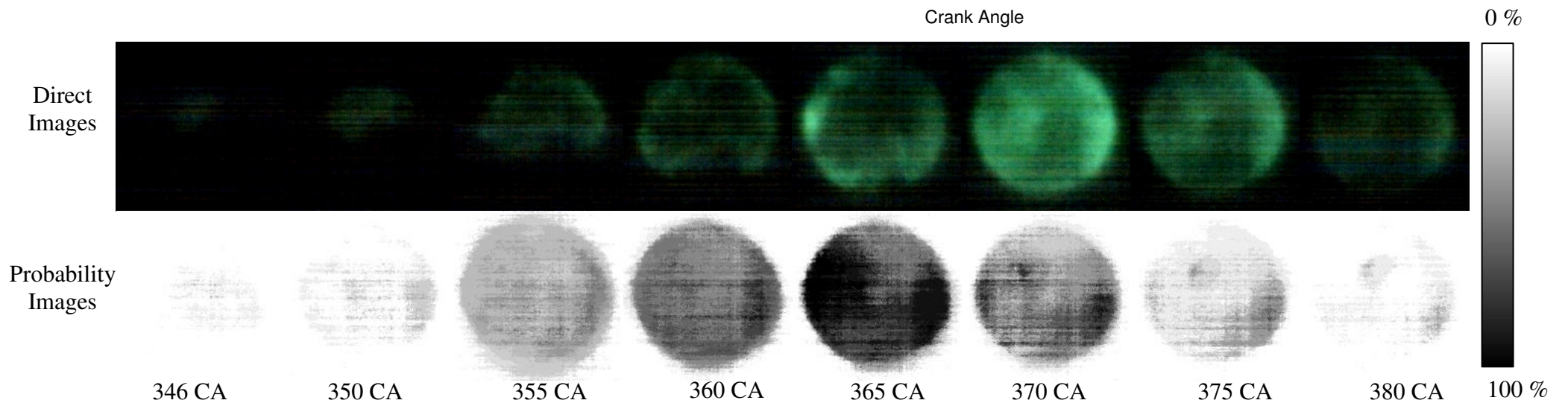
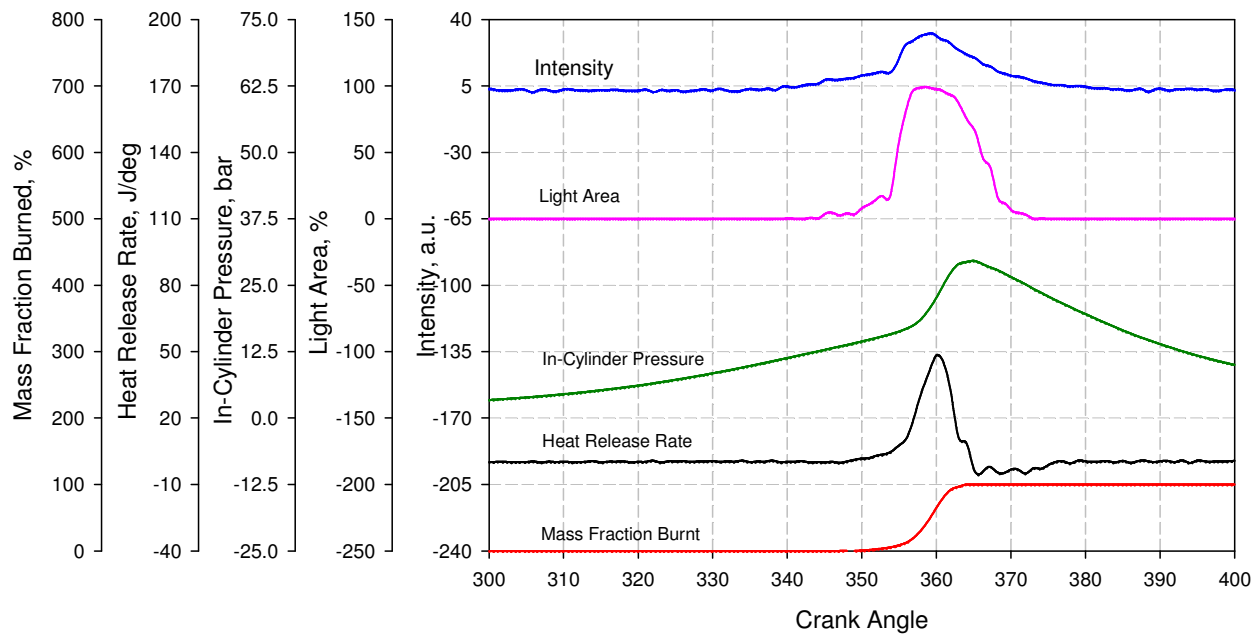


**Figure 5.19 CHO Chemiluminescence Image of Gasoline with Spark-Assisted Ignition**

## Ethanol

Like the total chemiluminescence images, no CHO formation was detected in neat ethanol combustion during the re-compression stroke. At the main combustion, CHO chemiluminescence in Figure 5.20 shows a similarity to gasoline where the first visible signal was recorded at a later crank angle than the total emissions images but its intensity is lower than that of gasoline. Due to spark-assisted ignition, hot combustion in the crank angle between the first total emission and the first CHO emission images was possibly dominated by CH and C<sub>2</sub> or formaldehyde. CHO is shown to be distributed around the periphery of the chamber corresponding well with the auto-ignition site areas. Although the occurrence of the first visible CHO is at approximately the same time of gasoline combustion, Figure 5.20 indicates CHO occupies the whole chamber and is totally consumed much earlier than with gasoline.

It is noted that the rise of the light area and average intensity curves coincides with the heat release rate and mass fraction burned curves. But CHO formation disappears before the heat release rate ceases. From the study of Benvenuti et al [98], most of the CHO radical is formed with the reaction of  $CH + O \rightarrow CHO^*$  in which CH comes from the CH<sub>3</sub> radical. The CH<sub>3</sub> radical is the precursor for all of the important species in ethanol combustion. It is possible that at the early stage of the combustion, CH<sub>3</sub> lead to more CHO radical formation. After the temperature increases, CH<sub>3</sub> changes to form other radical such as CH<sup>\*</sup>, C<sub>2</sub><sup>\*</sup>. To allow quantitative comparison of images and to prevent damage to the intensifier, the gain value was again set to 60%, the value which allowed for capturing the brightest combustion intensity of gasoline. This had limited the detectable level of CHO. Further investigation with higher gain or even an LIF technique should be continued.

The probability images of CHO show most CHO is in the outermost area of the combustion chamber near the cylinder walls. CHO emission disappears before the total light emission images subside, similar to gasoline.

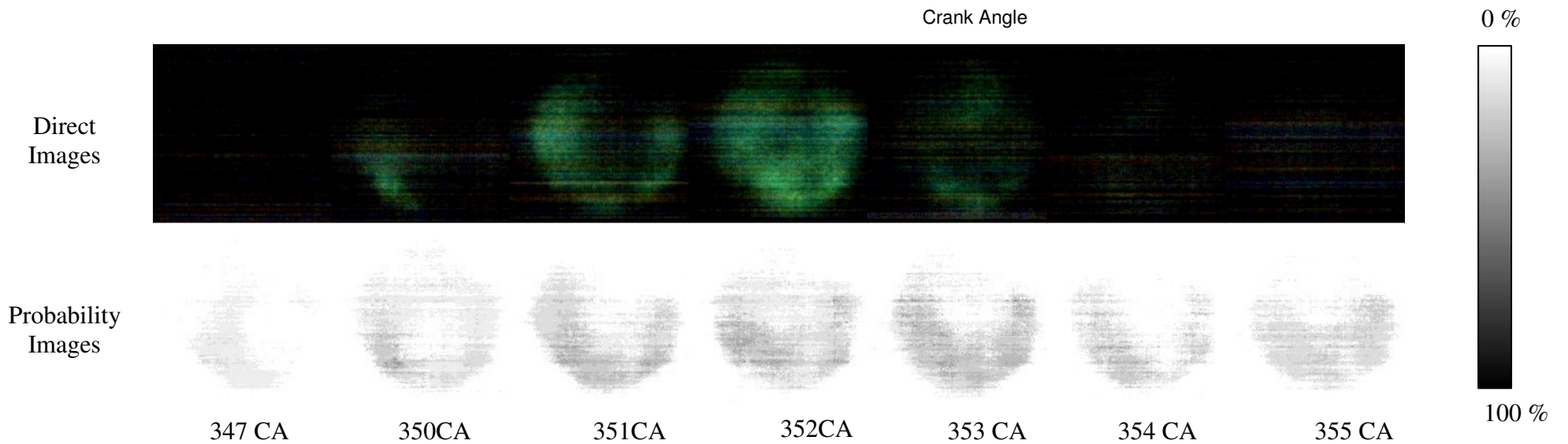
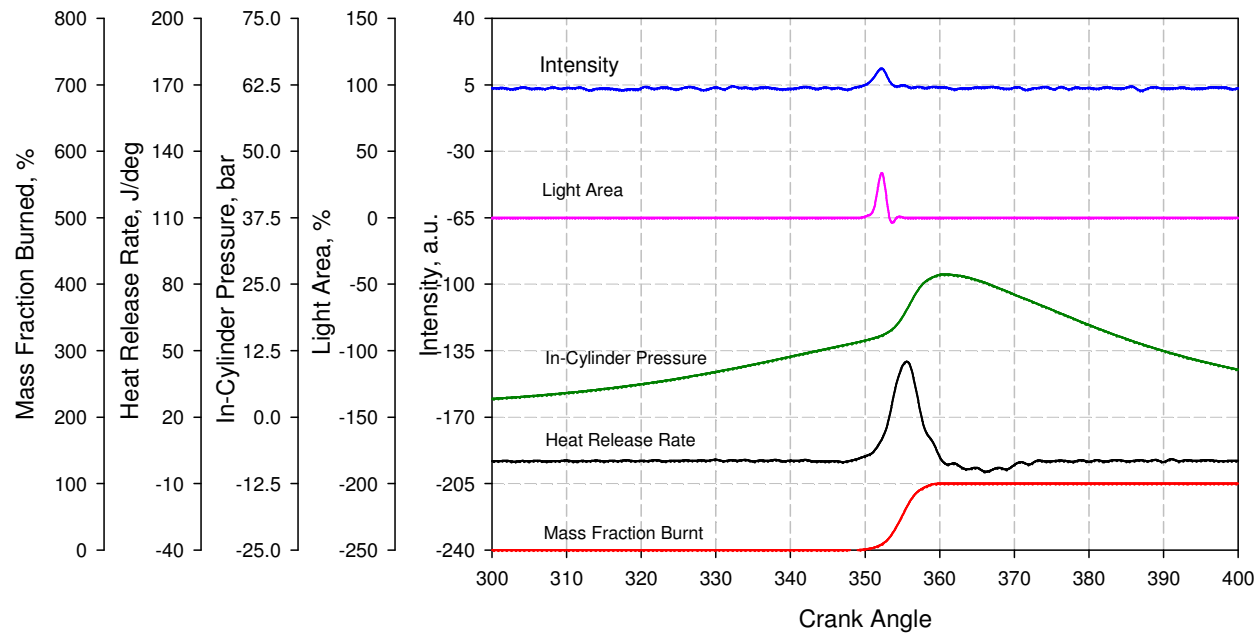


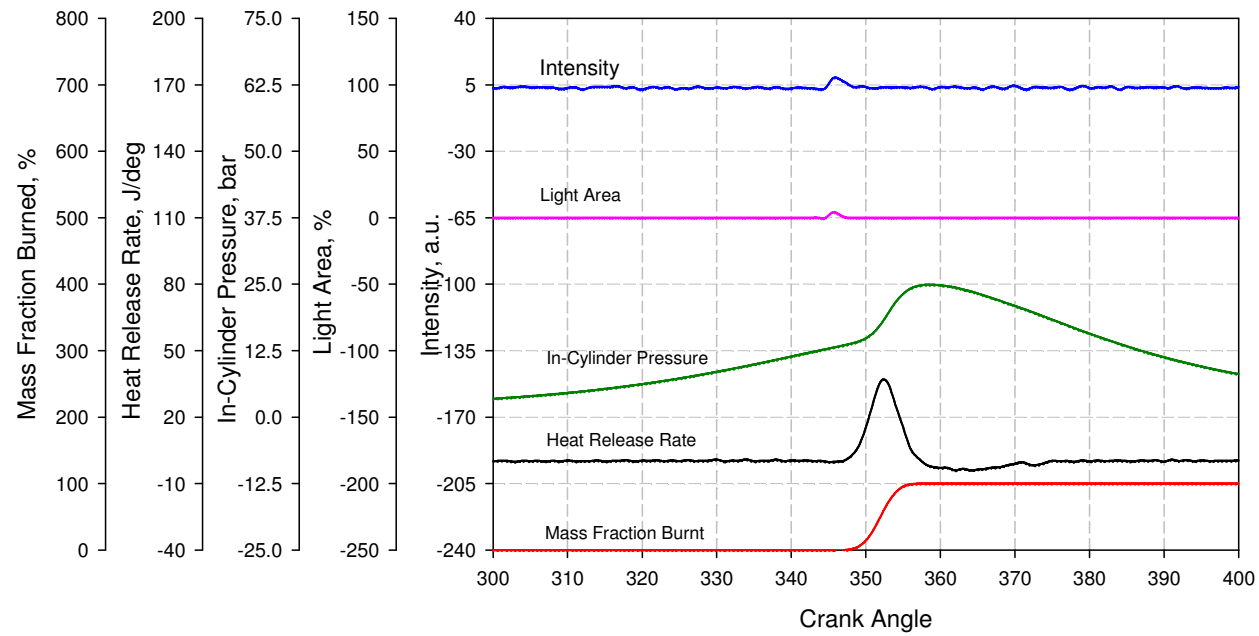
Figure 5.20 CHO Chemiluminescence Image of Ethanol with Spark-Assisted Ignition

## **Methanol**

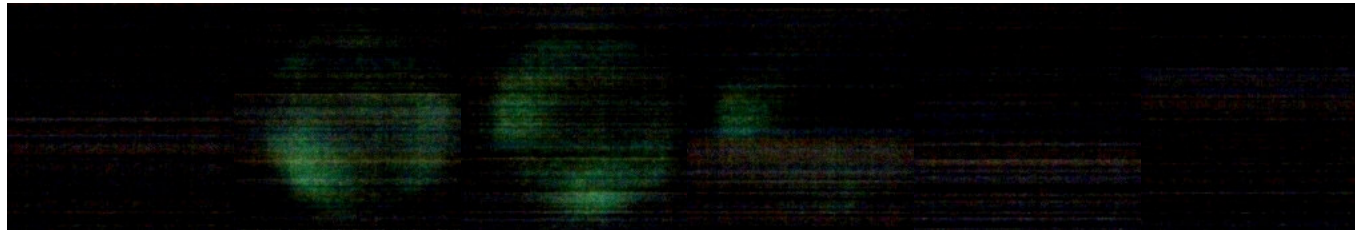
CHO Chemiluminescence images of methanol with spark-assisted combustion are shown in Figure 5.21. Compared with the previous two fuels, methanol emits the weakest CHO signal intensity. Due to less variety of chemical reactions and molecule species, alcohol fuels produce fewer CHO species than hydrocarbons in different reaction pathways. Even with the low intensity, the chemiluminescence images show that CHO appears spread throughout the combustion chamber at an early crank angle of 345 degree CA. This timing corresponds well with the crank angle of spontaneous auto-ignition after the spark-assisted combustion has begun as shown in the total chemiluminescence images. Also, the images indicate the area of CHO is located near the perimeter of the chamber.

CHO chemiluminescence appears for just 4 degree crank angle and then disappears. Moreover, the average intensity and light area curves indicate that CHO formation was terminated at nearly the same time as the main heat release started. A characteristic of interest is that the bright areas turn to dark areas while the dark areas change to bright areas from 345 degree CA to 346 degree CA. This implies that the first formed CHO precedes a rapid oxidation reaction and then decays, followed with CHO which is stimulated by previous combustion.

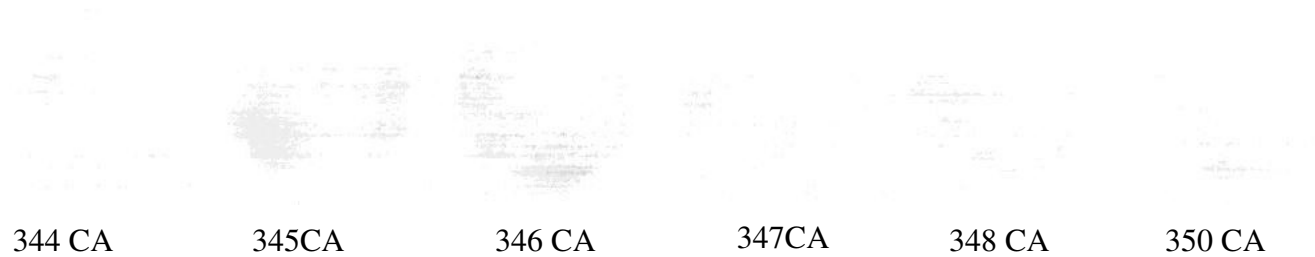
No probability images were produced as the combustion intensity of methanol combustion under this tested condition was too low.



Direct Images



Probability Images



0 %



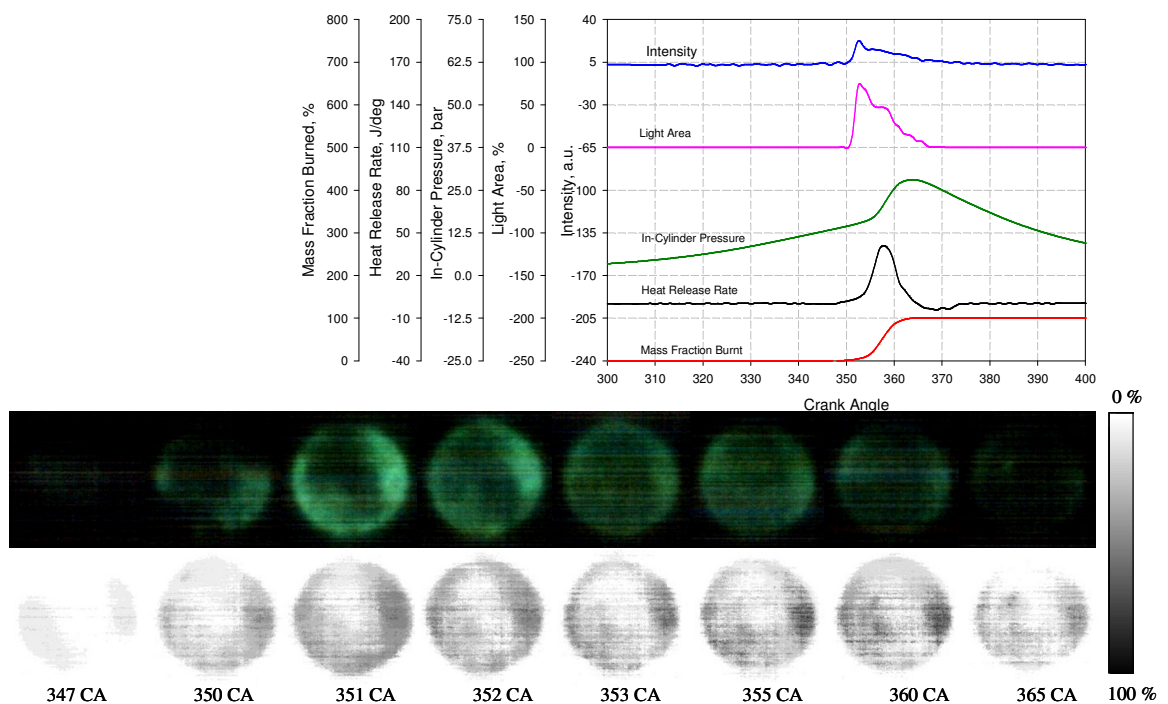
100 %

Figure 5.21 CHO Chemiluminescence Image of Methanol with Spark-Assisted Ignition

## Blended Fuels (E20, E50, E85, M20, M50 and M85)

The effects of alcohol blended fuels are shown in the CHO chemiluminescence of Figures 5.22-5.27. The crank angle of the first visible CHO formation is approximately the same for all blends. However, the crank angles at which CHO distributes over entire chamber and terminates are earlier with increasing percentage of alcohol. The light area curves indicate that the CHO chemiluminescence duration lasts for the duration of the total heat release with 20 % alcohol blend and then decreases to at 94 %, 96 %, 32 % and 12% of the total heat release with E50, M50, E85 and M85 respectively.

The light intensity curves show the same trend with regard to alcohol. Images show CHO distributes around the perimeter of the combustion chamber where auto-ignition dominates.



**Figure 5.22 CHO Chemiluminescence Image of E20 with Spark-Assisted Ignition**

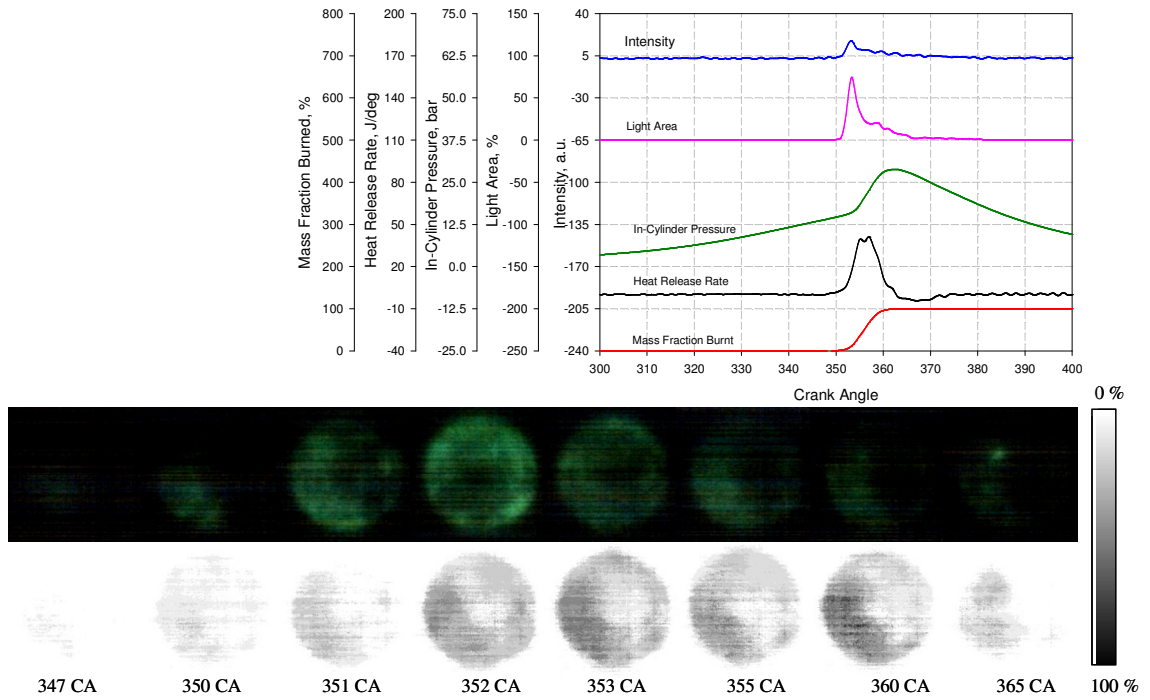


**Figure 5.23 CHO Chemiluminescence Image of M20 with Spark-Assisted Ignition**

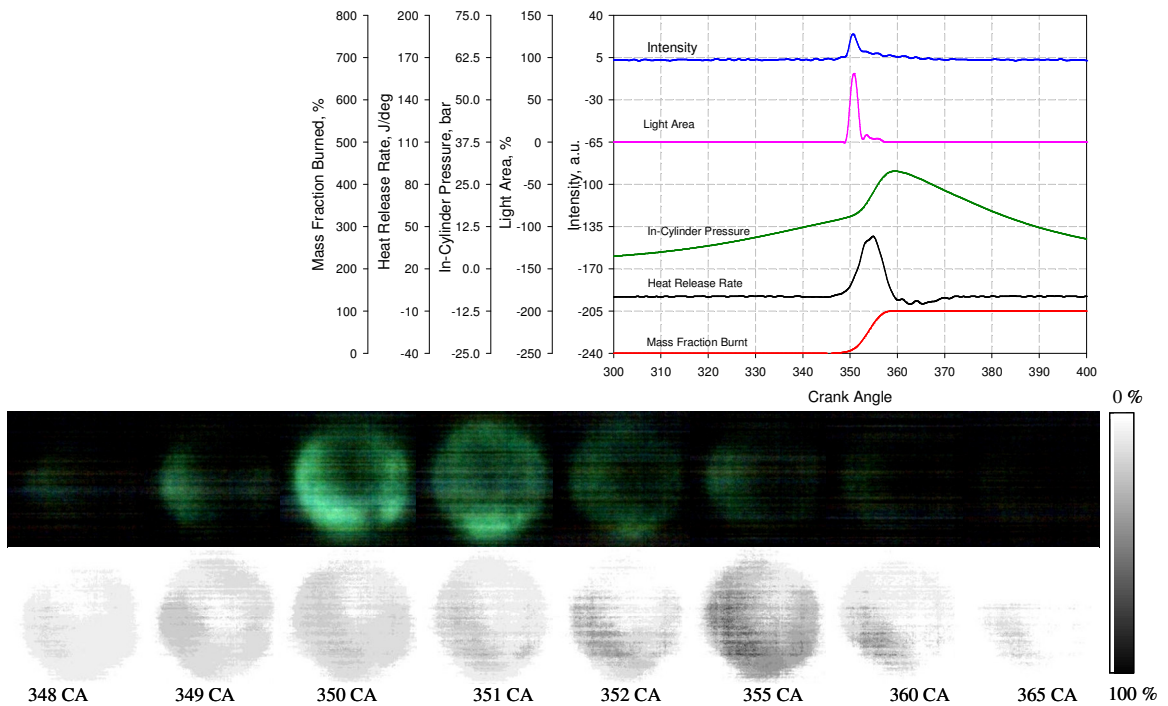


**Figure 5.24 CHO Chemiluminescence Image of E50 with Spark-Assisted Ignition**

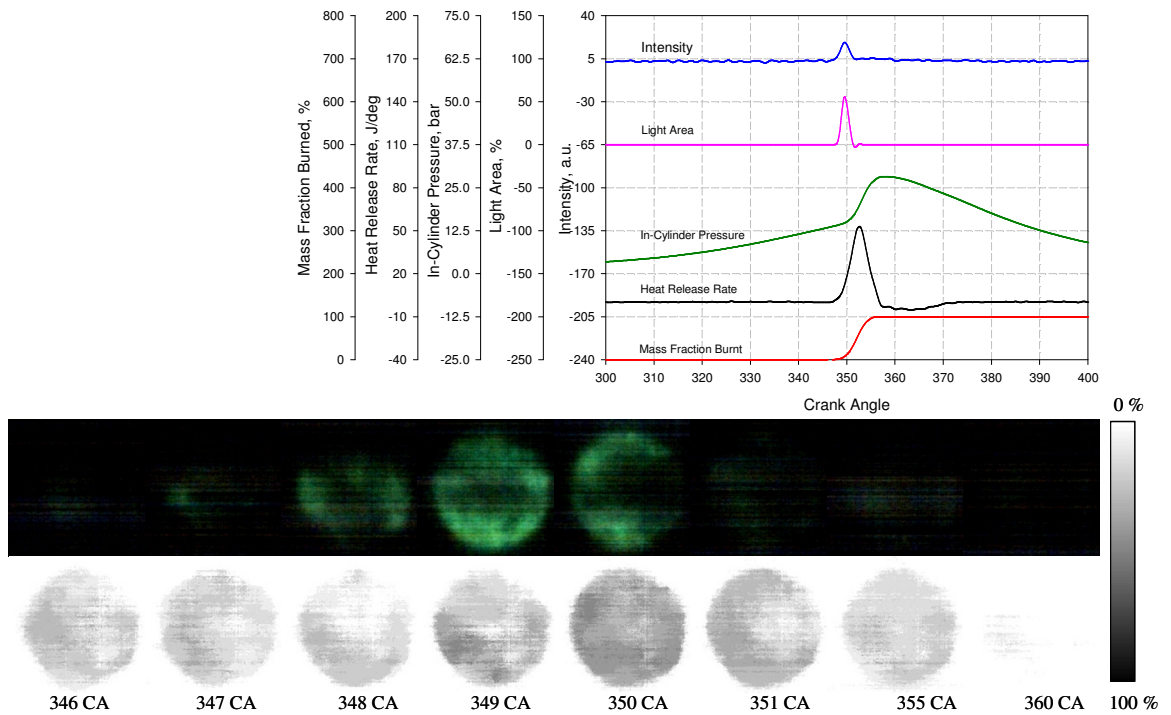


**Figure 5.25 CHO Chemiluminescence Image of M50 with Spark-Assisted Ignition**

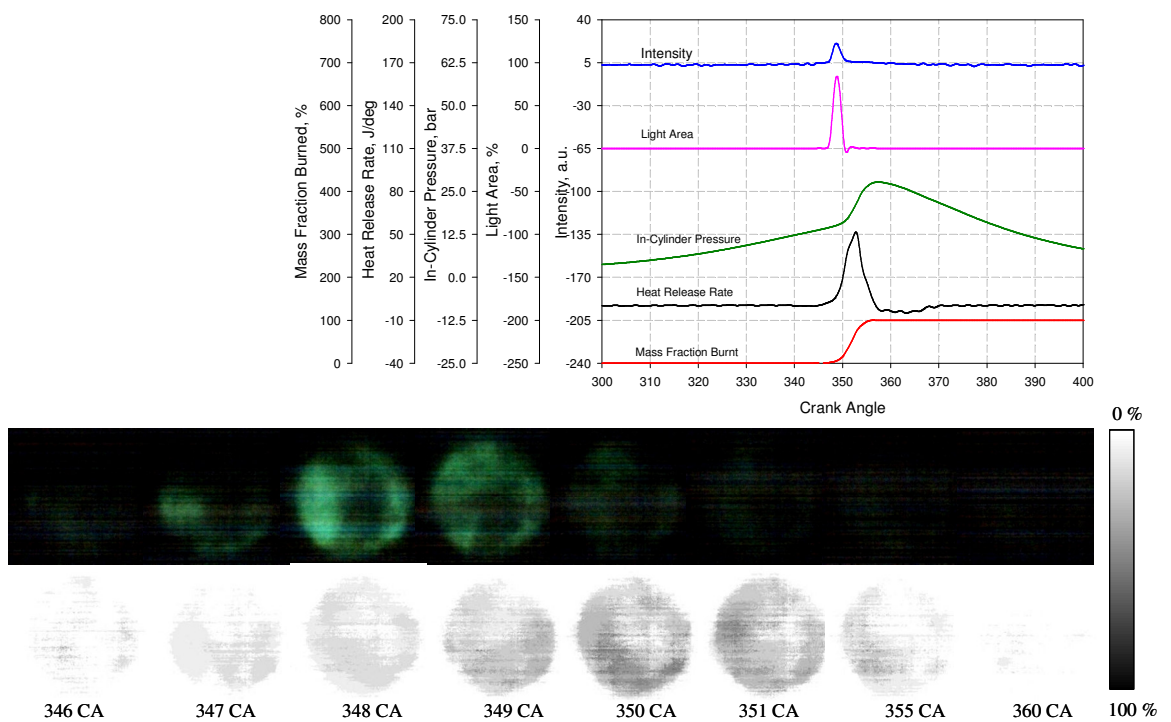


**Figure 5.26 CHO Chemiluminescence Image of E85 with Spark-Assisted Ignition**

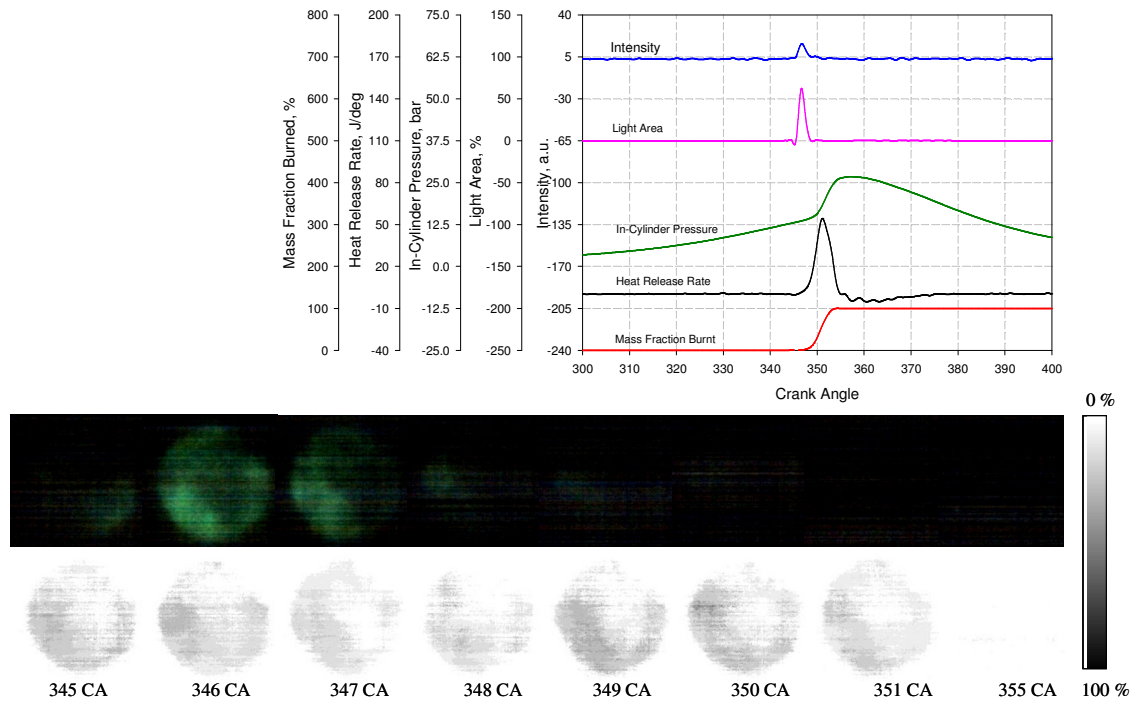


**Figure 5.27 CHO Chemiluminescence Image of M85 with Spark-Assisted Ignition**

### 5.3.2.2 Non-Spark-Assisted Ignition

#### Gasoline

Figure 5.28 presents the CHO chemiluminescence images of gasoline combustion without spark assistance. There is no CHO image signal captured during the negative valve overlap period.

The first image of CHO occurs at a later crank angle (354 degree CA) than that of with spark assistance (346 degree CA). Moreover, the first visible emission of CHO is at nearly the same crank angle as that of the total emission images. As discussed before, self ignition of the mixture dominates combustion in the current condition and hence CHO distribution provides an indication where the auto-ignition occurred.

The average intensity and light area plots indicate that the formation of CHO takes place before the main heat release and terminates at approximately the same time as the hot combustion. Of note for auto-ignition, the CHO emissions are of a higher intensity than those of spark-assisted combustion.

The probability images confirm the sites of auto-ignition as being located at the perimeter of the combustion chamber between the intake and exhaust valves. There is also the boundary layer present near the wall on the right hand side.

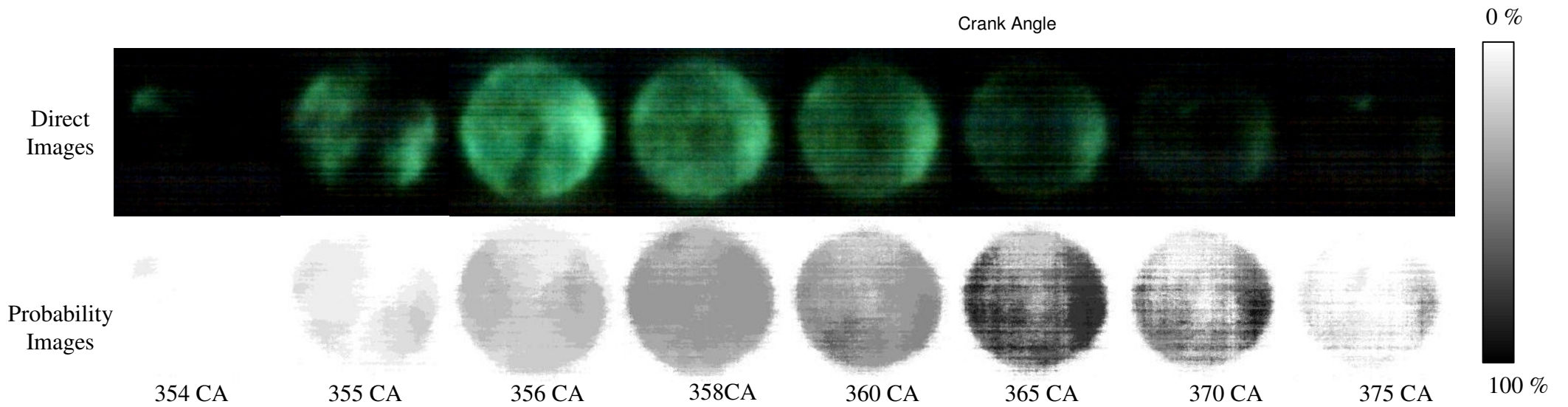
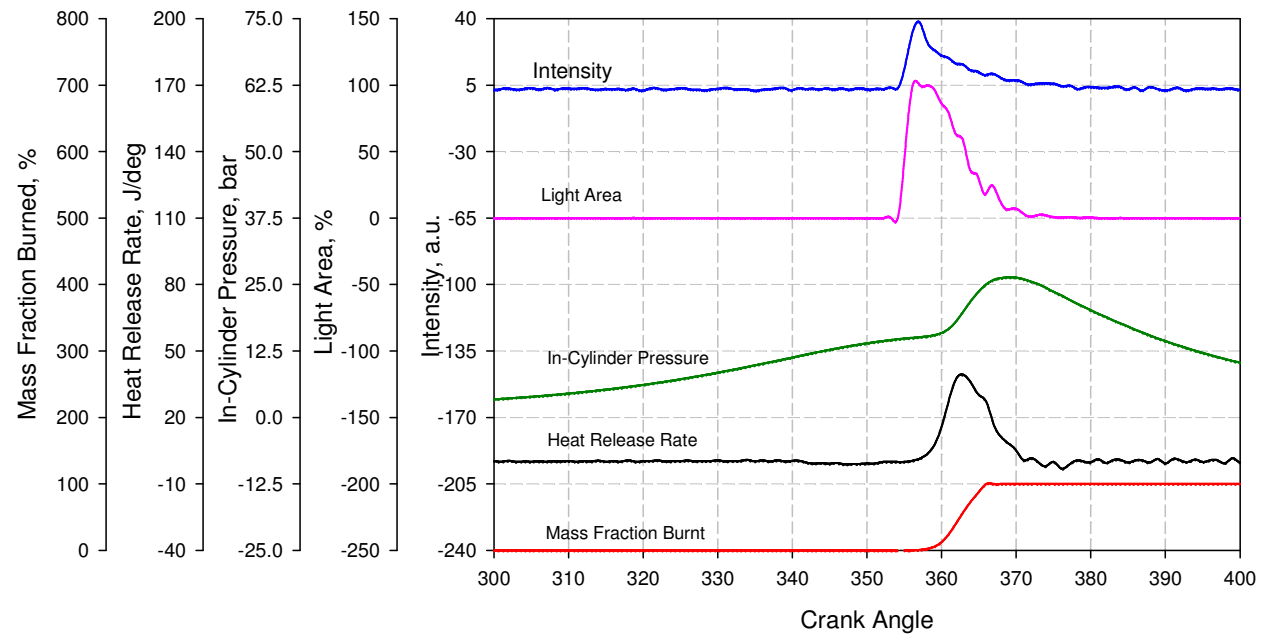


Figure 5.28 CHO Chemiluminescence Image of Gasoline without Spark-Assisted Ignition

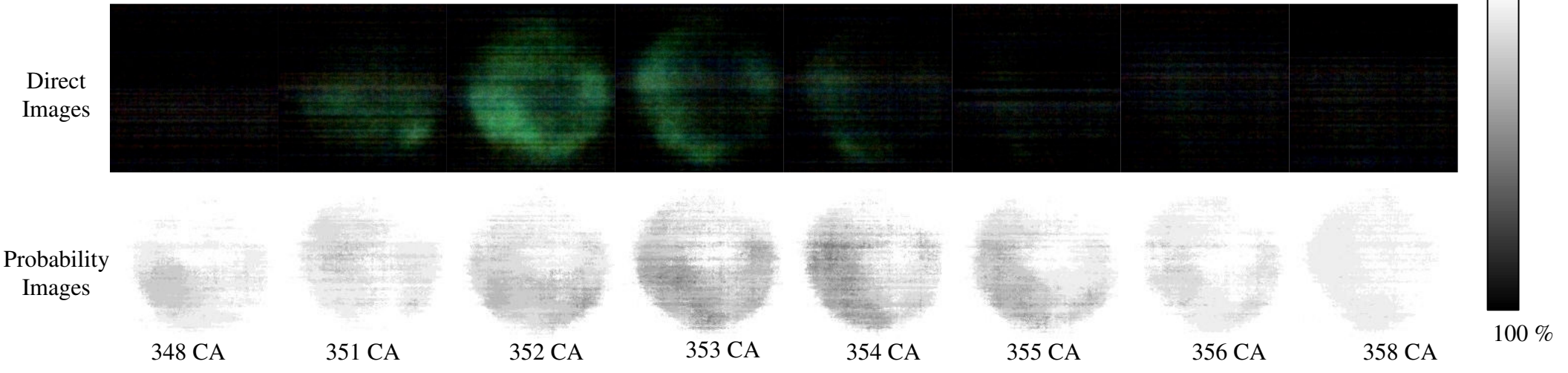
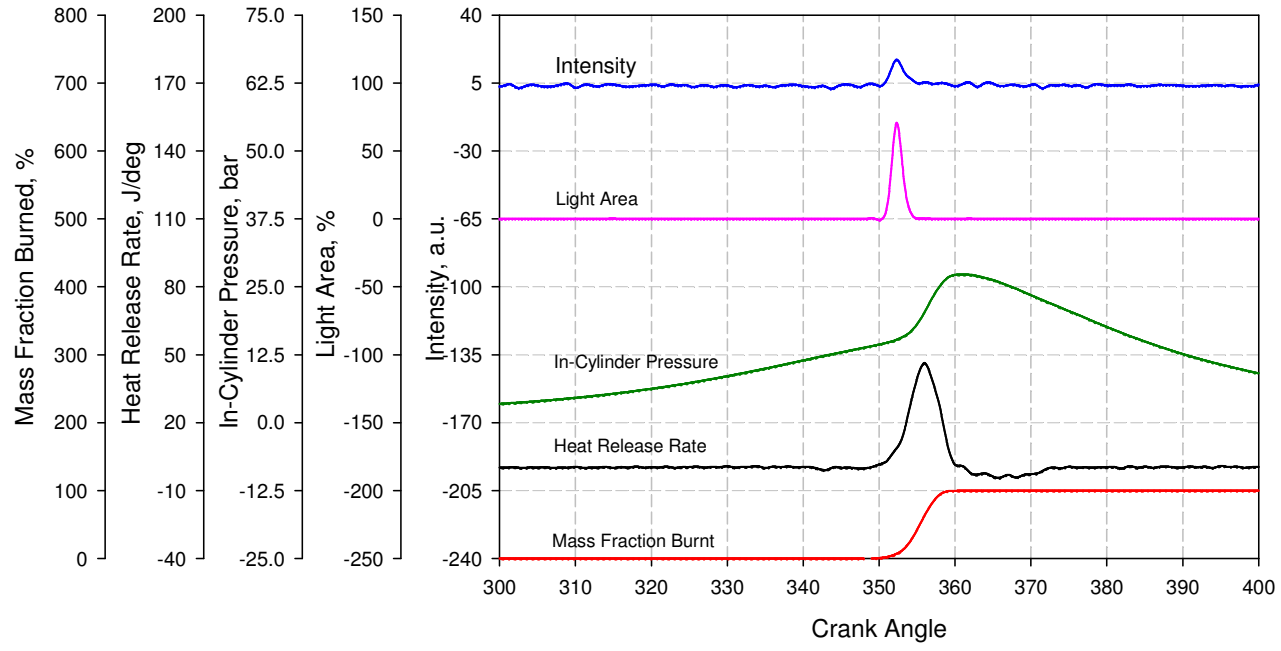
## **Ethanol**

Figure 5.29 shows CHO chemiluminescence of ethanol combustion without spark ignition. With a relatively weak signal, the images indicate similarities with the previously described gasoline combustion, even though they follow different reaction pathways and correspond well with the total chemiluminescence images. The first CHO light emissions from ethanol are seen at 348 degree CA, before those of gasoline at 354 degree CA because of the earlier auto-ignition as discussed previously. The images also show the short duration of CHO formation when compared with gasoline.

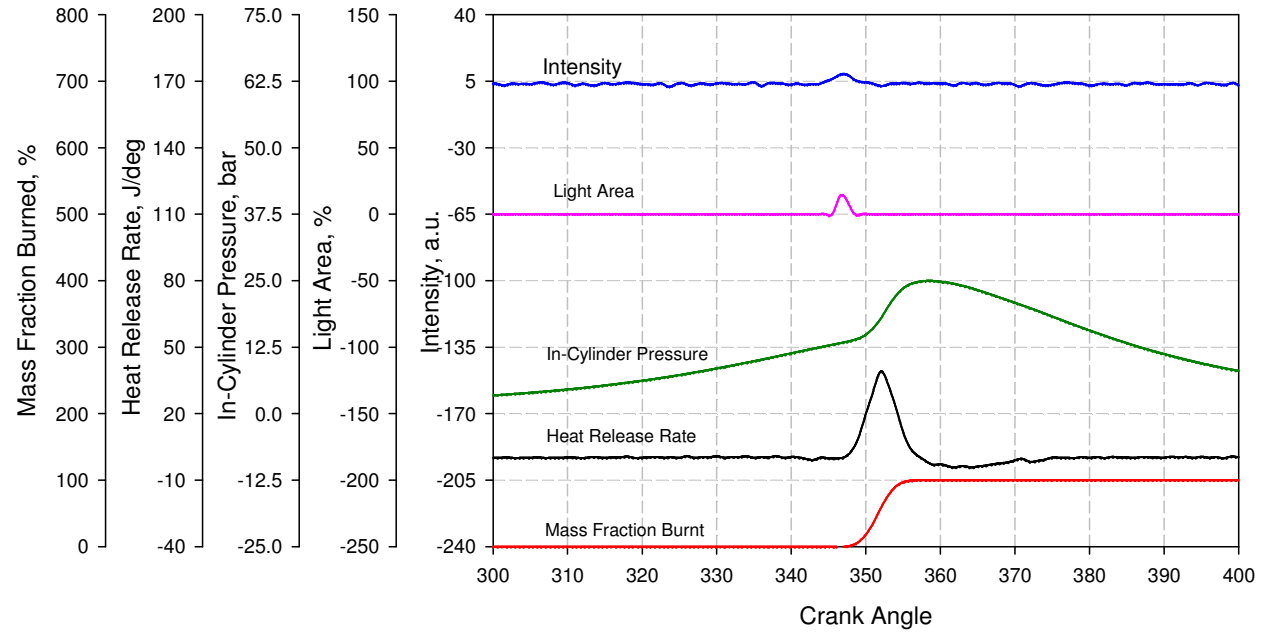
As with the spark-assisted ignition, the average intensity of ethanol is lower than that of gasoline. However, the intensity of CHO in pure CAI is higher than the spark-assisted combustion. The average intensity and light area show the CHO formation commences slightly earlier than the main combustion and terminated at 23 % through the heat release process. The dark areas in the probability images confirm the locations of auto-ignition sited at the perimeter of the combustion chamber.

## **Methanol**

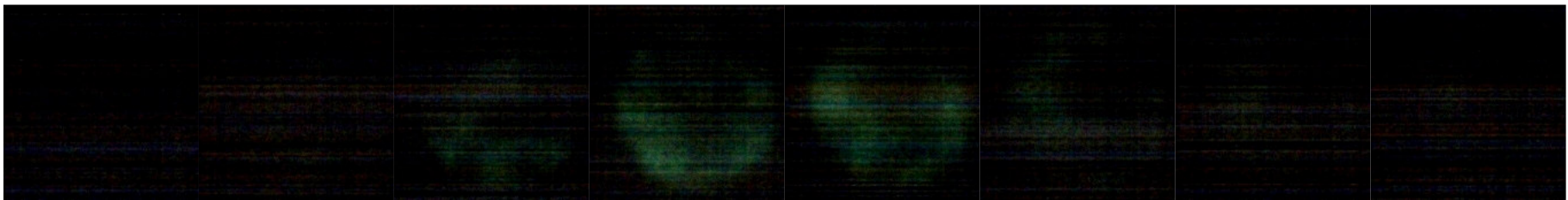
The CHO chemiluminescence images of methanol without spark assistance are illustrated in Figure 5.30. Even with the poor signal intensity, the images indicate fast and early CHO formation at 344 degree CA. Due to the domination of auto-ignition caused by the chemical kinetic reaction, CHO chemiluminescence show the same results as gasoline and ethanol without spark-assisted ignition. The images correlate well with total chemiluminescence images as discussed for the previous two cases. The average intensity shows the lowest CHO formation for methanol combustion whereas the light area shows the CHO is produced before the main heat release and terminates very early at 2 % of cumulative heat release.



**Figure 5.29 CHO Chemiluminescence Image of Ethanol without Spark-Assisted Ignition**



Direct  
Images



Probability  
Images

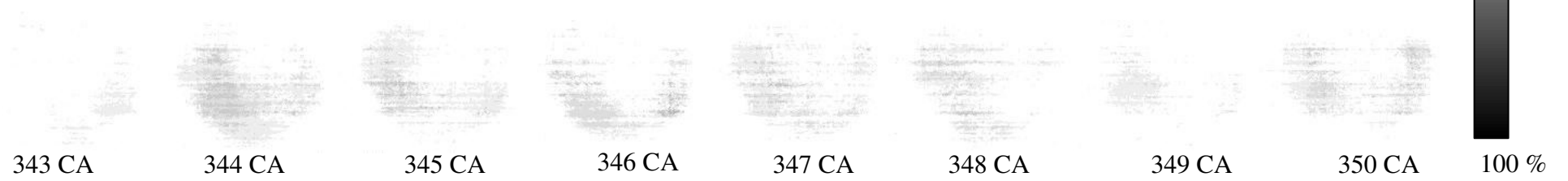


**Figure 5.30 CHO Chemiluminescence Image of Methanol without Spark-Assisted Ignition**

## Blended Fuels (E20, E50, E85, M20, M50 and M85)

Without spark-assisted ignition, the effects of alcohol blend on CHO formations are presented in Figures 5.31 – 5.36 for E20, M20, E50, M50, E85, and M85, respectively. In general, CHO appears earlier with increasing alcohol concentration. Also, the duration of CHO emission shortens and termination of its formation occurs earlier with increasing percentage of alcohol. The average intensity confirms the result of lower CHO concentration when blending higher percentages of oxygenated fuels. The light intensity curves indicate the CHO has disappeared after the high temperature heat release started when using E20 and M20. Meanwhile, its disappearance occurred at 51%, 44%, 10% and 2.24 % of total heat released with alcohol blend E50, M50, E85 and M85 respectively.

Noticeably, the probability images show the first CHO chemiluminescence is likely to first show up on the perimeter of the chamber. Also, spatial CHO distribution consistently occurs at the left hand side slightly biased to the exhaust valve.

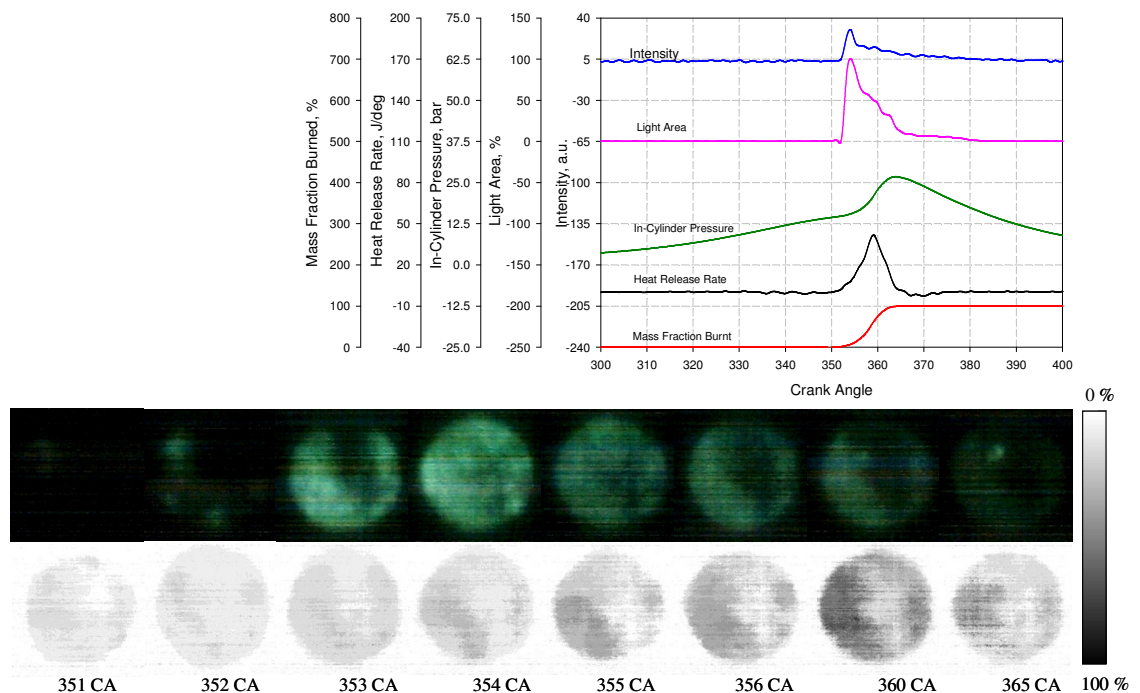


**Figure 5.31 CHO Chemiluminescence Image of E20 without Spark-Assisted Ignition**

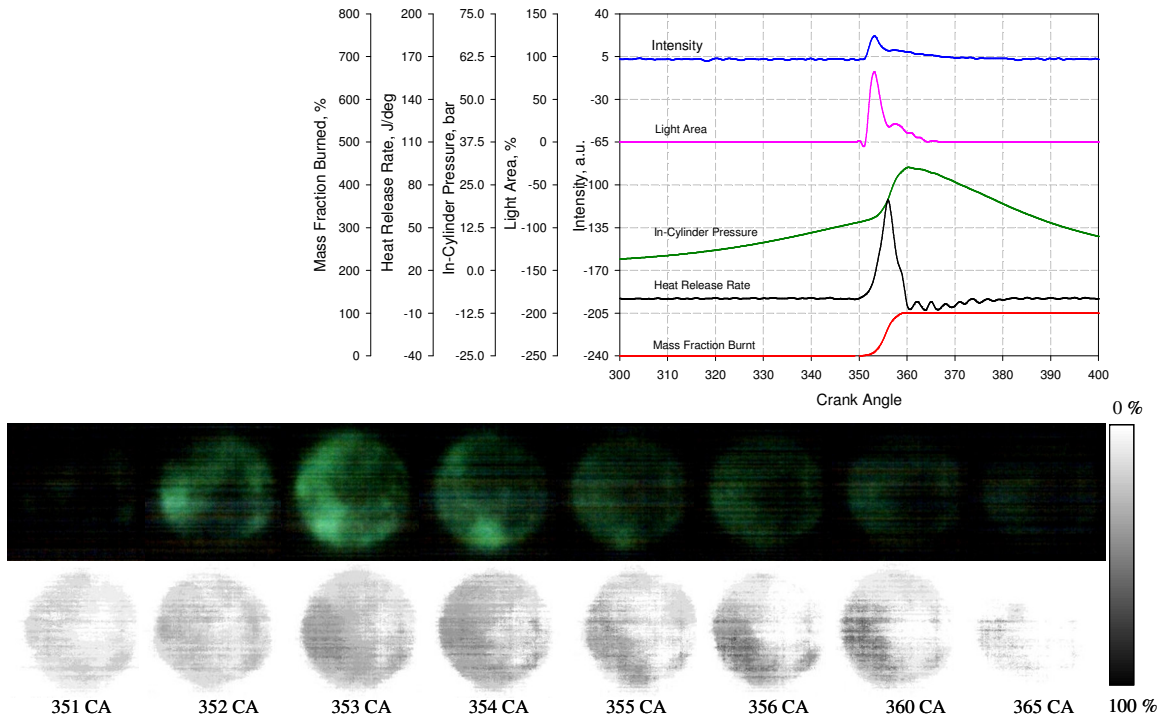


**Figure 5.32 CHO Chemiluminescence Image of M20 without Spark-Assisted Ignition**

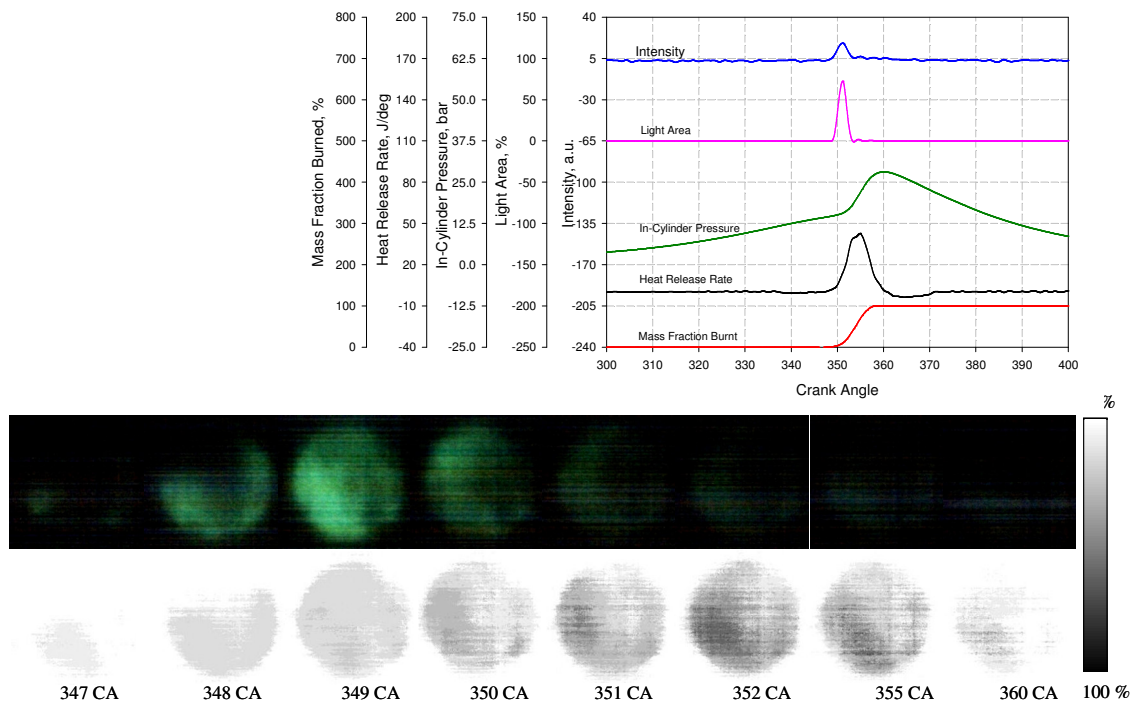


**Figure 5.33 CHO Chemiluminescence Image of E50 without Spark-Assisted Ignition**

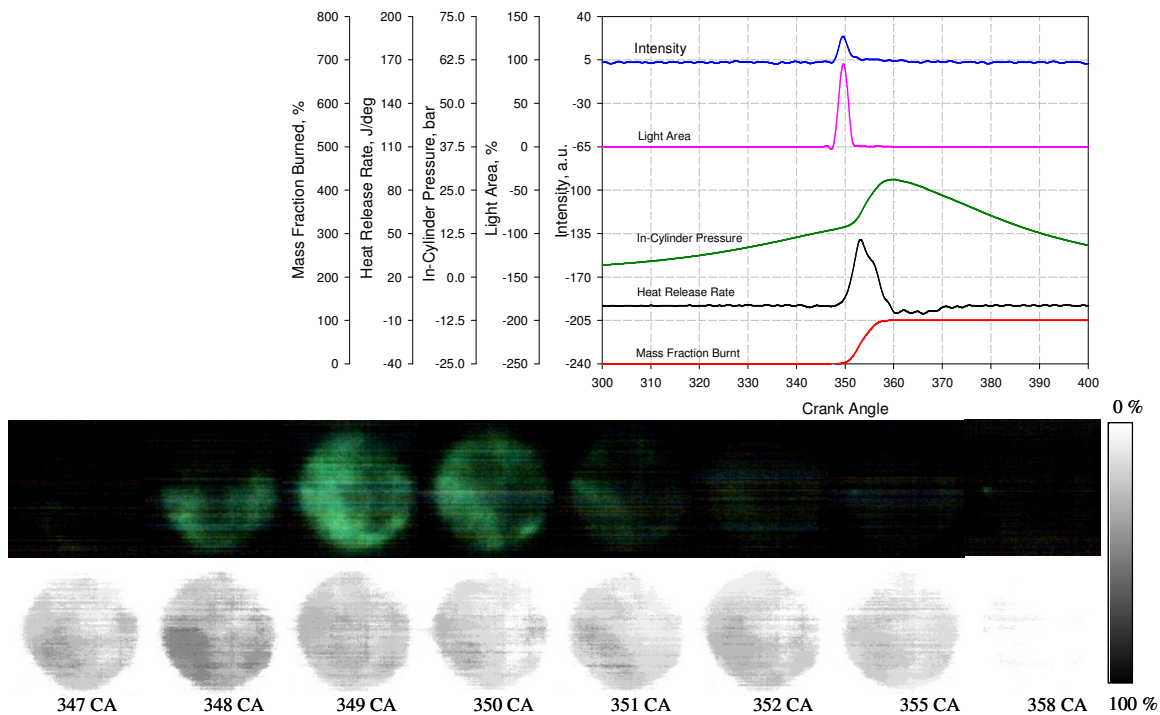


**Figure 5.34 CHO Chemiluminescence Image of M50 without Spark-Assisted Ignition**

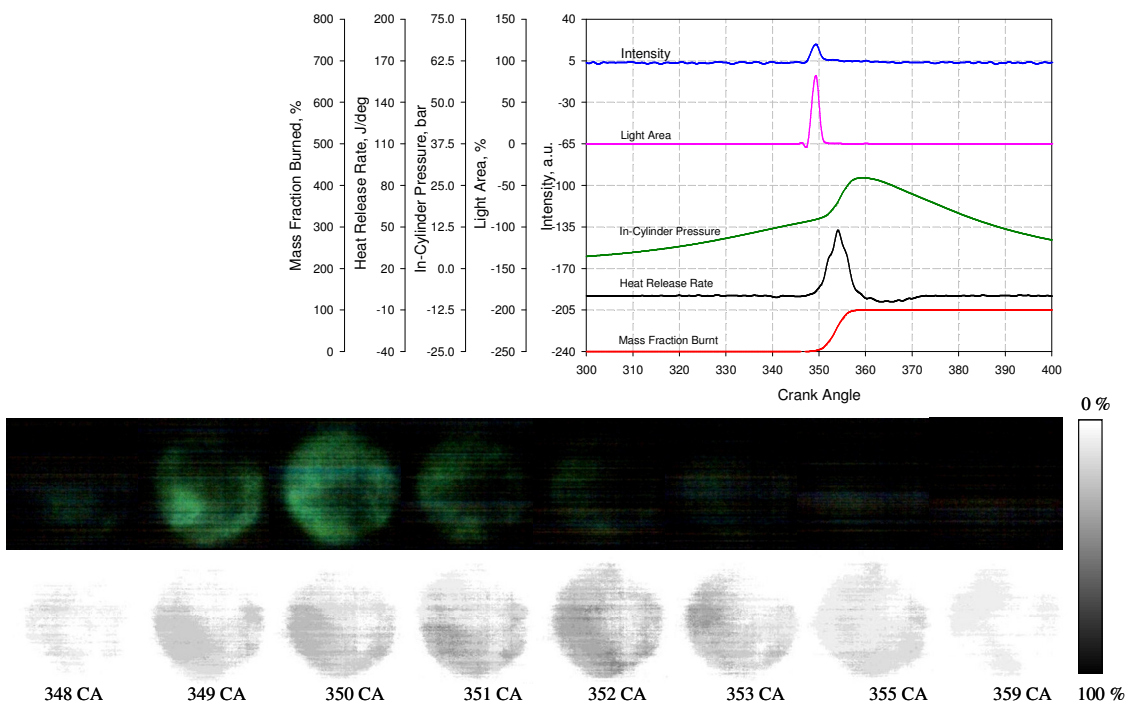


**Figure 5.35 CHO Chemiluminescence Image of E85 without Spark-Assisted Ignition**

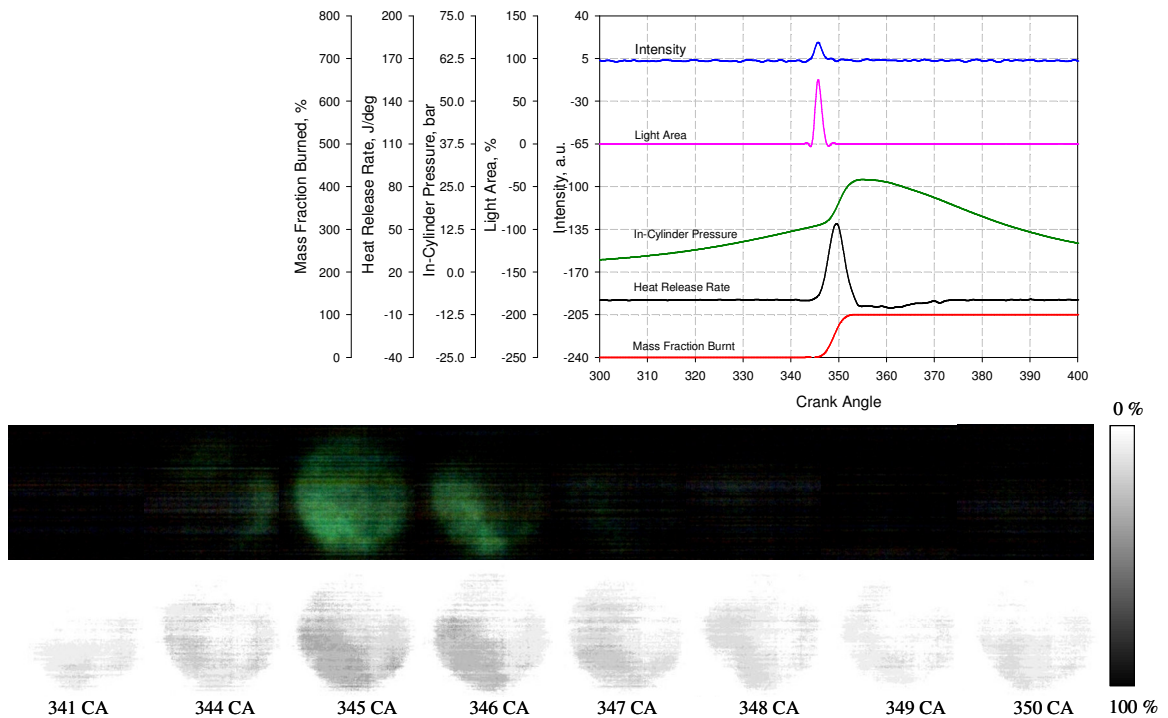


**Figure 5.36 CHO Chemiluminescence Image of M85 without Spark-Assisted Ignition**

### 5.3.3 OH Chemiluminescence Images

#### 5.3.3.1 Spark-Assisted Ignition

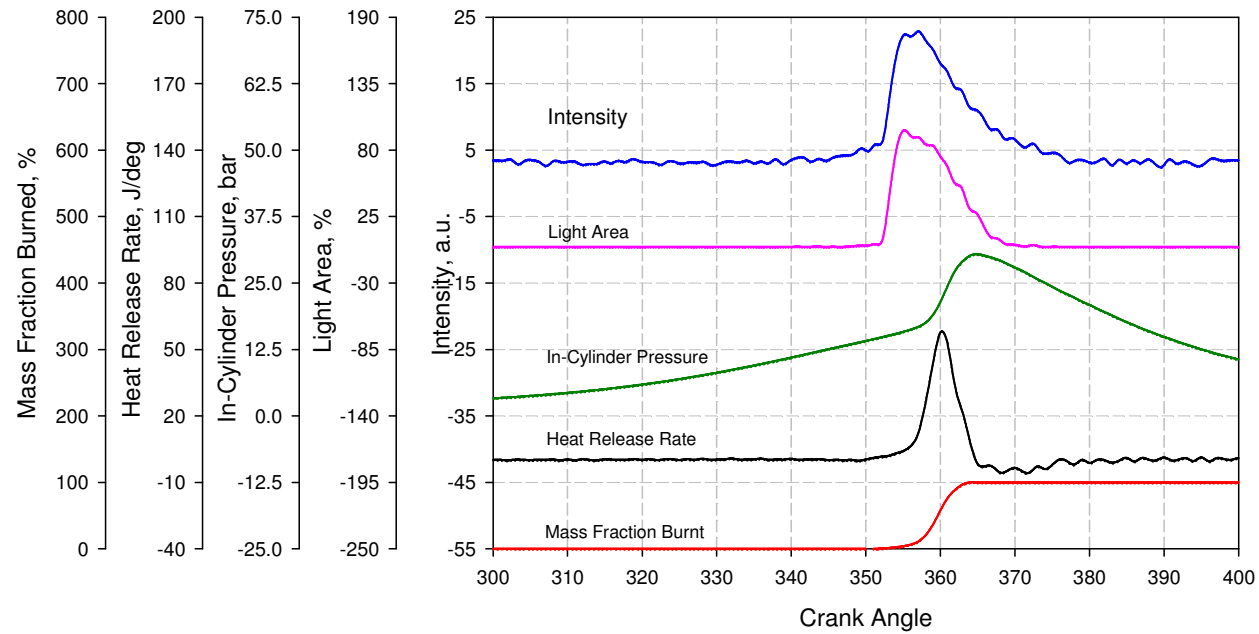
##### Gasoline

Figure 5.37 presents the OH chemiluminescence images of gasoline combustion with spark-assisted ignition. Although the gain of the intensifier was adjusted to its maximum level, no OH emission could be detected during the negative valve overlap period.

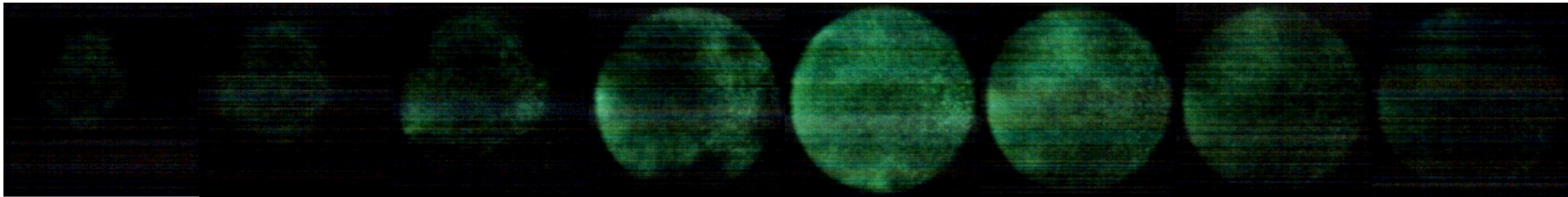
During the main combustion, the first OH chemiluminescence is shown at nearly the same crank angle as that of CHO but much later than that of the total emission. Due to the spark-assisted ignition, simultaneous CHO and OH formation was detected, as Noguchi et al [2] observed in their typical two-stroke SI combustion. Comparison

with CHO images show that OH emission diminished earlier than CHO. This may be caused by the later auto-ignition combustion at lower combustion temperature.

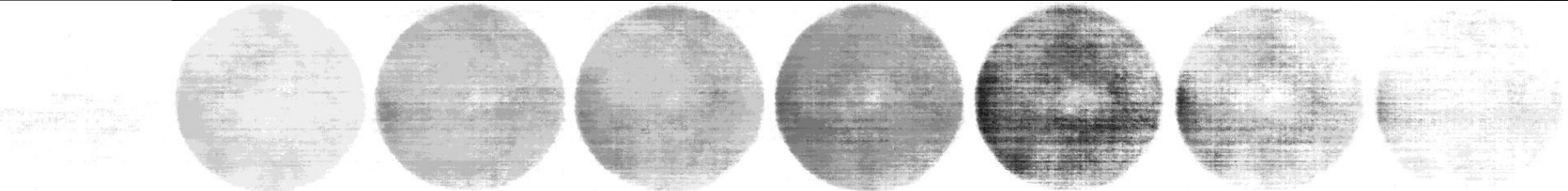
OH emission starts to appear slightly later than the beginning of the main heat release in terms of the light area curves. However, its subsequent disappearance follows the termination of the heat release process. Therefore, OH formation can be used as an indicator of high temperature combustion, as the previous literature shows.



Direct Images



Probability Images



347 CA      350 CA      352 CA      353 CA      355 CA      360 CA      365 CA      370 CA

0 %



100 %

**Figure 5.37 OH Chemiluminescence Image of Gasoline with Spark-Assisted Ignition**

## Ethanol

Figure 5.38 shows the OH emission images of ethanol with spark-assisted combustion. The first appearance of OH emission (348 degrees CA) is at nearly the same time as that of the CHO images (347 degrees CA) because of the predomination of spark discharge. Compared with gasoline combustion, OH emission from ethanol yields the lower average intensity. Two reasons could be responsible for this. From the study of Benvenuti et al [98], the  $H + O_2 \rightarrow O + OH^*$  is the most important reaction in ethanol. Gasoline, on the other hand, has many more molecules and reaction pathways to create OH. Secondly, the OH radical is formed during high temperature combustion and is highly temperature dependent. OH production is favoured at high temperature [54]. Therefore, as shown in Figure 4.15 of thermodynamic engine test, the lower maximum temperature of ethanol discouraged the formation of OH.

The light intensity shows the formation of OH occurs just after the main heat release, the same as for gasoline. However, the OH radical is consumed earlier, confirming the faster combustion of ethanol.

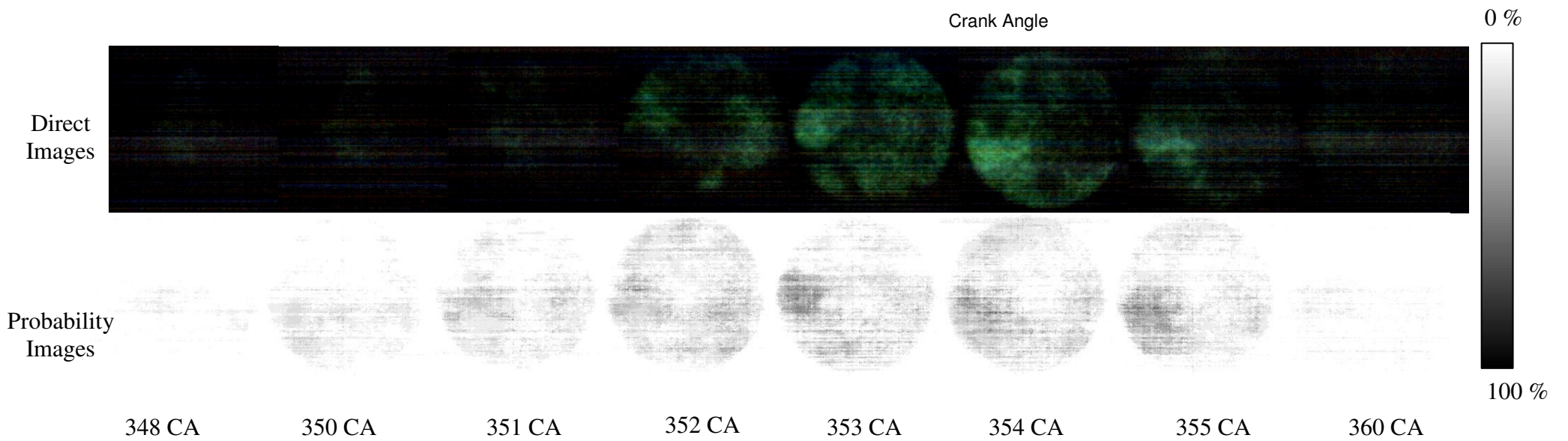
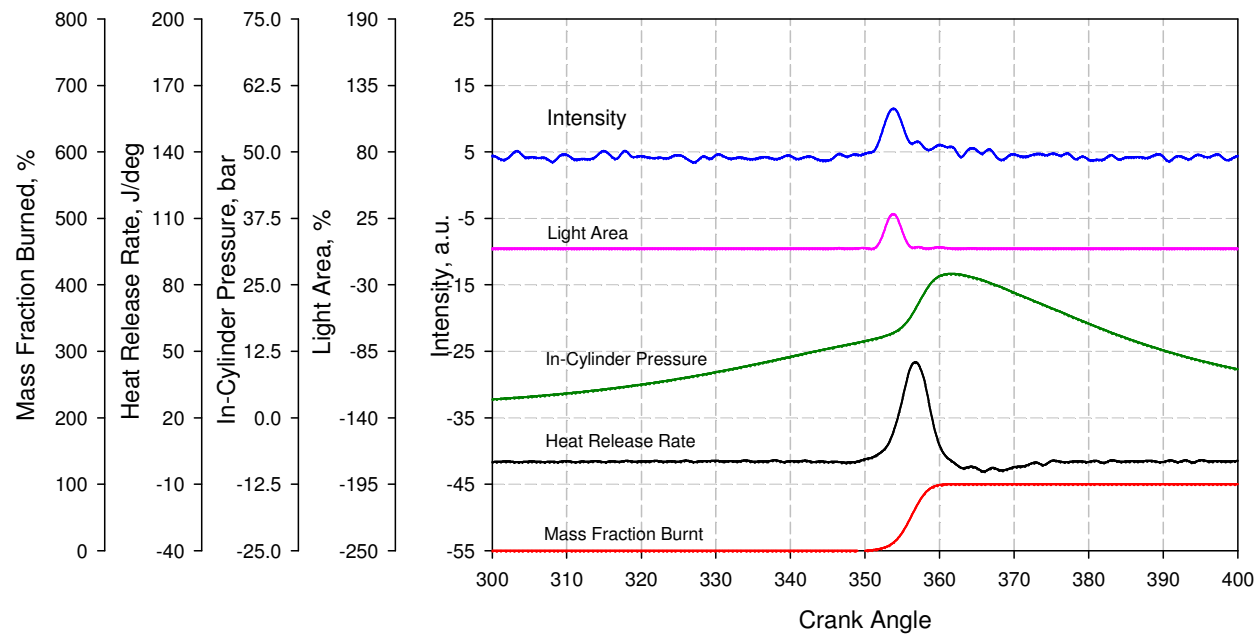


Figure 5.38 OH Chemiluminescence Image of Ethanol with Spark-Assisted Ignition

## **Methanol**

OH images of methanol combustion with spark-assisted ignition are shown in Figure 5.39. With the limited gain range of the intensifier, only poor images of the OH emission were captured. The images show different characteristics compared with gasoline and ethanol, whereby the first visible signal of OH (348 degree CA) appears later than that of CHO chemiluminescence (345 degree CA). This is a characteristic of combustion in which auto-ignition dominates.

Moreover, the lowest OH concentration can be confirmed with the highest carbon monoxide emission in Figure 4.20, which is due to insufficient OH being generated from lower peak in-cylinder temperatures for oxidizing CO as Dec et al stated [52]

It is noted that the first OH images occur at nearly the same time of about 347-348 degree CA for all three fuels. However, the termination of methanol is shown to be the earliest. With poor quality, the representative images show that OH radicals are distributed covering the centre to the perimeter at the bottom of the combustion chamber and then spread throughout the combustion chamber, except for the central region in which spark discharge plays the dominant role. The probability images also confirm this characteristic. Referring to the percentage of light area, the OH formation commenced after 5 % of total heat release. This indicates that OH radical can be used to represent as the start of combustion for methanol fuels.

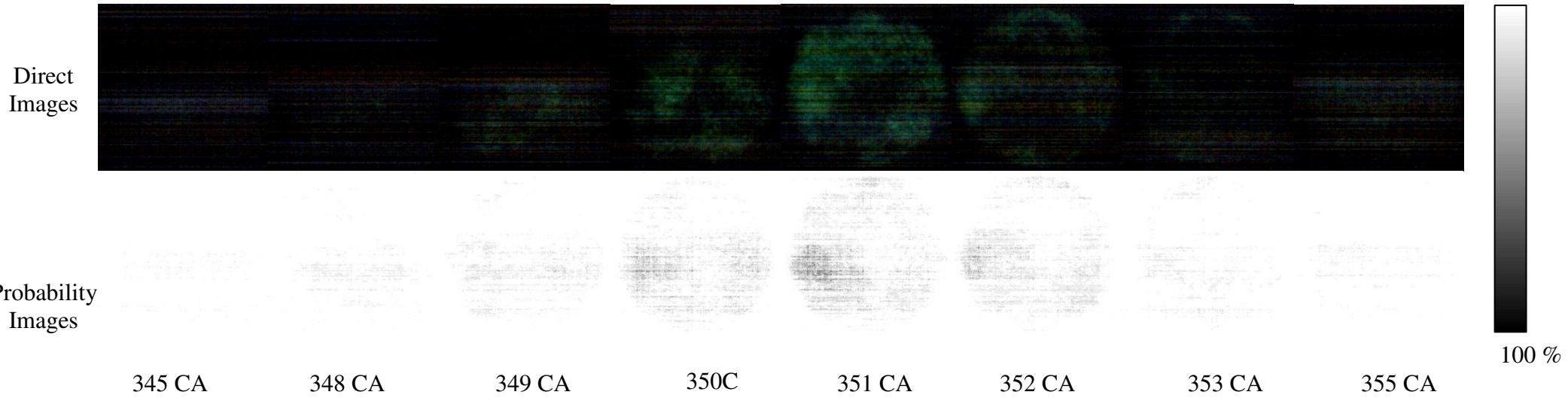
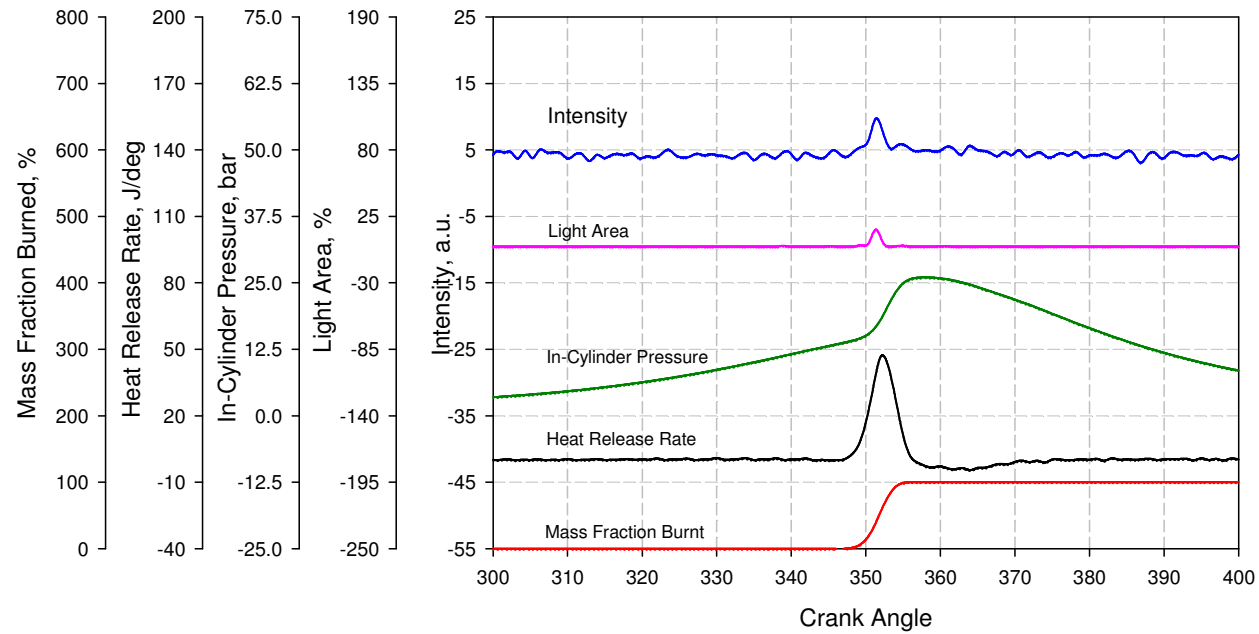


**Figure 5.39 OH Chemiluminescence Image of Methanol with Spark-Assisted Ignition**

## Blended Fuel (E20, E50, E85, M20, M50 and M85)

The effects of blended alcohol are shown in OH chemiluminescence images through Figures 5.40-5.45 for E20, M20, E50, M50, E85 and M85 respectively. The significant effect noticed is the average intensity. As the results discussed for ethanol and methanol, average light intensities decrease when the percentage of alcohol increases, in particular for methanol. Also, the amount of alcohol influences the relationship between the onset of OH formation and heat release process. From 20-85 %, the start of OH formation moves closer to the beginning of heat release and then occurs at 2% of total heat release with 85 % methanol. This effect remains evident with pure ethanol and methanol as discussed previously. Moreover, the duration of OH formation becomes shorter with increasing percentage of alcohol. The results correspond well with the fast combustion of oxygenated fuels.

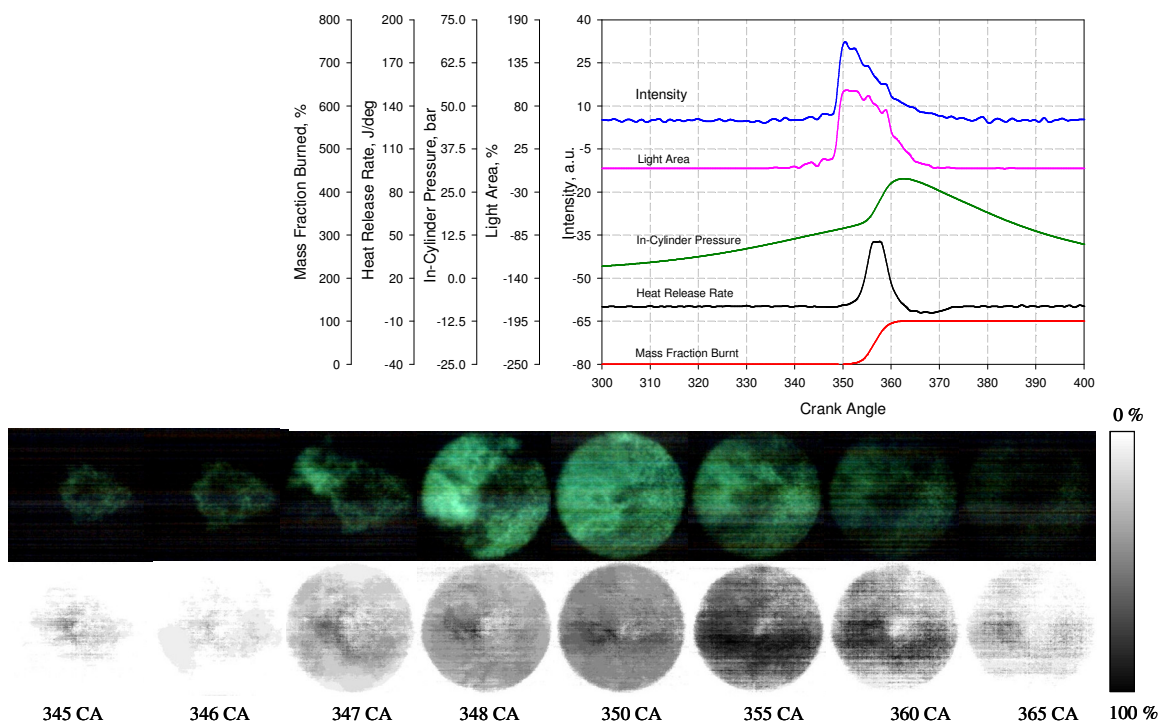
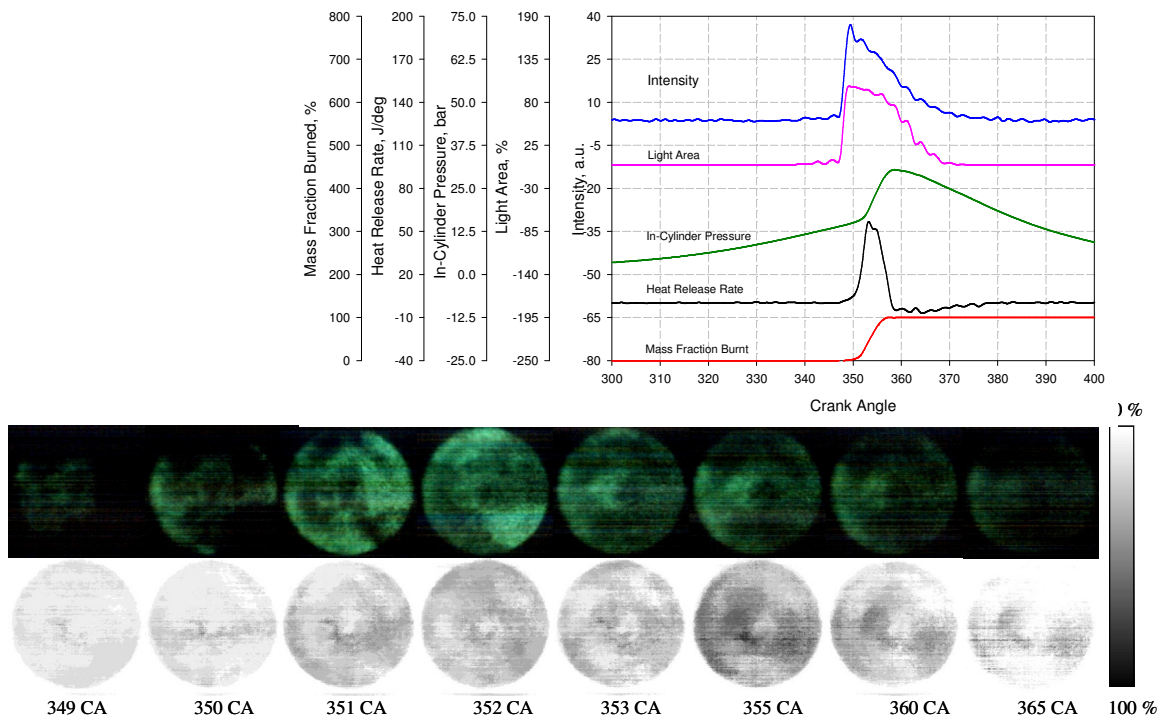
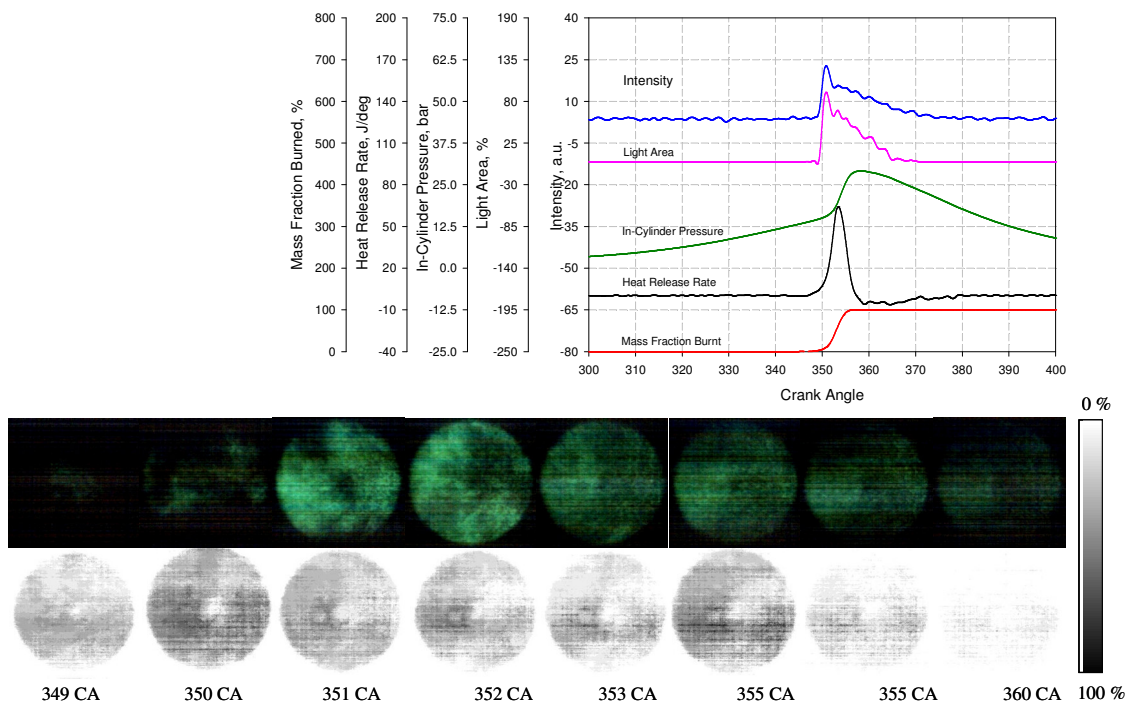


Figure 5.40 OH Chemiluminescence Image of E20 with Spark-Assisted Ignition



**Figure 5.41 OH Chemiluminescence Image of M20 with Spark-Assisted Ignition**



**Figure 5.42 OH Chemiluminescence Image of E50 with Spark-Assisted Ignition**

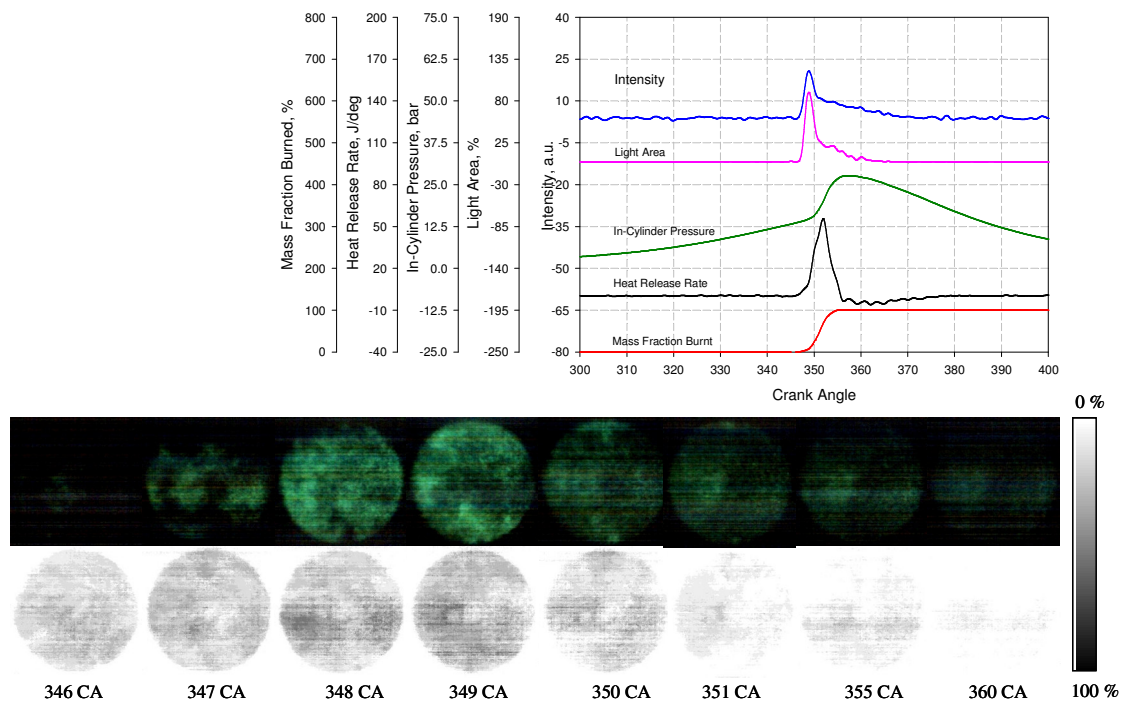


**Figure 5.43 OH Chemiluminescence Image of M50 with Spark-Assisted Ignition**

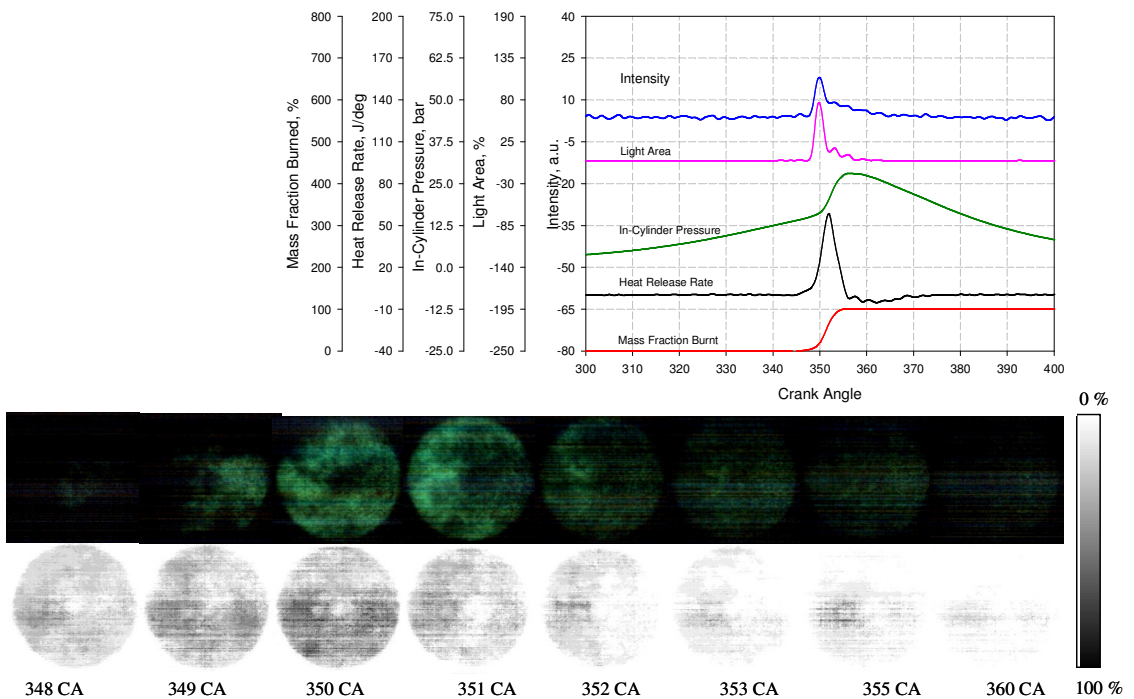


**Figure 5.44 OH Chemiluminescence Image of E85 with Spark-Assisted Ignition**

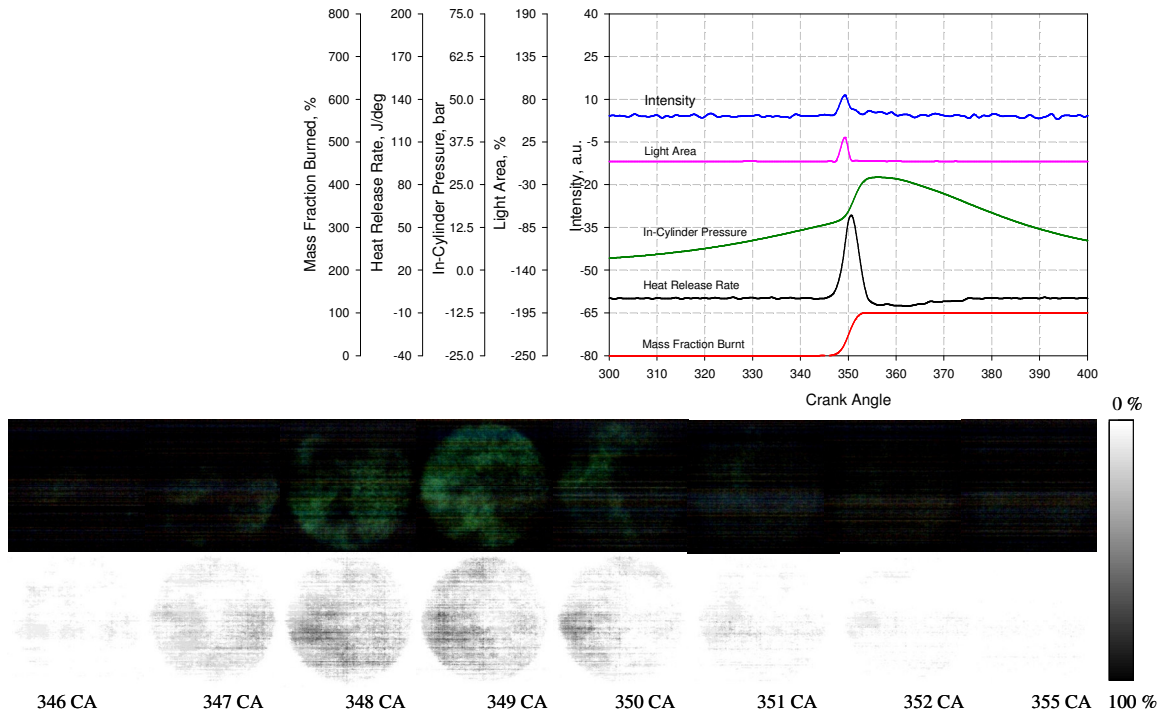


**Figure 5.45 OH Chemiluminescence Image of M85 with Spark-Assisted Ignition**

### 5.3.3.2 Non-Spark-Assisted Ignition

Figure 5.46 shows the OH chemiluminescence of gasoline without spark-assisted combustion. The images show dark areas forming a circular shape near the cylinder wall for every crank angle. This was caused by piston window fouling which blocked the transmission of OH emission. This is confirmed by the fact that the same locations and shape for all 15 cycles in this test.

Different from spark-assisted ignition, the first appearance of OH radical at 356 degree CA almost coincides with CHO at 354 degree CA and the total emission at 356 degree CA. OH radicals initially appear near the chamber wall and then continue forming throughout the whole chamber until 370 degree CA, when chain-branching reactions stop though the total chemiluminescence persists longer due to the light emission of CH, C or other species

According to the light area results, the formation of OH begins after the heat release has reached 3 % of its total value.

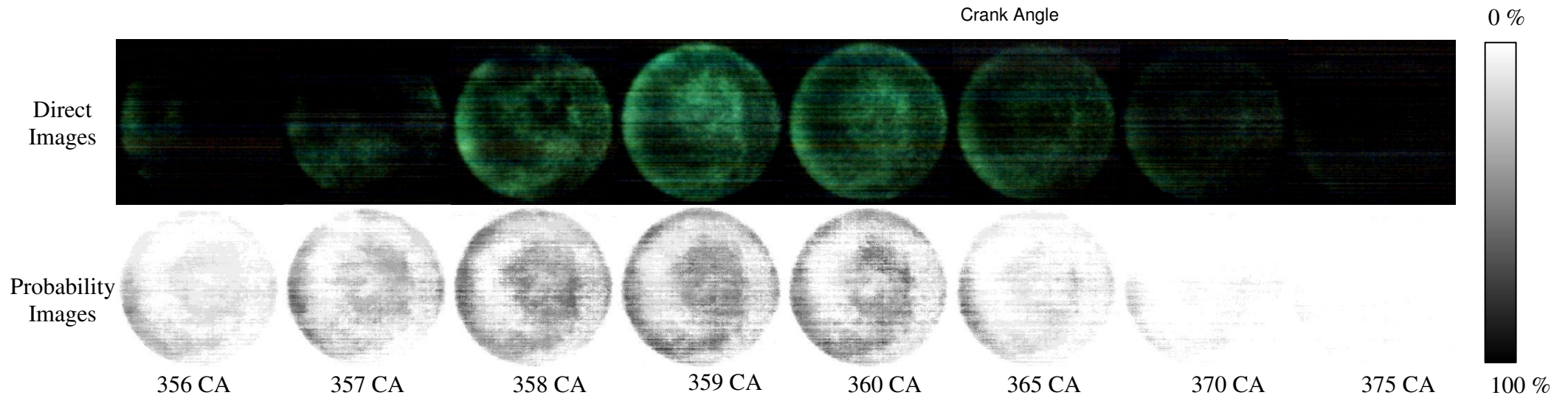
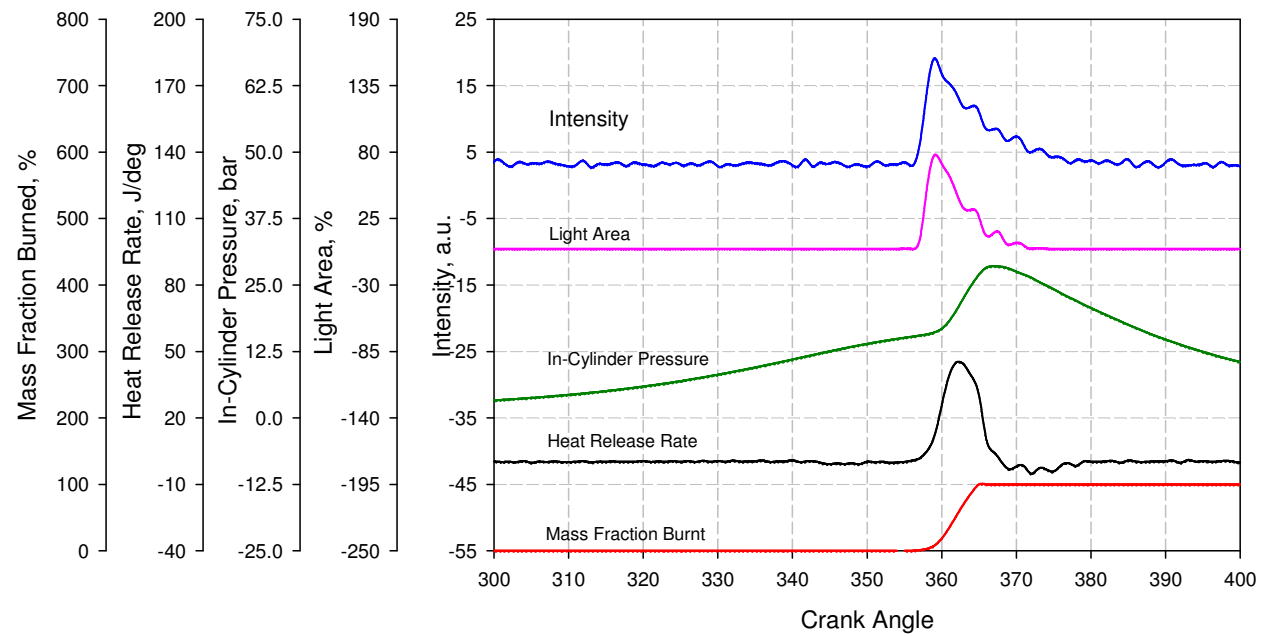


**Figure 5.46 OH Chemiluminescence Image of Gasoline without Spark-Assisted Ignition**

## **Ethanol**

Figure 5.47 presents the OH chemiluminescence images of ethanol combustion without spark discharge. Similar to gasoline, the OH formation appear after CHO emission. However, its intensity is lower than that of gasoline, the same results shown in the spark-assisted ignition case. Moreover, OH emission from ethanol combustion is earlier than that of gasoline. The start of OH formation happens at the same time as the start of heat release. The short duration of OH appearance confirms the fast combustion of ethanol.

## **Methanol**

Figure 5.48 demonstrates the relatively weak OH chemiluminescence signal of methanol combustion without spark ignition. Although the signal is very low, the images show that OH emission always appears after CHO. Moreover, the combustion process of methanol is faster and earlier than the other fuels. Methanol shows the lowest OH concentration during combustion.

## **Blended Fuel (E20, E50, E85, M20, M50 and M85)**

The effects of alcohol fuels in OH formation in pure CAI without spark discharge are shown in Figures 5.49 – 5.54. Similar to spark–assisted ignition, the intensity of OH decreases when the percentage of blended alcohol increases because of reduced OH formation pathways. However, the onset of OH formation for all blended fuels takes place after CHO. The average intensity curve and light area agree well with the heat release rate and mass fraction burned curves. However, the period of OH emission becomes shorter with increasing alcohol content.

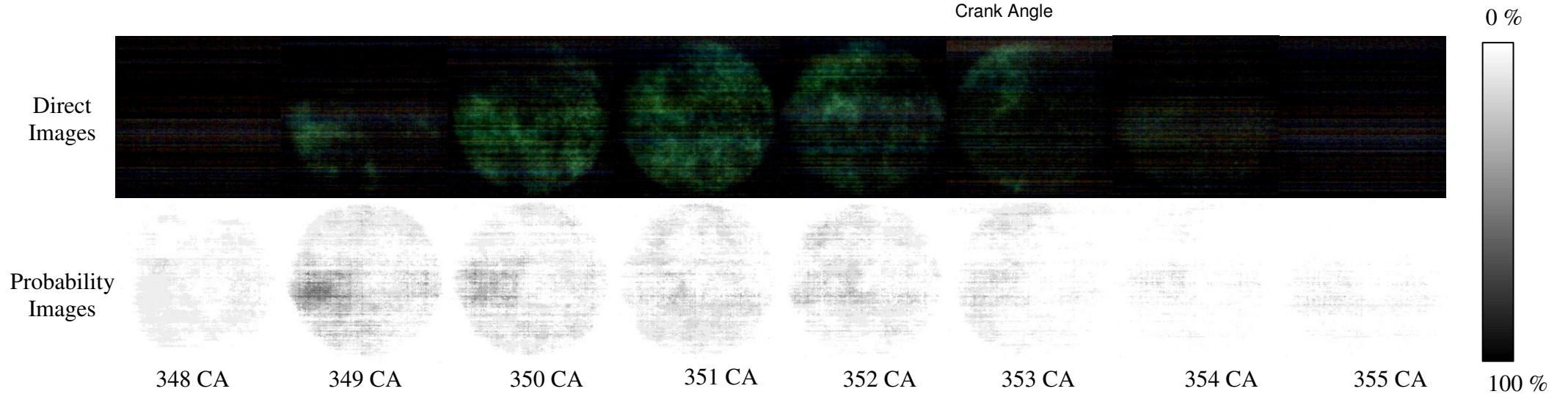
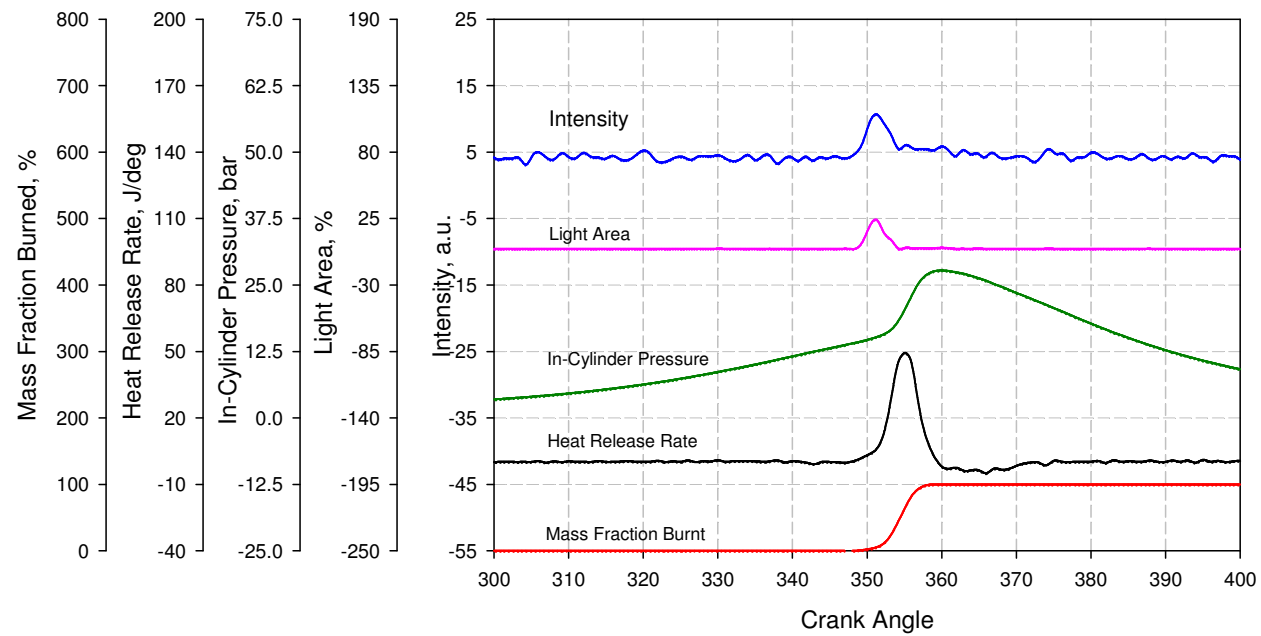
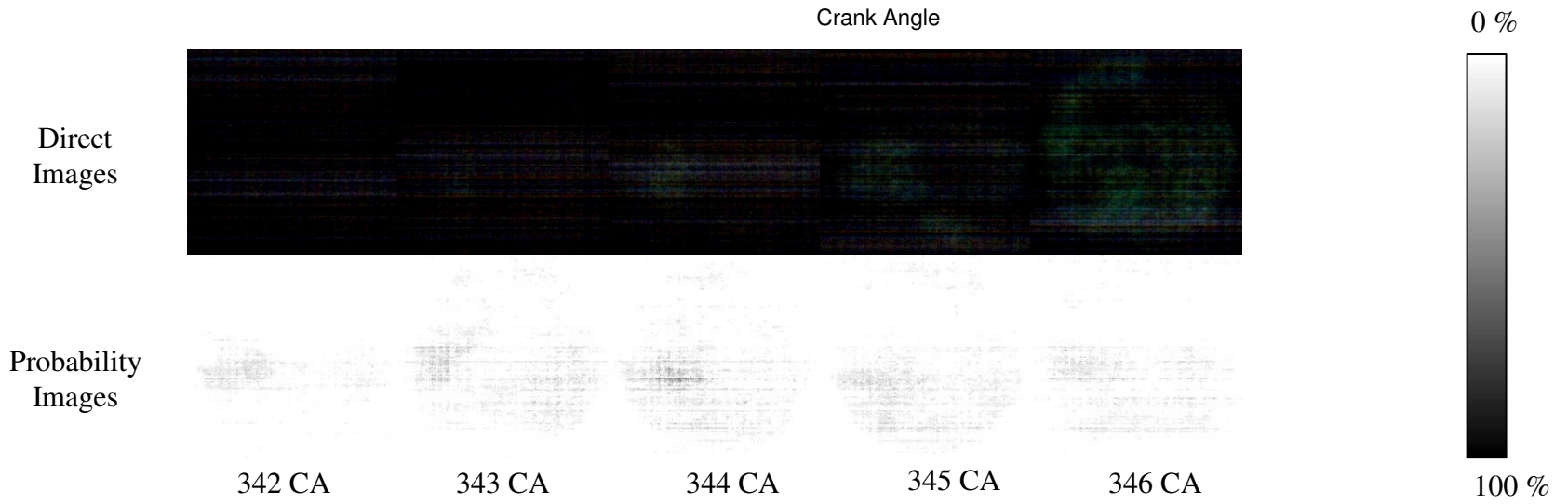
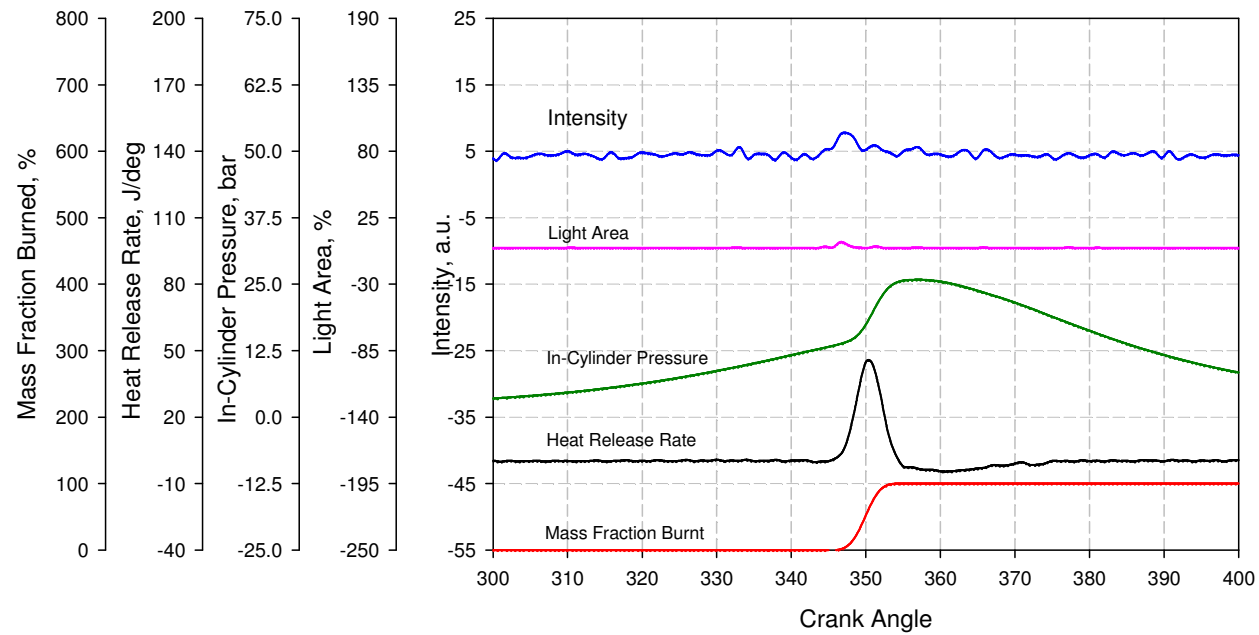
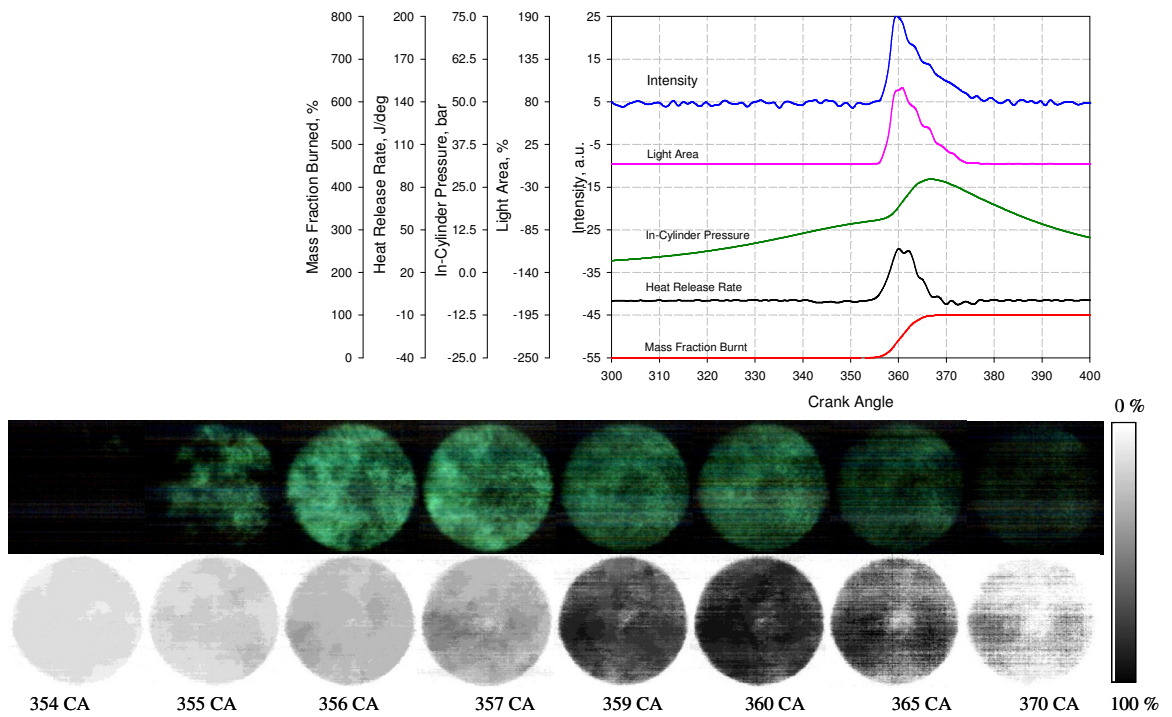


Figure 5.47 OH Chemiluminescence Image of Ethanol without Spark-Assisted Ignition



**Figure 5.48 OH Chemiluminescence Image of Methanol without Spark-Assisted Ignition**



**Figure 5.49 OH Chemiluminescence Image of E20 without Spark-Assisted Ignition**

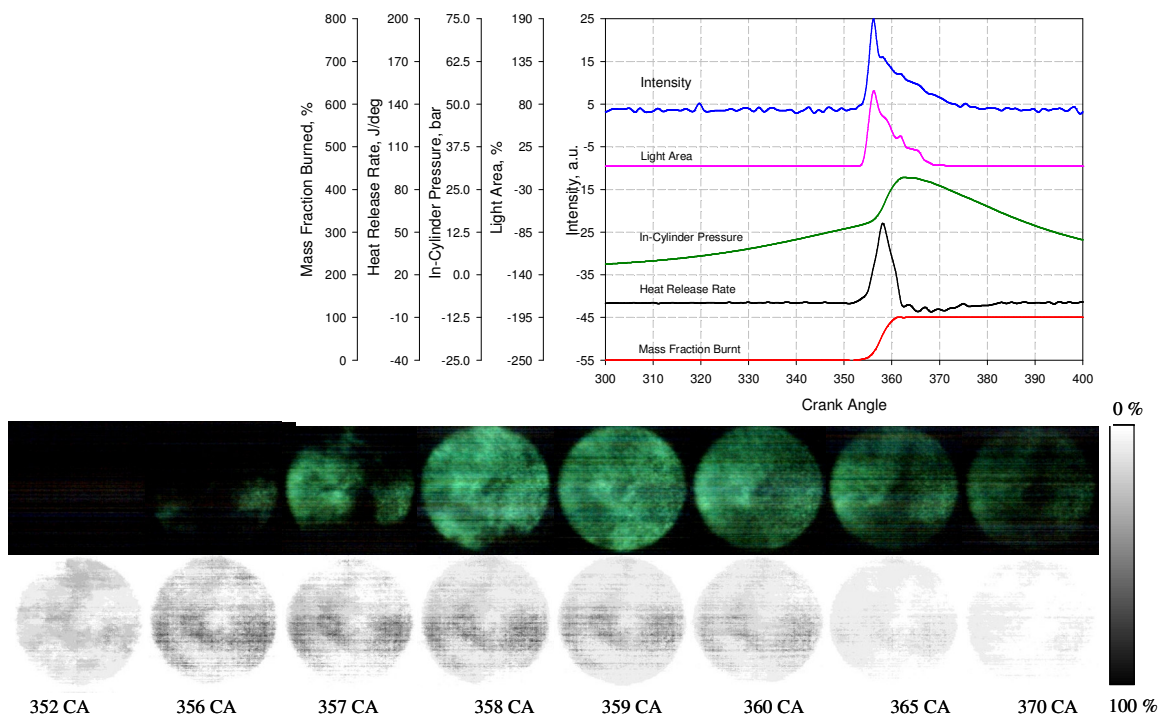


**Figure 5.50 OH Chemiluminescence Image of M20 without Spark-Assisted Ignition**

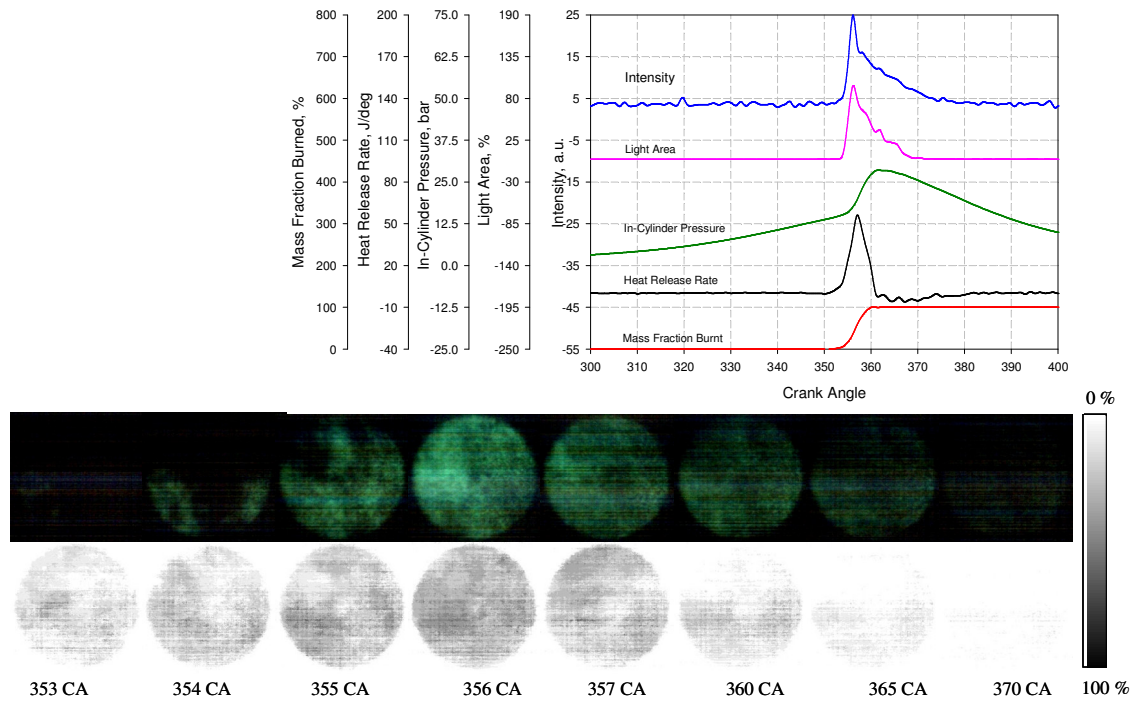


**Figure 5.51 OH Chemiluminescence Image of E50 without Spark-Assisted Ignition**

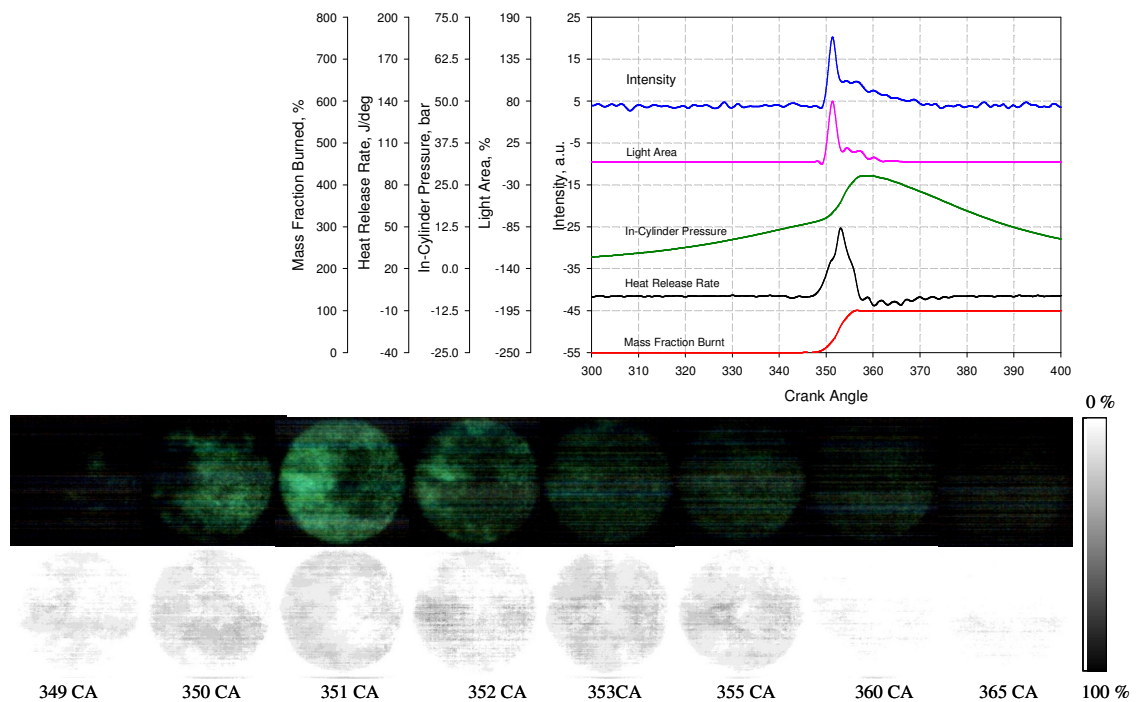


**Figure 5.52 OH Chemiluminescence Image of M50 without Spark-Assisted Ignition**

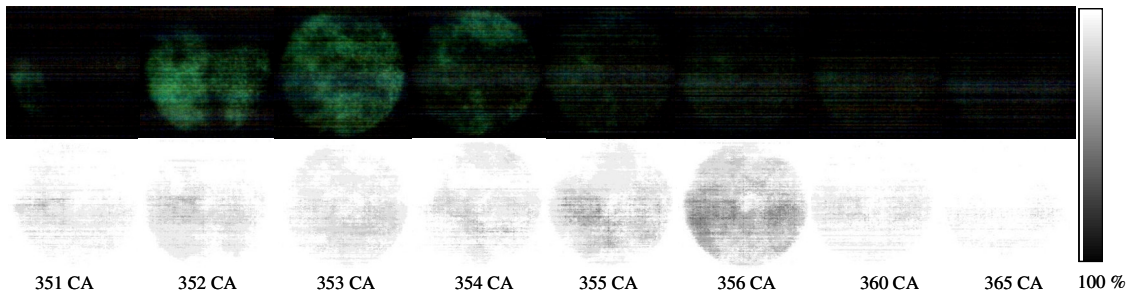
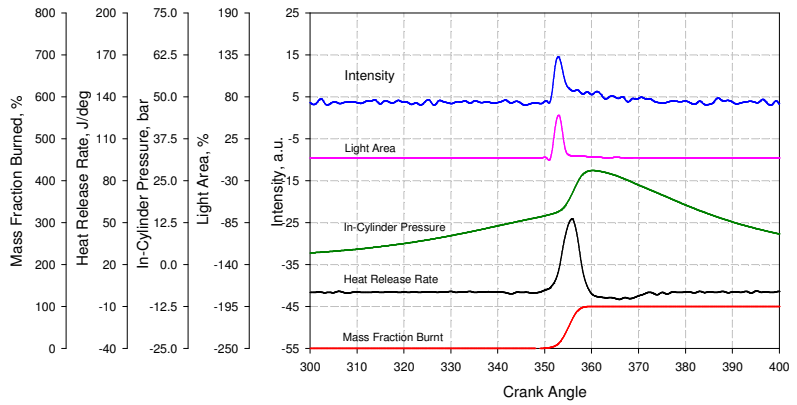


**Figure 5.53 OH Chemiluminescence Image of E85 without Spark-Assisted Ignition**

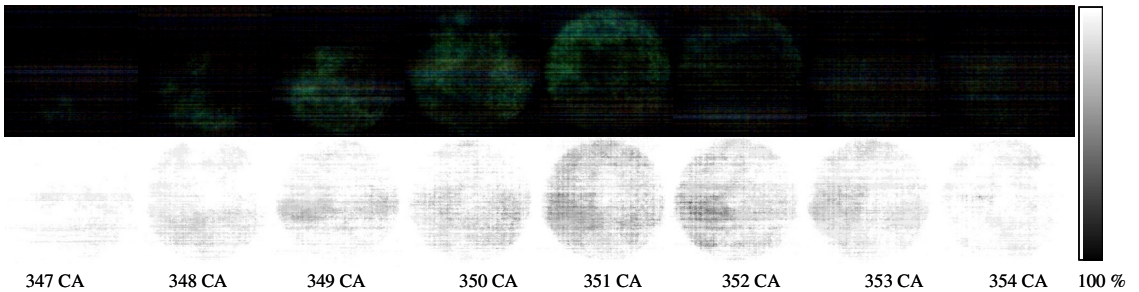
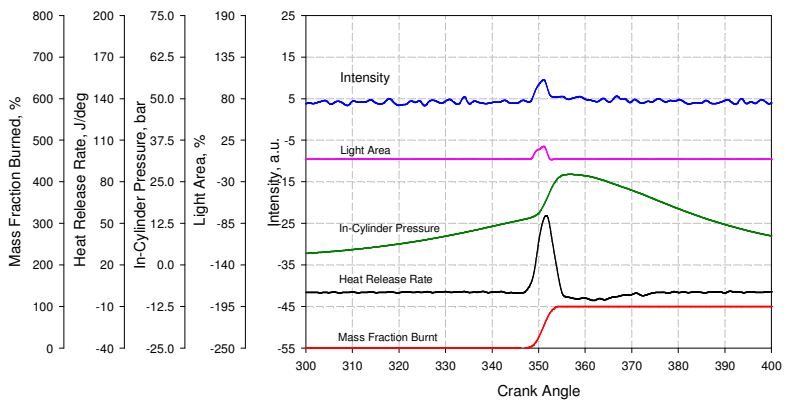


**Figure 5.54 OH Chemiluminescence Image of M85 without Spark-Assisted Ignition**

## 5.4 Summary

In this chapter, in-cylinder pressure and total, CHO as well as OH chemiluminescence results of methanol, ethanol, gasoline and their mixtures are presented and analysed. The heat release rate and the mass fraction burned data from the in-cylinder pressure measurements are compared with the high speed chemiluminescence images taken by an intensified high speed colour video camera. As a result, the effects of fuel properties and spark discharge on the combustion characteristics have been identified.

During the re-compression stroke, the heat release curves indicate more heat being released from directly injected alcohol fuels. However, no chemiluminescence was detected for alcohol fuels during this period. In comparison, gasoline fuel exhibited luminous emission but less heat release was registered by the heat release analysis. In-cylinder sampling and chemical kinetic analysis in the next chapter will be used to verify the presence and nature of the chemical reactions during the negative valve overlap period.

With certain mixture composition and temperature, spark discharge can advance the start of the heat release process and normally results in the location of ignition at the center of the chamber. As a result, flame propagation dominates the combustion at the early period followed by spontaneous auto-ignition for CAI combustion. Because of the high dilution rate, the flame propagates at a slow speed and accounts for a very small portion of the total heat released. The effect of spark discharge is prominently for the gasoline fuel but less for alcohol fuels. This is because the CAI combustion of alcohol fuels start earlier due to increased charge temperature caused by the heat released during the NVO period. When using oxygenated fuel, flame propagation diminished sooner due to earlier simultaneous self ignition of the charge mixture. With spark-assisted ignition, the light emission of CHO and OH takes place at nearly the same time and later than total chemiluminescence.

For pure CAI combustion, chemiluminescence images show that the perimeter area of the chamber is the preferred site for auto-ignition for all of the tested fuels. CHO formation occurs just before the OH species. On the other hand, OH terminates before CHO. CHO emission diminishes before total chemiluminescence. The average

intensity and light area of CHO emission terminate before the end of heat release. Moreover, due to reduced reaction pathways and resulting radicals, oxygenated fuels, particularly methanol, produce lower image intensity than gasoline.

## **Chapter 6 In-Cylinder and Exhaust Gas Species Analysis**

### **6.1 Introduction**

Chemical kinetic reactions play a vital role in controlling auto-ignition combustion. Measurement of gas compositions is a useful tool to better understand the chemical reactions involved in the CAI combustion. Chemiluminescence imaging, detailed in Chapter 5, detects the radiative emission from chemically excited molecules whilst the detailed gas composition is better measured by the GC-MS technique. First, exhaust speciation was conducted for various fuel blends using the GC-MS technique. In order to identify the in-cylinder species, a fast acting sampling valve was used to collect the in-cylinder gases at a given crank angle which were then analysed by a GC-MS.

Due to the time consuming process, in-cylinder sampling and species analyses were conducted for neat gasoline, methanol and ethanol. In addition, isooctane and 40/60 percent of n-heptane/isooctane blend (60 PRF) were included for comparison. The current study was focused on clarifying alkanes, alkenes, aldehydes and ketones compounds. With off-line gas chromatography, it is impossible to detect peroxide species which are important species in auto-ignition chemistry.

### **6.2 Test Methodology**

#### **6.2.1 Test Conditions**

In order to compare the results with the chemiluminescence imaging, injection timing was set at 80 degree BTDC during the NVO period. Measurement with gasoline was carried out for both with/without spark-assisted ignition. Ethanol, methanol and 60 PRF were used for pure CAI combustion engine operation. Due to unstable operation, spark-assisted ignition was examined when using isooctane as fuel. Engine speed and air/fuel equivalent ratio were kept constant throughout the experiment at 1600 rpm and  $\lambda = 1$ , respectively.

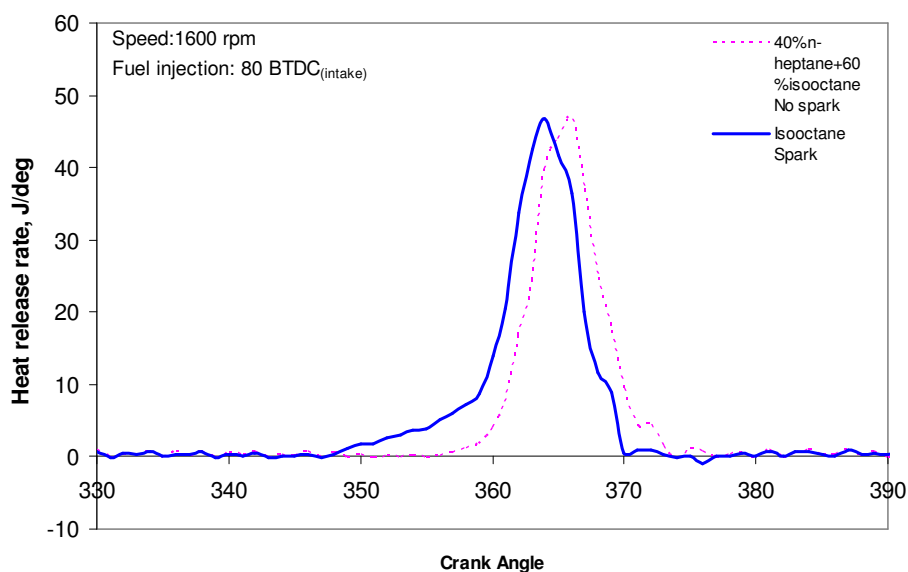


**Figure 6.1 Heat Release Rate of Isooctane and 60 PRF**

For detailed exhaust speciation analysis, eleven fuels were used in the experiments, including gasoline, ethanol and methanol blended fuels and single component hydrocarbon, isooctane and 60 PRF.

## 6.2.2 Experimental Procedure

Detailed species composition of exhaust gas emission was firstly analyzed to complement the thermodynamic results. Samples were taken from the same location as the exhaust gas analyser. Gas flowed into a sampling bag from the exhaust and then was taken for analysis by a GC-MS equipment.

Once exhaust gas speciation measurements were completed, time-resolved in-cylinder gas sampling measurements at different crank angles were carried out. During the in-cylinder sampling measurements, the engine was operated with the same fuel for all the experiment before the engine was dismantled and prepared for the next fuel. The positions and duration for sampling were adjusted by an Angle Set Unit before the test started. In order to withdraw the gas, the sample valve solenoid actuator was activated by a switch on the 24 volt power supply. It took about one minute to fill up the sampling bag. After the sample had been taken the 24 V power supply was switched off and the engine was stopped from running. The sampling gas in the bag was then

injected into the GC-MS by a gas type hypodermic syringe of 9 ml volume. The results were displayed and recorded by a Mass Lab computer base software after 30 minutes controlled operation. Once each measurement finished, the GC-MS was cleaned to make sure that no residual species retained in the column which could contaminate the next measurement. GC-MS was then run without any injected gas before the next measurement.

Since the sampling valve was positioned horizontally in the centre of the side window, the sampling process was limited by the position of the piston crown. The piston crown would reach the sampling valve position at 54 degree BTDC. Taking into account of the opening period, the most retarded crank angle position which could be used was 60 degree BTDC. There are eighteen positions for the valve to extract the gas in every 30 degree increment from 60 degree BTDC during the compression and expansion stroke as seen in Figure 6.2. Unfortunately, the experiments could not be performed during 120 and 150 degree ATDC of the intake stroke due to insufficient in-cylinder pressure to push the gas into the valve.

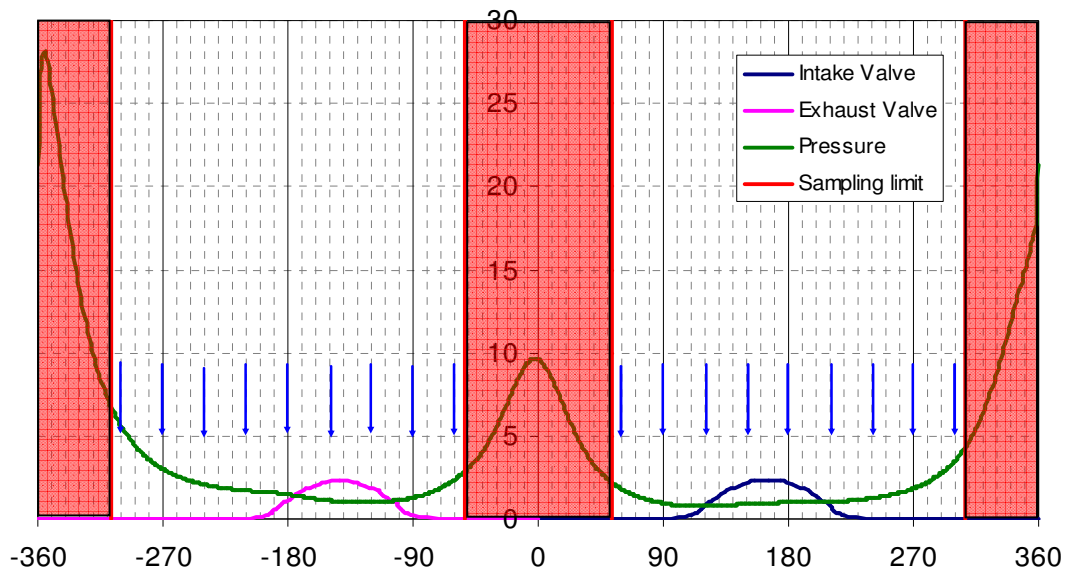


**Figure 6.2 Sampling Positions**

The valve opening duration depended on the in-cylinder pressure for a preset electrical drive current and varied with crank angle as shown in Table 6.1.

Sampling Position (TDC)	Sampling Duration (CA)		Sampling Position (TDC)	Sampling Duration (CA)
-300	8.0		60	16.5
-270	10.3		90	26.8
-240	15.0		120	-
-210	12.3		150	-
-180	16.5		180	23.5
-150	19.2		210	16.7
-120	19.2		240	11.3
-90	17.6		270	10.3
-70	11.7		300	8.0

**Table 6.1 Sampling Duration at Each Crank Angle**

## **6.3 Results and Discussion**

### **6.3.1 GC-MS Spectrum of the Standard Gas**

Known concentrations of standard gases comprising of alkane, alkene (C1-C6 hydrocarbon) and 1, 3-butadiene as detailed in Table 3.5 were used for calibration. Their retention time and area of peak chromatograms were used to identify and quantify the species of sample gases. In general, at least three different concentrations of each standard gas were required for accurate measurement. However, only one known concentration of standard gas was sufficient for this work. Table 6.2 summarizes the retention time of each compound in the standard gas and also Figure 6.3 presents peak chromatogram for each retention time.

Peak Number	Compound	Retention Time RT (min)	Peak Number	Compound	Retention Time RT (min)
1	Air	1.754	10	Butene	12.012
2	Methane	1.966	11	1,3-Butadiene	12.154
3	CO2	2.477	12	Butane	12.409
4	Ethene	3.298	13	Pentene	15.710
5	Ethane	3.879	14	Pentane	16.065
6	Water	5.651	15	Hexene	18.884
7	Propene	7.648	16	Hexane	19.153
8	Propane	8.031	17	Benzene	19.777
9	Cyclopropane	8.527			

**Table 6.2 Retention Time of Each Compound in the Standard Gas**

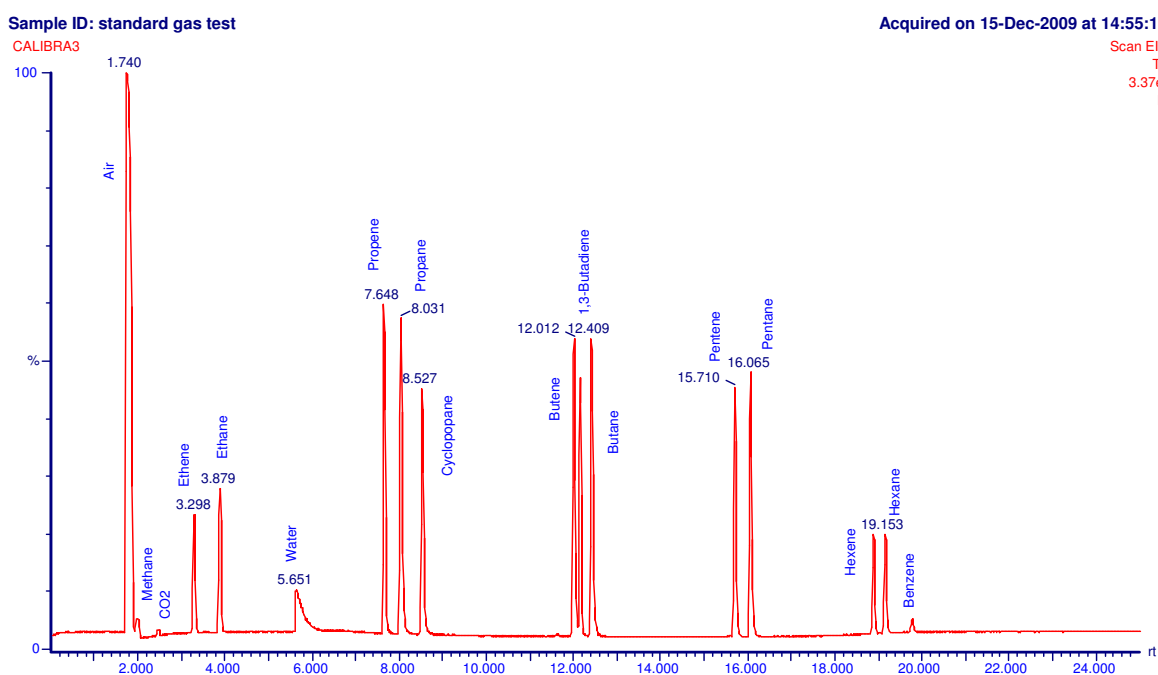


**Figure 6.3 Retention Time and Peak chromatogram of each Compound in the Standard Gas**

In the following results, gas species contained in the standard gas will be presented in % and those not calibrated will be shown in arbitrary unit (a.u.).

### 6.3.2 Engine-Out Exhaust Gas Speciation

Before the in-cylinder sampling measurement was carried out, exhaust gas speciation was performed. The exhaust gas sample was taken by the Telda sampling bag covered with a black bag, with one minute sampling time. Then, a hypodermic syringe was used to transfer the sample into GC-MS. Subsequently, peak gas chromatogram was plotted by the Mass lab program. By comparing to the retention times of standard gases in conjunction with library search spectra of the Mass lab program, sampled species could be identified. For quantitative analysis, area under each peak chromatograms was calculated and compared to a known concentration of the standard gas. Chromatograms of species from the exhaust of gasoline, ethanol, methanol, isooctane and 60 PRF are illustrated in Figure 6.4 and 6.5 with/without spark discharge, respectively.

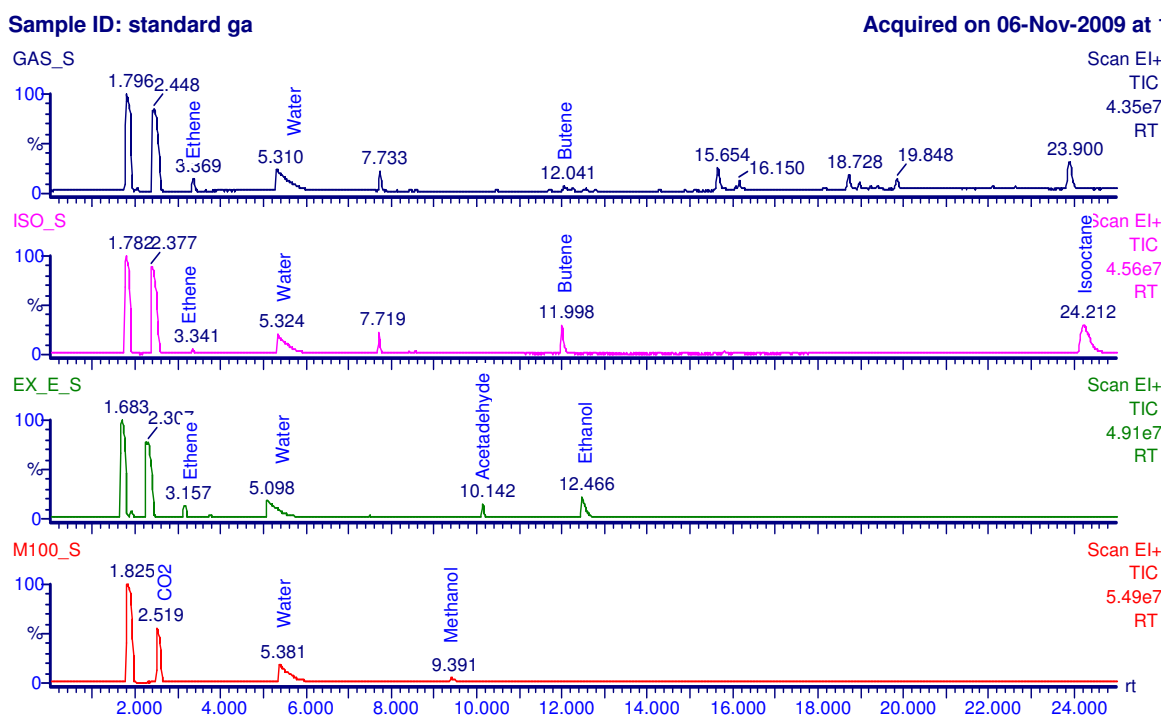
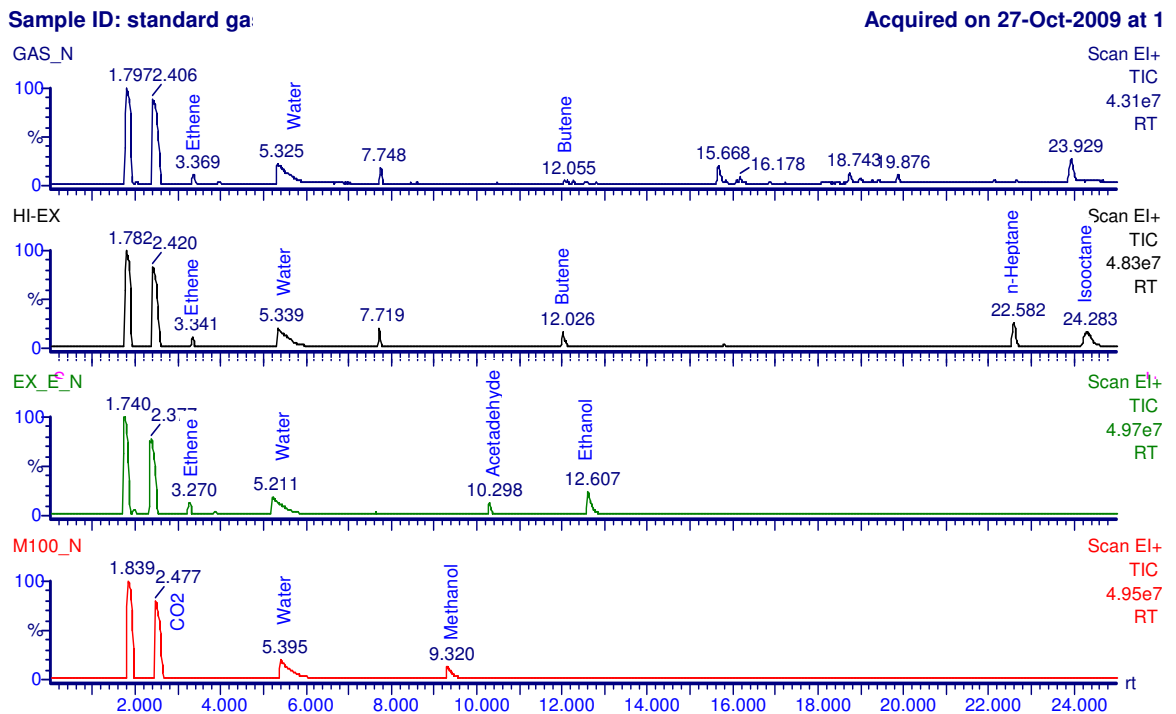


Figure 6.4 Chromatogram of Gasoline (top), Isooctane (2<sup>nd</sup> order), Ethanol (3<sup>rd</sup> order) and, Methanol (bottom) with Spark -Assisted Ignition



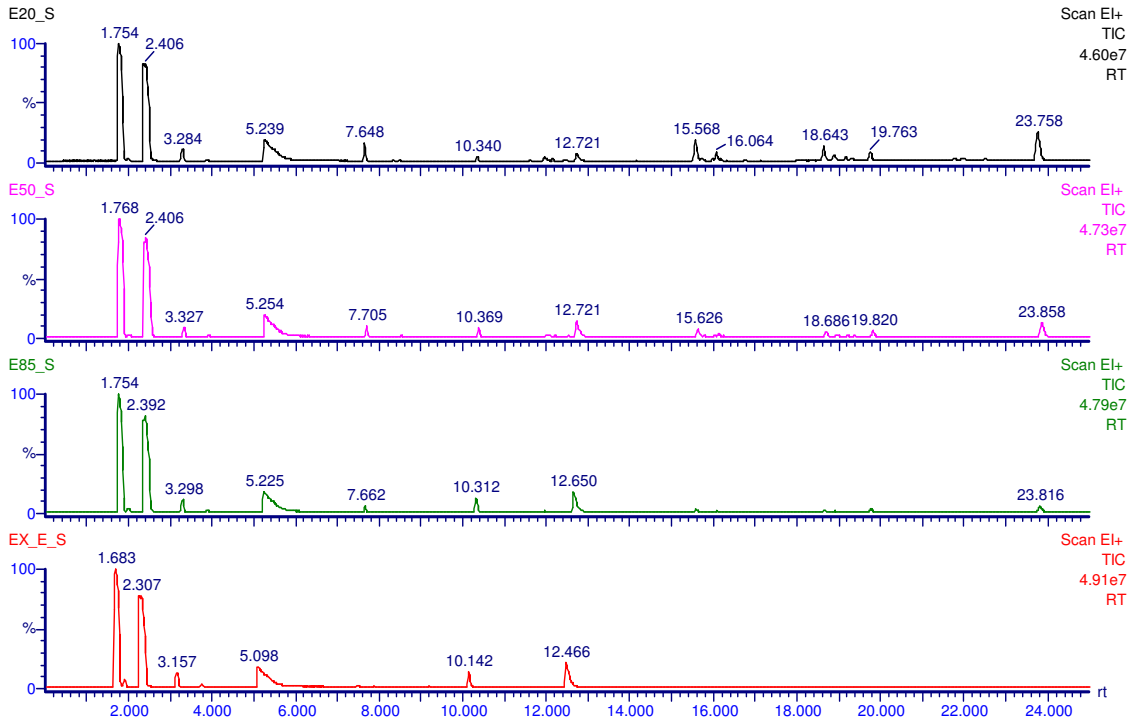
**Figure 6.5 Chromatogram of Gasoline (top), 60 PRF (2<sup>nd</sup> order), Ethanol (3<sup>rd</sup> order) and, Methanol (bottom) Without Spark -Assisted Ignition**

The presence of spark did not have any effect on the exhaust gas composition and hence the following discussions will be applicable to both pure and spark-assisted CAI operation. Because of the presence of various hydrocarbon components in gasoline, gasoline exhaust chromatogram exhibits many more peaks of species than neat alcohols. Both alcohol fuels produced the same exhaust species but at different concentrations, including aldehyde, low molecular weight of olefin and alkane with less than C<sub>3</sub>. Of interest, formaldehyde was detected at significant amount from methanol exhaust whilst ethanol exhaust contained a large concentration of acetaldehyde. This corresponds with the results of Houilang et al [64]. The reason for these two aldehydes will be explained later in this chapter.

In order to see the effect of amount of alcohol fuels on engine-out emissions, exhaust gases from blends of gasoline and alcohol were also analysed. The peak chromatograms are shown in Figure 6.6 and 6.7 for gasoline ethanol blend and gasoline methanol blend, respectively.

Sample ID: standard gas te

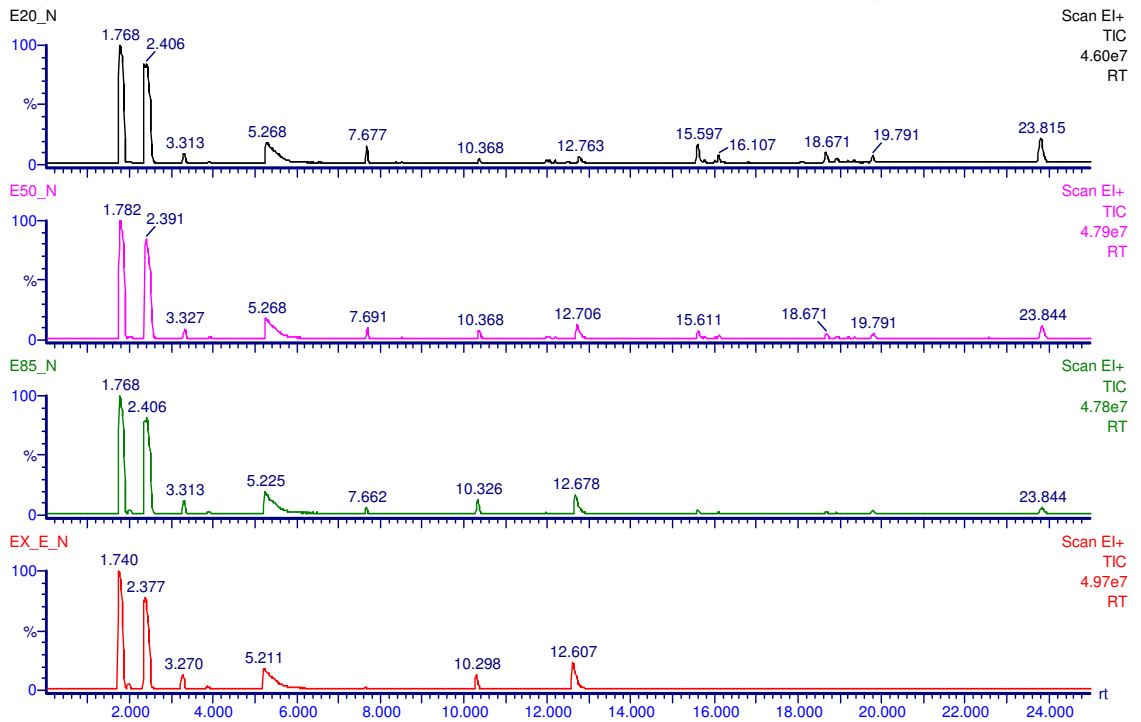
Acquired on 05-Oct-2009 at 10:46



(a)

Sample ID: standard gas te

Acquired on 05-Oct-2009 at 11:50

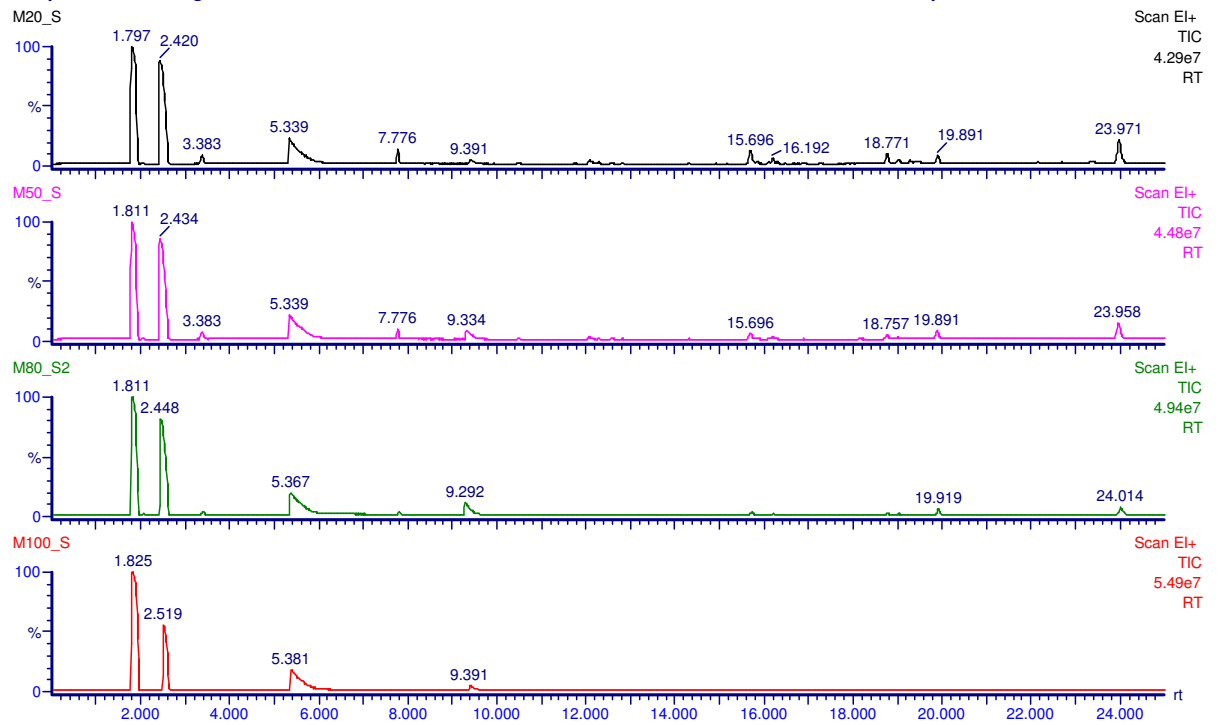


(b)

Figure 6.6 Chromatogram of Blended Ethanol: 20, 50, 85 and 100 from Top to Below (a) Spark-Assisted Ignition (b) Without Spark-Assisted Ignition

Sample ID: standard gas test

Acquired on 26-Oct-2009 at 12:22:0:



(a)

Sample ID: standard gas tes

Acquired on 26-Oct-2009 at 13:41:5

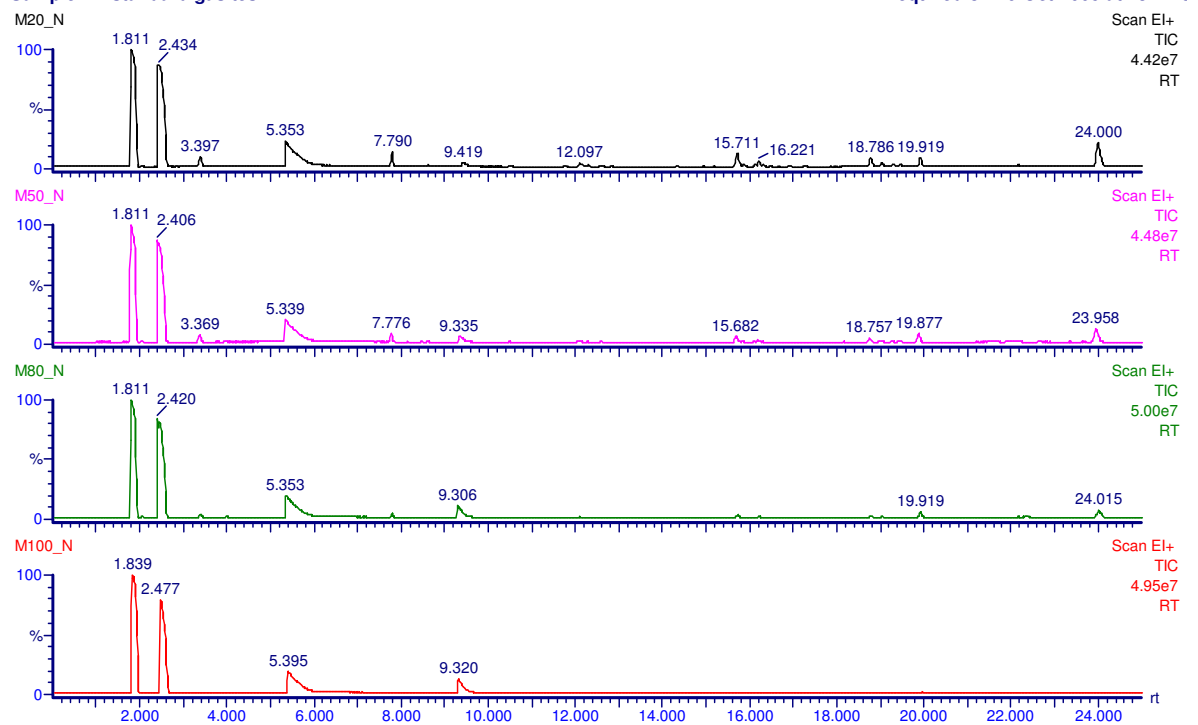
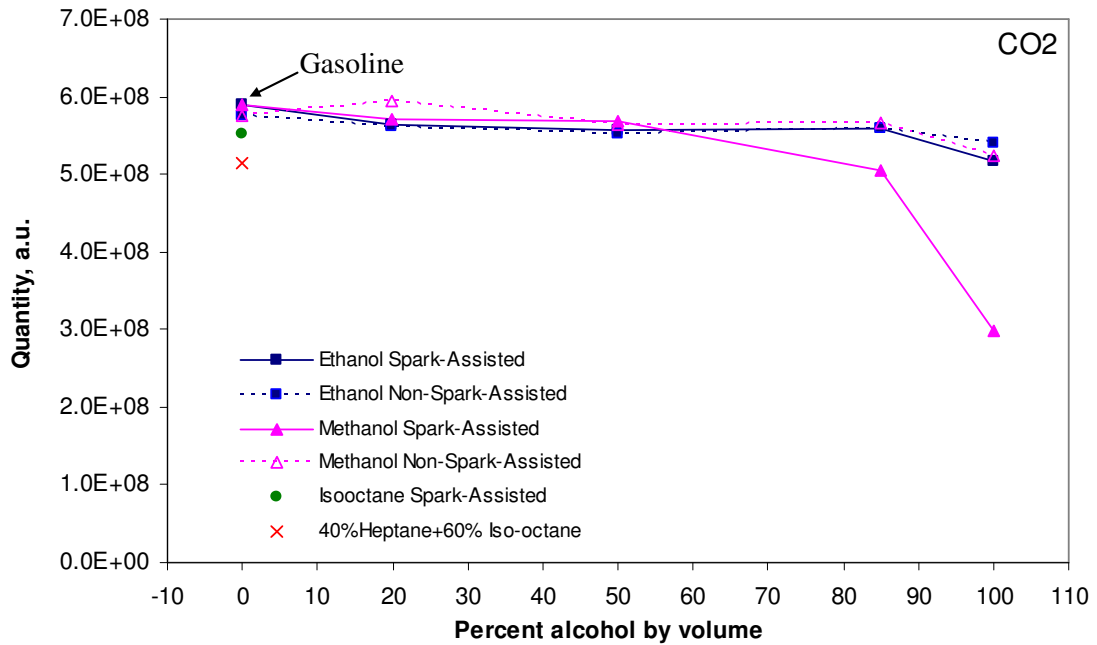


Figure 6.6 Chromatogram of Blended Methanol: 20, 50, 85 and 100 from Top to Below (a) Spark-Assisted Ignition (b) Without Spark -Assisted Ignition

The concentration of relevant species are plotted as a function of alcohol contents in Figure 6.7 – Figure 6.12 in which solid lines represent spark-assisted ignition and dash lines are for pure CAI combustion. In addition, triangle marks are the symbol for methanol blended fuels and square ones represent ethanol blended fuels.



**Figure 6.7 Concentration of Carbon Dioxide**

The concentrations of carbon dioxide in the exhaust emission are presented in Figure 6.7. The presence of alcohol produces slight less carbon dioxide initially. The significant drop in CO<sub>2</sub> for methanol was a result of lower energy input. Due to the lower temperature of the burnt gas, post oxidation of carbon monoxide to carbon dioxide was less complete as indicated by the higher amount of CO shown in Chapter 4 for alcohol fuels.

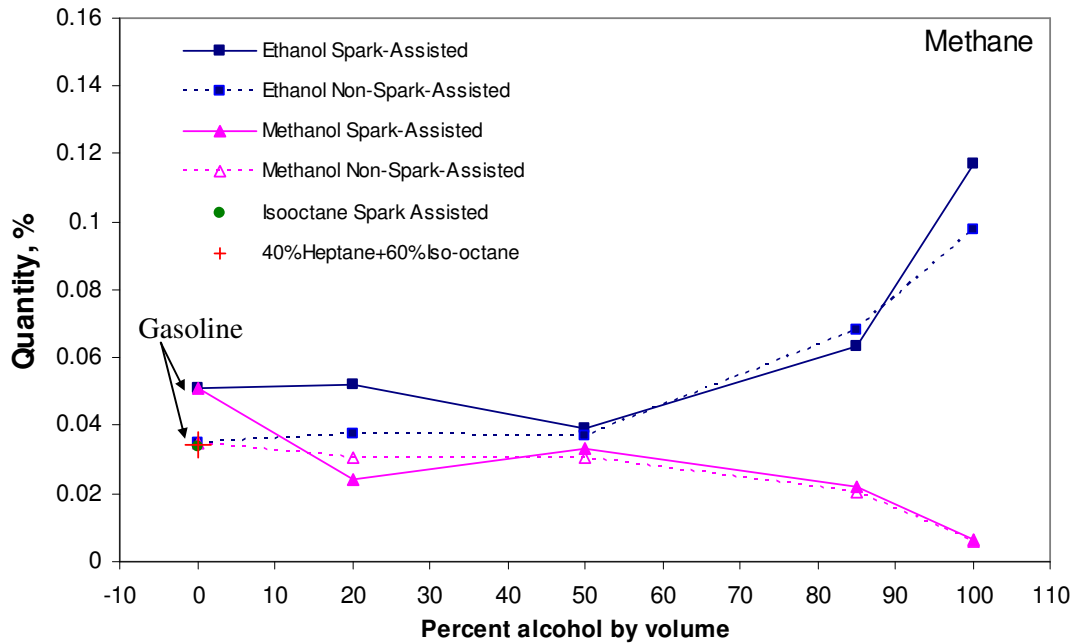


**Figure 6.8 Concentration of Methane**

Figure 6.8 shows the concentrations of methane in the exhaust gas. Production of methane from ethanol and methanol combustion exhibits the opposite trend. On one hand, when the percentage of ethanol increases beyond 50 %, the concentration of methane also rises. This corresponds well with the in-cylinder gas sampling results to be shown later. On the other hand, the amount of methane is lower when the percentage of methanol is higher than 50 %. The reason will be discussed in the in-cylinder sampling section.

The concentration of methane from burning gasoline is affected by the combustion process. The spark-assisted combustion produces more methane emission than pure CAI combustion, consistent with the in-cylinder measurement. In addition, pure hydrocarbons (Isooctane and 60 PRF) produce less methane in the exhaust.

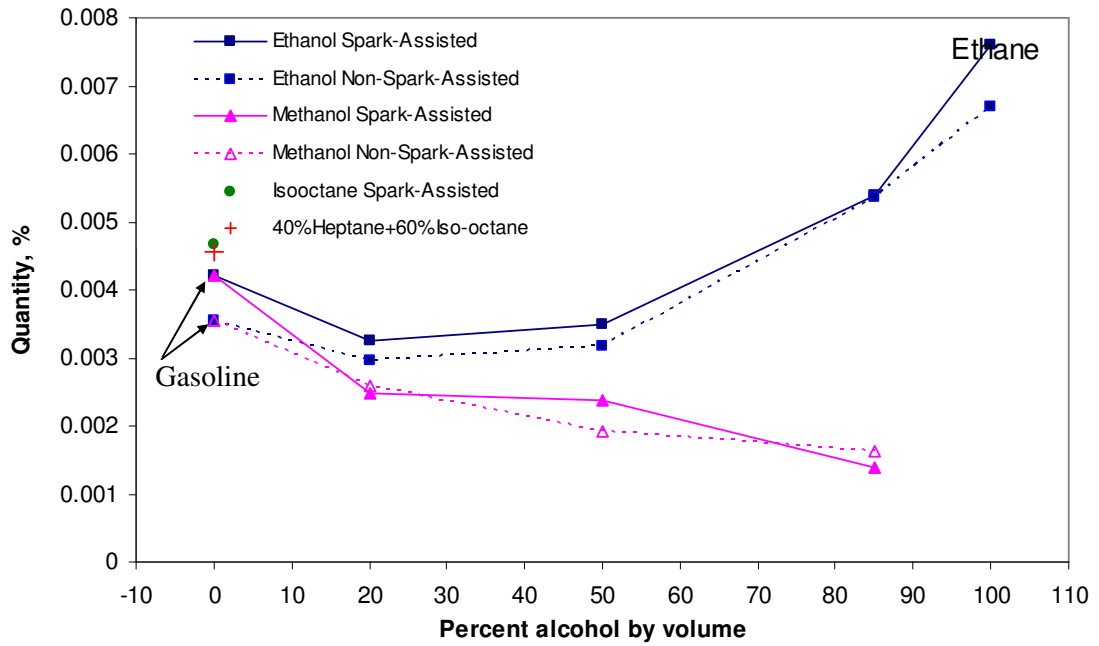


**Figure 6.9 Concentration of Ethane**

Like methane concentration, ethane concentration increases with ethanol content but decreases with methanol content as shown in Figure 6.9. However, the concentration of ethane is much lower than methane and it could not be detect for pure methanol. Neat isooctane and 60 PRF produce relative higher amounts of ethane. Similar to methane, the spark ignited flame produced more ethane from gasoline combustion.

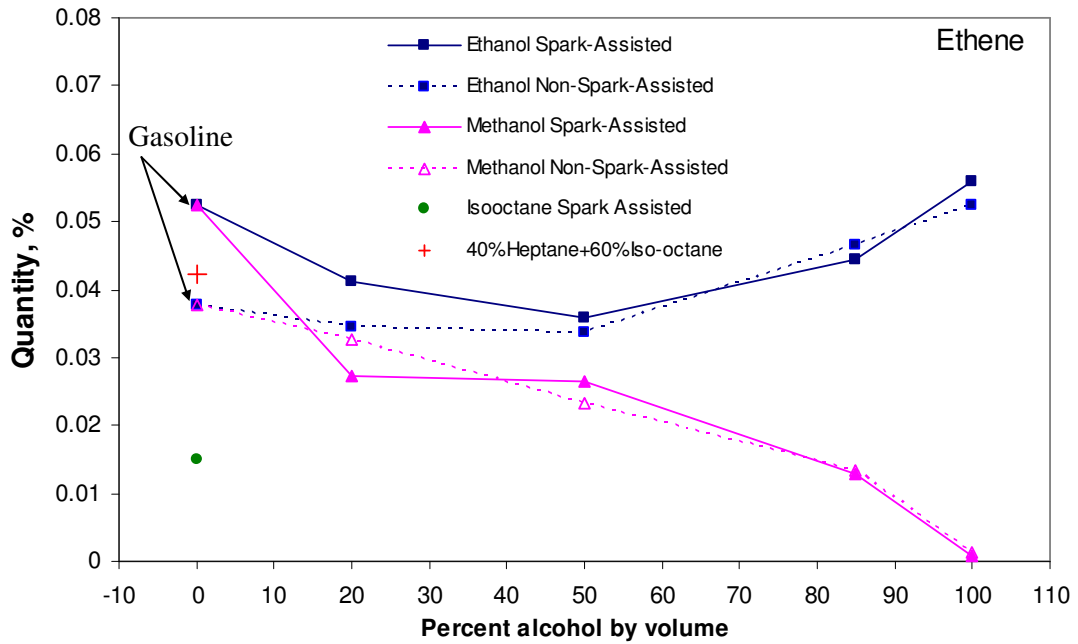


**Figure 6.10 Concentration of Ethene (Ethylene)**

Opposite to methane and ethane, ethene concentrations decrease initially with alcohol content but increase with the increased percentage of ethanol as shown in Figure 6.10. Eventually the pure ethanol produces almost the same amount of ethene as gasoline. In contrast, the amount of ethene decreases steadily with methanol content. The spark ignited flame produces more ethene than pure CAI combustion. Neat isooctane emits lower amount of ethene than that of gasoline whereas heptane in 60 PRF was responsible for higher ethene concentration.

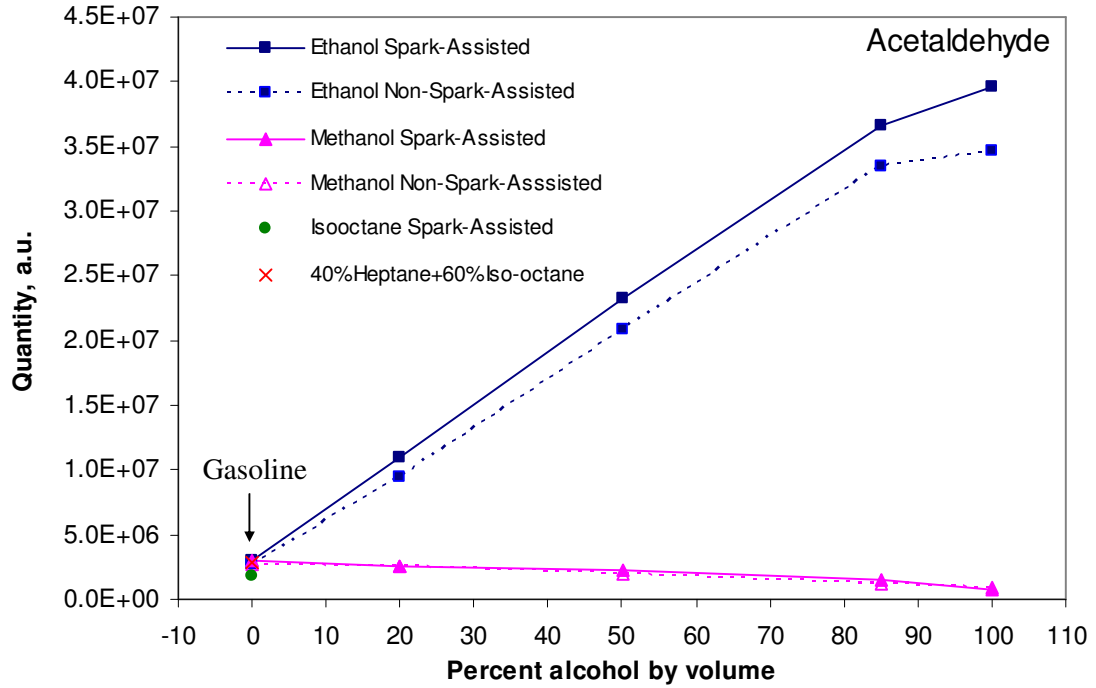


**Figure 6.11 Concentration of Acetaldehyde**

As expected, the concentration of acetaldehyde increases linearly with the percentage of ethanol. On the other hand, increasing the percentage of methanol causes a small reduction in the amount of acetaldehyde. The major chemical reaction concerning acetaldehyde formation will be detailed in the section of in-cylinder gas analysis. Interestingly, the presence of flame apparently increased the amount of acetaldehyde noticeably in neat ethanol, indicating more complete combustion of ethanol with CAI. Ethanol produces less HC but more acetaldehyde. Hence, the different speciation in ethanol and gasoline exhaust emissions should be taken into account in the after-treatment device design.

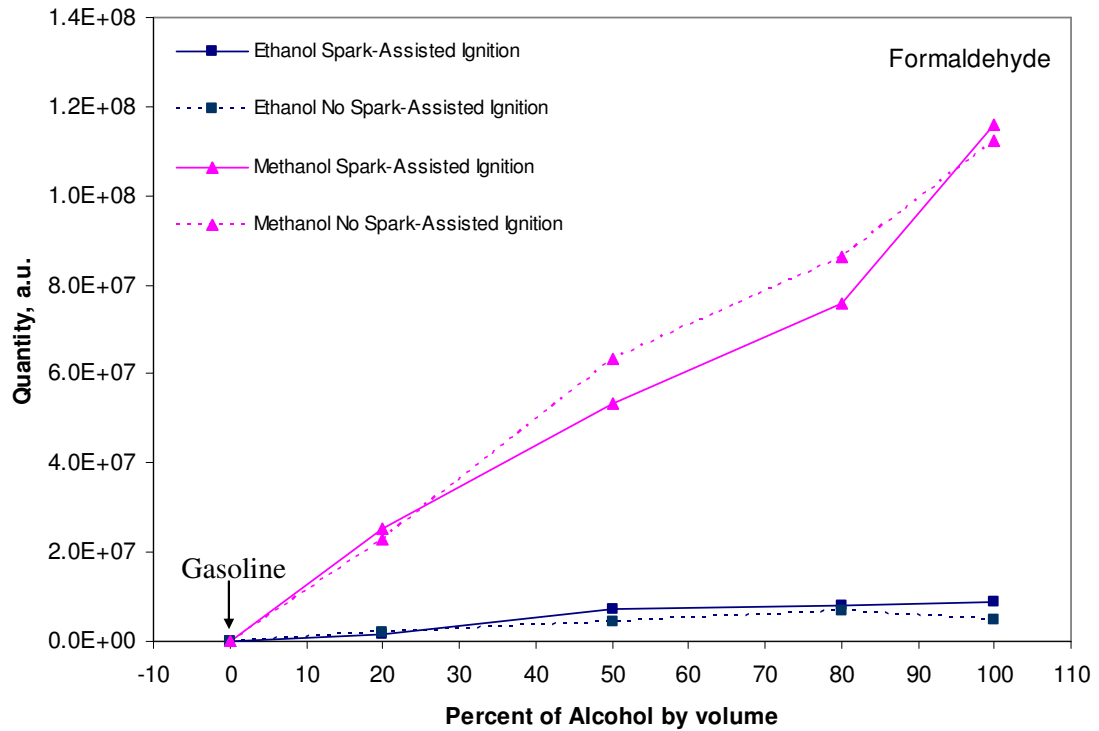


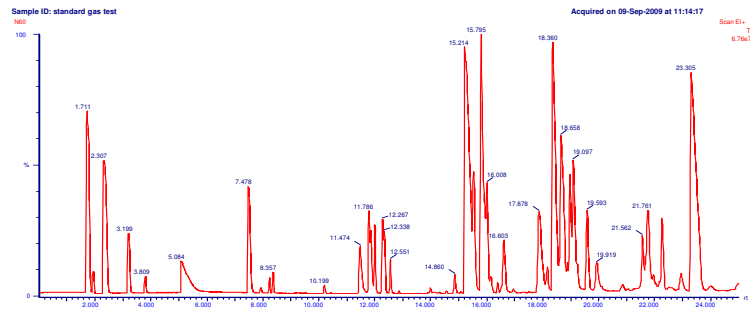
**Figure 6.12 Concentration of Formaldehyde**

Formaldehyde concentration is presented in Figure 6.12. As expected, methanol combustion is accompanied by large amount of formaldehyde emission. As to ethanol, although methanol can reduce HC in exhaust emission, the reduction of significant amount of formaldehyde should be considered by the exhaust catalyst.

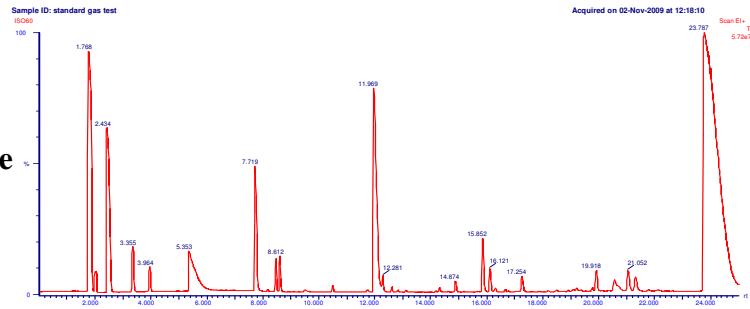
### 6.3.3 In-Cylinder Gas Speciation

Many in-cylinder gas species were detected by CG-MS analysis as shown in Figure 6.13. In order to better understand and clarify the importance of each species, the results are classified by their structure as follows; alkanes, olefins, aldehydes and ketones, as modeled in the detailed chemical kinetic reaction mechanisms [69, 70].

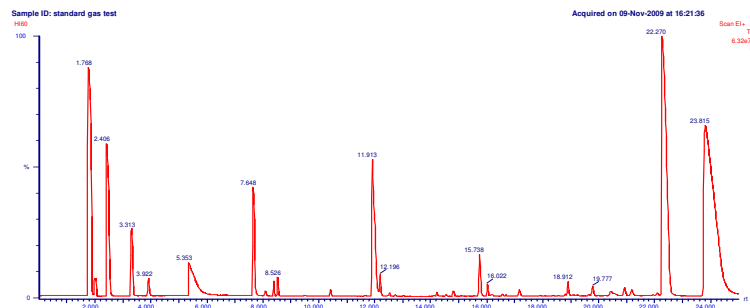
(a) Gasoline



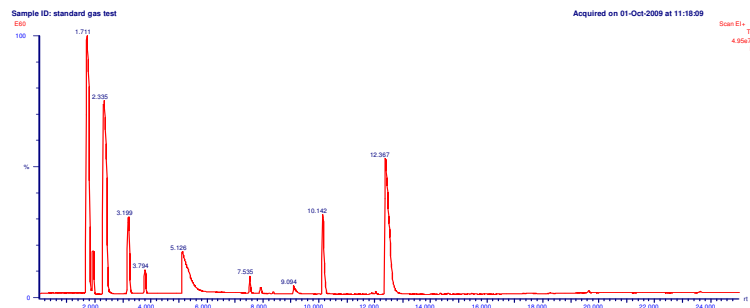
(b) Isooctane



(c) 60 PRF



(d) Ethanol



(e) Methanol

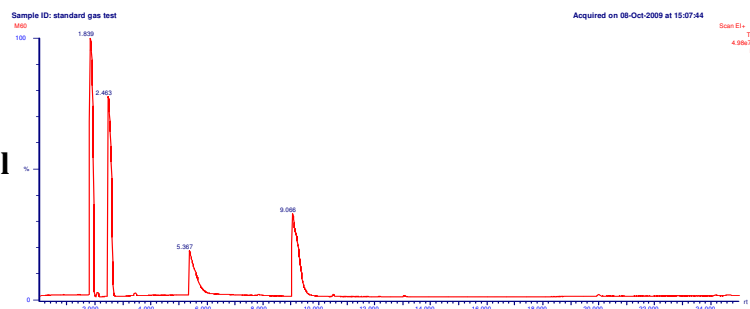


Figure 6.13 Typical GC-MS Graphs of Different Fuels

When analyzing the in-cylinder results, the timing of sampling should be taken into account. From 300 – 210 degree BTDC during the expansion stroke, the combustion chamber is a closed system and the changes in the species concentration is related to post combustion oxidation. During 180 – 90 degree BTDC of the exhaust stroke, burned gases leave the combustion chamber and no air or fuel can be added to the cylinder. From 90 degree BTDC – 90 degree ATDC of the NVO period, fuel reforming reactions are expected and hence changes of species. During the intake process, the concentration of species will be diluted by air causing the significant drop of concentration of all species.

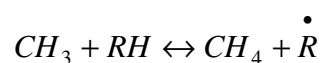
Due to the presence of a large number of hydrocarbon compounds, gasoline combustion produces many overlapping peaks, in particular for species of longer retention times. In addition, lack of information from the previous literature results in less confidence to identify specific species of those peaks. Therefore, longer carbon compound (Carbon atom >5), are not included in the subsequent analysis.

### 6.3.3.1 Alkanes

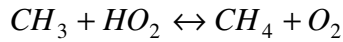
#### Methane

Figure 6.14 presents concentrations of methane at different crank angles. At 180° CA, methane concentrations show the significant dip for all of fuels due to the dilution of the intake air. During the re-compression stroke, methane concentration increases soon after each fuel was injected into the cylinder. Ethanol exhibits the most increased methane formation. This confirms the presence of fuel reforming reactions during the NVO period. As there was only a little oxygen from the air-assisted injection, oxidation reactions were limited.

According to previous studies [63, 69, 70], methane is formed mainly with the H-atom abstraction from hydrocarbon fuels by methyl radical,



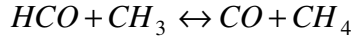
whereas 27 percent of total methane in ethanol is created from



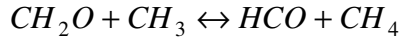
following with 19 percent of



For methanol oxidation [74],



and



are the major routes. The necessary precursor for the methane is methyl radical ( $CH_3$ ).

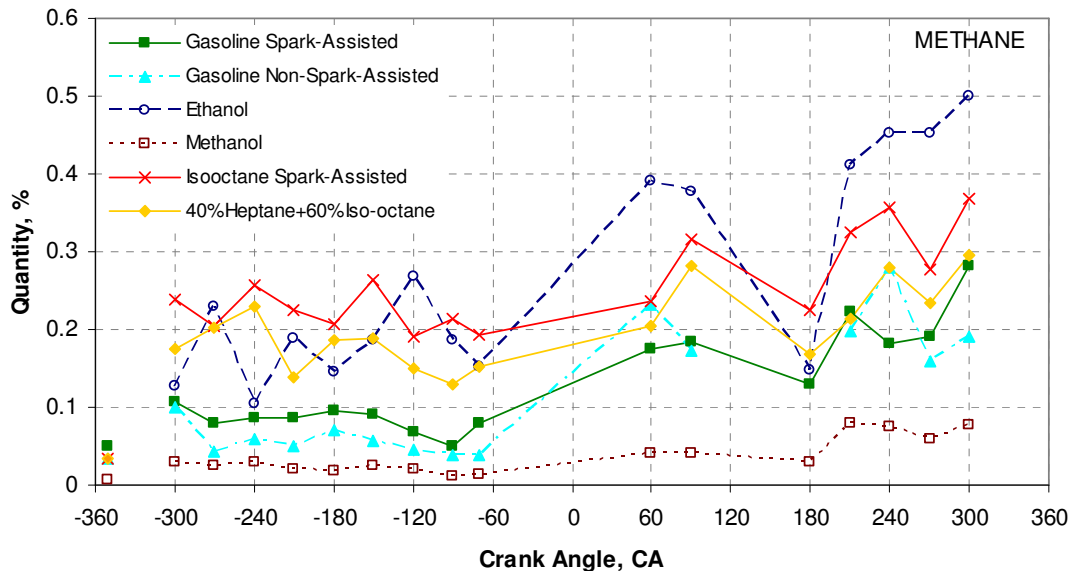


**Figure 6.14 Concentration of Methane**

The previous study [73] has shown that the primary reaction to produce methyl radical is an ethanol decomposition



followed with



in which  $CH_3CH_2O$  is the radical from H-atom abstraction of fuel. Methane is consumed later by radicals such as  $H,OH$ , and  $O$  generating chain branching

reaction to initiate auto-ignition. As a result, ethanol produced the highest amount of methane during the re-compression and compression stroke.

Although isooctane and heptane have many routes to produce methyl radical, for instance, fuel decomposing, H-atom abstraction or even alkyl radical decomposition and abstraction. Due to its higher paraffinic molecule structure, the production of higher alkyl radical ( $C_4H_9, C_5H_{11}, C_7H_{15}, C_8H_{17}$ ,  $C > C_4$ ) are more favored than methyl radical reaction. Therefore, the lower methane concentration was observed for hydrocarbon fuels, including isooctane, PRF and gasoline.

Surprisingly, neat isooctane produces more concentration of methane than 60 PRF. This implies that most of the methane comes from isooctane oxidation, opposite to the previous work [63] which showed methane from neat heptane combustion. The cause of this difference is that the previous paper focused on low temperature oxidation whereas fuel is subject to much higher temperature in the current study. It is noted that the rate of methane formation is nearly the same for isooctane and 60 PRF. The rate of methane formation is higher during the NVO and compression stroke when the gas temperature is higher.

The lowest concentration of methane was produced by methanol. According to the mechanism of methanol oxidation by Held and Dryer [74], there are a few routes to form methyl radicals. Methanol pyrolysis and H-atom abstraction are the major route to produce methyl radicals. However, fuel pyrolysis and H-atom abstraction to hydroxymethyl ( $CH_2OH$ ) productions are more favored than methyl radical production.

## Ethane

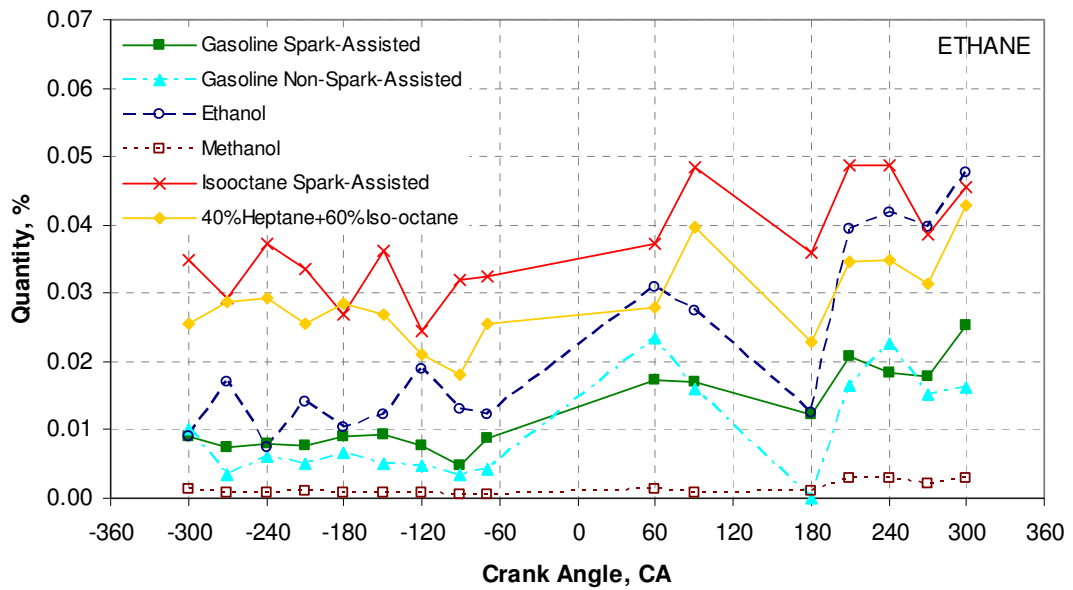
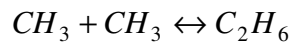
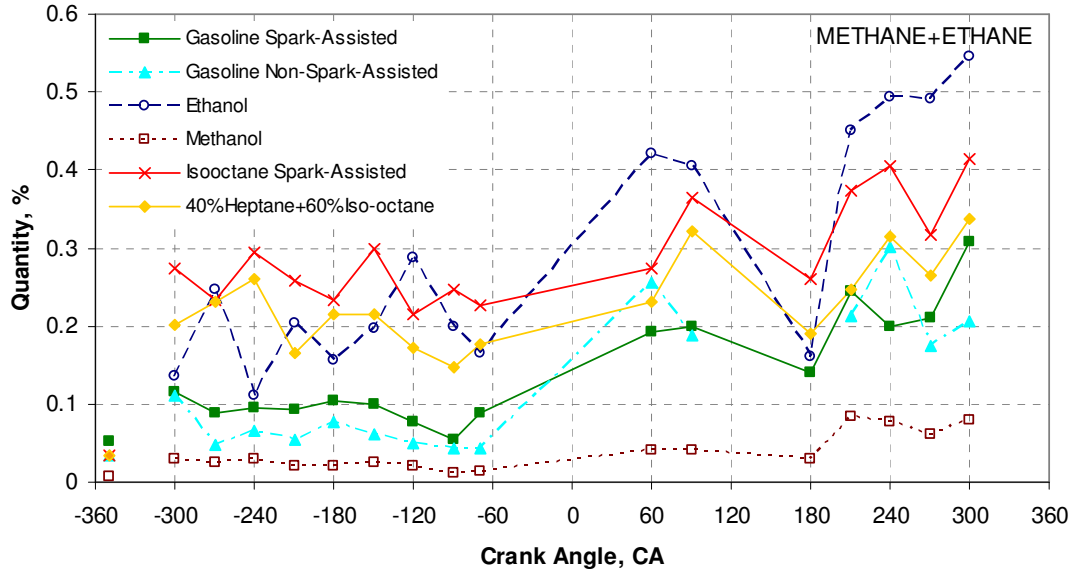


**Figure 6.15 Concentration of Ethane**

Like methane formation, ethane species strongly depend upon the methyl radical along the route of

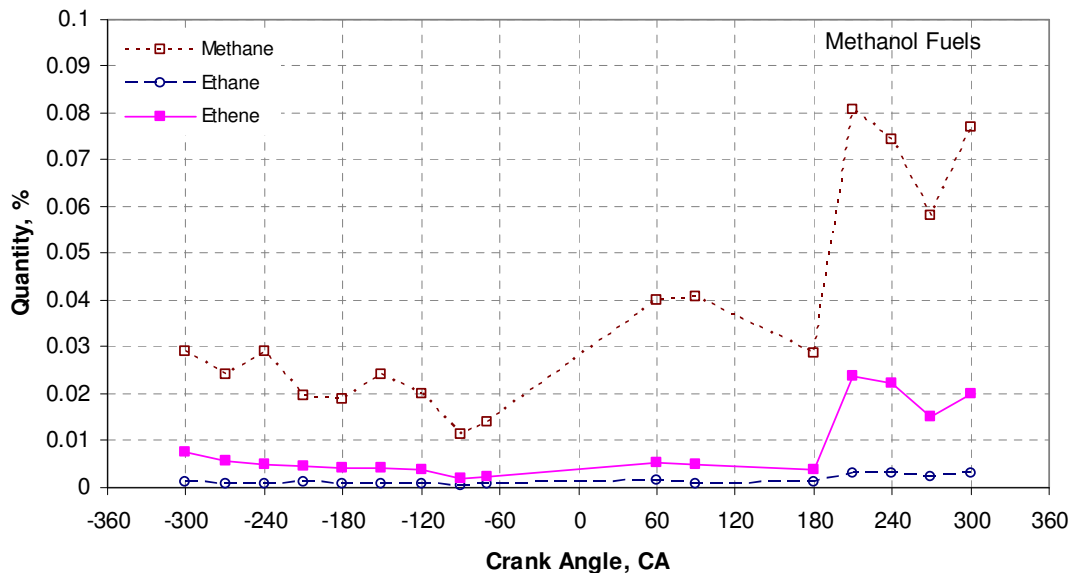


for all of the fuels. Results show the highest concentration from isooctane, followed by 60 PRF, ethanol, gasoline and a very small trace from methanol. Most of the ethane from 60 PRF is created from isooctane because of the slower heptane oxidation in the NTC region. Although more residual ethane is present in the burned gases of isooctane than ethanol, more ethane is produced from ethanol during the NVO period and compression.



**Figure 6.16 Concentration of Methane and Ethane**

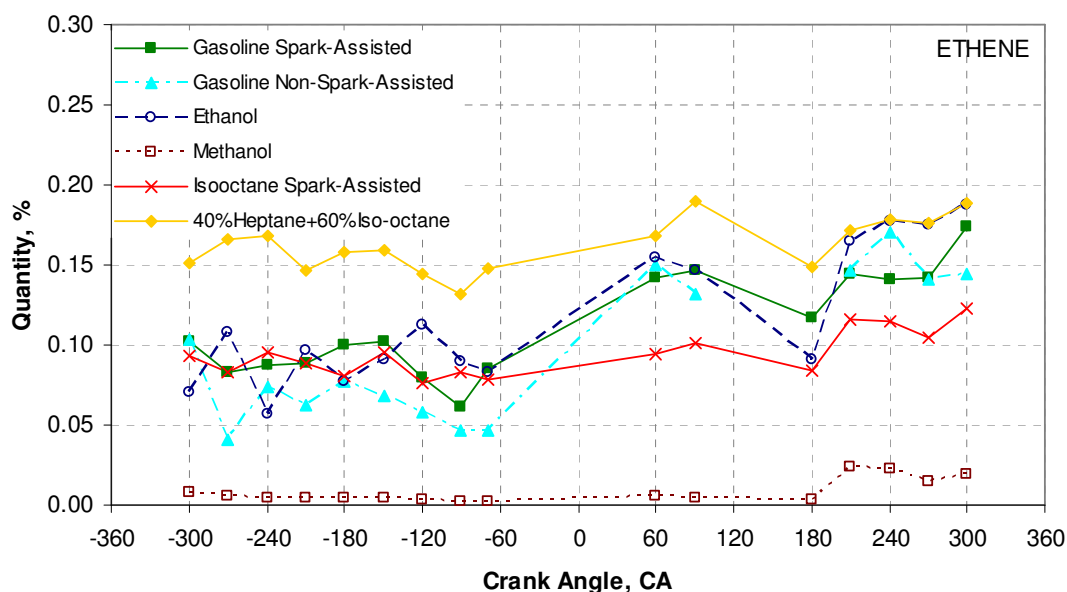
Figure 6.16 shows the sum of methane and ethane produced due to methyl radical, observed during the re-compression stroke. In the case of ethanol, methane production dominates the fuel reforming reaction during the NVO period when there is limited oxygen in the high temperature residual gas. During the compression stroke, the availability of abundant oxygen molecules leads to more ethene production.



**Figure 6.17 Concentration of Methane, Ethane and Ethene in Ethanol Oxidation**

### 6.3.3.2 Olefins

#### Ethene



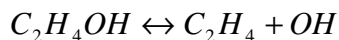
**Figure 6.18 Concentration of Ethene**

Figure 6.18 presents the concentration of ethene which is an intermediate product of fuel reforming reactions as suggested by Aroonsrisopon et al [24] and Song et al [25, 26].

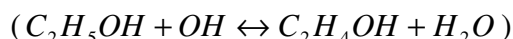
The result shows that 60 PRF generates the highest ethene concentration. Compared with neat isooctane, most of the ethene from 60 PRF is produced from heptane. During low temperature, this ethene is generated through paths 1, 2, 7, 8 and 5 of Figure 2.8. Due to the straight chain paraffinic structure which has a 6-8 membered transition state (TS) ring, heptane is readily to experience alkylperoxy isomerization reaction 2 and  $\dot{O}_2 QOOH$  isomerization reaction 4. Reaction path 8 is responsible for a major part of the NTC region in heptane oxidation [69, 70]. The ethene concentration of gasoline is in the range between that of the 60 PRF and isooctane. In addition, 60 PRF yields the highest ethene in the burned gases due to reaction at high temperature [71].



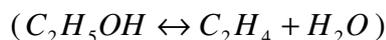
During the expansion and exhaust stroke, ethanol produces a comparable amount of ethene with gasoline and isooctane, but the concentration of ethene is higher with ethanol during the NVO and compression stroke. Fifty-five percent of ethylene formation is principally produced from



in which  $C_2H_4OH$  radical is formed by H-atom abstraction of ethanol by OH radical



followed with ethanol dehydration



producing twenty-seven percent of ethene.

## Propene

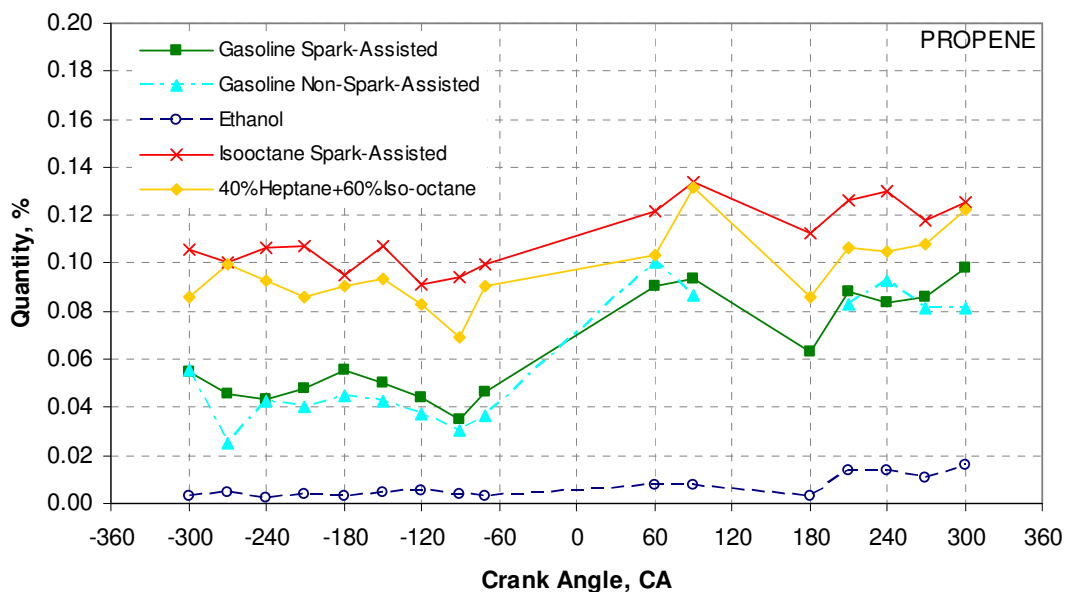
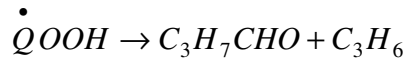


**Figure 6.19 Concentration of Propene**

Concentrations of propene are presented in Figure 6.19. The reaction pathways to generate propene are the same as ethene in paraffinic fuels. However, the amount of propene from isooctane is shown to be higher than that of 60 PRF. Hence, propene is more readily formed from the isooctane than heptane. Houliang et al [63] noted that propene in heptane reaction via reaction 7



whilst



is the route of propene formation from isooctane which takes place at intermediate temperature. The faster propene production rate from heptane during the compression stroke is a result of



reaction according to Tsurushima [71].

There is no trace of propene in methanol exhaust while a relatively small concentration of it was detected from ethanol combustion due to the combination of vinyl and methyl radical ( $C_2H_3 + CH_3 \rightarrow C_3H_6$ ). As methyl radical is the major reactant to create methane, ethane, and propene in ethanol oxidation, the concentration of those intermediate is shown in Figure 6.20. The results show the most favourable product of methyl radical reactions is methane production.

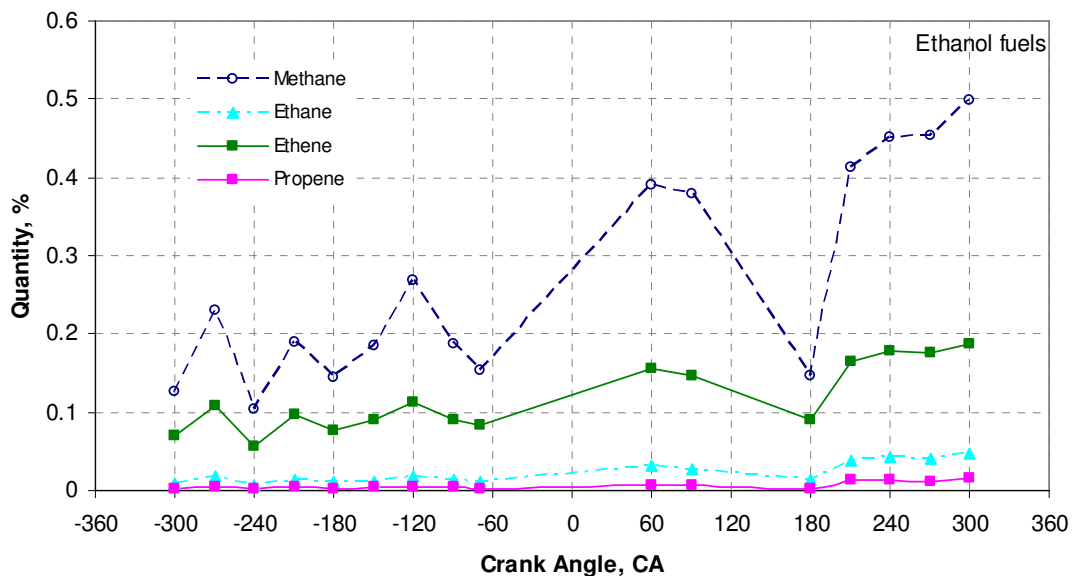


**Figure 6.20 Concentrations of Methane, Ethane, Ethene and Propene in Ethanol Oxidation**

## Butene

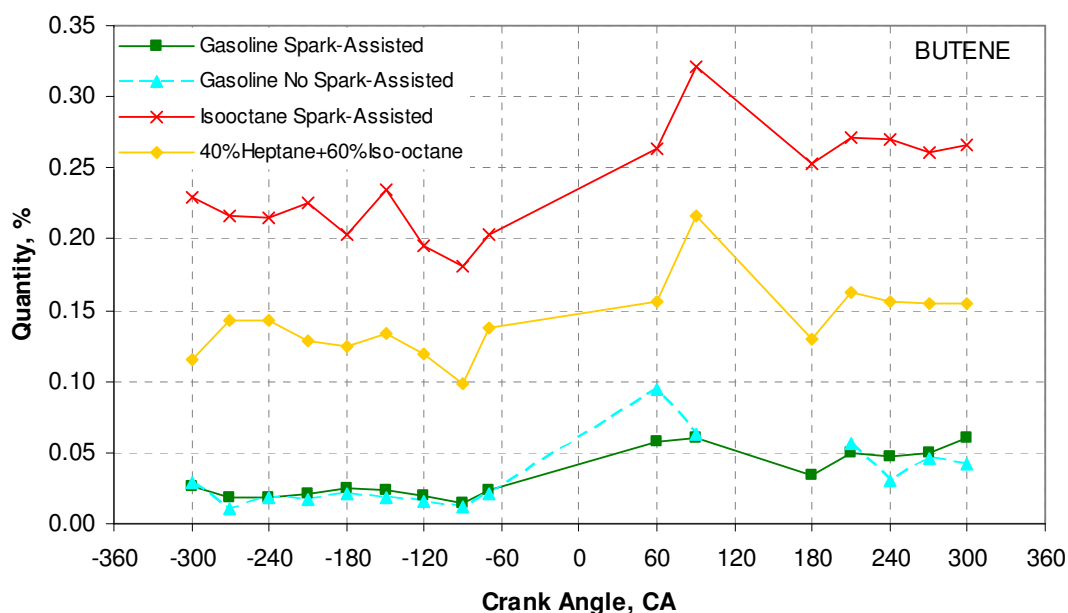
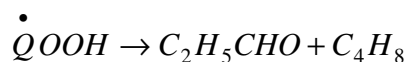


**Figure 6.21 Concentration of Butene**

Figure 6.21 presents the concentration of butene. The result shows the same trend as propene. However, no trace of its was detected from ethanol combustion. Butene and propene take the same reaction path. In the case of heptane, it is produced by



and for isooctane, it is generated by



## Pentene

Due to the higher molecular weight, olefins which have carbon above 4 atoms are difficult to specify in gasoline oxidation. Therefore, only olefins from isooctane and 60 PRF are presented here.

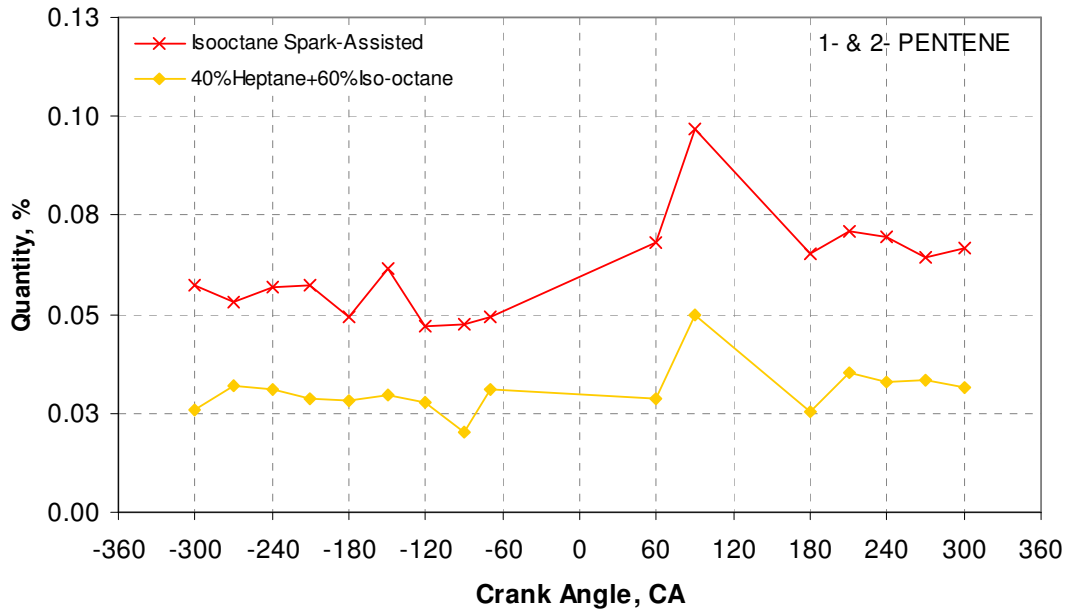


**Figure 6.22 Concentration of 1-, 2- Pentene**

Figure 6.22 shows 1- and 2- pentene while Figure 6.23 presents hexene concentration. The results show opposite trends between isooctane and heptane/isooctane blend. Most 1-& 2-pentene are created from isooctane oxidation. For heptane, pentene is produced from reaction



and



is the reaction leading to pentene from isooctane. Hexene is generated mostly from heptane due to



As both Figure 6.22 and Figure 6.23 show fuel reforming reactions leading to n-pentene and hexene are particularly noticeable during the NVO period. In contrast, low temperature oxidation at the early compressions stroke shows the modest n-pentene and hexene formations.

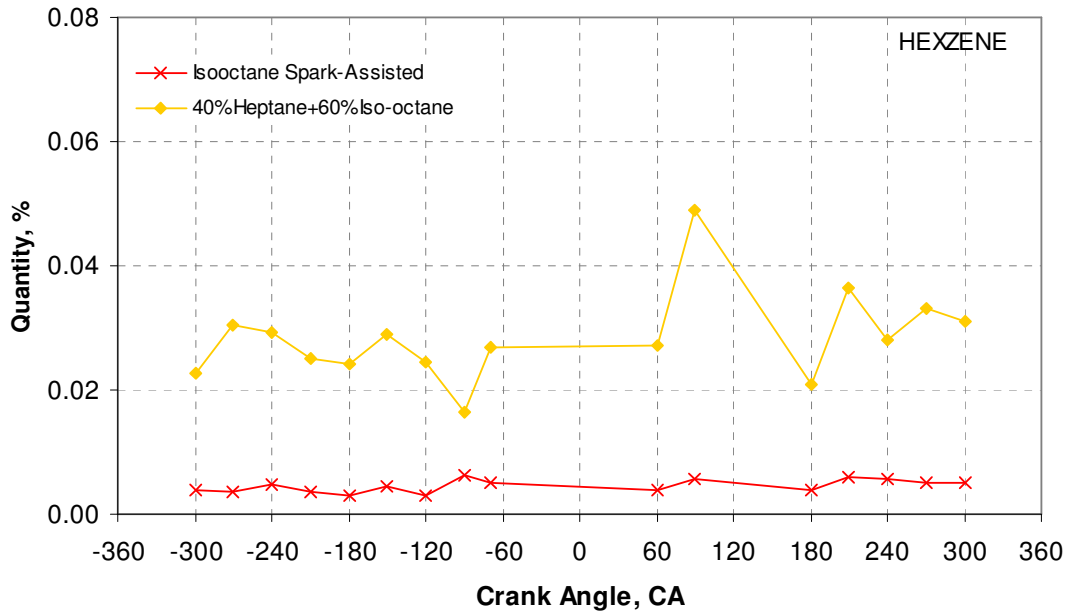


**Figure 6.23 Concentration of Hexene**

Figure 6.24 shows heptene concentration from isooctane and heptane/isooctane. The result shows the expected trend in which heptene, a conjugate olefin, is formed mostly from heptane oxidation. During the re-compression stroke, fuel pyrolysis takes place to produce heptene. On the other hand, during the early compression stroke, the concentration is relatively stable. This may be understood that after fuels are fragmented into smaller olefins during the re-compression NVO period, those small molecules will follow the low and intermediate temperature reaction path ways to produce smaller olefins and alkanes at the early compression stroke. Due to increased intake air temperature, reactions pass to the NTC region quickly resulting in low concentration of intermediate species and retarding auto-ignition.

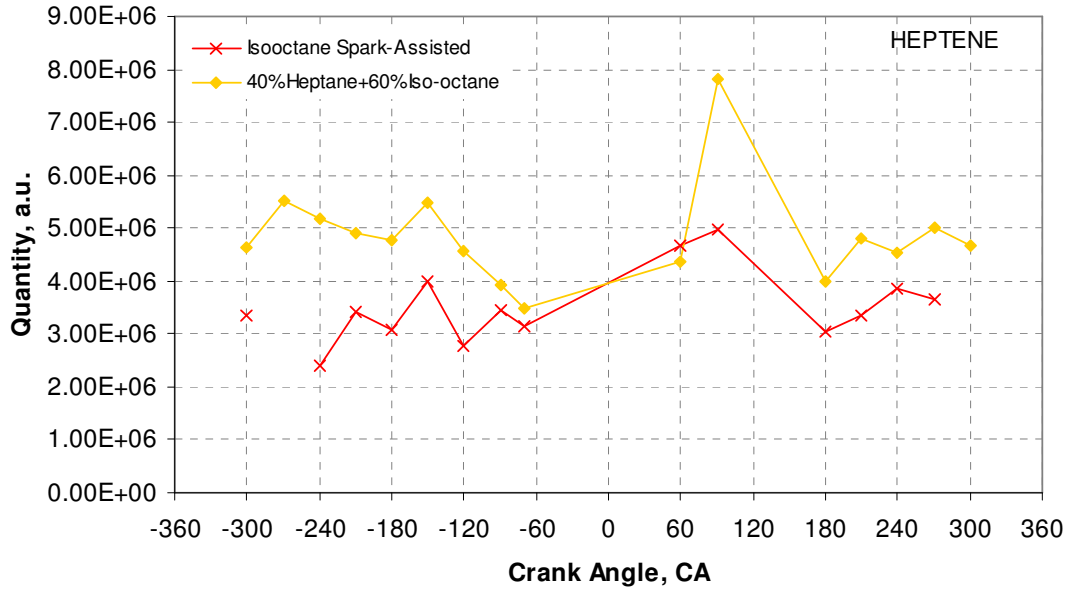


**Figure 6.24 Concentration of Heptene**

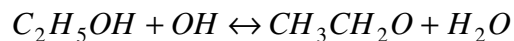
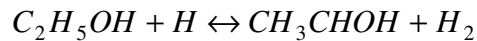
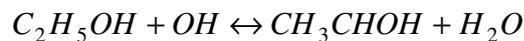
The olefin results shown above confirm that there are fuel reforming reactions taking place, in particular fuel pyrolysis. In the case of alcohol fuels, ethanol reforming reactions lead mainly to methane and ethene during the re-compression and early compression stroke. Similar to ethanol, methanol oxidation produces mostly methane and ethane during the re- and compression stroke through at lower concentration. For isooctane and 60 PRF fuels, there is fuel pyrolysis during the re-compression stroke. However, fuel decomposition is terminated during the early compression stroke. The smaller olefins are mainly produced from heptane during the NTC region which inhibits the cool flame heat release. The absence of the cool flame heat release corresponds with the study of Eng et al [99] with an n-heptane and a residual gas level of 70 %. They claimed that the reaction between alkyl radicals and oxygen ( $\dot{R} + O_2 \leftrightarrow R\dot{O}_2$  reaction 1 in Figure 2.8) is reversed due to an increased initial temperature of 530 K. This result also agrees with the experiment of Iida and Igarashi [100]. They performed the experiment with n-butane and increased the intake temperature from 297 K to 355 K. There was no evidence of the low temperature heat release.

### 6.3.3.3 Aldehydes

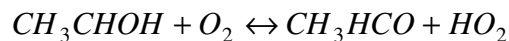
Aldehyde is an organic compound which comprises of double-bounded carbon to oxygen. In chemical kinetic reactions of CAI combustion and knock phenomena in the SI engine, aldehydes are generated and they strongly affect the auto-ignition process. In general, many kinds of aldehydes are generated during oxidation reactions. However, formaldehyde is the most important species which is generated during the cool flame combustion. But it needs some effort to be detected due to its low concentration.

#### Acetaldehyde

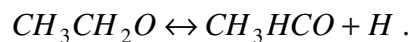
Acetaldehyde concentration for all fuels is shown in Figure 6.25. The result shows that ethanol oxidation produces an order of magnitude higher acetaldehyde concentration than the other fuels. Most of it is generated through the H-atom abstraction reaction at the primary site by molecule of  $OH$  and  $H$  radicals



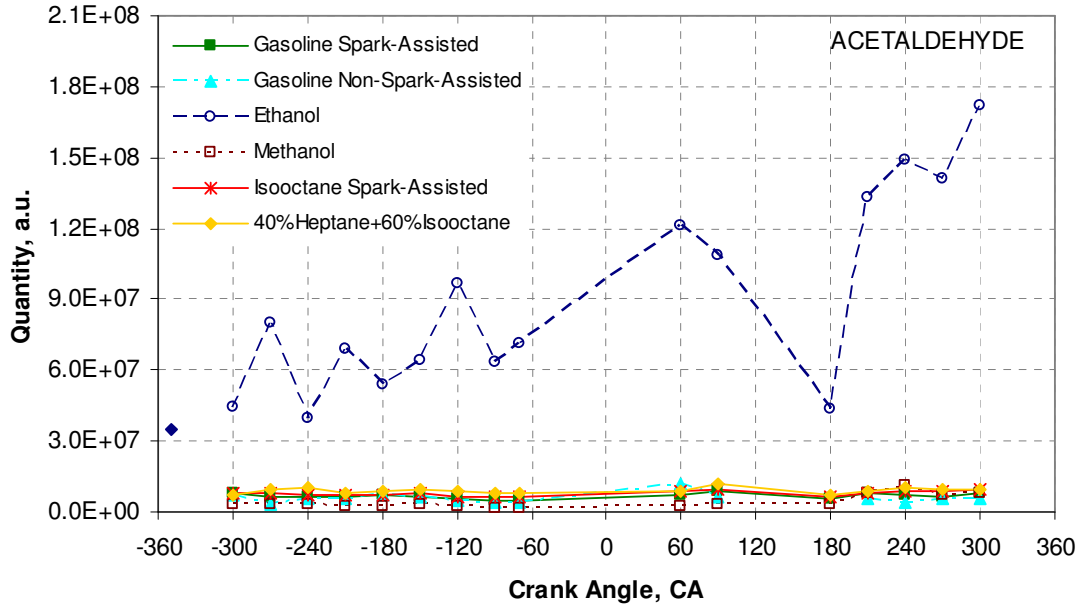
and then followed with the reaction



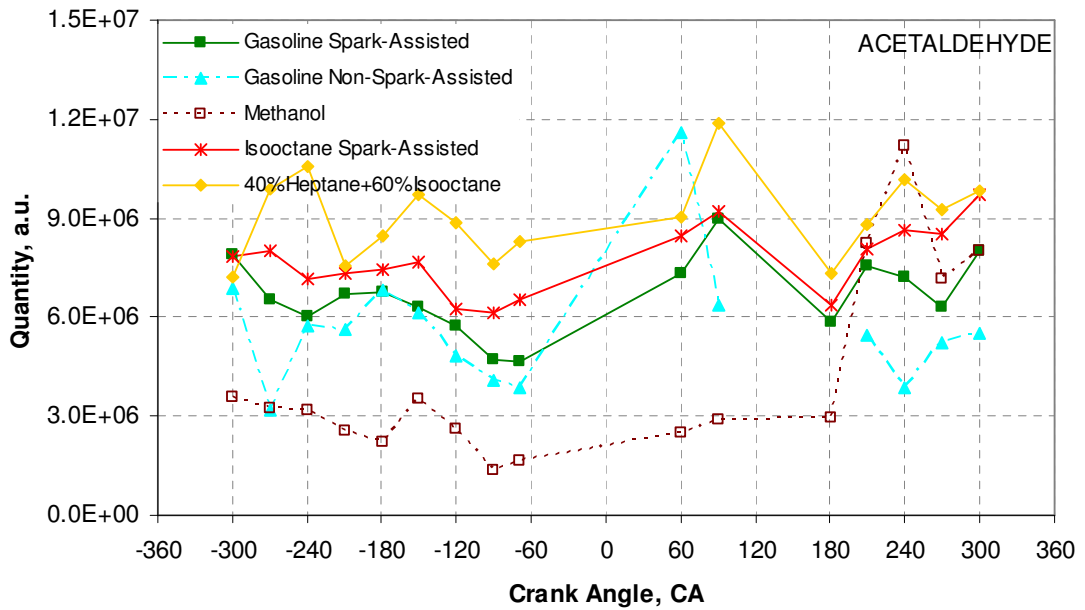
as well as decomposition of



During the re-compression stroke, acetaldehyde is generated through the decomposition reaction. During the compression stroke, acetaldehyde concentration reaches its peak due to the above reaction. This increased acetaldehyde will be consumed later during the hot ignition process. However, its concentration is still higher in the expansion and exhaust stroke of ethanol combustion which corresponds with the exhaust emission results presented earlier.



(a)



(b)

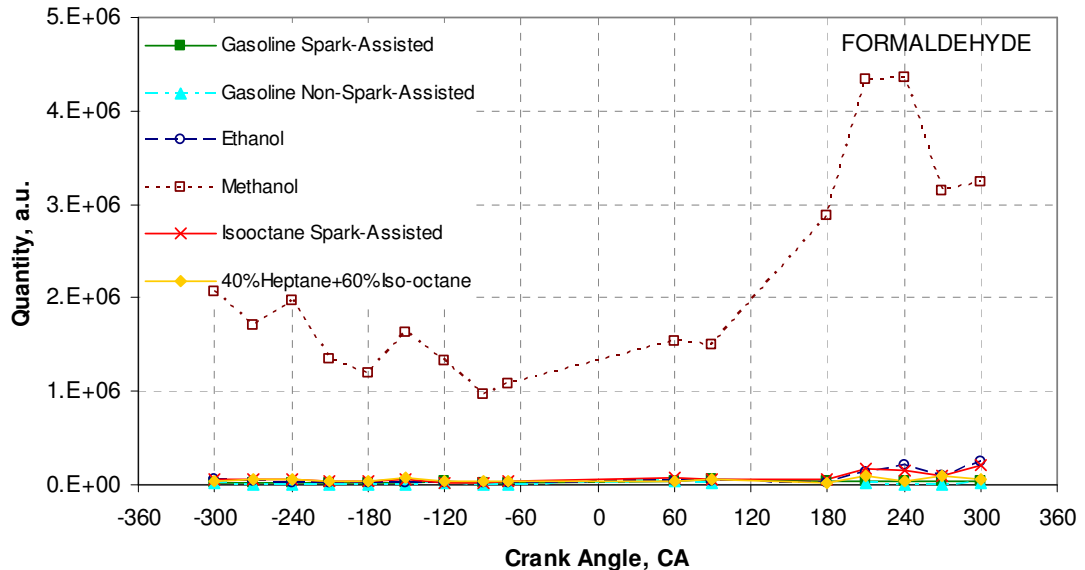
**Figure 6.25 Concentration of Acetaldehyde**

In order to study the acetaldehyde formation from other fuels, Figure 6.25(b) excludes the ethanol results. For all fuels, acetaldehyde is the product from fuel fragmentation during the NVO period and the intermediate species at low temperature reactions. Heptane seems to produce more acetaldehyde than isooctane, whereas gasoline has lower concentration than both of heptane and isooctane. For isooctane and 60 PRF,

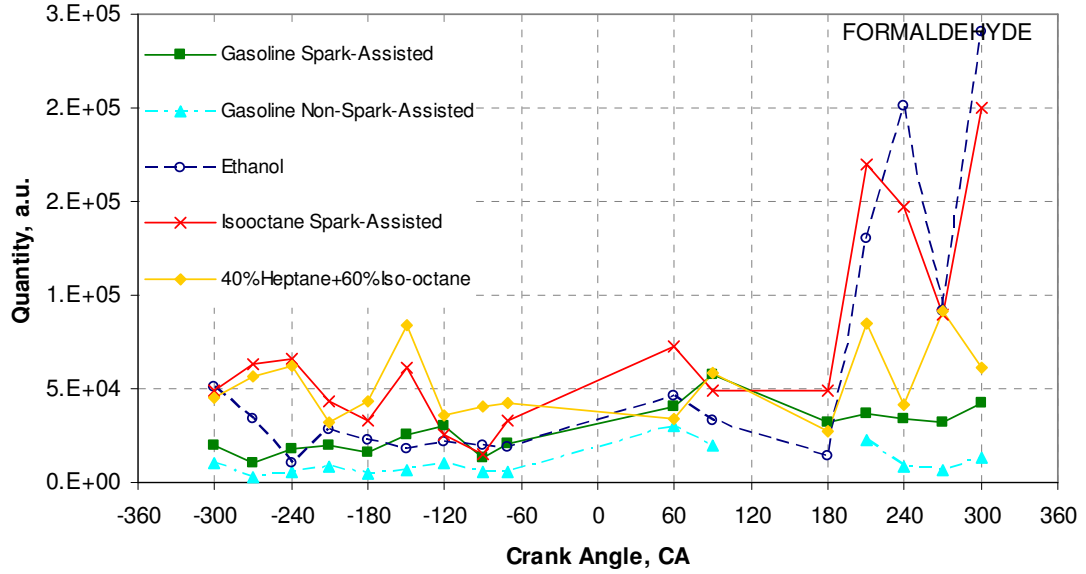
acetaldehyde follows the reaction pathways 1,2,7,8 and 5 as given in section 2.6.1. The level of acetaldehyde of 60 PRF remains relative constant and isooctane increases slightly. But there is a significant increase during the compression stroke from alcohol. This implies that very low chemical reactions take place at the early compression stroke for neat isooctane and 60 PRF but alcohol fuels react more readily. Gasoline shows the same trend with isooctane. Such results are consistent with the delayed auto-ignition seen with gasoline.

### Formaldehyde

Figure 6.26 presents the concentration of formaldehyde. During the experiments, noticeable variation between each sample is noted for formaldehyde, due to its reactive nature. The concentration of formaldehyde is very low even with methanol oxidation. In addition, in some conditions, the amount is too low to produce adequate signal/noise ratio. Therefore, the formaldehyde concentration is only semi-quantitative. Nevertheless, the trend between fuels can be observed.

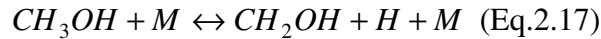


(a)

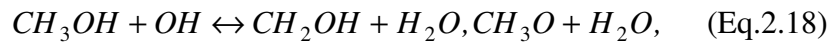


(b)  
**Figure 6.26 Concentration of Formaldehyde**

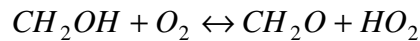
Methanol produces an order of magnitude more of formaldehyde than other fuels as in Figure 6.26 (a). This corresponds well with the known chemical kinetics [74]. At first, fuel decomposition



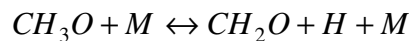
and H-atom abstraction by OH radical



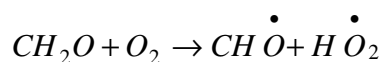
generate substantial hydroxymethyl ( $CH_2OH$ ) and methoxy radical ( $CH_3O$ ) which are the precursor of formaldehyde. Afterward, hydroxymethyl oxidizes by  $O_2$ ,



and methoxy radical is decomposed



to generate formaldehyde. In the current study, formaldehyde concentration increases slightly from the re-compression stroke but rises rapidly to its peak in the compression stroke. Afterwards, formaldehyde is consumed by the chain branching reaction

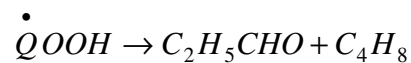


to produce two radical species which set off the auto-ignition process of methanol.

As shown in Figure 6.26(b) formaldehyde formation of ethanol, gasoline, isooctane and 60 PRF shows the same pattern as that of methanol but at a very low concentration. Ethanol, isooctane and 60 PRF form formaldehyde in the compression stroke whereas gasoline does not. The concentration of formaldehyde correlates well with the auto-ignition timing determined from the heat release analyse i.e. high formaldehyde concentration leads to advanced auto-ignition.

### Propionaldehyde

Propionaldehyde or propanal is a 3-carbon atom aldehyde. Figure 6.27 shows that the concentration of propionaldehyde is almost constant except one outlier at the end of NVO period. The propionaldehyde is formed mostly from heptane through the reaction



Therefore, as the temperature increases during compression propanal concentration rises slightly for the PRF.

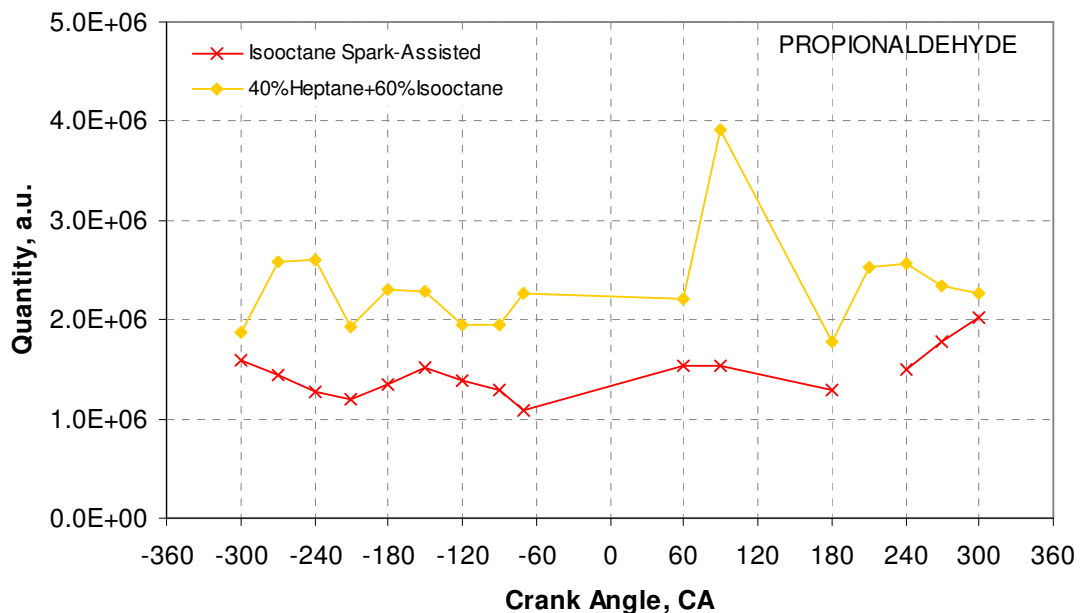


**Figure 6.27 Concentration of Propionaldehyde**

## Acrolein

Acrolein or 2-propenal ( $C_3H_4O$ ) is an unsaturated aldehyde and its formation could not be directly related to the specific reactions. As shown in Figure 6.28 Acrolein formation takes place during the early compression stroke in isooctane and its concentrations are higher than that of 60 PRF combustion.

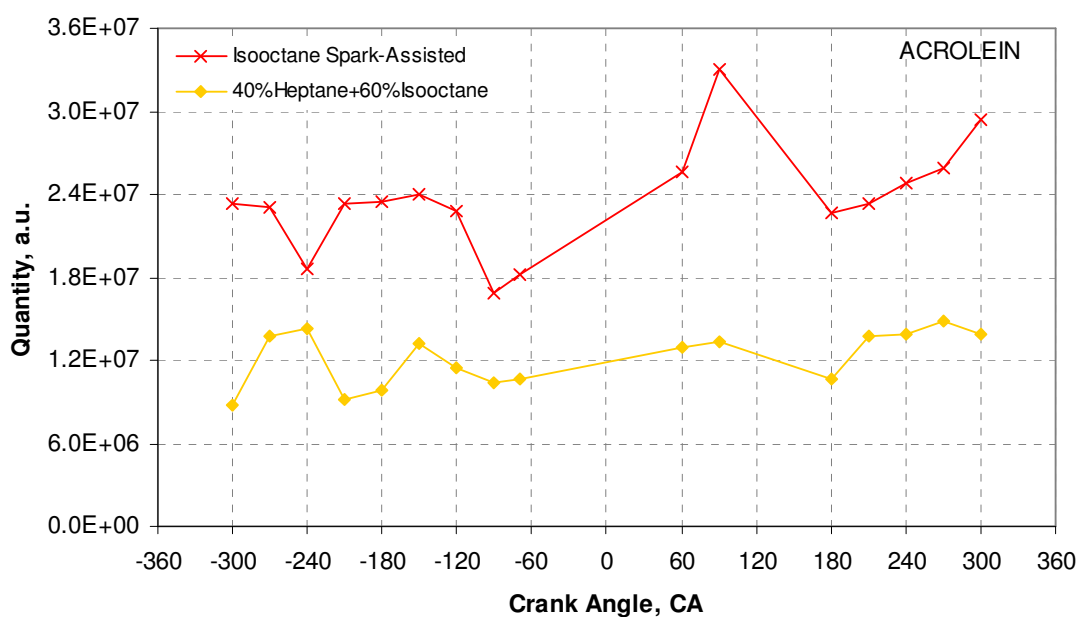
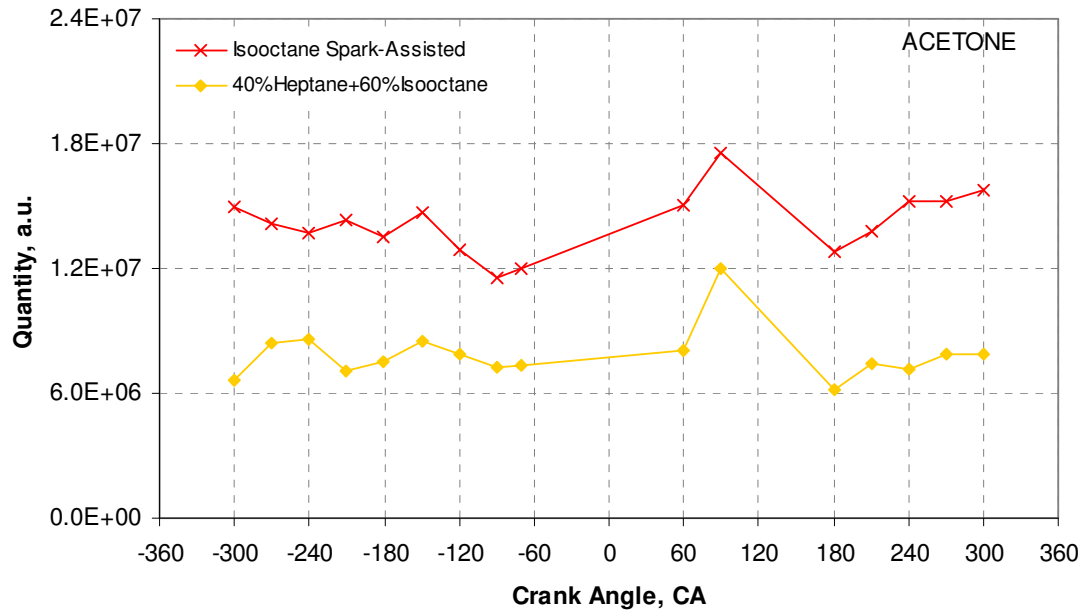


Figure 6.28 Concentration of Acrolein

### 6.3.3.4 Ketones

A ketone is an organic compound which comprises of the double bond carbonyl group ( $C=O$ ). According to Curran et al [69, 70], ketones are formed at low temperature through the reaction type 18 ( $RO\dot{O}$  Decomposition) and 24 (Ketohydroperoxide decomposition). However, only acetone species were detected in the current study as shown in Figure 6.29.



**Figure 6.29 Concentration of Acetone**

For both fuels shown, acetone concentration reaches its peak at the end of the NVO period, indicating the presence of partial oxidation reactions. But its concentration drops soon after the intake valves open due to increased charge. However, its concentration starts creeping up, in particular with isooctane, during the compression at relatively low values.

### 6.3.3.5 Carbon dioxide

CO<sub>2</sub> is one of the main constituents of burned gas. It can be used to measure the residual gas concentration. Therefore, the addition of fresh air causes the reduction in CO<sub>2</sub> concentration during the intake stroke as seen in the graph.

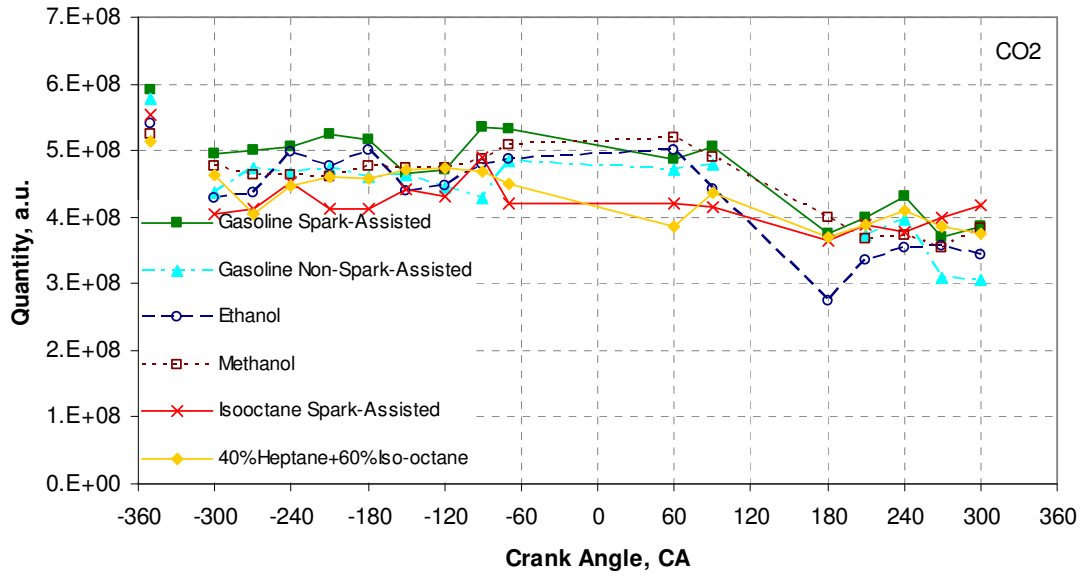


Figure 6.30 Concentration of Carbon Dioxide

### 6.3.3.6 Gas Species in Gasoline

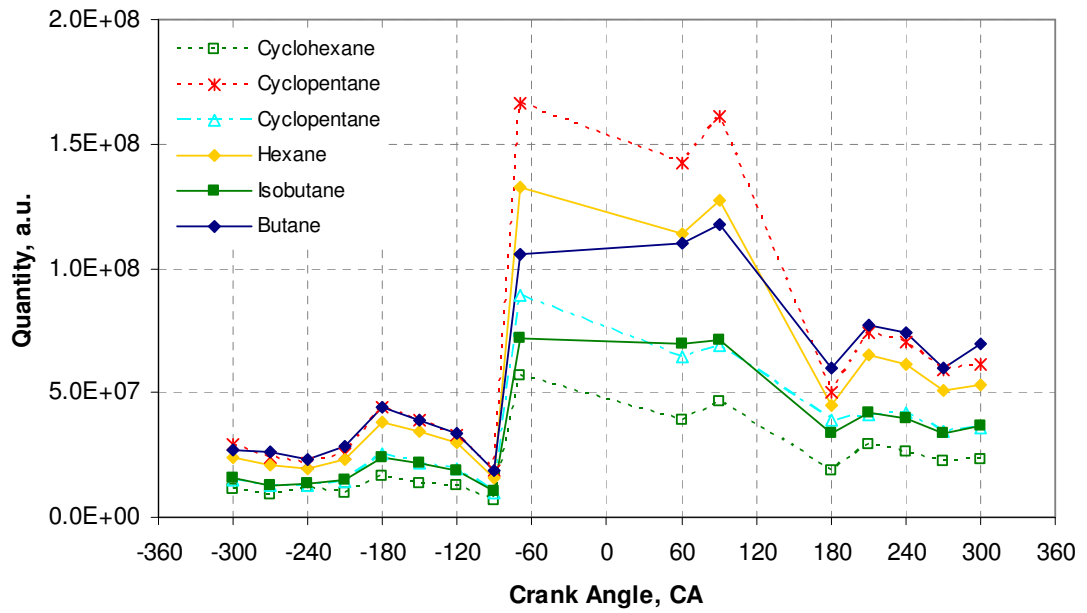
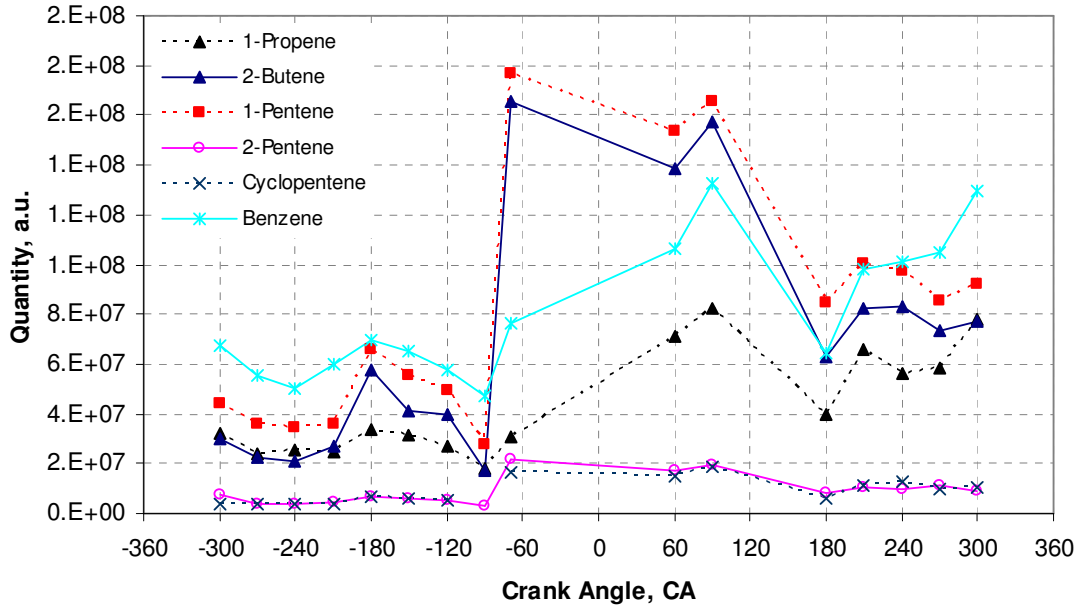


Figure 6.31 Concentrations of Alkanes



**Figure 6.32 Concentrations of Olefins**

As gasoline fuel contains a variety of hydrocarbons it is not appropriate to compare directly with the other pure hydrocarbon fuels or alcohols. For illustration, Figure 6.31 shows the alkanes and their sudden rise coinciding with the fuel injection. According to Figure 6.32, 2-Butene and 1-pentene seems to be part of the original gasoline but the delayed rise in 1-propene and cyclopentene suggest that they are formed during the NVO period.

## 6.4 Summary

The above results from in-cylinder gas speciation measurements are consistent with the chemical kinetic reaction mechanisms published previously. With the current engine operation, the prominent reactions in each fuel were observed including the reaction which resulted in advanced ignition in alcohol fuels. Moreover, the reason for advanced stable combustion of alcohol fuels has been clarified.

Olefin and aldehyde related to the reaction of  $\dot{Q}OOH$  and ketohydroperoxide of low temperature oxidation were observed. However, acetone was the only ketone species detected. In addition, due to increased intake charge temperature and high dilution, no

cool flame heat release was detected for 60 PRF. In addition, the presence of higher concentration of methane, ethene and acetaldehyde demonstrate the importance of H-atom abstraction and decomposition on primary sites in ethanol oxidations. In comparison, the significant presence of formaldehyde from methanol confirms the major route of methanol combustion is through the H-atom abstraction with OH radical in the hydroxyl and methyl sites. Accumulated formaldehyde further oxidizes with oxygen generating two radicals which leads to rapid consumption of the remaining fuels. As a result, ignition timing of methanol occurs earlier than the gasoline combustion.

The fuel reforming process during the re-compression stroke has been confirmed by the presence of olefin, conjugate olefin, smaller alkane and aldehyde species. Fuel pyrolysis occurred for all fuels after the fuels were injected directly into hot trapped residual gas referring to the increased concentration of smaller molecular olefin, alkane and aldehyde. Such reactions fragment the big molecular of fuel into smaller structures for the further reactions but they do not affect the temperature in the cylinder as they are the endothermic reactions. This is a possible reason for unstable combustion of isooctane without spark-assisted ignition. Only alcohol fuels showed the exothermic reactions which led to the increased amount of carbon dioxide at the re-compression stroke and higher charge temperature. As a result, the auto-ignition of methanol occurred earlier than gasoline.

## Chapter 7 Conclusions and Future Work

### 7.1 Summary

CAI combustion characteristics of alcohol fuels were investigated in the current study. In addition, the effects of spark discharge and injection timing were clarified. Three experimental techniques were applied to a single cylinder engine to better understand the combustion process. The thermodynamic engine test was firstly conducted to understand primary combustion characteristics and exhaust emissions of alcohol fuels and their blend with gasoline. The effects of injection timing and spark-assisted ignition were also investigated. These preliminary results were used to select the test conditions for the subsequent in-cylinder combustion and speciation studies.

Secondly, flame structure and chemiluminescence emissions of excited intermediate species of CAI combustion with gasoline and alcohol fuels were studied by high speed imaging technique. In order to focus on the thermal/chemical effect from fuel reforming reactions, injection timing was fixed in the negative valve overlap period. The flame structure was captured by total chemiluminescence. Excited CHO and OH radicals were detected with the appropriate bandpass filters. As a result, flame structure and auto-ignition sites were elucidated.

Finally, fuel reforming reactions and chemical kinetic reactions were investigated by means of the in-cylinder gas sampling technique. It was used to obtain time-resolved speciation of in-cylinder gases in order to identify the reactions involved. With this in-cylinder sampling gas experiment, the fuel reforming process was confirmed and the subsequent effect on early auto-ignition and faster combustion of alcohol fuels was identified.

## 7.2 Conclusions

### 7.2.1 Effect of Alcohol Fuels on CAI Combustion Performance

Alcohol fuels were characterised with advanced auto-ignition timing and the faster combustion over gasoline. Methanol had the most advanced auto-ignition timing and shortest combustion duration. When alcohol was added to gasoline up to 50% in volume, the combustion process was brought forward and lasted for a shorter period. Increasing the percentage of alcohol beyond 50 % decreased this effect. Two causes were identified for advanced and fast combustion of alcohol fuels. Firstly, the charge temperature was elevated due to the heating effect of a large amount of residual gas. It was noted that alcohol fuels resulted in higher charger temperature during the compression stroke. Secondly, when fuel was injected directly into hot trapped residual gas, more fuel reforming reactions and heat release took place with alcohol fuels which resulted in the advanced ignition and faster combustion.

As a result of advanced auto-ignition,  $P_{\max}$ ,  $\left(\frac{dP}{d\theta}\right)_{\max}$ , and  $\left(\frac{dQ}{d\theta}\right)_{\max}$  of alcohol fuels were higher than that of gasoline. On the other hand, too early combustion phasing contributed to lower IMEP. Lower cyclic variation in  $P_{\max}$  but higher cycle to cycle variation in IMEP were observed with alcohol fuels.

With regard to exhaust emissions, alcohol fuels produced lower emissions of HC and  $\text{NO}_x$ . Due to a lower combustion temperature of alcohol fuels,  $\text{NO}_x$  formation was reduced. However, the lower combustion temperature caused higher CO emission from neat alcohol, because of incomplete CO to  $\text{CO}_2$  oxidation.

### 7.2.2 Effect of Injection Timing

CAI combustion could be achieved with all fuels with injection timing during the re-compression stroke. After injection timing was retarded to the intake stroke, neat alcohol could not achieve CAI combustion without the aid of spark discharge. Due to higher heat of vaporization of alcohol fuels, charge cooling effect caused the charge

temperature to be lower than the attainable auto-ignition temperature. In addition, no reforming reaction took place to enhance the main combustion. After injection timing was further delayed to the compression stroke, pure CAI combustion could not be achieved for all fuels because of the shorter mixing and residence time for fuel to mix with air and hot residual gas to undergo pre-combustion reactions.

The thermal/chemical effects from the fuel reforming reaction when injecting fuel directly into hot trapped residual gas were observed to advance combustion timing for all fuels except gasoline with spark-assisted ignition. Compared with gasoline, alcohol fuels showed more pronounced fuel reforming and heat release reactions. In comparison, charge cooling effect was noticed for late injection to delay the combustion process except gasoline with spark-assisted ignition.

### **7.2.3 Effect of Spark-Assisted Ignition**

Spark discharge was found to advance the combustion of gasoline as indicated by the 10% MFB values. On the other hand, spark had little effect on alcohol blended fuels. At the same injection timing, the crank angle of 10 % MFB remained unchanged for alcohol fuels with/without spark-assisted ignition. This can be explained by the fact that auto-ignition combustion under the current operating condition dominated the heat release process.

### **7.2.4 Flame Structure and Auto-Ignition Sites**

#### **7.2.4.1 Flame Structure through Total Chemiluminescence Image**

Flame structure and the in-cylinder processes of CAI combustion were recorded by total chemiluminescence imaging and compared to the heat release characteristics from in-cylinder pressure measurements. Chemiluminescence emission was detected from gasoline during the NVO period although little heat release was registered by the heat release analysis. In comparison, no chemiluminescence was detected for alcohol fuels whilst the heat release curves indicated heat being released from directly injected alcohol fuels during the re-compression stroke.

With spark-assisted ignition, flame propagation played the prominent role during the early period followed by spontaneous auto-ignition for CAI combustion. The presence of spark advanced the start of the heat release process and resulted in the location of initial ignition being at the center of the chamber. In comparison, flame propagation lasted for a much shorter period because of earlier self ignition at multiple sites. As a result, spark discharge showed little effect on alcohol fuel combustion.

Chemiluminescence images showed that auto-ignition mostly started in the perimeter area of the combustion chamber. Methanol showed the fastest and earliest auto-ignition combustion, followed by ethanol while gasoline was the slowest and most retarded combustion.

#### **7.2.4.2 CHO and OH chemiluminescence Image**

The presence of CHO and OH for all fuels showed the sequential order relating to the auto-ignition and combustion process of pure CAI without spark-assisted ignition. CHO formation took place just before the creation of OH species during the main combustion. The intensity curves of OH followed the same trend as the heat release rate. Therefore, OH formation can be used as an indicator of the start of main heat release.

On the other hand, with spark-assisted ignition CHO and OH formation were observed during the main combustion at relatively the same time. However, the terminations of CHO formations were attained before OH species. Due to the limited reaction pathways alcohol fuels showed lower image intensity for OH and CHO species when compared with gasoline.

### **7.2.5 Time-Resolved Detailed Species Composition**

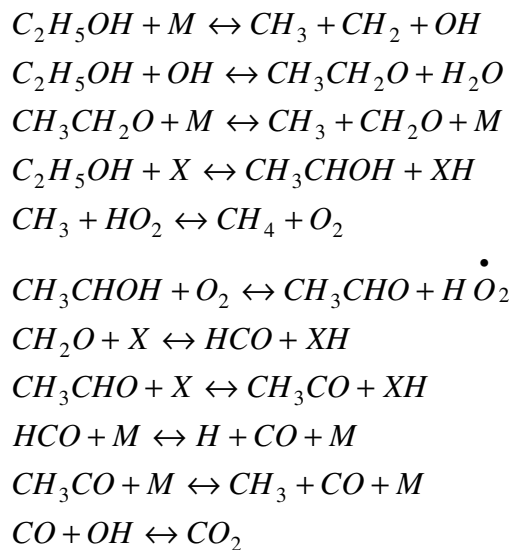
#### **7.2.5.1 60 PRF and Gasoline**

From time-resolved speciation measurement of gasoline and PRF fuels, fuel pyrolysis during the NVO period from fuel reforming reaction was confirmed. According to

reaction pathways shown in Figure 2.8 low temperature oxidations produced olefins and aldehyde. The small amount of ketone detected was a result of the reaction 4 of ketohydroperoxide production. Due to the increased intake temperature and high engine speed, chemical reactions took place in the NTC region. As a result, no cool flame was detected for the current engine even with 60 PRF. The ignition timing was delayed than that of alcohol fuels.

### 7.2.5.2 Ethanol

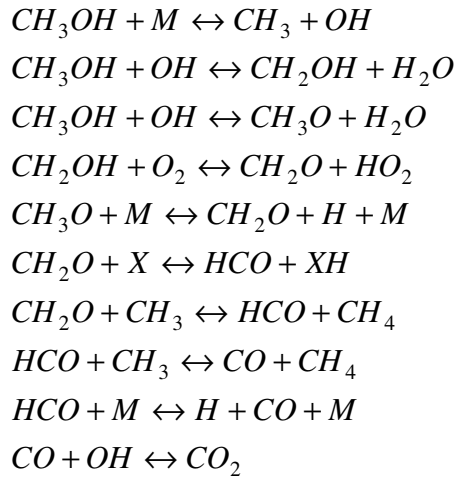
Exothermic fuel reforming reactions of ethanol fuel was confirmed by measured species composition during the re-compression stroke. The reactions increased charge temperature and contributed to advancing the main combustion. The reaction pathways for ethanol oxidation are favoured to produce methyl radical, a main intermediate species, and acetaldehyde, a main combustion product. The main reaction pathways are shown as below:



### 7.2.5.3 Methanol

Chemical species detected confirmed the presence of significant fuel reforming reactions including fuel pyrolysis and oxidation which resulted in advanced main combustion. The major reaction pathways of methanol combustion for the

formaldehyde formation, the main important product, and intermediate, as well as methane are presented below.



### 7.3 Recommendation for Future Work

In the future, optical diagnosis based on the PLIF technique should be carried out to measure in-cylinder temperature and fuel distribution for better understanding of the auto-ignition sites observed at the perimeter of the combustion chamber.

The using alcohol fuels in CAI combustion should be investigated in a suitable CAI engine in which inlet and exhaust valve timing should be varied to allow the differences between alcohol and gasoline fuels at fixed engine speed and loads.

In order to avoid the clash of the sampling valve with the piston, detailed speciation of in-cylinder gas can not be analyzed at the late compression stroke which is the crucial crank angle for ignition process. Therefore, the sampling near to TDC should be considered by mounting a smaller gas sampling valve tip in the cylinder head.

Peroxide is the most important species relating to auto-ignition. Therefore, a small amount of its formation should be detected with time-resolved detailed species composition by using an on-line gas chromatography or modifying the special collection technique.

Liquid chromatography or DNPH method which is one of the best techniques for detection of formaldehyde should be applied and compared to gas chromatography in order to improve the accuracy of formaldehyde concentration.

## Reference

1. Shigeru Onishi, Souk Hong Jo, Katsuji Shoda, Pan Do Jo, and Satoshi Kato (1979), “ Active Thermo-Atmosphere Combustion (ATAC) - A New Combustion Process for Internal Combustion Engines” , SAE Paper 790501.
2. Noguchi, M., Tanaka, Y., Tanaka, T., and Takeuchi, Y., (1979), “A Study on Gasoline Engine Combustion by Observation of Intermediate Reactive Products during Combustion “, SAE Paper 790840.
3. Fuquan Zhao, Thomas W. Asmus, Dennis N. Assanis, John E. Dec , James A. Eng and Paul M. Najt (2003), “ Homogeneous Charge Compression Ignition (HCCI) Engines Key Research and Development Issues”, PT-94 , SAE Inc, ISBN 0-7680-1123-X.
4. Hua Zhao (2007), “HCCI and CAI engines for the automotive industry”, CRC Press LLC, ISBN 978-1-4200-4459-1, Woodhead Publishing Lt., ISBN 978-1-84569-128-8.
5. Paul M. Najt and David E. Foster (1983), “Compression-Ignited Homogeneous Charge Combustion”, SAE Paper 830264.
6. Thring, R.H., (1989), “Homogeneous-Charge Compression-Ignition (HCCI) Engines”, SAE Paper 892068.
7. Aoyama, T., Hattori, Y., Mizuta, J., and Sato, Y., (1996), “An Experimental Study on Premixed-Charge Compression Ignition Gasoline Engine”, SAE Paper 960081.
8. Magnus Christensen, Anders Hultqvist and Bengt Johansson (1999), “Demonstrating the Multi Fuel Capability of a Homogeneous Charge Compression Ignition Engine with Variable Compression Ratio”, SAE Paper 1999-01-3679.
9. Hiraya, K., Hasegawa, K., Urushihara, T., Iiyama, A., and Itoh, T., (2002), “A Study on Gasoline Fueled Compression Ignition Engine ~ A Trial of Operation Region Expansion~”, SAE Paper 2002-01-0416.
10. Yoichi Ishibashi and Masahiko Asai (1996), “Improving the Exhaust Emissions of Two-Stroke Engines by Applying the Activated Radical Combustion”, SAE Paper 960742.

11. Willand, J., Nieberding, R., Vent, G., and Enderle, C., (1998), "The Knocking Syndrome – Its Cure and Its Potential", SAE Paper 982483.
12. Lavy, J., Dabadie, J., Angelberger, C., Duret, P.(IFP), Willand, J., Juretzka, A., Schaflein, J. (Daimler-Chrysler), Ma, T. (Ford), Lendresse, Y., Satre, A. (PSA Peugeot Citroen), Schulz, C.,Kramer, H. (PCI - Heidelberg University), Zhao, H., Damiano, L.(Brunel University) (2000), "Innovative Ultra-low NOx Controlled Auto-Ignition Combustion Process for Gasoline Engines : the 4-SPACE Project", SAE Paper 2000-01-1837.
13. Zhao, H., Li, J., Ma, T., and Ladommatos, N., (2002), "Performance and Analysis of a 4-Stroke Multi-Cylinder Gasoline Engine with CAI Combustion", SAE Paper 2002-01-0420.
14. Law, D., Kemp, D., Allen, J., Kirkpatrick, G., and Copland, T., (2001), "Controlled Combustion in an IC-Engine with a Fully Variable Valve Train", SAE Paper 2001-01-0251.
15. Lucien Koopmans and Ingemar Denbratt (2001), "A Four Stroke Camless Engine, Operated in Homogeneous Charge Compression Ignition Mode with Commercial Gasoline", SAE Paper 2001-01-3601.
16. Navin Kalian, Richard Standing and Hua Zhao (2005), "Effects of Ignition Timing on CAI Combustion in a Multi-Cylinder DI Gasoline Engine", SAE Paper 2005-01-3720.
17. Standing, R., Kalian, N., Ma, T., and Zhao, H., (2005), "Effects of Injection Timing and Valve Timings on CAI Operation in a Multi-Cylinder DI Gasoline Engine", SAE Paper 2005-01-0132.
18. Hyvönen, J., Haraldsson, G., and Johansson, B., (2005), "Operating Conditions Using Spark Assisted HCCI Combustion During Combustion Mode Transfer to SI in a Multi-Cylinder VCR-HCCI Engine", SAE Paper 2005-01-0109.
19. Leach, B., Zhao, H., Li, Y., and Ma, T., (2005), "Control of CAI Combustion through Injection Timing in a GDI Engine with an Air-Assisted Injector", SAE Paper 2005-01-0134.
20. Li, Y., Zhao, H., Nikolaos, B., Ma, T., and Leach, B., (2006), "Effect of Injection timing on Mixture and CAI Combustion in a GDI Engine with an Air-Assisted Injector", SAE Paper 2006-01-0206.

21. Li, Y., Zhao, H., Nikolaos, B., and Ma, T., (2007), "Parametric Study on CAI Combustion in a GDI Engine with an Air-Assisted Injector", SAE Paper 2007-01-0196.
22. Urushihara, T., Hiraya, K., Kakuhou, A., and Itoh, T., (2003), "Expansion of HCCI Operating Region by the Combination of Direct Fuel Injection, Negative Valve Overlap and Internal Fuel Reformation", SAE Paper 2003-01-0749.
23. Waldman, J.O., Nitz, D.G., Aroonsrisopon, T., Foster, D.E., and Iida, M., (2007), "Experimental Investigation into the Effects of Direct Fuel Injection during the Negative Valve Overlap Period in an Gasoline Fueled HCCI Engine", SAE Paper 2007-01-0219.
24. Aroonsrisopon, T., Nitz, D.G., Waldman, J. O., Foster, D. E., and Iida, M., (2007), "A Computational Analysis of Direct Fuel Injection During the Negative Valve Overlap Period in an Iso-Octane Fueled HCCI Engine", SAE Paper 2007-01-0227.
25. Song, H.H., Padmanabha, A., Kaahaaina N.B., and Edwards, C.F., (2009), "Experimental Study of Recompression Reaction for Low-load Operation in Direct-Injection Homogeneous Charge Compression Ignition Engines with n-Heptane and i-Octane fuels", International Journal of Engine Research, Volume 10 Number 4 page 215-229.
26. Song, H.H., and Edwards, C.F., (2009), "Understanding Chemical Effects in Low-Load-Limit Extension of Homogeneous Charge Compression Ignition Engines via Recompression Reaction", International Journal of Engine Research, Volume 10 Number 4 page 231-250.
27. Nasser, S. H., (1997), "Alternative Fuels for the 21st Century Vehicles in Europe", Automotive Flues for the 21st Century, IMechE Seminar Publication 1997-1, page 21-33.
28. Norimasa Iida, (1994), "Combustion Analysis of Methanol-Fueled Active Thermo-Atmosphere Combustion (ATAC) Engine Using Spectroscopic Observation", SAE Paper 940684.
29. Inoue, K., Takei, K., Yoshida, K., Shoji, H., and Yamazaki, A., (2000), "Effect of EGR-Induced Hot Residual Gas on Combustion when Operating a Two-Stroke Engine on Alcohol Fuels", SAE Paper 2000-01-2972.

30. Aaron Oakley, Hua Zhao, Nicos Ladommatos and Tom Ma (2001), "Dilution Effects on the Controlled Auto-Ignition(CAI) Combustion of Hydrocarbon and Alcohol Fuels", SAE Paper 2001-01-3606.
31. Tsuchiya, K., and Seko, T., (1995), "Combustion Improvement of Heavy-Duty Methanol Engine by Using Autoignition System", SAE Paper 950060.
32. Seko, T., Kuroda, E., and Hamano, Y., (1998), "Methanol Lean Burn in an Auto-Ignition DI Engine", SAE Paper 980531.
33. Seko, T., and Kuroda, E., (2001), "Combustion Improvement of a Premixed Charge Compression Ignition Methanol Engine using Flash Boiling Fuel Injection", SAE Paper 2001-01-3611.
34. Maurya, R. K., and Agarwal, A. K., (2009), "Experimental Investigation of Cycle-by-Cycle Variations in CAI/HCCI Combustion of Gasoline and Methanol Fuelled Engine", SAE Paper 2009-01-1345.
35. Christensen, M., Johansson, B., and Einewall, P., (1997), " Homogeneous Charge Compression Ignition ( HCCI) Using Isooctane, Ethanol and Natural Gas - A Comparison with Spark Ignition Operation", SAE Paper 972874.
36. Maurya, R.K., and Agarwal, A.K., (2008), "Combustion and Emission Behavior of Ethanol Fuelled Homogeneous Charge Compression Ignition (HCCI) Engine", SAE Paper 2008-28-0064.
37. Gnanam, G., Sobiesiak, A., Reader, G., and Zhang, C., (2006), "An HCCI Engine Fuelled with Iso-octane and Ethanol", SAE Paper 2006-01-3246.
38. Zhang, Y., He, B., Xie, H., and Zhao, H., (2006), "The Combustion and Emission Characteristics of Ethanol on a Port Fuel Injection HCCI Engine", SAE Paper 2006-01-0631.
39. Hui Xie, Zhipeng Wei, Bangquan He and Hua Zhao (2006), "Comparison of HCCI Combustion Respectively Fueled with Gasoline, Ethanol and Methanol through the Trapped Residual Gas Strategy", SAE Paper 2006-01-0635.
40. Li, Y., Zhao, H., and Brouzos, N., (2008), "CAI Combustion with Methanol and Ethanol in a Air-Assisted Direct Injection Engine", SAE Paper 2008-01-1673.
41. Kohtaro Hashimoto, (2007), "Effect of Ethanol on the HCCI Combustion", SAE Paper 2007-01-2038.
42. Kohtaro Hashimoto, (2008), "Inhibition Effect of Ethanol on Homogeneous Charge Compression Ignition of Heptane", SAE Paper 2008-01-2504.

43. Kamio, J., Jurotani, T., Kuzuoka, K., Kubo, Y., Taniguchi, H., and Hashimoto, K., (2007), "Study on HCCI-SI Combustion Using Fuels Containing Ethanol", SAE Paper 2007-01-4051.
44. Xingcai, L., Yuchun, H., Linlin, Z., and Zhen, H., (2006), "Experimental study on the auto-ignition and combustion characteristics in the homogeneous charge compression ignition (HCCI) combustion operation with ethanol/n-heptane blend fuels by port injection", *The Science and Technology of Fuel and Energy*, Volume 85, Issues 17-18, Pages 2622-2631.
45. John E. Dec and Christoph Espey, (1998), "Chemiluminescence Imaging of Autoignition in a DI Diesel Engine", SAE Paper 982685.
46. Mancaruso, E., Merola, S.S., and Vaglieco, B.M., (2008), "Extinction and Chemiluminescence Measurements of HCCI Mode in Diesel Engine Operation with Late Injection", SAE Paper 2008-01-0027.
47. Augusta, R., Foster, D.E., Ghandhi, J.B., Eng, J., and Najt, P.M., (2006), "Chemiluminescence Measurements of Homogeneous Charge Compression Ignition (HCCI) Combustion", SAE paper 2006-01-1520.
48. Persson, H., Hultqvist, A., and Johansson, B., (2007), "Investigation of the Early Flame Development in Spark Assisted HCCI Combustion Using High Speed Chemiluminescence Imaging", SAE Paper 2007-01-0212.
49. Yang, C., Zhao, H., and Megaritis, T., (2009), "In-Cylinder Study of CAI Combustion with Negative Valve Overlap", SAE Paper 2009-01-1103.
50. Aleiferis, P.G., Charalambides, A.G., Hardalupas, Y., Taylor, A. M. K. P. , and Urata, Y., (2006), "Autoignition Initiation and Development of n-heptane HCCI Combustion Assisted by Inlet Air Heating, Internal EGR or Spark Discharge: An Optical Investigation", SAE Paper 2006-01-3273.
51. Hultqvist, A., Christensen, M., Johansson, B., Franke, A., Richter, M., and Alde'n, M., (1999), "A Study of Homogeneous Charge Compression Ignition Combustion Process by Chemiluminescence Imaging", SAE Paper 1999-01-3680.
52. John E. Dec, W. Hwang and M. Sjöberg, (2006), "An Investigation of Thermal Stratification in HCCI Engines Using Chemiluminescence Imaging", SAE Paper 2006-01-1518.

53. Hall, J.M., and Petersen, E. L., (2006), “An Optimized Kinetics Model for OH Chemiluminescence at High Temperatures and Atmospheric Pressures”, Wiley Periodicals, Inc. *Int J Chem Kinet* 38, page 714–724.
54. Collin, R., Nygren, J., Richter, M., Alden, M., Hildingsson, L., and Johansson, B., (2003), “Simultaneous OH- and Formaldehyde-LIF Measurements in an HCCI Engine”, SAE Paper 2003-01-3218.
55. Graf, N., Gronki, J., Schulz, C., Baritaud, T., Chernel, J., Duret, P., and Lavy, J., (2001), “ In-Cylinder Combustion Visualization in an Auto-Igniting Gasoline Engine using Fuel Tracer- and Formaldehyde-LIF Imaging”, SAE Paper 2001-01-1924.
56. Zhao, H., Peng, Z., and Ma, T., (2004), “Investigation of the HCCI/CAI Combustion Process by 2-D PLIF Imaging of Formaldehyde”, SAE Paper 2004-01-1901.
57. Levedahl, W.J., and Broida, H. P., (1952), “Emission Spectra on Autoignited Heptane-Air Mixtures”, *Analytical Chemistry*, 1952, 24 (11), pp 1776–1780.
58. A. G. Gaydon, F. R. S., N. P. W. Moore and J. R. Simonson, (1955), “Chemical and Spectroscopic Studies of Blue Flames in the Auto-ignition of Methane”, *Proceedings of the Royal Society of London. Series A, Mathematical and Physical Sciences*, Vol. 230, No. 1180 pp. 1-19.
59. William G. Agnew and John T. Agnew, (1956), “ Visible Emission Spectra of Two-Stage Flames of Diethyl Ether Produced in Flat-Flame Burner”, *Industrial and Engineering Chemistry* , Volume 48, No.12 page 2224-2231.
60. Hua Zhao and Nicos Ladommatos, (2001), “Engine Combustion Instrument and Diagnostics”, ISBN0-7680-0665-1.
61. A. Egerton, F.R.S., F. LL. Smith, D. Phil., and A.R. Ubbelohde, M.A. (1935), “ Estimation of the Combustion Products from the Cylinder of the Petrol Engine and its Relation to Knock”, *Philosophical Transactions of the Royal Society of London. Series A, Mathematical and Physical Sciences*, Volume 234, Issue 744, pp. 433-521.
62. D. Downs, A.D. Walsh and R. W. Wheeler, (1951), “A Study of the Reaction that Lead to Knock in the Spark-Ignition Engine”, *Philosophical Transactions of the Royal Society of London. Series A, Mathematical and Physical Sciences*, Volume 243, Issue 870, pp. 463-524.

63. Houliang Li, Srinivasa K. Prabhu, David L. Miller, and Nicholas P. Cernansky, (1994), “ Autoignition Chemistry Studies on Primary Reference Fuels in a Motored Engine”, SAE Paper 942062.
64. Houliang Li, Srinivasa K. Prabhu, David L. Miller, and Nicholas P. Cernansky, (1995), “The Effects of Methanol and Ethanol on the Oxidation of a Primary Reference Fuel Blend in a Motored Engine”, SAE Paper 950682.
65. Tsurushima, T., Shimazaki, N., and Asami, Y., (2000), “Gas Sampling Analysis of Combustion Process in a Homogeneous Charge Compression Ignition Engine”, Int J Engine Research, Volume 1, No. 4, Page 337-352.
66. Tezaki, A., Yamada, H., and Ohtomo, M., (2007), “Mechanism Controlling Autoignition Derived from Transient Chemical Composition Analysis in HCCI”, SAE Paper 2007-01-1882.
67. Westbrook, C. K., and Pitz, W. J., (1987), “Detailed Kinetic Modeling of Autoignition Chemistry”, SAE Paper 872107.
68. Griffiths, J.F., and Barnard, J.A., (1995), “Flame and Combustion”, Third Edition, ISBN 0 7514 0199 4.
69. Curran, H.J., Gaffuri, P., Pitz, W. J., and Westbrook, C. K., (1998), “A Comprehensive Modeling Study of n-Heptane Oxidation”, Combustion and Flame, 114:149-177.
70. Curran, H.J., Gaffuri, P., Pitz, W. J., and Westbrook, C. K., (1998), “A Comprehensive Modeling Study of iso-Octane Oxidation”, Combustion and Flame, 129:253-280.
71. Tsurushima, T., (2009), “A new Skeletal PRF Kinetic Model for HCCI Combustion”, Proceedings of the Combustion Institute 32, page 2835-2841.
72. William R. Leppard, (1989), “A Comparison of Olefin and Paraffin Autoignition Chemistries: A Motored-Engine Study”, SAE Paper 892081.
73. Marinov, N. M., (1998), “A Detailed Chemical Kinetic Model for High Temperature Ethanol Oxidation”, International Journal of Chemical Kinetics Volume 31 Issue 3, Pages 183 – 220.
74. Timothy J., Held, and Frederick L. Dryer, (1998), “A Comprehensive Mechanism for Methanol Oxidation”, International Journal of Chemical Kinetics, Volume 30 Issue 11, Page 805-830.

75. Westbrook, C.K., (2000), "Chemical Kinetics of Hydrocarbon Ignition in Practical Combustion Systems", Proceeding of the Combustion Institute, Volume 28, 2000, pp. 1563-1577.
76. Carl, L. J., Andy, D. B. Y., Andre, S., Gillian, B., and Klaus, M., (2005), "An Investigation of the Ignition Delay Character of Different Fuel Components and an Assessment of Various Autoignition Modelling Approaches", SAE Paper 2005-01-2084.
77. Bollentin, J. W., and Wilk, R. D., (1996), "Autoignition Characteristics of Ethanol", SAE Paper 961175.
78. Lee, D., Hochgreb, S., and Keck, J. C., (1993), "Autoignition of Alcohols and Ethers in a Rapid Compression Machine", SAE Paper 932755.
79. Westbrook, C.K., Pitz, W.J. , and Lepperd, W.R., (1991), "The Autoignition Chemistry of Paraffinic Fuels and Pro-Knock and Anti-Knock Additives: A Detailed Chemical Kinetic Study", SAE Paper 912314.
80. Shigeyuki, T., Ferran, A., James, C. K., and Heywood, J.B., (2003), "Two-stage ignition in HCCI combustion and HCCI control by fuels and additives", *Combustion and Flame* 132 (2003) p.219-239.
81. Leach, Ben Thomas, (2004), "In-cylinder flow and combustion studies in an air-assisted direct injection gasoline engine", PhD Thesis, 2004.
82. Leighton, S., Cebis, M., Southern, M., Ahern, S., and Horner, L., (1994), "The OCP Small Engine Fuel Injection System for Future Two-Stroke Marine Engines", SAE Paper 941687.
83. Houston, R., and Cathcart, G., (1998), "Combustion and Emissions Characteristics of Orbital's Combustion Process Applied to Multi-Cylinder Automotive Direct Injected 4-Stroke Engines", SAE Paper 980153.
84. Cathcart, G., and Zavier, C., (2000), "Fundamental Characteristics of an Air-Assisted Direct Injection Combustion Systems as Applied to 4-Stroke Automotive Gasoline Engines", SAE Paper 200-01-0256.
85. Stephen R. Turns, (1996), "An Introduction to Combustion: Concepts and Applications", ISBN 0-07-114783-7.
86. Borman, G. L., and Ragland, K.W., (1998), "Combustion Engineering", ISBN 0-07-006567-5.

87. Zhao, H., Lowry, G., and Ladommatos, N., (1996), "Time-Resolved Measurements and Analysis on In-Cylinder Gases and Particulates in Compression-Ignition Engines", SAE Paper 961168.
88. Ladommatos, N., Balian, R., Horrocks, R., and Cooper, L., (1996) "The Effect of Exhaust Gas Recirculation on Combustion and NO<sub>x</sub> Emissions in a High-Speed Direct-Injection Diesel Engine", SAE Paper 960840.
89. Ladommatos, N., Balian, R., Horrocks, R., and Cooper, L., (1996) "The Effect of Exhaust Gas Recirculation on Soot Formation in a High-Speed Direct-Injection Diesel Engine", SAE Paper 960841.
90. Heywood, J. B., (1988), "Internal Combustion Engine Fundamentals", McGraw-Hill, ISBN 0-07-100499-8, 1988.
91. Iida, N., Yamasaki, Y., Sato, S., Kumano, K., and Kojima, Y., (2004), "Study on Auto-Ignition and Combustion Mechanism of HCCI Engine", SAE Paper 2004-32-0095.
92. Jeuland, N., Montagne, X., and Duret, P., (2003), "Engine and Fuel Related Issues of Gasoline CAI (Controlled Auto-Ignition) Combustion ", SAE Paper 2003-01-1856.
93. Tsurushima, T., Harada, A., Iwashiro, Y., Enomoto, Y., Asaumi, Y., and Aoyagi, Y., (2001), "Thermodynamic Characteristics of Premixed Compression Ignition Combustion", SAE Paper 2001-01-1891.
94. Schuetzle, D., Siegl, W. O., Jensen, T. E., Dearth, M.A., Kaiser, E.W., Gorse, R., Kreucher, W., and Kulik, E., (1994), "The Relationship between Gasoline Composition and Vehicle Hydrocarbon Emissions: A Review of Current Studies and Future Research Needs", Environmental Health Perspectives, Vol.102, pp. 3-12.
95. Elghawi, U., Mistal, J., Tsolakis, A., Wyszynski, M.L., Xu, H.M., and Qiao, J., (2008), "GC-MS Speciation and Quantification of 1, 3 Butadiene and Other C1-C6 Hydrocarbons in SI/HCCI V6 Engine Exhaust", SAE Paper 2008-01-0012.
96. Dec, J.E., Davisson, M.L. Sjöberg, M., Leif, R.N. and Hwang, W., (2008), "Detailed HCCI Exhaust Speciation and the Sources of Hydrocarbon and Oxygenated Hydrocarbon Emissions", SAE Paper 2008-01-0053.

97. Li Cao, Hua Zhao and Xi Jiang, (2007), "Investigation into Controlled Auto-Ignition Combustion in a GDI Engine with Single and Split Fuel Injections", SAE Paper 2007-01-0211.
98. Benvenuti, L.H., Marques, C.S.T., and Bertran C., A., (2005), "Chemiluminescent Emission Data for Kinetic Modeling of Ethanol Combustion", *Combust. Sci. and Tech.*, 177 p 1-26.
99. Eng, J.A., Leppard, W.R. and Sloane, T.M., (2002), "The Effect of Pox on the Autoignition Chemistry of n-Heptane and Isooctane in an HCCI Engine", SAE Paper 2002-01-2861.
100. Iida, N., and Igarashi, T., (2000), "Auto-Ignition and Combustion of n-Butane and DME/Air Mixtures in a HCCI Engine", SAE Paper 2000-01-1832.
101. Huang, Y., Sung, C.J., Eng, J.A., (2004), "Laminar flame speeds of primary reference fuels and reformer gas mixtures", *Combustion and Flame* 139, p 239–251.

## Appendix A Results for Injection Timing at 40 degree ATDC

### A.1 In-cylinder pressure data

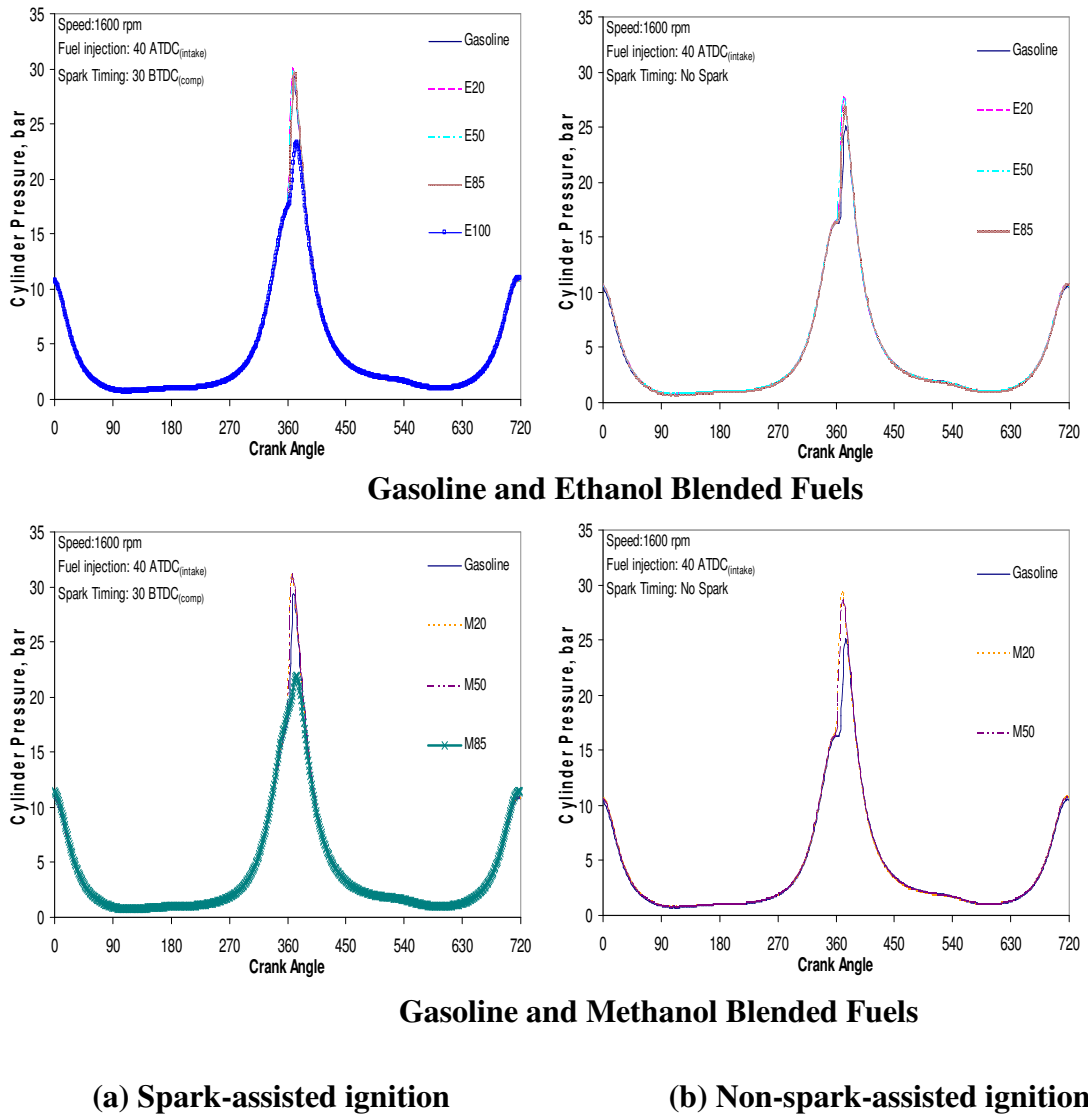
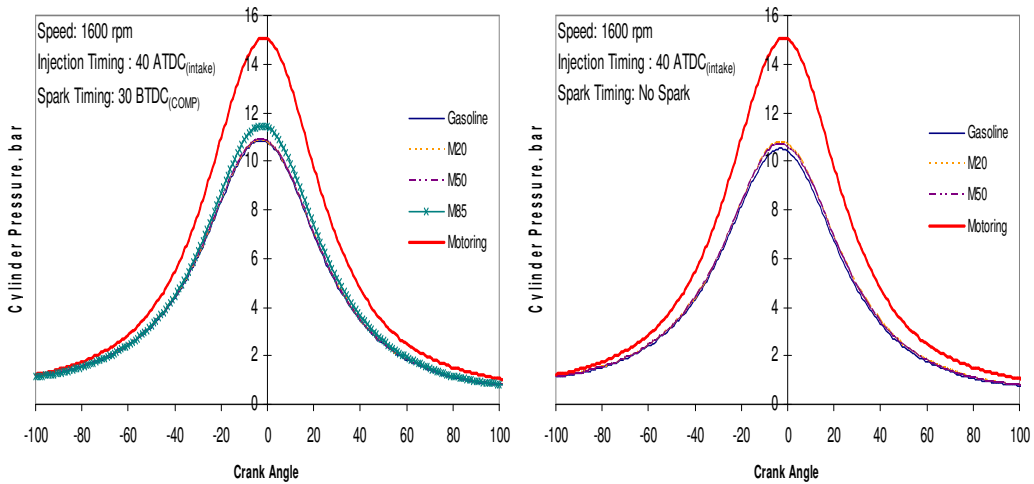
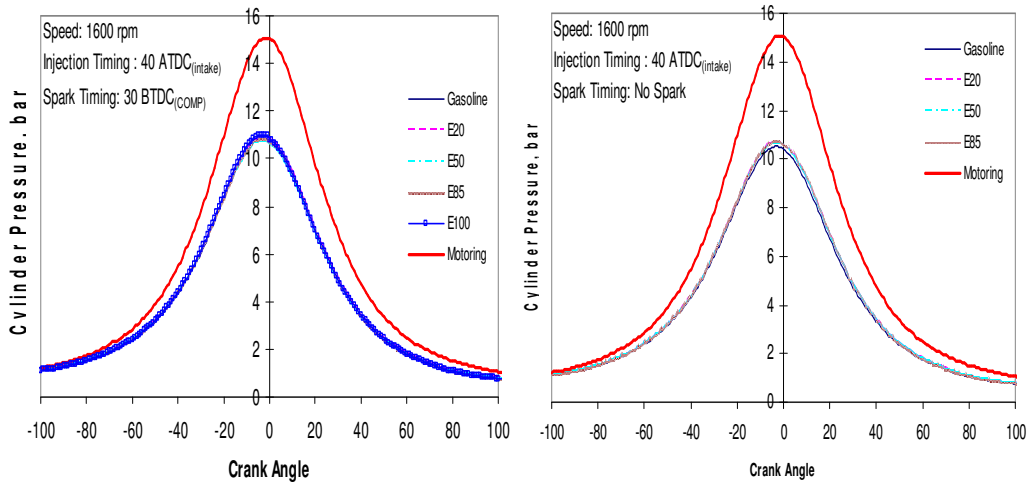


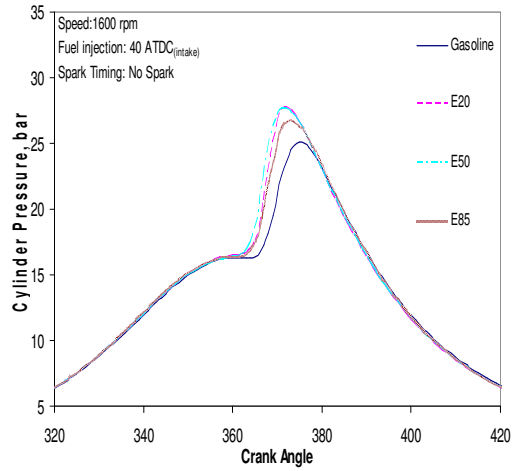
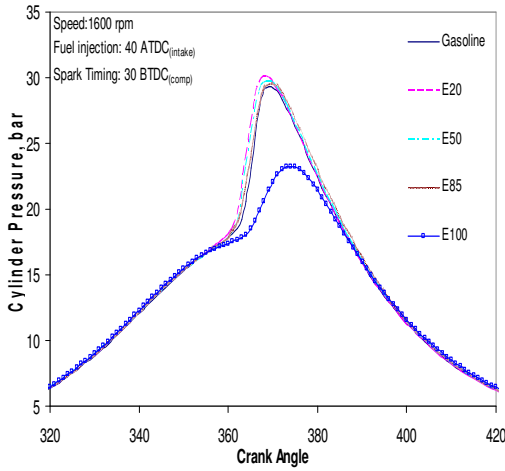
Figure A.1 In-Cylinder Pressure Traces with SOI 40 ATDC



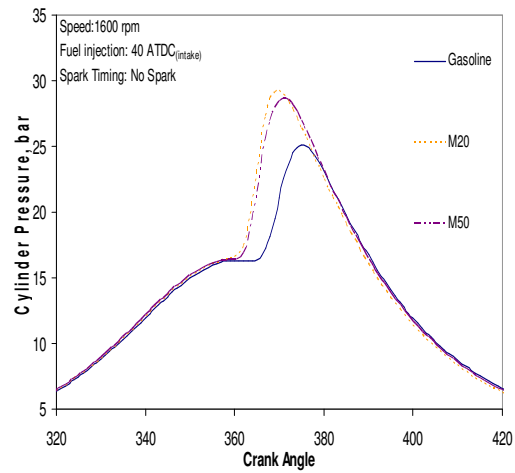
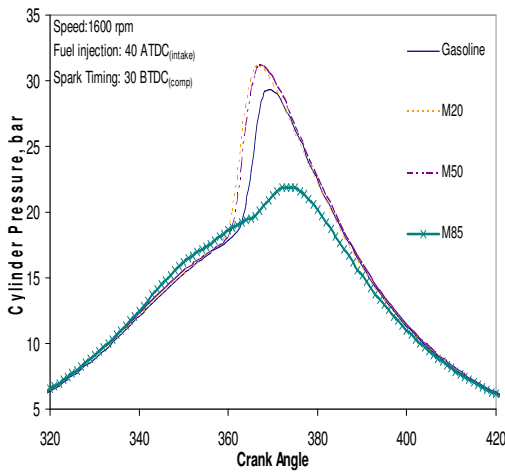
(a) Spark-assisted ignition

(b) Non-spark-assisted ignition

**Figure A.2 In-Cylinder Pressures during the Negative Overlap Period**



**Gasoline and Ethanol Blended Fuels**

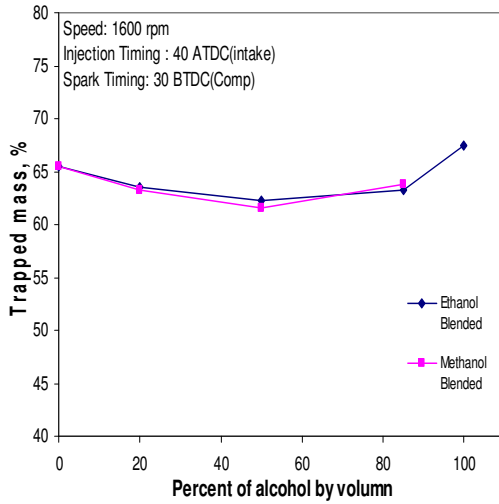


**Gasoline and Methanol Blended Fuels**

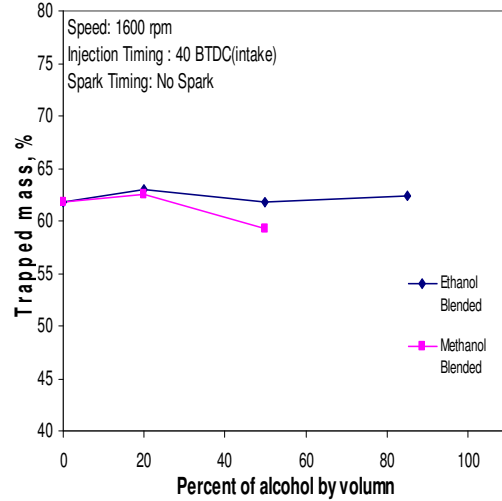
**a) Spark-assisted ignition**

**(b) Non-spark-assisted ignition**

**Figure A.3 In-Cylinder Pressures during the Main Combustion Process**

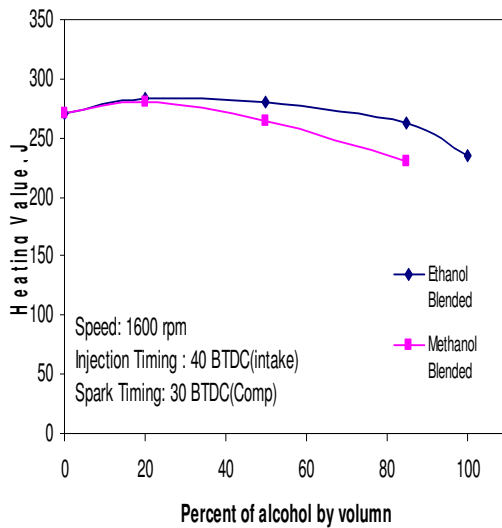


(a) Spark-assisted ignition

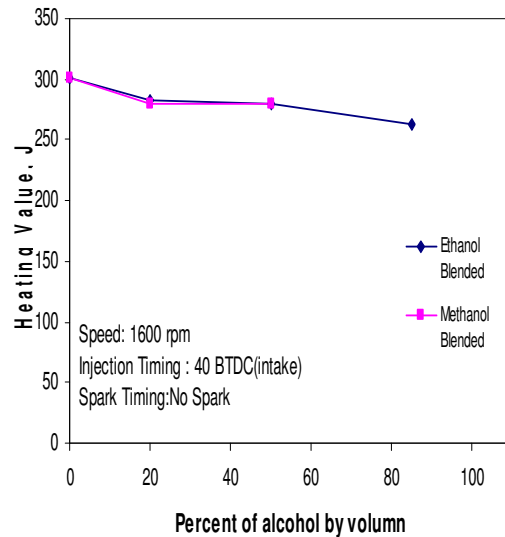


(b) Non-spark-assisted ignition

Figure A.4 Trapped mass residual for any Fuels



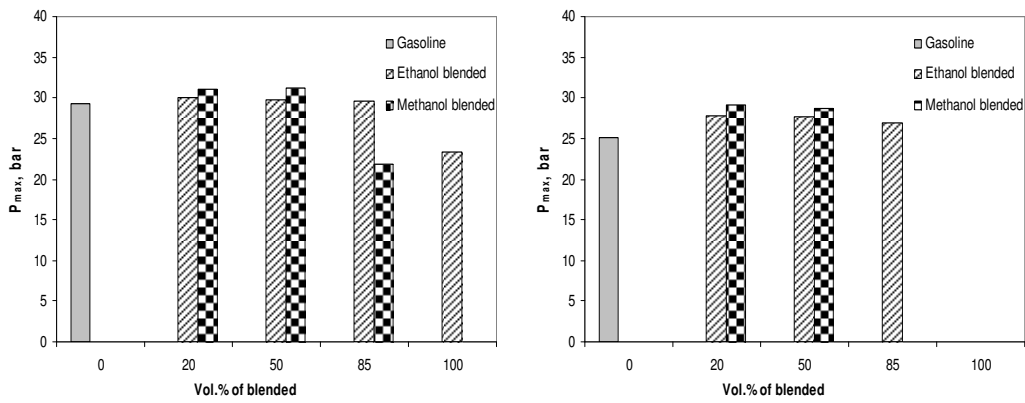
(a) Spark-assisted ignition



(b) Non-spark-assisted ignition

Figure A.5 Input Energy per Cycle for any Fuels

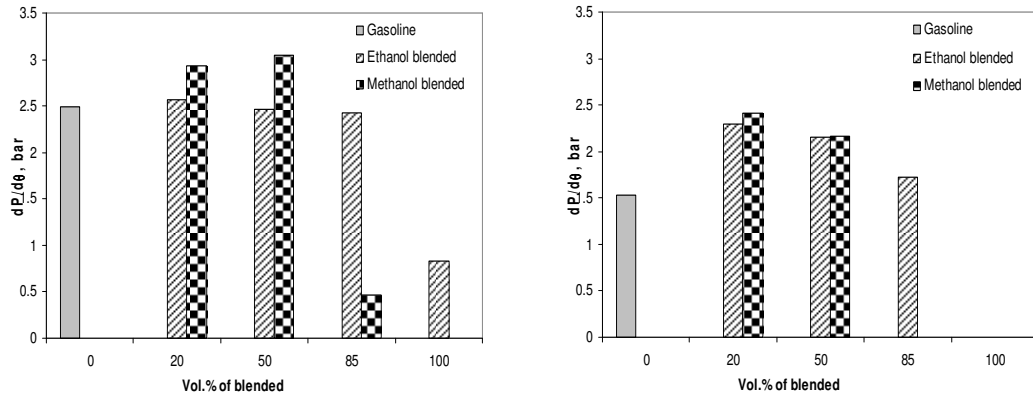
### Peak Pressure



(a) Spark-assisted ignition

(b) Non-spark-assisted ignition

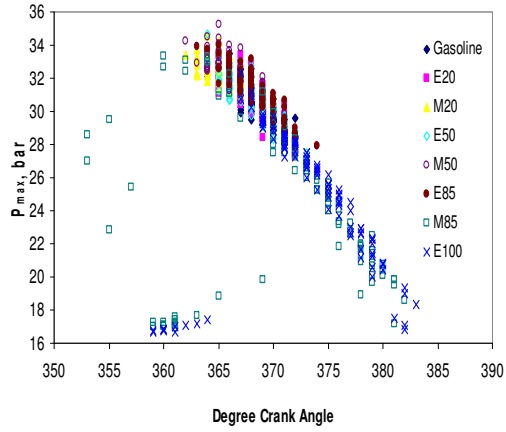
Figure A.6 Peak Pressure for all Fuels



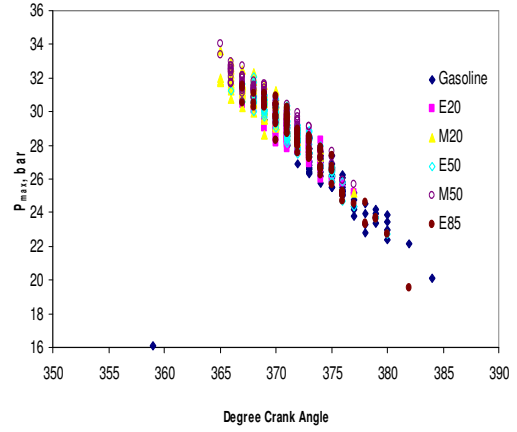
(a) Spark-assisted ignition

(b) Non-spark-assisted ignition

Figure A.7 Maximum of  $\frac{dP}{d\theta}$  for all Fuels

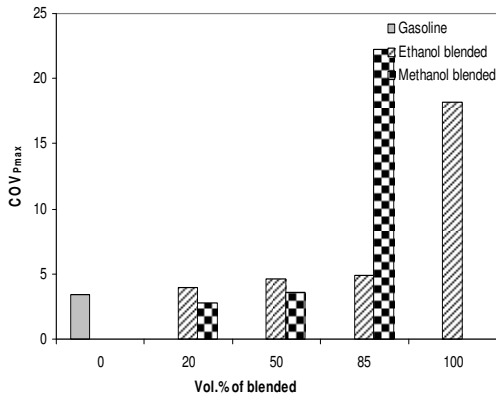


(a) Spark-assisted ignition

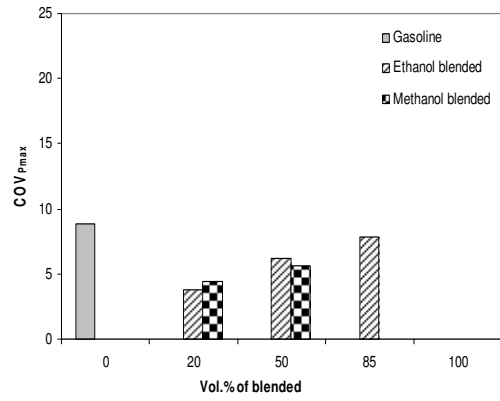


(b) Non-spark-assisted ignition

Figure A.8 Pmax and  $\theta_{Pmax}$



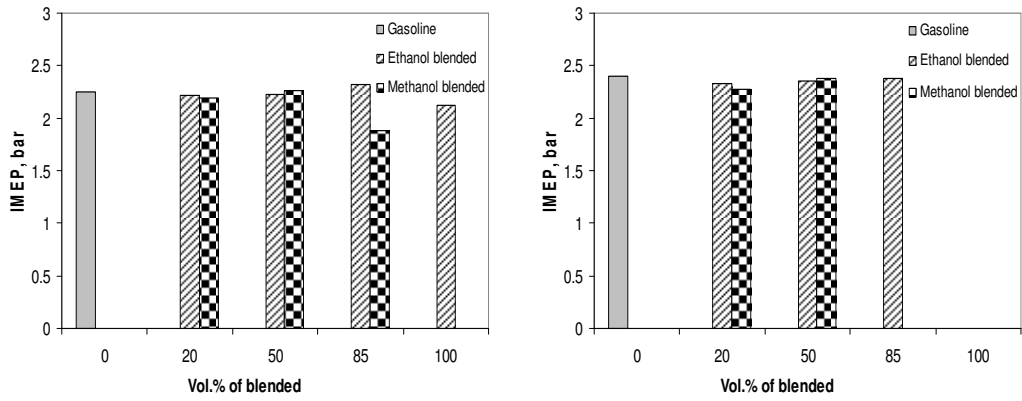
(a) Spark-assisted ignition



(b) Non-spark-assisted ignition

Figure A.9 Coefficient of Variation of Maximum Pressure

### Indicated Mean Effective Pressure



(a) Spark-assisted ignition

(b) Non-spark-assisted ignition

Figure A.10 Indicated Mean Effective Pressure for all Fuels

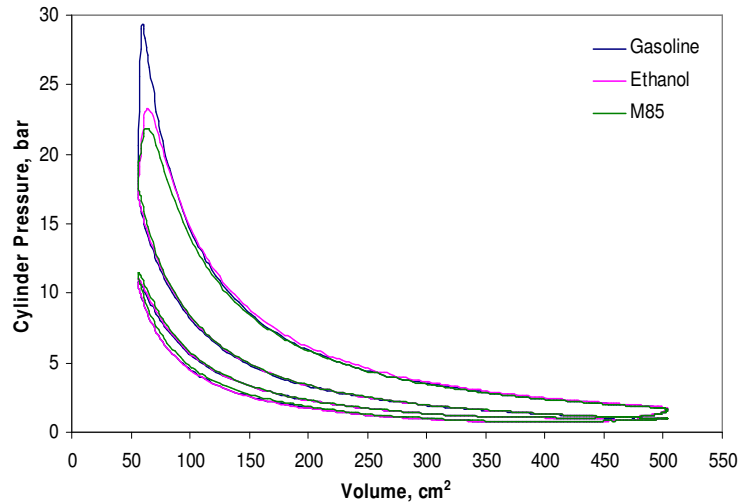
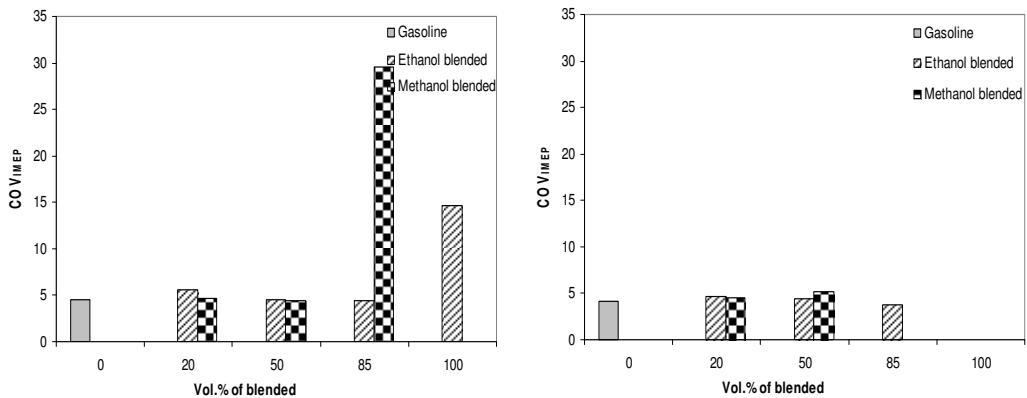


Figure 4.11 In-Cylinder Pressures against Volume



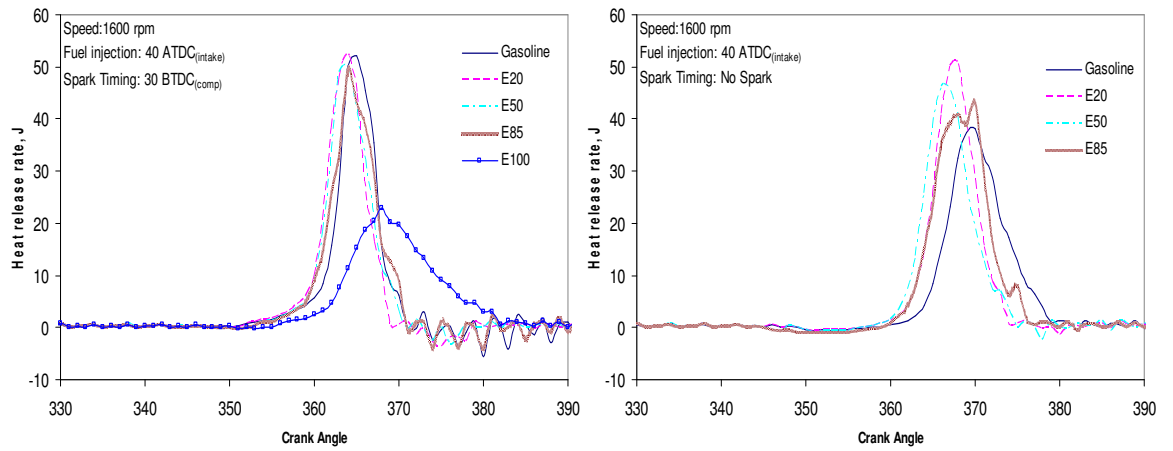
(a) Spark-assisted ignition

(b) Non-spark-assisted ignition

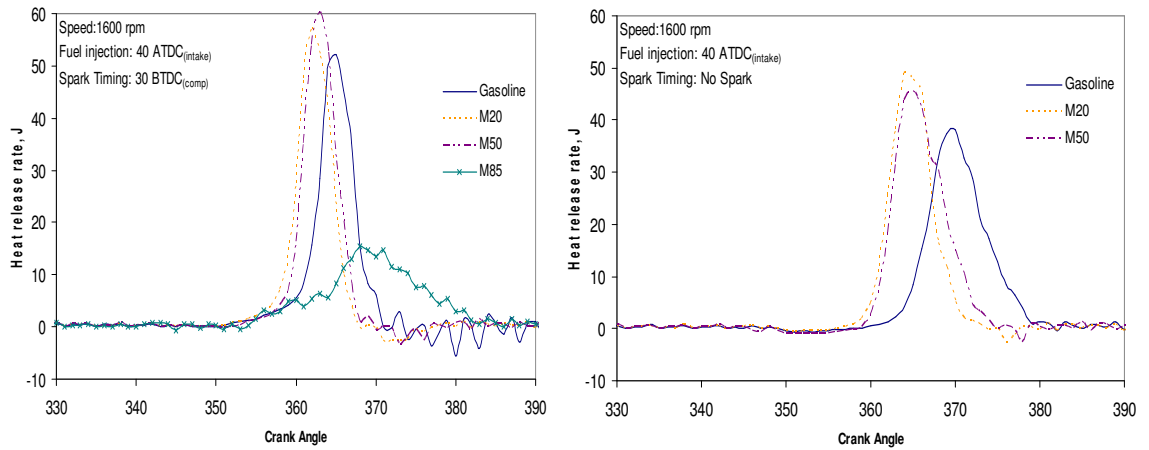
Figure 4.12 Coefficient of Variation of Indicated Mean Effective Pressure

## A.2 Thermodynamic and Combustion Characteristics results

### Heat Release Rate



### Gasoline and Ethanol Blended Fuels

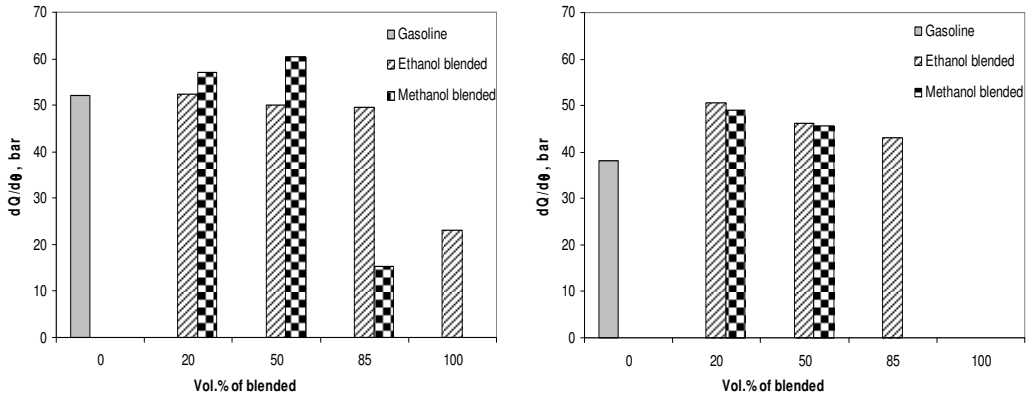


### Gasoline and Methanol Blended Fuels

(a) Spark-assisted ignition

(b) Non-spark-assisted ignition

Figure A.13 Heat Release Rate Curves

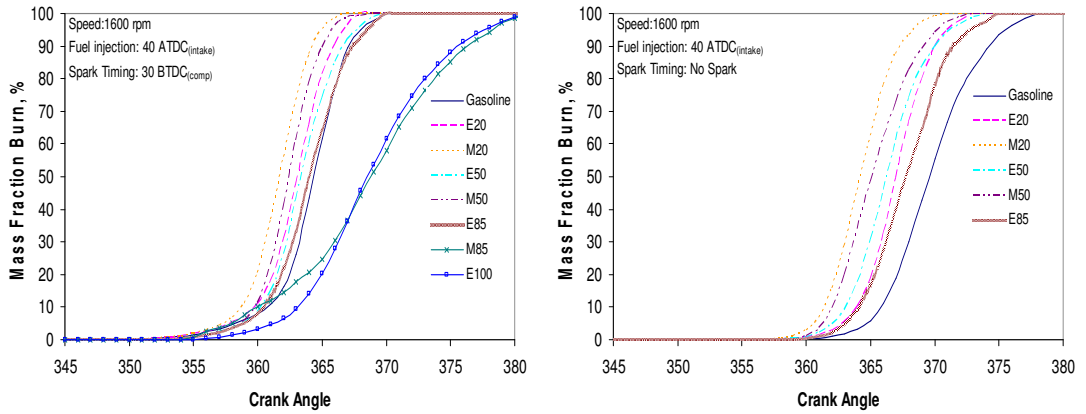


(a) Spark-assisted ignition

(b) Non-spark-assisted ignition

Figure A.14 Maximum of  $\frac{dQ}{d\theta}$  for All of Fuels

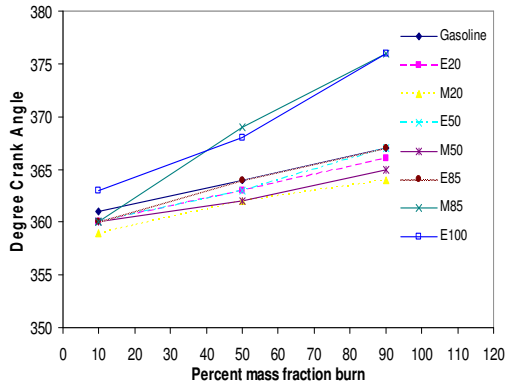
Mass Fraction Burned and Combustion Period



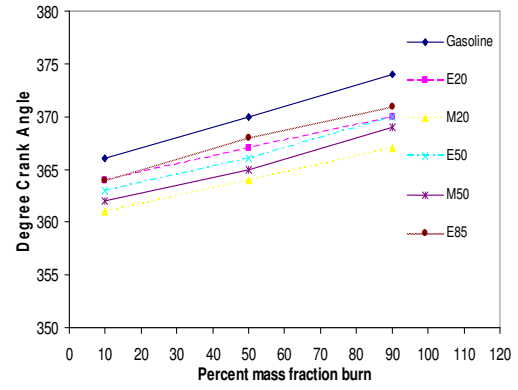
(a) Spark-assisted ignition

(b) Non-spark-assisted ignition

Figure A.15 Mass Fraction Burned

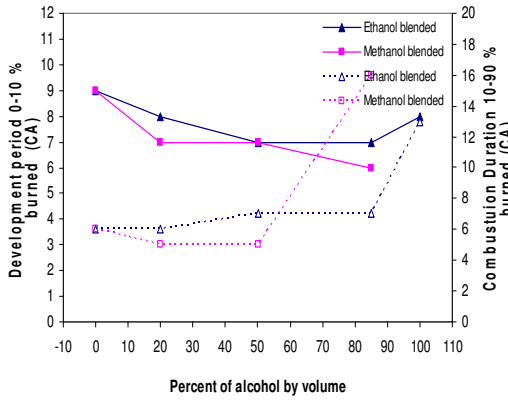


(a) Spark-assisted ignition

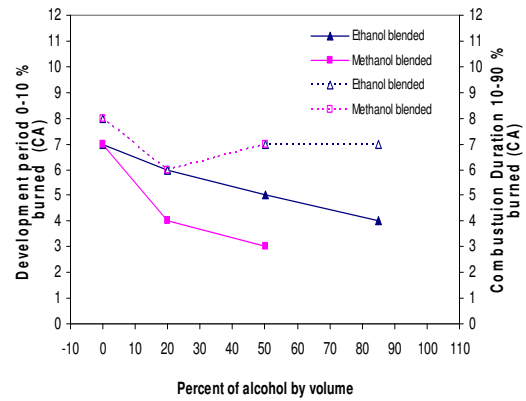


(b) Non-spark-assisted ignition

Figure A.16 Crank Angle at Any Percentage of Mass Fraction Burned



(a) Spark-assisted ignition

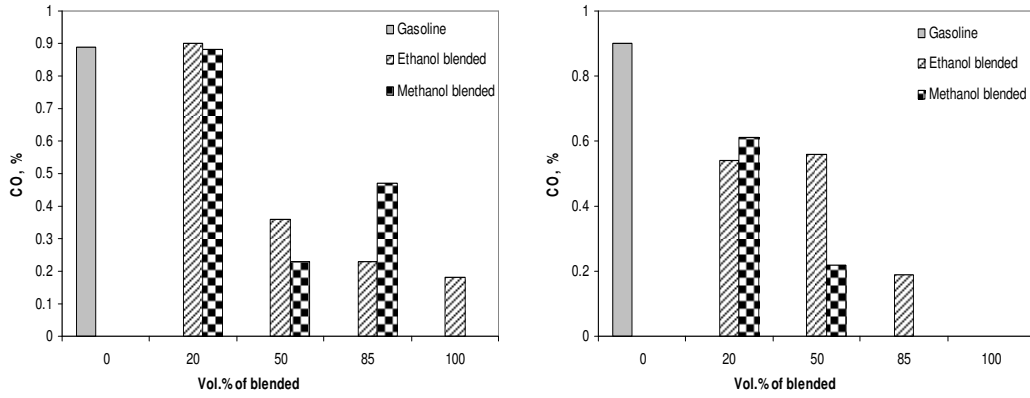


(b) Non-spark-assisted ignition

Figure A.17 Flame Development Period and Combustion Duration

### A.3 Engine-Out Exhaust Emission

#### Carbon Monoxide

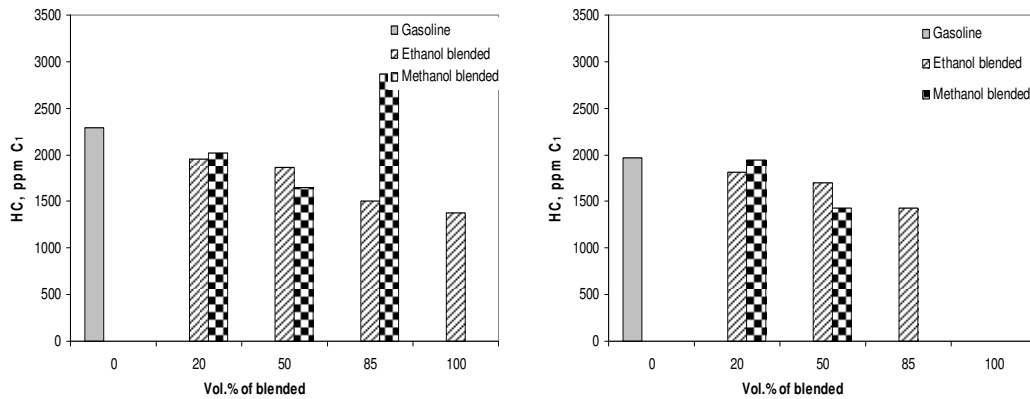


a) Spark-assisted ignition

b) Non-spark-assisted ignition

Figure A.18 Carbon Monoxide Emissions of All Fuels

#### Hydrocarbon

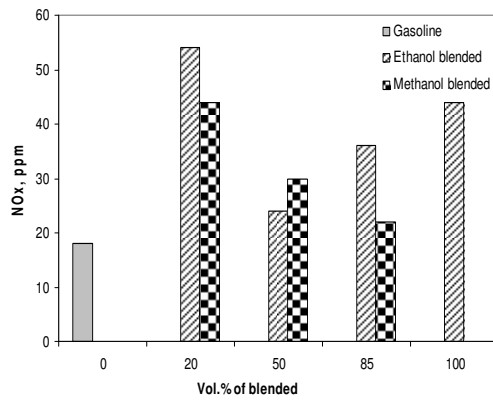


a) Spark-assisted ignition

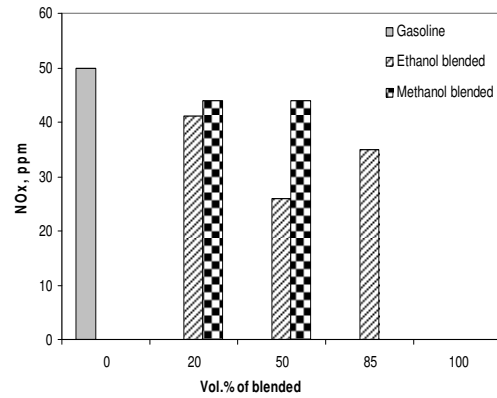
b) Non-spark-assisted ignition

Figure A.19 Hydrocarbon Emissions of All Fuels

## Oxide of Nitrogen



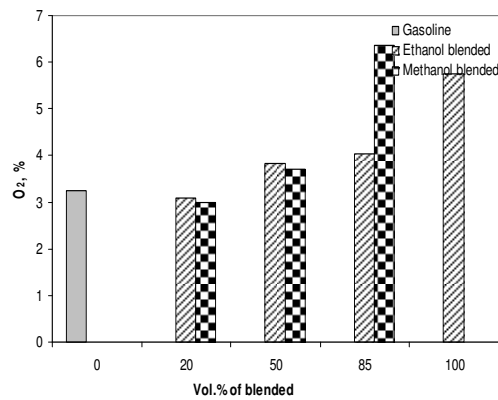
a) Spark-assisted ignition



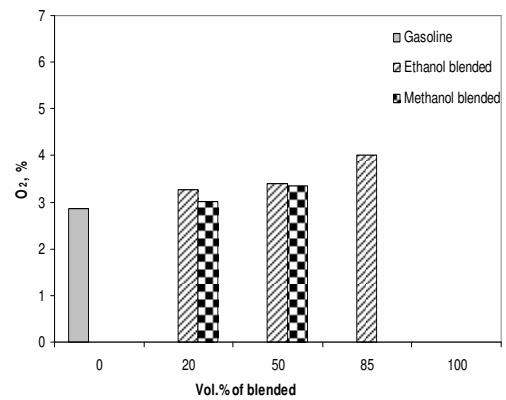
(b) Non-spark-assisted ignition

Figure A.20 Oxide of Nitrogen Emission of All Fuels

## Oxygen



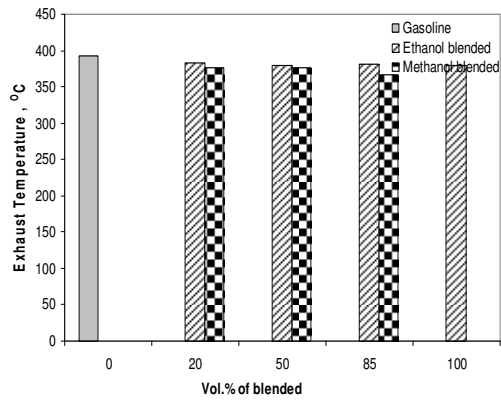
a) Spark-assisted ignition



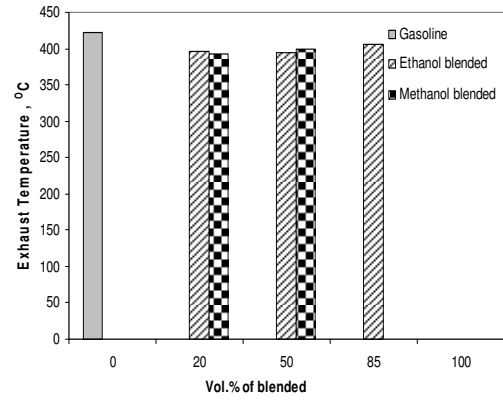
(b) Non-spark-assisted ignition

Figure A.21 Oxygen of all Fuels

## Exhaust Gas Temperature



(a) Spark-assisted ignition



(b) Non-spark-assisted ignition

Figure A.22 Exhaust Gas Temperatures of All Fuels

## Appendix B Results for Injection Timing at 80 degree ATDC

### B.1 In-cylinder pressure data

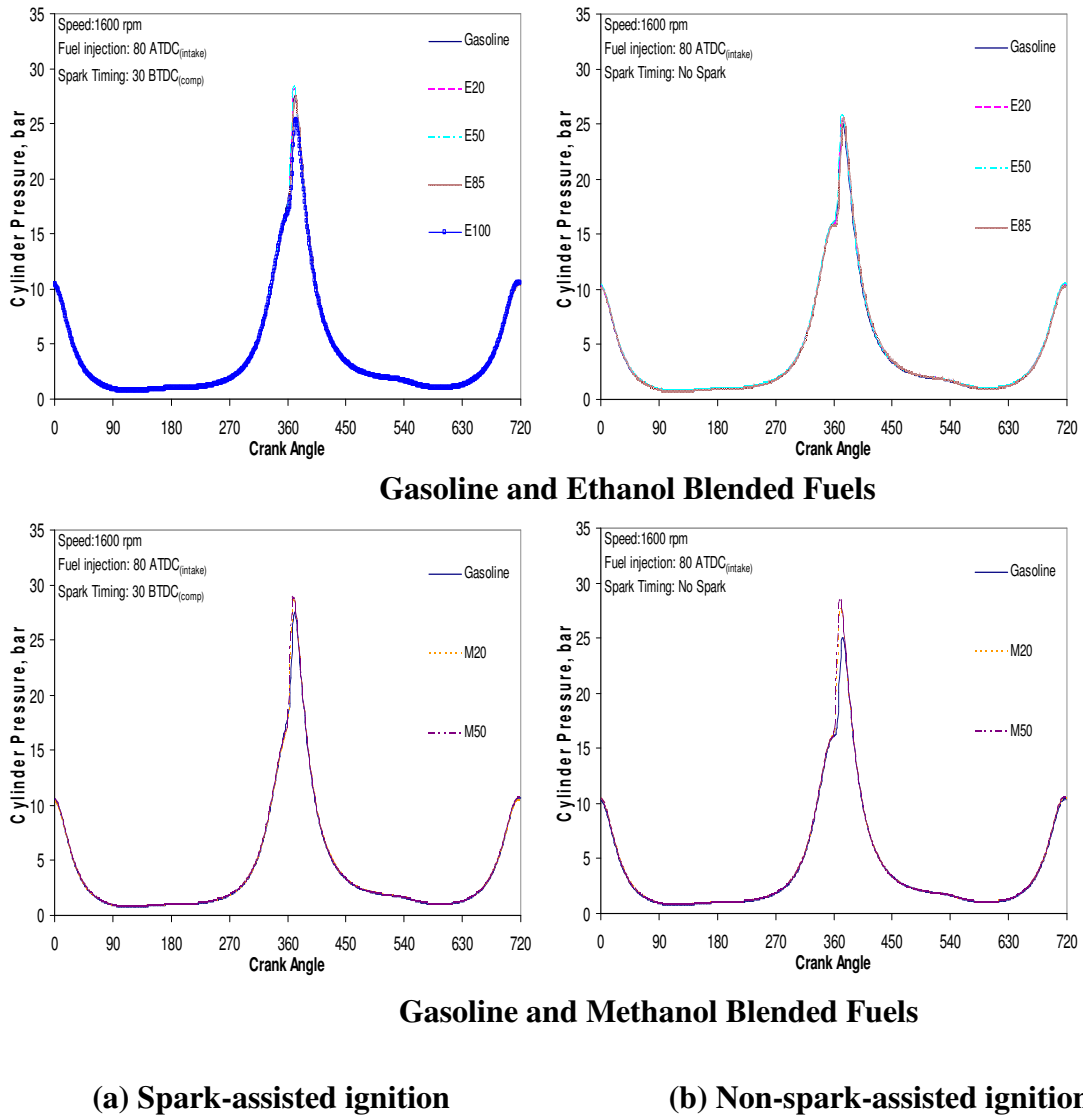
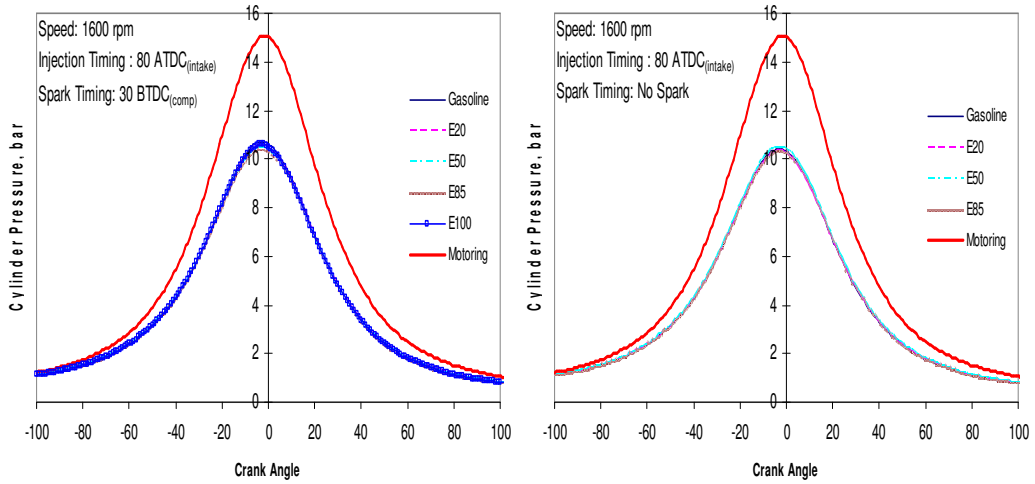
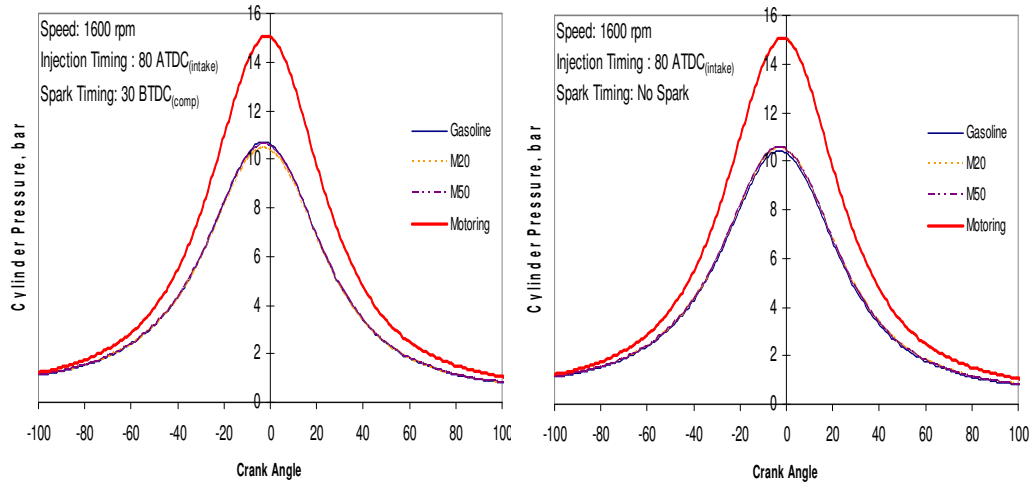


Figure B.1 In-Cylinder Pressure Traces with SOI 80 ATDC



**Gasoline and Ethanol Blended Fuels**

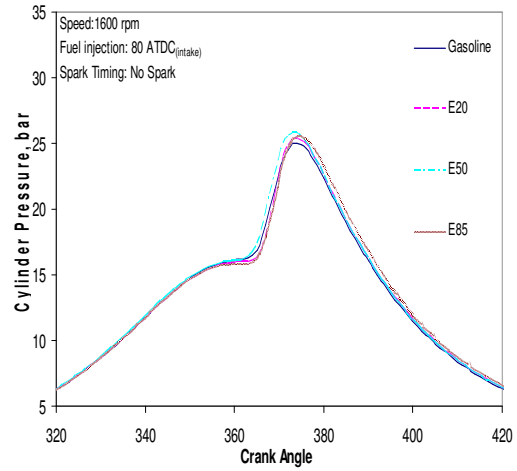
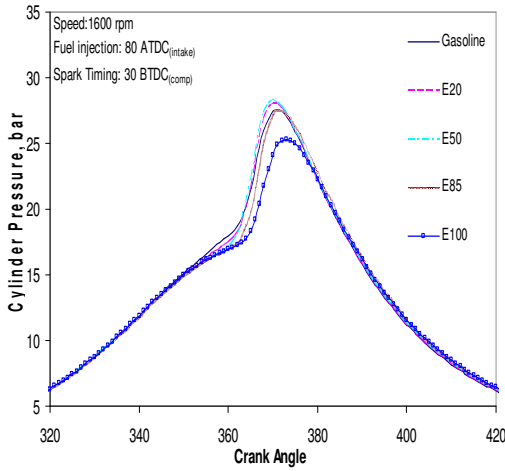


**Gasoline and Methanol Blended Fuels**

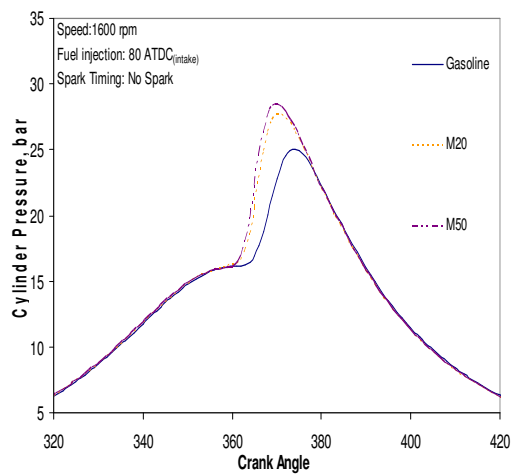
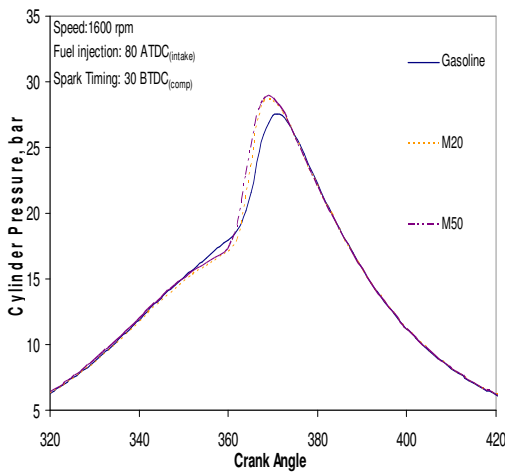
(a) Spark-assisted ignition

(b) Non-spark-assisted ignition

**Figure B.2 In-Cylinder Pressures during the Negative Overlap Period**



**Gasoline and Ethanol Blended Fuels**

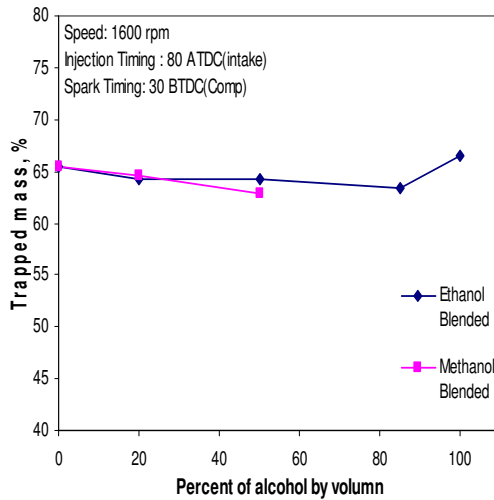


**Gasoline and Methanol Blended Fuels**

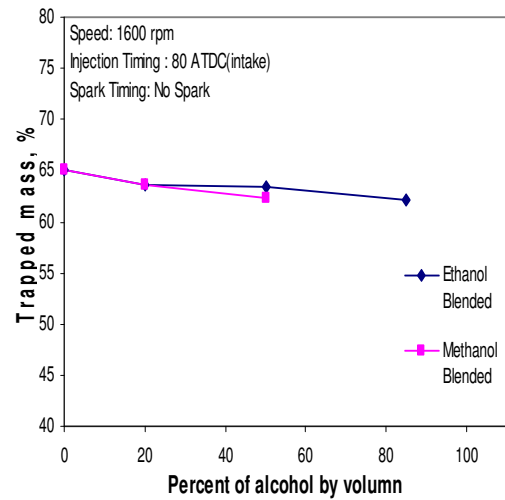
**a) Spark-assisted ignition**

**(b) Non-spark-assisted ignition**

**Figure B.3 In-Cylinder Pressures during the Main Combustion Process**

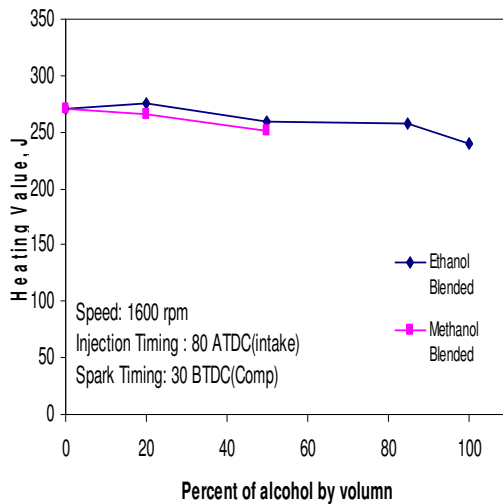


(a) Spark-assisted ignition

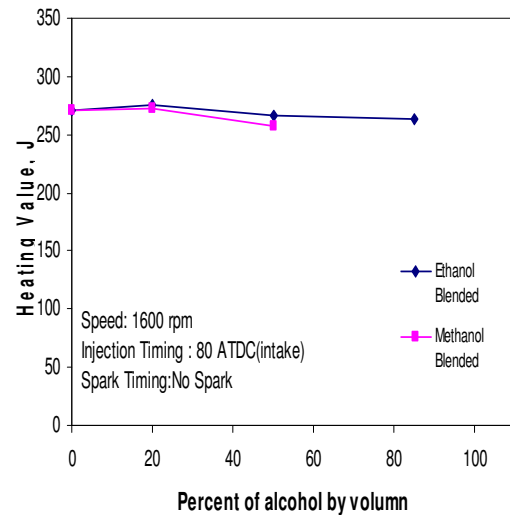


(b) Non-spark-assisted ignition

**Figure B.4 Trapped Mass Residual for any Fuels**



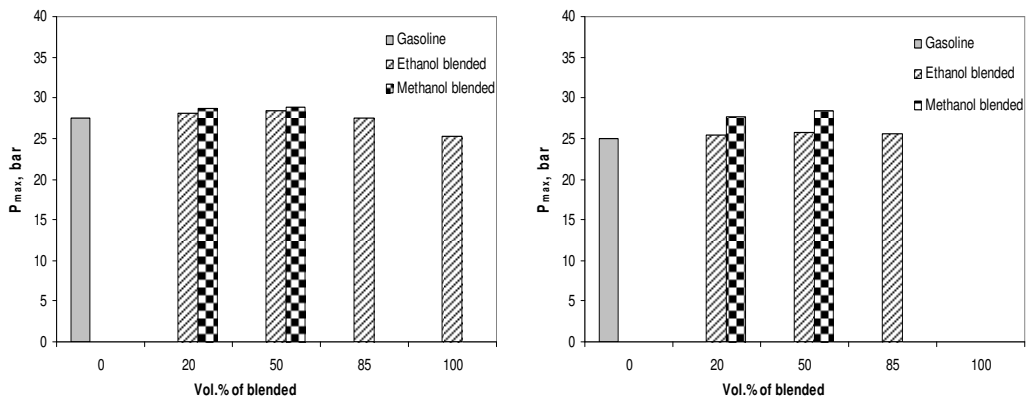
(a) Spark-assisted ignition



(b) Non-spark-assisted ignition

**Figure B.5 Input Energy per Cycle for any Fuels**

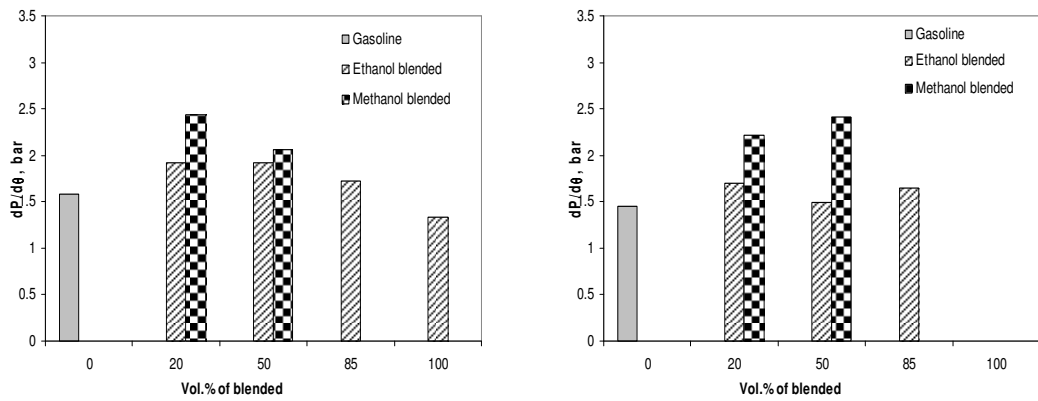
### Peak Pressure



(a) Spark-assisted ignition

(b) Non-spark-assisted ignition

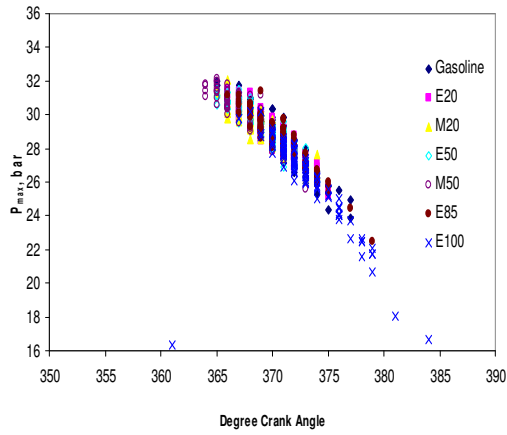
Figure B.6 Peak Pressure for all Fuels



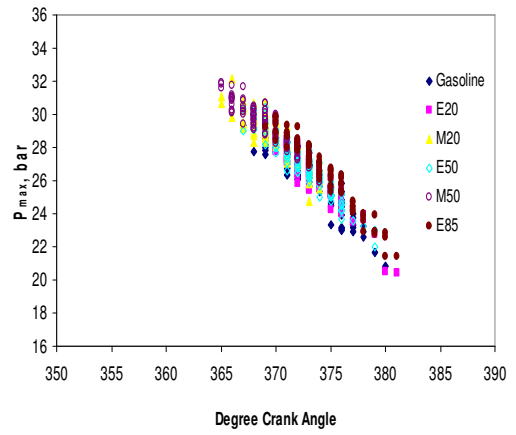
(a) Spark-assisted ignition

(b) Non-spark-assisted ignition

Figure B.7 Maximum of  $\frac{dP}{d\theta}$  for all Fuels

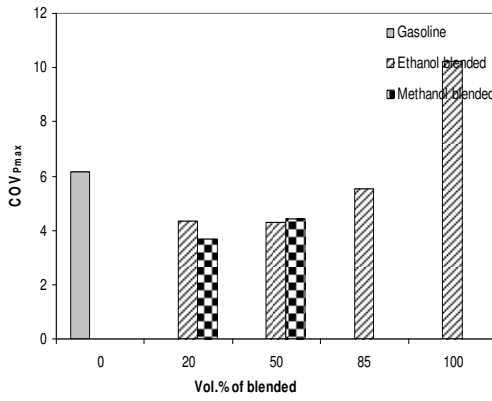


(a) Spark-assisted ignition

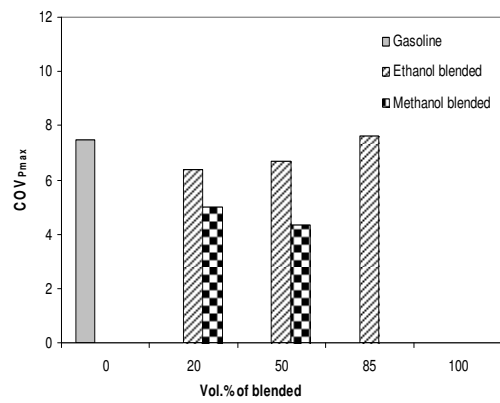


(b) Non-spark-assisted ignition

Figure B.8  $P_{max}$  and  $\theta_{P_{max}}$



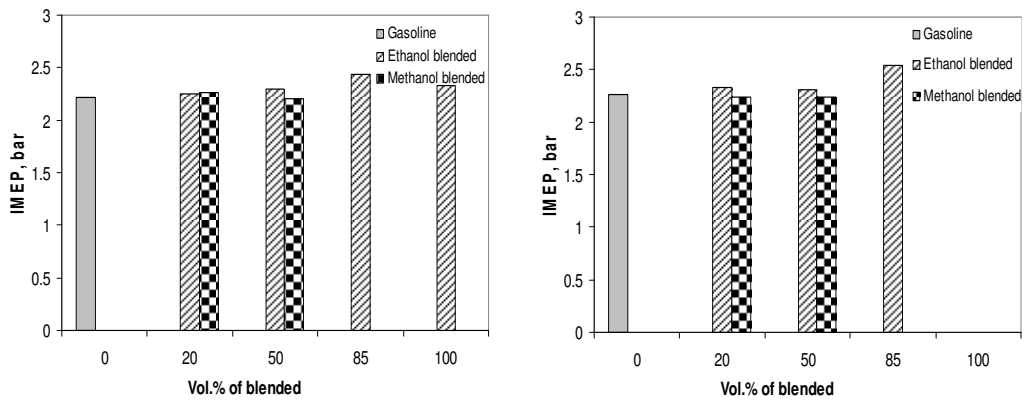
(a) Spark-assisted ignition



(b) Non-spark-assisted ignition

Figure B.9 Coefficient of Variation of Maximum Pressure.

### Indicated Mean Effective Pressure



(a) Spark-assisted ignition

(b) Non-spark-assisted ignition

Figure B.10 Indicated Mean Effective Pressure for all Fuels

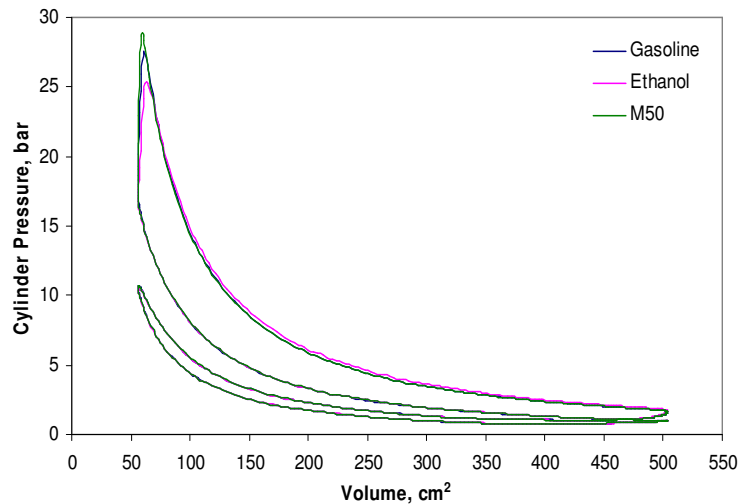
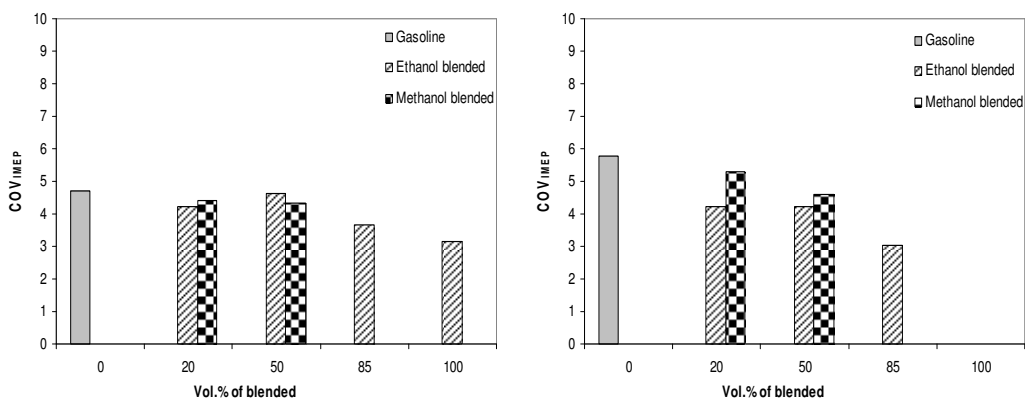


Figure B.11 In-Cylinder Pressures against Volume



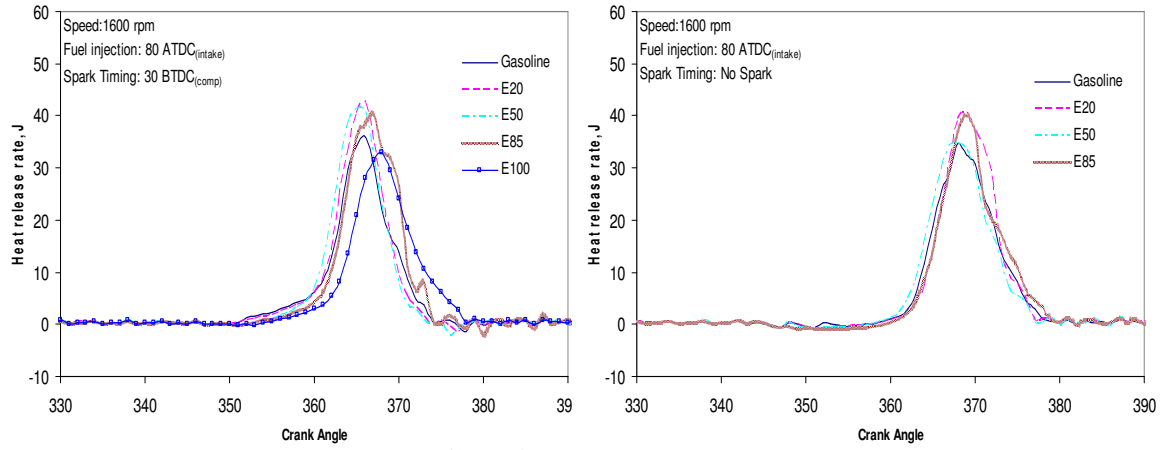
(a) Spark-assisted ignition

(b) Non-spark-assisted ignition

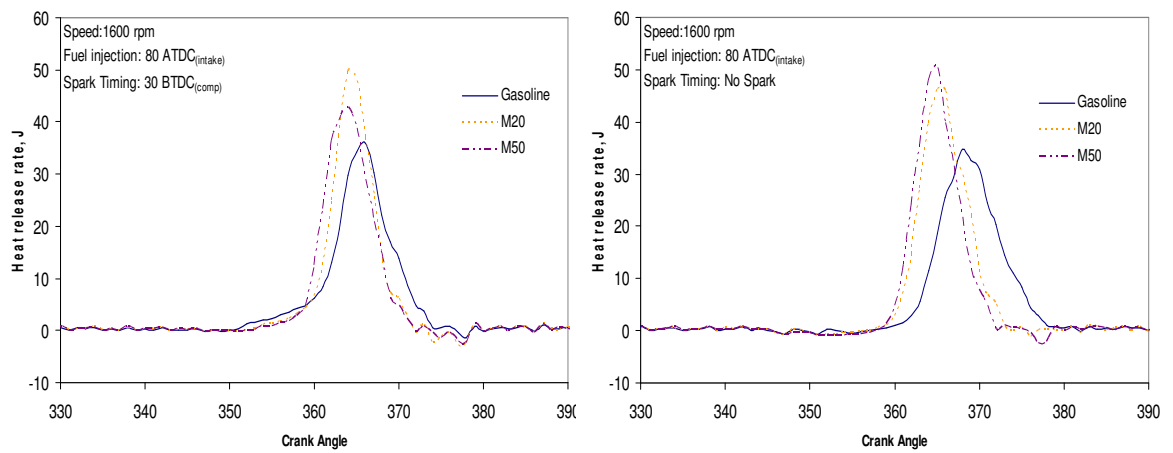
Figure B.12 Coefficient of Variation of Indicated Mean Effective Pressure

## A.2 Thermodynamic and Combustion Characteristics results

### Heat Release Rate



### Gasoline and Ethanol Blended Fuels

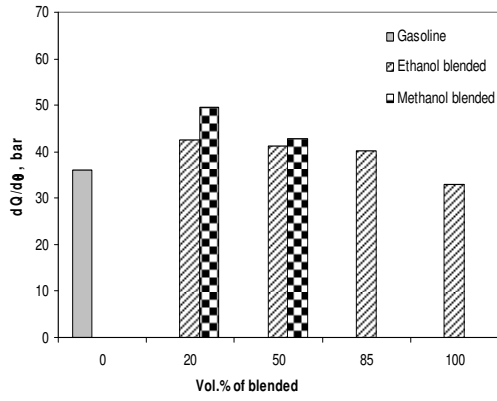


### Gasoline and Methanol Blended Fuels

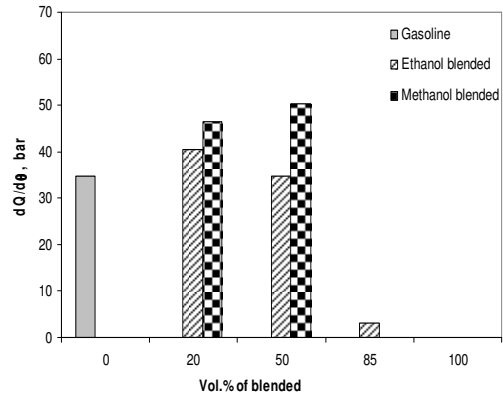
(a) Spark-assisted ignition

(b) Non-spark-assisted ignition

Figure B.13 Heat Release Rate Curves



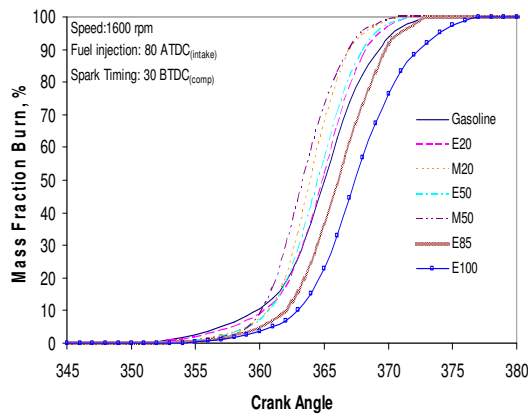
(a) Spark-assisted ignition



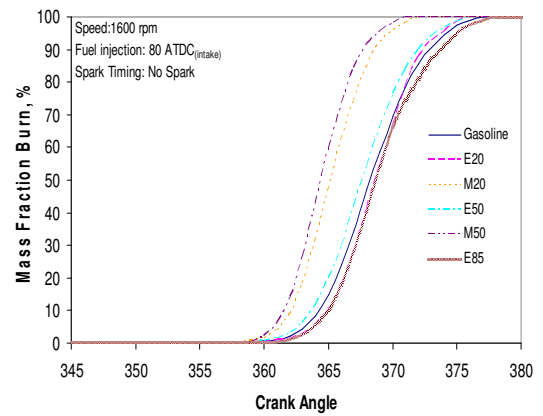
(b) Non-spark-assisted ignition

Figure B.14 Maximum of  $\frac{dQ}{d\theta}$  for All of Fuels

Mass Fraction Burned and Combustion Period

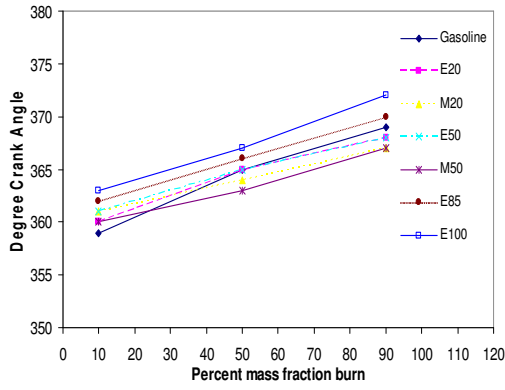


(a) Spark-assisted ignition

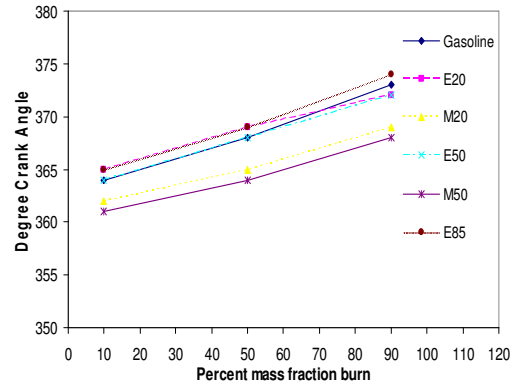


(b) Non-spark-assisted ignition

Figure B.15 Mass Fraction Burned

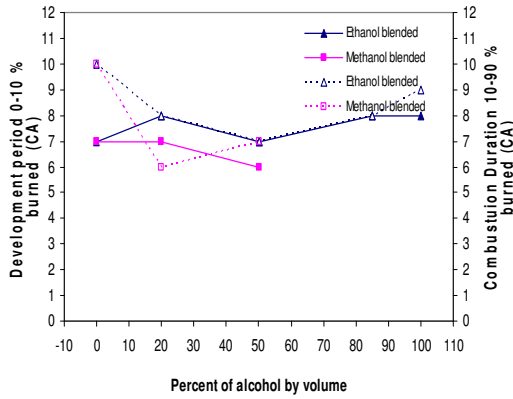


(a) Spark-assisted ignition

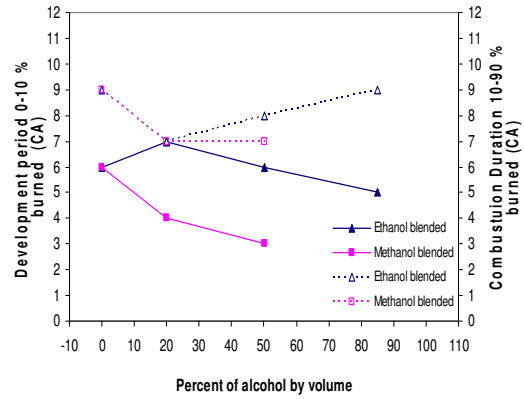


(b) Non-spark-assisted ignition

Figure B.16 Crank Angle at Any Percentage of Mass Fraction Burned



(a) Spark-assisted ignition

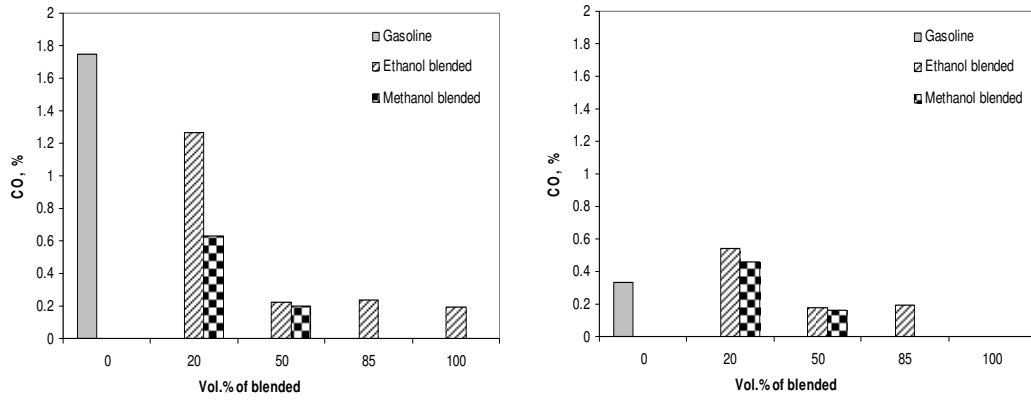


(b) Non-spark-assisted ignition

Figure B.17 Flame Development Period and Combustion Duration

## B.3 Engine-Out Exhaust Emission

### Carbon Monoxide

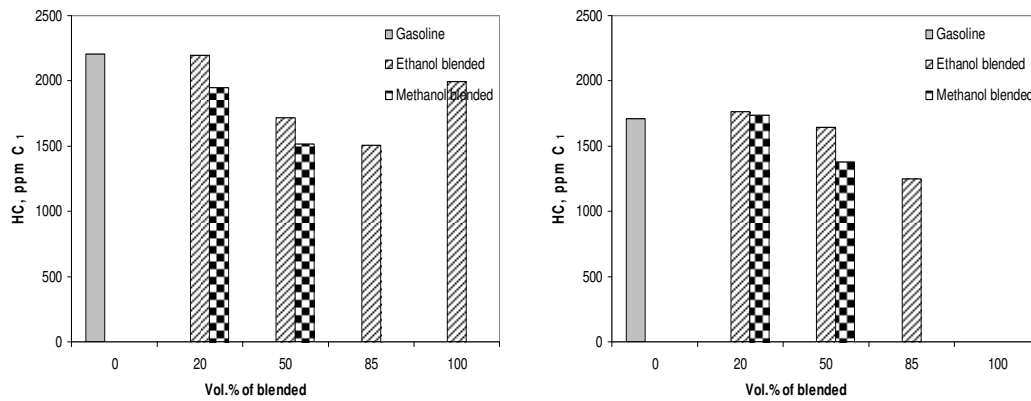


a) Spark-assisted ignition

(b) Non-spark-assisted ignition

Figure B.18 Carbon Monoxide Emissions of All Fuels

### Hydrocarbon

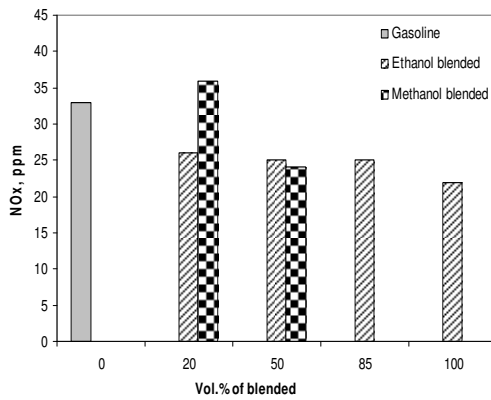


(a) Spark-assisted ignition

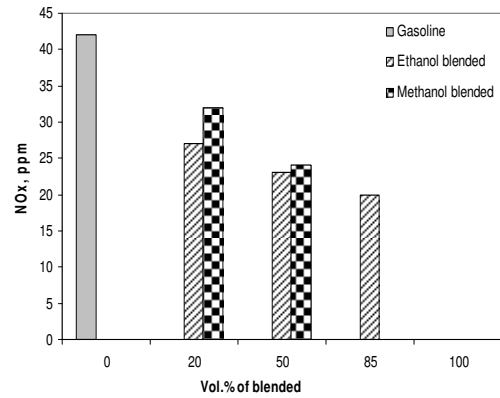
(b) Non-spark-assisted ignition

Figure B.19 Hydrocarbon Emissions of All Fuels

## Oxide of Nitrogen



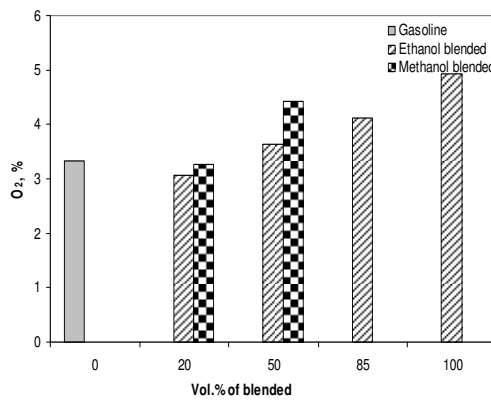
a) Spark-assisted ignition



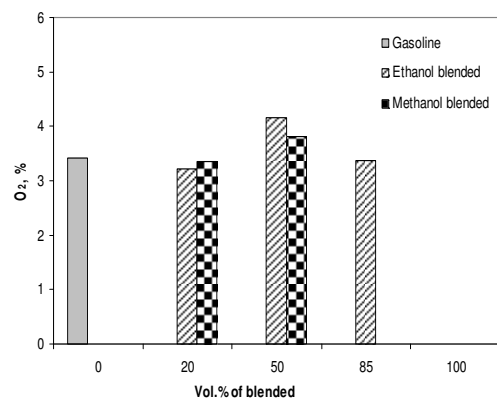
(b) Non-spark-assisted ignition

Figure B.20 Oxide of Nitrogen Emission of All Fuels

## Oxygen



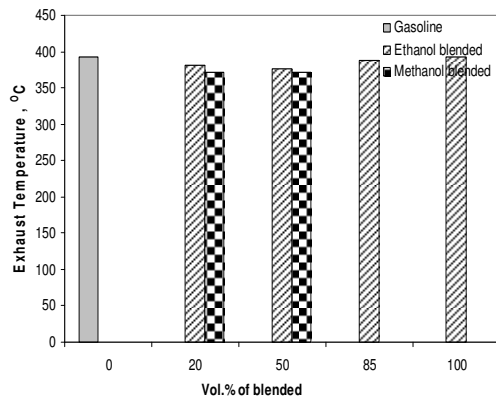
a) Spark-assisted ignition



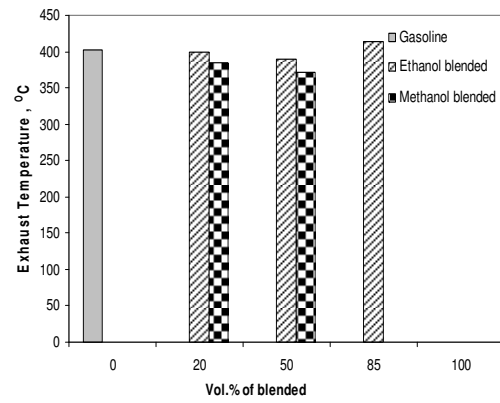
(b) Non-spark-assisted ignition

Figure B.21 Oxygen of all Fuels

## Exhaust Gas Temperature



(a) Spark-assisted ignition

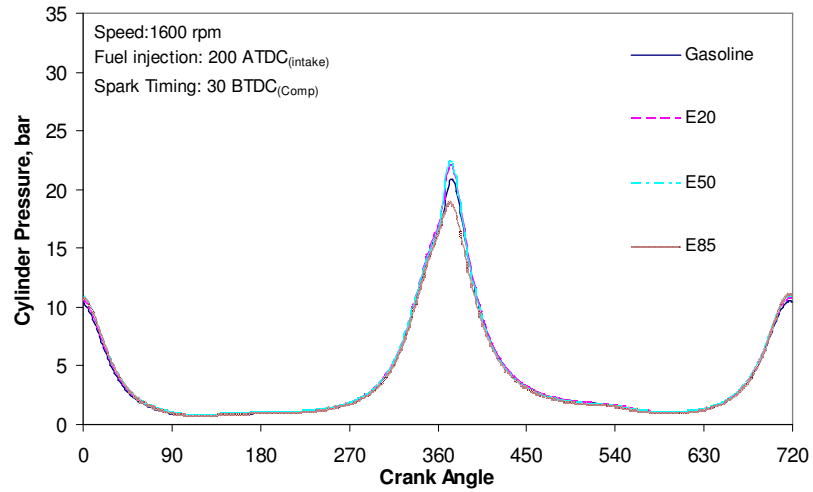


(b) Non-spark-assisted ignition

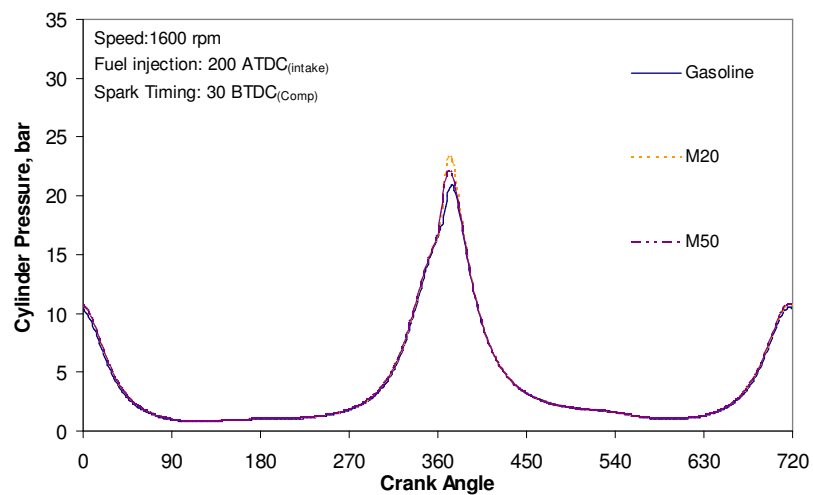
Figure B.22 Exhaust Gas Temperature of All Fuels

## Appendix C Results for Injection Timing at 200 degree ATDC

### C.1 In-cylinder pressure data

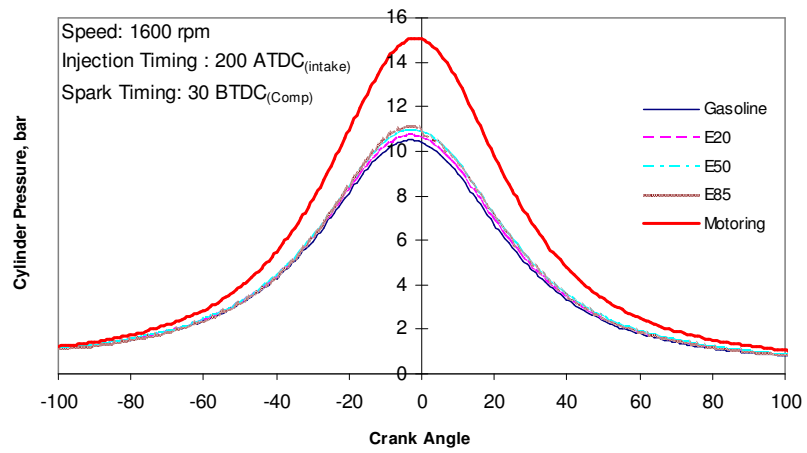


#### Gasoline and Ethanol Blended Fuels

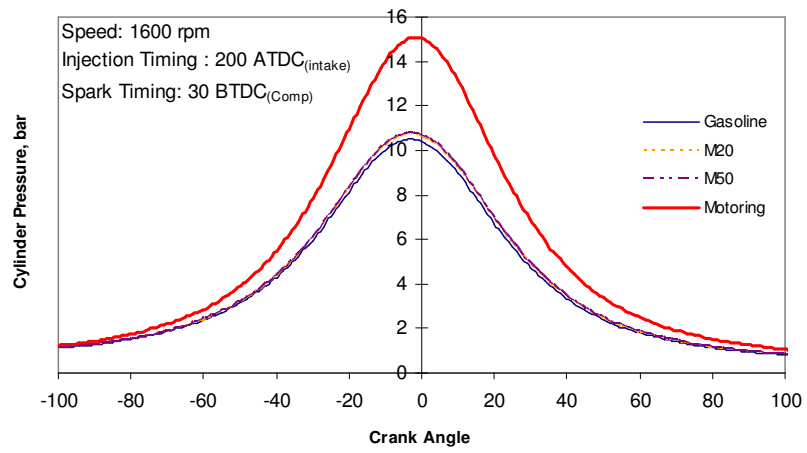


#### Gasoline and Methanol Blended Fuels

Figure C.1 In-Cylinder Pressure Traces with SOI 200 ATDC

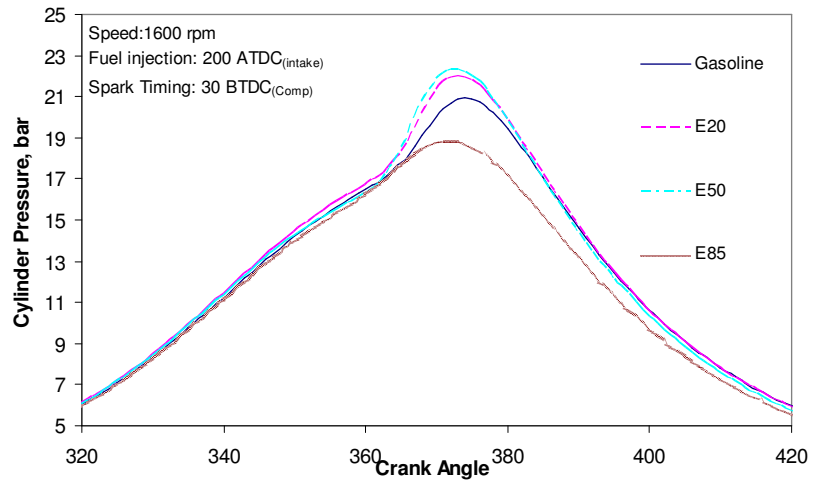


### Gasoline and Ethanol Blended Fuels

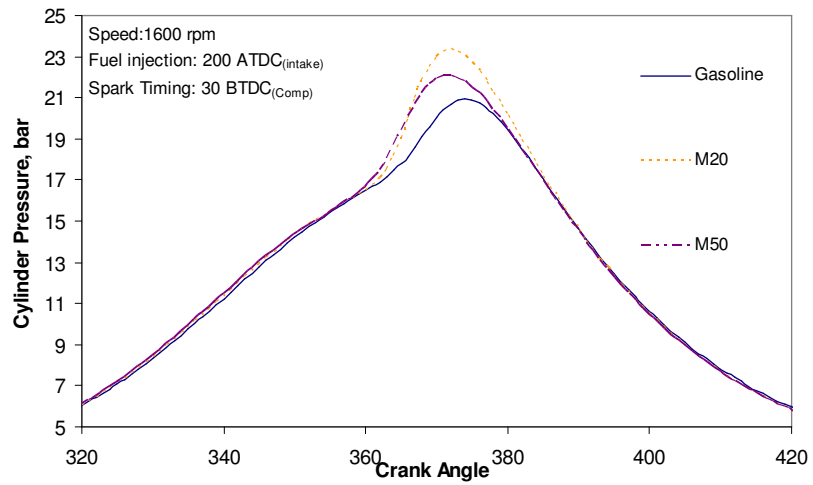


### Gasoline and Methanol Blended Fuels

**Figure C.2 In-Cylinder Pressures during the Negative Overlap Period**



**Gasoline and Ethanol Blended Fuels**



**Gasoline and Methanol Blended Fuels**

**Figure C.3 In-Cylinder Pressures during the Main Combustion**

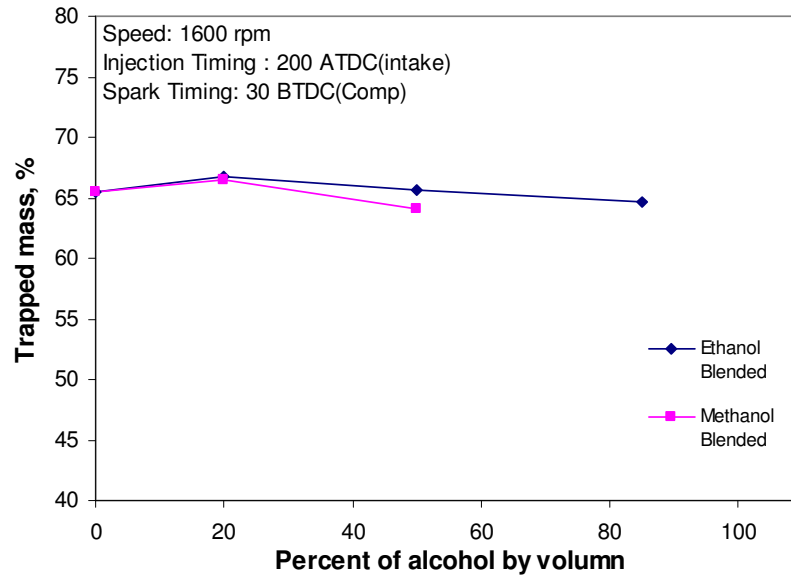


**Figure C.4 Trapped Mass Residual for any Fuels**

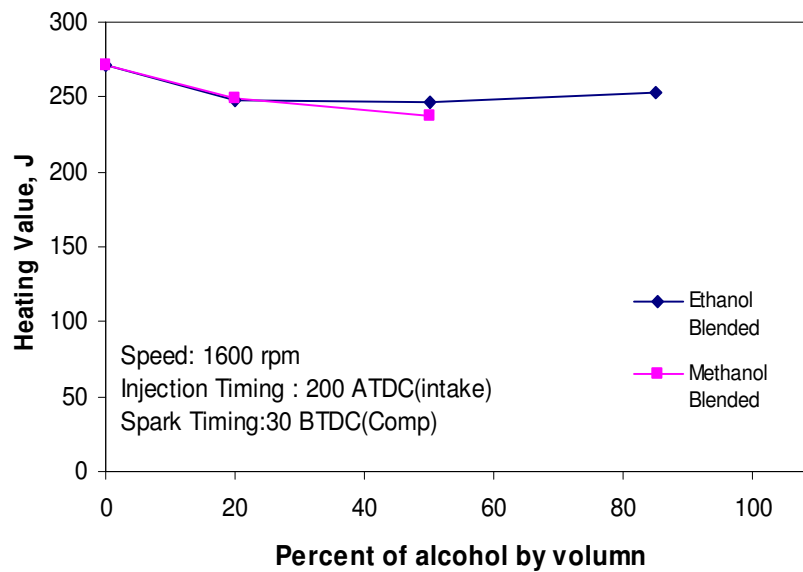


**Figure C.5 Input Energy per Cycle for any Fuels**

## Peak Pressure

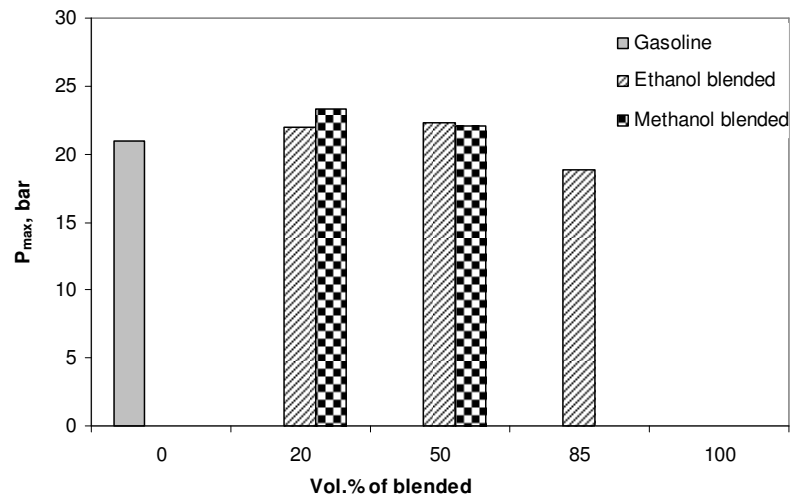


Figure C.6 Peak Pressure for all Fuels

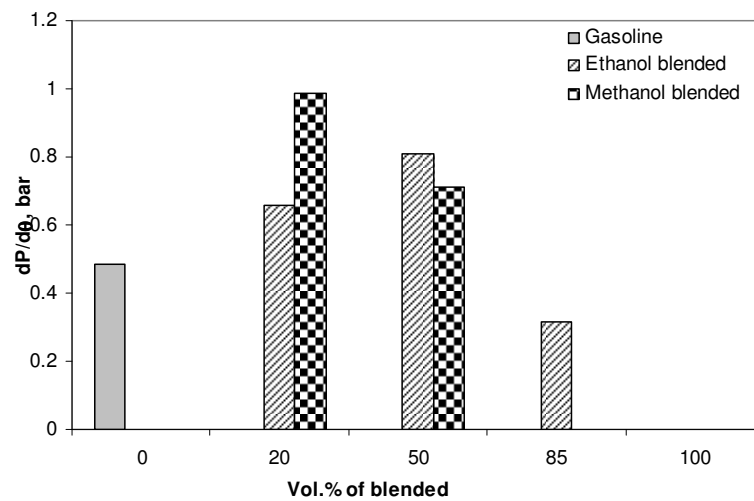
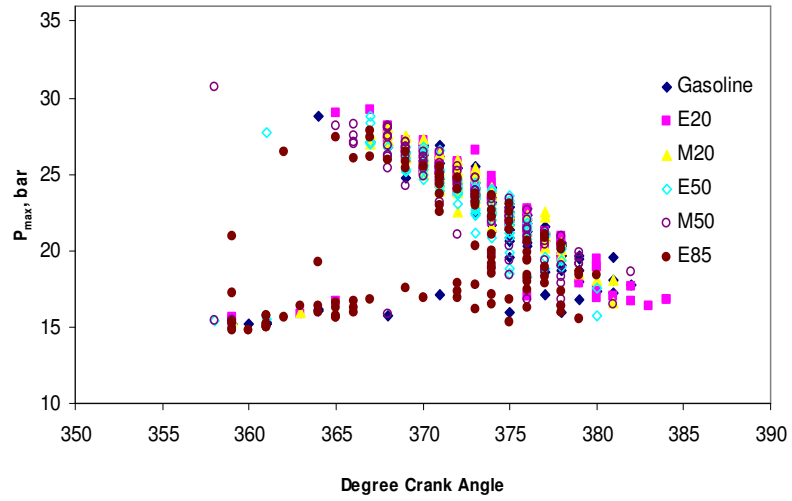
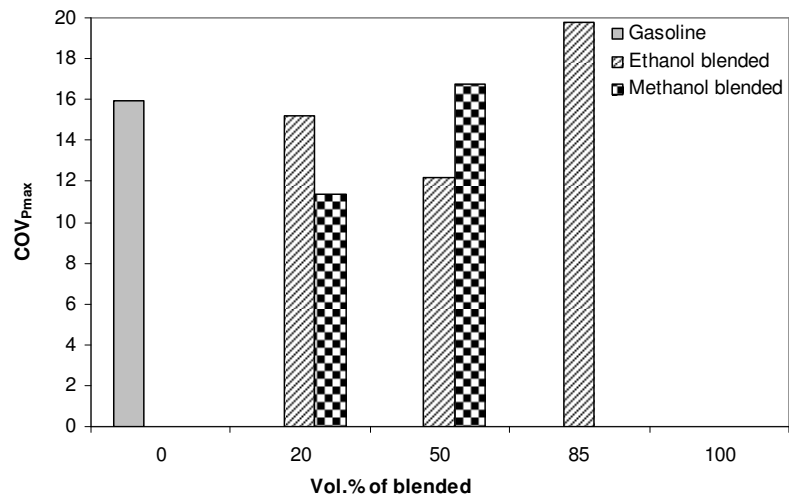


Figure C.7 Maximum of  $\frac{dP}{d\theta}$  for all Fuels



**Figure C.8 Pmax and  $\theta_{Pmax}$**



**Figure C.9 Coefficient of Variation of Maximum Pressure**

### Indicated Mean Effective Pressure

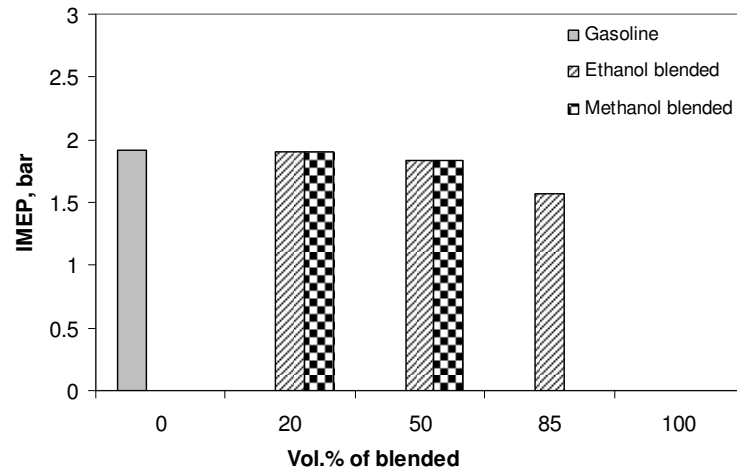


Figure C.10 Indicated Mean Effective Pressure for all Fuels

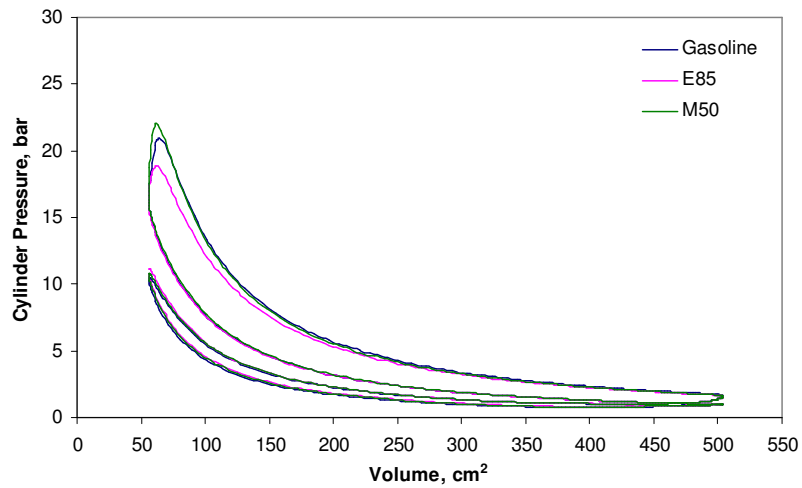


Figure C.11 In-Cylinder Pressures against Volume

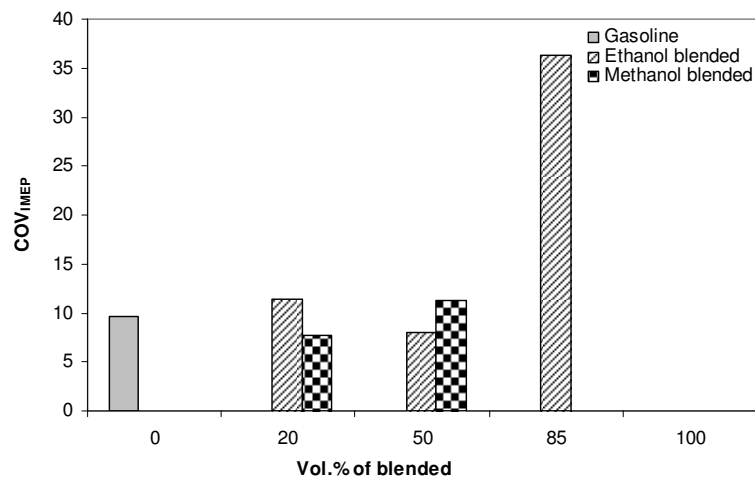
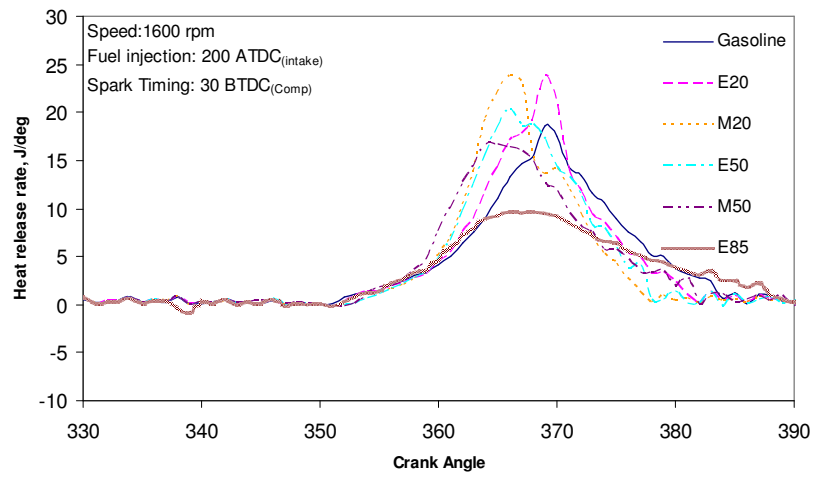


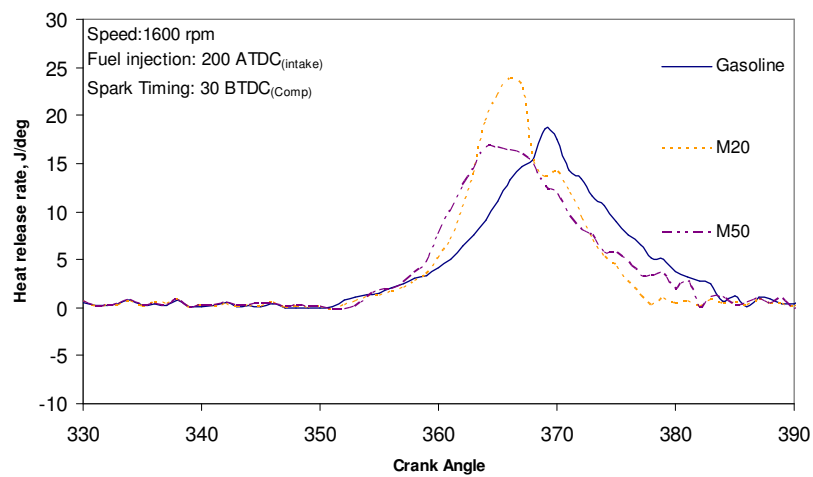
Figure C.12 Coefficient of Variation of Indicated Mean Effective Pressure

## C.2 Thermodynamic and Combustion Characteristics results

### Heat Release Rate

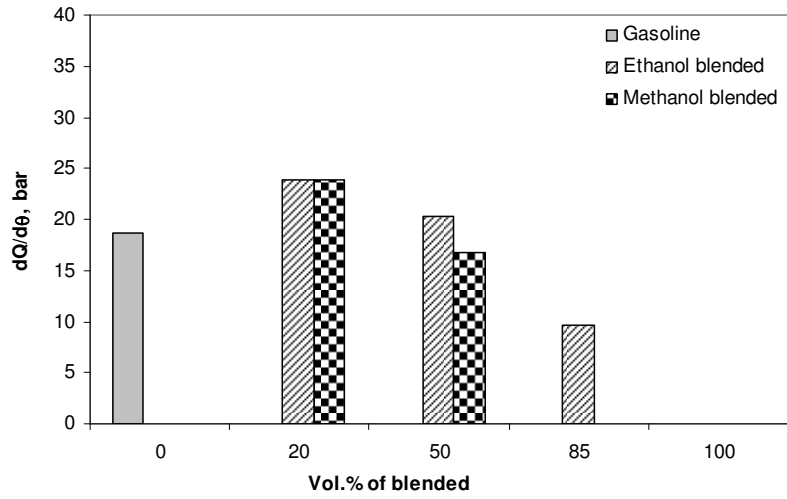


### Gasoline and Ethanol Blended Fuels



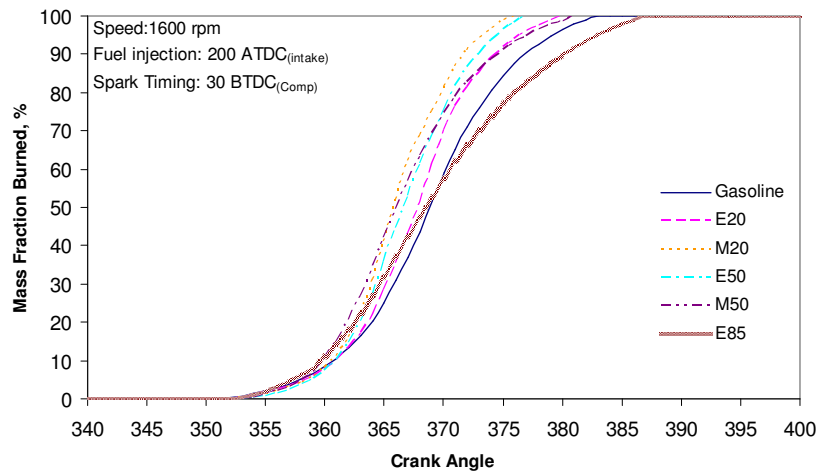
### Gasoline and Methanol Blended Fuels

Figure C.13 Heat Release Rate Curves



**Figure C.14** Maximum of  $\frac{dQ}{d\theta}$  for All Fuels

### Mass Fraction Burned and Combustion Period



**Figure C.15** Mass Fraction Burned

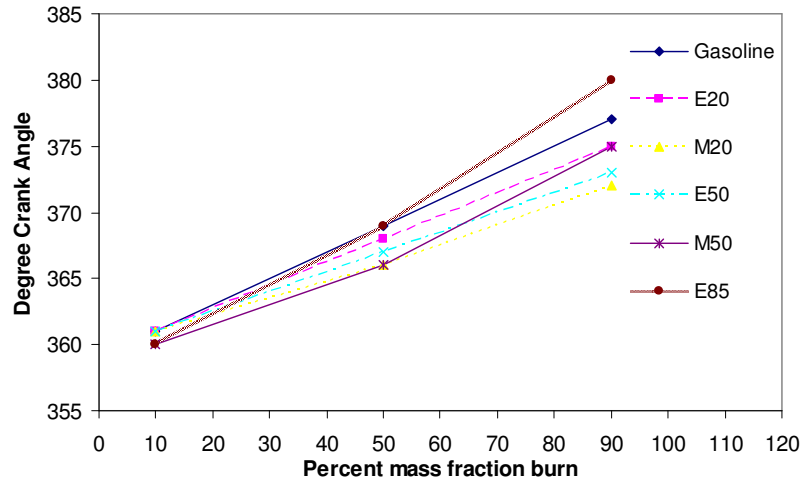


Figure C.16 Crank Angle at Any Percentage of Mass Fraction Burned

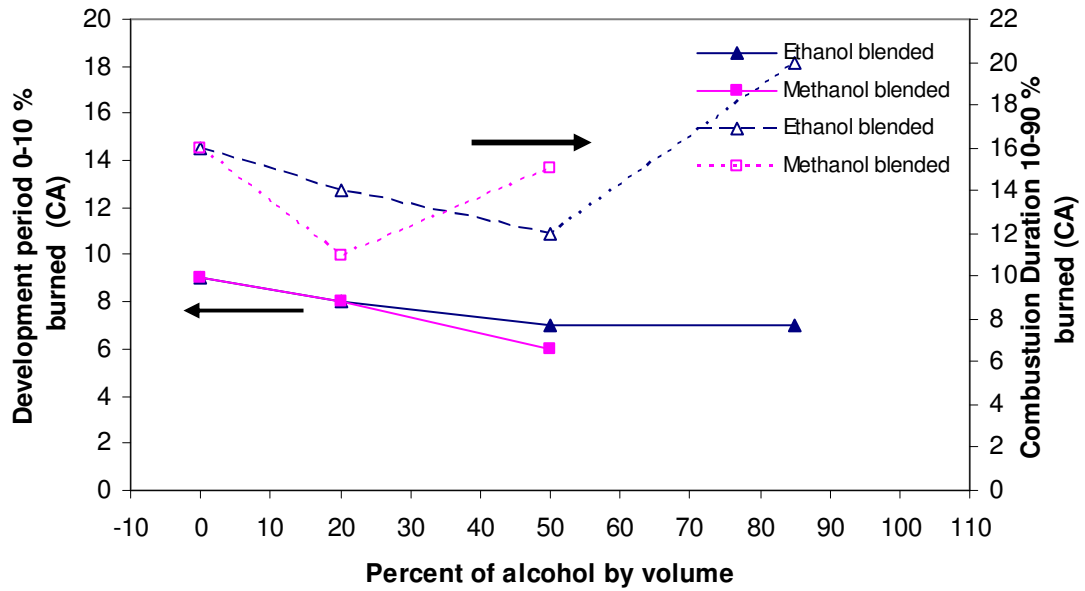


Figure C.17 Flame Development Period and Combustion Duration

### C.3 Engine-Out Exhaust Emission

#### Carbon Monoxide

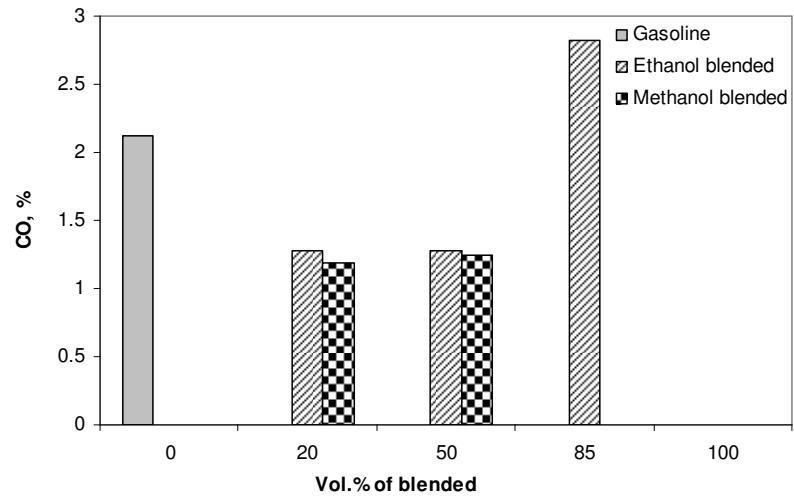


Figure C.18 Carbon Monoxide Emissions of All Fuels

#### Hydrocarbon

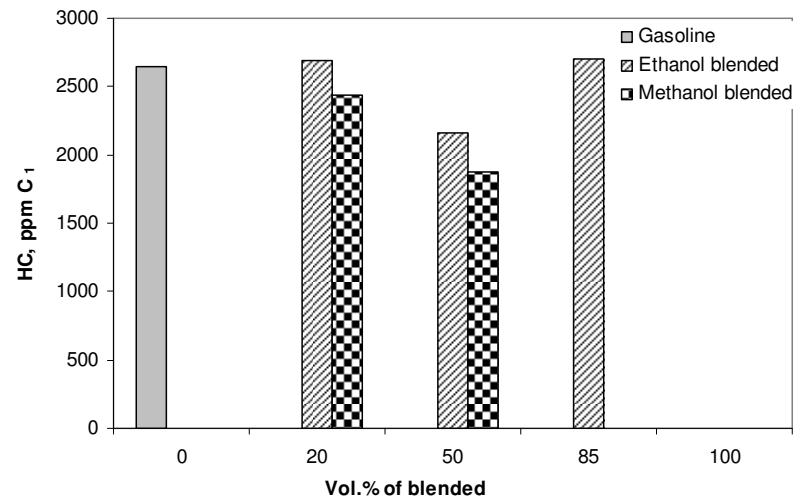


Figure C.19 Hydrocarbon Emissions of All Fuels

## Oxygen

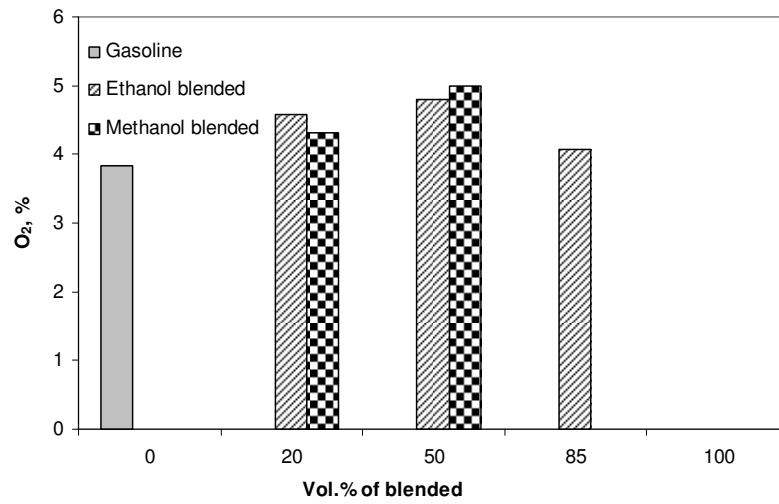


Figure C.20 Oxygen of all Fuels with Spark-Assisted Ignition

## Exhaust Gas Temperature

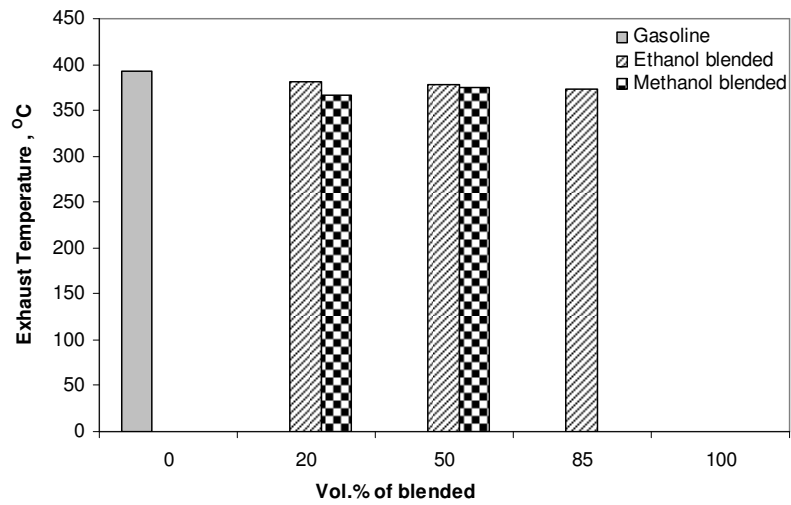


Figure C.21 Exhaust Gas Temperatures of All Fuels